Synthesis of Graphene Quantum Dots (GQDs) and Carbon Quantum Dots (CQDs) for their Sensing Applications

Thesis submitted for the award of degree of

Doctor of Philosophy

by

Aayushi

(Regn. No: 901909001)

Under the supervision of

Dr. Soumen Basu
(Professor)

Dr. Banibrata Maity
(Assistant Professor)

SCHOOL OF CHEMISTRY AND BIOCHEMISTRY

THAPAR INSTITUTE OF ENGINEERING & TECHNOLOGY

PATIALA-147004

September, 2023

Certificate

This is to certify that thesis entitled "**Synthesis of Graphene Quantum Dots (GQDs) and Carbon Quantum Dots (CQDs) for their Sensing Applications**", is being submitted by Ms. Aayushi in fulfilment of the requirement for the award of the Degree of Doctor of Philosophy in the School of Chemistry and Biochemistry, Thapar Institute of Engineering and Technology, Patiala, is a record of candidate's own independent and original research work carried out by her under my supervision and guidance. The matter presented in the thesis has not been submitted in part or full for the award of any degree in any university or institution.

(**Supervisor**)
Dr. Soumen Basu
Professor
School of Chemistry and Biochemistry
TIET, Patiala-147004, Punjab, India

(**Supervisor**)
Dr. Banibrata Maity
Assistant Professor
School of Chemistry and Biochemistry
TIET, Patiala-147004, Punjab, India

11/9/2023

(**Head**)
Prof. Satnam Singh
Professor
School of Chemistry and Biochemistry
TIET, Patiala-147004, Punjab, India

Candidate's Declaration

I, hereby declare that the present work in the thesis entitled **"Synthesis of Graphene Quantum Dots (GQDs) and Carbon Quantum Dots (CQDs) for their Sensing Applications"**, in the fulfillment of the requirement for the award of the Degree of Doctor of Philosophy in the School of Chemistry and Biochemistry, Thapar Institute of Engineering and Technology, Patiala is an authentic record of my work carried out under the supervision of Dr. Soumen Basu, Professor and Dr. Banibrata Maity, Assistant Professor, School of Chemistry and Biochemistry, Thapar Institute of Engineering and Technology, Patiala, India. The matter embodied in the thesis has not been submitted in part or fully to any other University or Institute for the reward of any degree in India or Abroad.

Aayushi

Acknowledgements

First and foremost, I sincerely express my gratitude to the divine power for granting me the fortitude, patience, endurance, and determination to complete this project.

In this section of the thesis, I wish to extend my appreciation to every individual who has played a role in my journey and has made direct or indirect contributions to my research work.

I would like to extend heartfelt thanks to my supervisors, **Prof. Soumen Basu and Dr. Banibrata Maity** for giving me the opportunity to work in this project and for consistently offering unwavering support and encouragement. The invaluable discussions, and continuous guidance provided during the experimental and thesis phase have proven to be immensely advantageous. I am grateful to them for consistently believing in me and motivating me to strive for excellence in all aspects of my life.

I am infinitely thankful to the TIET-Virginia Tech Center of Excellence in Emerging Materials (CEEMS) for the research fellowship.

I am extremely thankful to **Prof. Padmakumar Nair**, Director, and **Prof. N. Tejo Parkash**, Dean of Research & Sponsored Projects. My sincere thanks to **Prof. Satnam Singh**, Professor and Head, School of Chemistry and Biochemistry, Thapar Institute of Engineering and Technology, for his ever-helping nature and best wishes. I would also like to express my sincere regards to my doctoral committee members, **Prof. Kulvir Singh**, **Prof. Bonamali Pal**, and **Prof. Vijay Luxami**, for the scientific discussions and valuable advices that have always been very helpful. I am extremely grateful to **Prof. Roop Lal Mahajan**, Chair Professor TIET-Virginia Tech CEEMS, **Prof. Rajeev Mehta**, Coordinator, and **Prof. Kamaldeep Paul,** Deputy-Coordinator, CEEMS for their perspective comments and suggestions. I express my sincere thanks to Mr. Mayank Sharma and Ms. Mrinmoyee Kanjilal for constant official help and cooperation. I also want to thank Mr. Chander Thakur, Mr. Hemant Sharma, Mr. Vishwanath, Mr. Shekhar for their support.

I would like to express my gratitude to all the individuals and organizations who provided instrumental facilities for my research; SAI Labs at TIET Patiala, SPMS at TIET Patiala, CEEMS at TIET, CIL at PU Chandigarh, and IIT Roorkee. I also want to acknowledge all the faculty members in the School of Chemistry and Biochemistry for their cooperation and

support. Additionally, I extend thanks to Prof. Vijay Luxami for lifetime facility and Prof. B.N. Chudasama for zeta potential analysis. Special thanks to Dr. Raj Kumar Das for helping me in XPS analysis.

I heartfully extend my thanks to Dr. Neeraj who always helped and motivated me as an elder sister and frequently came up in discussions of my work. I especially want to acknowledge Dr. Surbhi, who has taught me to be optimistic in adversity and has always inspired me to excel in all aspects. I am thankful to all my lab seniors, Dr. Shagun, Dr. Aanchal, Dr. Aashna, Dr. Divya, and Dr. Zaid. I also want to thank my lab mates Dr. Shelly, Ranjeet Jha, Pritam, Mandeep Kaur, and Mallika for great time, moral support, and co-operation. I am truly grateful to Parminder Singh and Sandeep Nain who motivated and supported me as an elder brother. I will always be thankful to Sahil, Sukhpreet, Arzoo, Nidhi, Anushka, Akanksha, Nikhil, Jaydeep, Vikash, Smriti, Priya, and Geetika for their precious friendship. I also want to thank all my friends, specially, Anshu Malik, Sanya Singh, Jaideep Gujral, Dr. Neha, Swell Nain, Raman Poswal, Vicky Yadav, and Akanksha Kharub for always believing in me. Special thanks to all the lab members of G-133 (Organic Synthesis Lab). I am also grateful to Amritpal Singh for his help.

My Ph.D. journey was undoubtedly a once-in-a-lifetime experience and a massive learning experience for me in every way, making me a lot stronger person.

My final and truly the most special ‘thank you’ is for my parents; **Mrs. Anju** and **Mr. Shamsher Singh**. I want to acknowledge the unmatchable support and unconditional love extended by them. They always kept faith in me and let me do things my way and were always there for me in every high and low phase of my life. My father is truly my biggest supporter. It is absolute truth that behind every successful girl, there is a progressive and supportive father. My heartfelt gratitude and biggest credit go to my younger brother; **Aditya**, who has been an unwavering source of support throughout my research journey. He never let me fall and I always had his back. I know that he would be the happiest to see me reaching new heights. I don’t think I would ever be able to repay whatever these ‘three pillars of my strength’ have done for me. I also want to thank my other family members for their blessings and best wishes.

I am eternally thankful to everyone who has been a part of my journey and has knowingly or unknowingly helped me accomplish this work.

This thesis is dedicated to my brother, Aditya

TABLE OF CONTENTS

List of Figures	i
List of Tables	vii
List of Schemes	x
List of Abbreviations	xi
List of Symbols	xiii
Abstracts	xiv

Chapter 1

Introduction and Literature

1.1 Background	1
1.1.1 Nanomaterials	1
1.1.2 Carbon-Based Nanomaterials	1
1.1.3 Carbon Dots (CDs)	2
1.1.3.1 Graphene Quantum Dots (GQDs)	2
1.1.3.2 Carbon Quantum Dots (CQDs)	2
1.1.4 Nanosensor	3
1.1.5 Optical Properties of GQDs and CQDs	5
1.1.6 Synthesis Methods	8
1.1.7 Fluorescence Quenching Mechanism	9
1.1.8 Fluorescence Restoration Mechanism	12
1.1.9 Coal-Derived GQDs	13
1.1.10 Importance of Natural Resources-Derived CQDs	14
1.1.11 Sensing Application (Detection of Various Analytes)	15
1.2 Research Gaps	18
1.3 Objectives	18
References	18

Chapter 2

Coal-derived Graphene Quantum Dots with Mn^{2+}/Mn^{7+} Nanosensor for Selective Detection of Glutathione

2.1 Introduction	31
2.2 Experimental Section	32
2.2.1 Materials	32
2.2.2 Synthesis of GQDs	32
2.2.3 Characterizations	33
2.2.4 Preparation of Sample Solutions	33
2.3 Results and Discussions	34
2.3.1 Characterizations	34
2.3.2 Optical Properties	36
2.3.3 Effect of Irradiation Time, pH, Temperature	38
2.3.4 Selectivity Studies of Different Metal Ions	39
2.3.5 Fluorescence Quenching of GQDs by Mn^{n+} Ions (n=2,7)	40
2.3.6 Fluorescence Quenching of A and B-GQDs by Mn^{2+} Ions	42
2.3.7 Fluorescence Quenching of A and B-GQDs by Mn^{7+} Ions	44
2.3.8 Fluorescence Restoration of GQDs and GSH Detection	45
2.3.9 Selectivity and Sensitivity Studies of Different Analytes for Fluorescence Restoration	48
Conclusions	51
References	51

Chapter 3

Rice-Husk Derived Carbon Quantum Dots-Based Dual-Mode Nanoprobe for Selective and Sensitive Detection of Fe^{3+} and Fluoroquinolones

3.1 Introduction	57
3.2 Experimental Section	59
3.2.1 Materials and Reagents	59

3.2.2 Synthesis of Rice Husk-Carbon Quantum Dots (RH-CQDs) 59
3.2.3 Characterizations 60
3.2.4 Methodology of Metal Ion Sensing 60
3.2.5 Sensing of Tablet Supplement 60
3.3 Results and Discussions 61
3.3.1 Characterizations 61
3.3.2 Optical Properties of RH-CQDs 63
3.3.3 Stability Studies of RH-CQDs 64
3.3.4 Method Validation 65
3.3.4.1 Linearity and Range 65
3.3.4.2 Limit of Detection and Limit of Quantification 66
3.3.4.3 Binding Efficacy 67
3.3.4.4 Precision and Accuracy 67
3.3.4.5 Robustness 67
3.3.5 Selectivity Studies for Detection of Fe^{3+} Ions 68
3.3.6 Plausible Reason of High Selectivity of RH-CQDs with Fe^{3+} Ions 69
3.3.7 Sensitivity Studies for Detection of Fe^{3+} Ions 69
3.3.8 Fluorescence Quenching Mechanism 71
3.3.9 Detection of Fe^{3+} in Tablet Supplement 71
3.3.10 Detection of Fluoroquinolone with Fluorescence Enhancement Technique 72
3.3.11 Selectivity Measurements 76
3.3.12 Plausible Mechanism for Fluorescence Restoration 76
Conclusions 78
References 78

Chapter 4

Orange Pomace Derived Fluorescent Carbon Quantum Dots: Detection of Cr (VI) and 4-Nitrophenol in Nanomolar Range

4.1 Introduction 86
4.2 Experimental Section 87

4.2.1 Materials 87
4.2.2 Synthesis of Orange Pomace-Derived CQDs 87
4.2.3 Characterizations 88
4.2.4 Sample Solutions Preparation 88
4.2.5 Real Sample Analysis 89
4.3 Results and Discussions 89
4.3.1 Characterizations 89
4.3.2 Optical Properties 91
4.3.3 Stability Studies of CQDs 92
4.3.4 Selectivity Studies for Cr (VI) Ions 93
4.3.5 Plausible Reason for High Selectivity of Cr (VI) Ions 94
4.3.6 Method of Validation 95
4.3.6.1 Linearity and Range 95
4.3.6.2 Limit of Detection and Limit of Quantification 95
4.3.6.3 Binding Efficiency 97
4.3.6.4 Analysis of Precision 97
4.3.7 Sensitivity Studies for Detection of Cr (VI) Ions 97
4.3.8 Possible Fluorescence Sensing Mechanism of Cr (VI) Ions 98
4.3.9 Analysis of Real Samples 99
4.3.10 Detection of 4-Nitrophenol (4-NP) 99
4.3.10.1 Selectivity Studies 99
4.3.10.2 Sensitivity Studies of 4-NP 100
4.3.10.3 Quenching Mechanism 102
4.3.10.4 Real Sample Analysis for Method Validation 103
Conclusions 104
References 104

Chapter 5

Upcycling Waste: *Citrus limon* peels derived Carbon Quantum Dots for Sensitive Detection of Tetracycline in Nanomolar Range

5.1 Introduction 112

5.2 Experimental Section 113
5.2.1 Materials and Methods 113
5.2.2 Synthesis of Lemon Peel-Carbon Quantum Dots (LP-CQDs) 113
5.2.3 Characterizations 114
5.2.4 Sample Solution Formulation 114
5.2.5 Real Sample Analysis 115
5.3 Results and Discussions 115
5.3.1 Characterizations 115
5.3.2 Optical Studies of LP-CQDs 117
5.3.3 Stability Studies 118
5.3.4 Method Validation 119
5.3.4.1 Linearity and Range 120
5.3.4.2 Limit of Detection and Limit of Quantification 120
5.3.4.3 Binding Efficiency 121
5.3.4.4 Precision Analysis 122
5.3.5 Sensing of Tetracycline by LP-CQDs 122
5.3.6 Quenching Mechanism 124
5.3.7 Real Sample Analysis 125
5.3.8 Application of the Synthesized LP-CQDs as Fluorescent Ink 126
Conclusions 127
References 127

Conclusions and Future Perspectives 132
List of Publications 134
Conferences and Workshops 136

LIST OF FIGURES

Figure No.	Title	Page No.
	Chapter 1	
Figure 1.1	Structural depiction of GQDs.	2
Figure 1.2	Structure of CQDs.	3
Figure 1.3	Working scheme of nanosensor.	4
Figure 1.4	The PL mechanism of GQDs/CQDs based on band-gap transitions of conjugated π-π bonds or surface defects.	6
Figure 1.5	PL mechanism showing excitation-dependent and excitation-independent emission.	7
Figure 1.6	Quenching mechanism of GQDs/CQDs.	11
Figure 1.7	Representation of fluorescence restoration mechanism.	13
	Chapter 2	
Figure 2.1	TEM and inset HR-TEM image of (a) A-GQDs, (b) B-GQDs; the size distribution histogram of (c) A-GQDs, and (d) B-GQDs.	34
Figure 2.2	XRD spectra of (a) A-GQDs, (b) B-GQDs, FTIR spectra of (c) A-GQDs and (d) B-GQDs.	35
Figure 2.3	(a) XPS survey scan of A-GQDs, (b) high-resolution spectra of C 1s of A-GQDs, (c) O 1s of A-GQDs and B-GQDs, (d) survey spectrum of B-GQDs, (e) C 1s of B-GQDs, and (f) N 1s of B-GQDs.	36
Figure 2.4	(a) EDX spectra of A-GQDs, (b) B-GQDs, (c) UV-Visible spectra of A-GQDs and B-GQDs, (d) PL spectra of A-GQDs, and (e) B-GQDs.	37
Figure 2.5	PL spectra of (a) A-GQDs, (b) B-GQDs at different excitation wavelength.	37
Figure 2.6	The effect of irradiation time on the PL intensity of (a) A-GQDs, and (b) B-GQDs.	38

Figure 2.7	Effect of pH on (a) A-GQDs, (b) B-GQDs, effect of temperature on the fluorescence of (c) A-GQDs, and (d) B-GQDs.	39
Figure 2.8	Fluorescence response studies of (a) A-GQDs, (b) B-GQDs with cations, (c) A-GQDs, and (d) B-GQDs with anions.	40
Figure 2.9	Fluorescence quenching spectra of (a) A-GQDs in the presence of Mn^{2+}, (b) B-GQDs in the presence of Mn^{2+}, (c) A-GQDs in presence of Mn^{7+}, and (d) B-GQDs in the presence of Mn^{7+}.	41
Figure 2.10	UV-Visible absorption spectrum of A-GQDs and B-GQDs before and after the addition of (a) Mn^{2+}, (b) Mn^{7+}, Time-resolved fluorescence emission decays of (c) A-GQDs with Mn^{2+} and GSH, and (d) B-GQDs with Mn^{7+} and GSH.	42
Figure 2.11	Stern-Volmer quenching plot of (a) A-GQDs with Mn^{2+} quencher, (b) B-GQDs with Mn^{2+}, B-H binding plot of (c) A-GQDs with Mn^{2+}, and (d) B-GQDs with Mn^{2+}.	43
Figure 2.12	Stern-Volmer quenching plot of (a) A-GQDs with Mn^{7+} quencher, (b) B-GQDs with Mn^{7+}, B-H binding plot of (c) A-GQDs with Mn^{7+}, and (d) B-GQDs with Mn^{7+}.	44
Figure 2.13	Bar graph showing comparison study of quenching and turn-on of (a) A-GQDs and B-GQDs with Mn^{2+}, (b) A-GQDs and B-GQDs with Mn^{7+}.	45
Figure 2.14	Fluorescence restoration of (a) A-GQDs with Mn^{2+}, (b) B-GQDs with Mn^{2+}, c) A-GQDs with Mn^{7+}, and (d) B-GQDs with Mn^{7+} upon addition of GSH.	46
Figure 2.15	B-H binding plot of (a) A-GQDs with Mn^{2+}, (b) B-GQDs with Mn^{2+}, c) A-GQDs with Mn^{7+}, and (d) B-GQDs with Mn^{7+} in presence of GSH.	48
Figure 2.16	Fluorescence response of (a) A-GQDs with Mn^{2+}, (b) B-GQDs with Mn^{2+}, c) A-GQDs with Mn^{7+}, and (d) B-GQDs with Mn^{7+} as a sensing system towards various analytes.	49
Figure 2.17	Fluorescence response of (a) A-GQDs, (b) B-GQDs in presence of GSH.	49
Figure 2.18	A plot of fluorescence response of (a) A-GQDs-Mn^{2+}, (b) B-GQDs-Mn^{2+}, (c) A-GQDs-Mn^{7+}, and (d) B-GQDs-Mn^{7+} systems $[(F-F_0)/F_0]$ vs. GSH concentration.	50

Chapter 3

Figure 3.1	(a) XPS survey spectrum of RH-CQDs, (b) High-resolution C 1s spectrum, (c) O1s, and (d) FT-IR spectra of RH-CQDs.	61
Figure 3.2	EDX Spectra of (a) Rice husk (RH), and (b) Rice husk carbon (RHC).	62
Figure 3.3	(a) HR-TEM image of RH-CQDs with inset showing lattice spacing, (b) TEM image of agglomerated particles with inset size distribution histogram, and (c) lattice fringes in the synthesized RH-CQDs.	62
Figure 3.4	(a) Raman spectrum of RH-CQDs exhibiting D and G bands, (b) UV-Visible absorption spectrum of RH-CQDs with inset image showing RH-CQDs under visible and UV light illumination, and (c) PL excitation and emission spectra of RH-CQDs.	63
Figure 3.5	(a) PL emission spectra of RH-CQDs at different excitation wavelengths (280-410 nm), (b) effect of pH (1-13) on PL intensity, (c) effect of irradiation time (mins), and (d) impact of storage time (days) on the fluorescence stability of RH-CQDs.	65
Figure 3.6	(a) PL quenching spectrum of RH-CQDs with different concentration of Fe^{3+}, and (b) linear plot of F_0/F with Fe^{3+} ions (0-1300 nM).	65
Figure 3.7	(a) B-H binding plot of RH-CQDs with quencher (Fe^{3+}), and (b) selectivity study of RH-CQDs on addition of different metal ions.	67
Figure 3.8	Time-resolved fluorescence emission decays of RH-CQDs in presence of Fe^{3+}, OFX, CPX.	70
Figure 3.9	(a) Fluorescence quenching spectra with distinct concentrations of Fe^{3+}, and (b) linear plot of F_0/F and Fe^{3+}concentrations in tablet supplement.	72
Figure 3.10	Fluorescence enhancement spectra of RH-CQDs in presence of (a) OFX, (b) CPX, (c) linear plot of F_0-F/F_0 with OFX (0-1150 nM), and (d) linear relationship of F_0-F/F_0 with different concentrations of CPX.	73
Figure 3.11	B-H binding plot of RH-CQDs with (a) OFX, (b) CPX, and (c) selectivity studies of RH-CQDs with different analytes.	75
Figure 3.12	Interaction of test system with increasing the proportion of	77

	aprotic solvent (a) DMF, (b) DMSO, (c) ACN.	

Chapter 4

Figure 4.1	(a) Survey spectra of CQDs, (b) high-resolution spectra of C 1s, (c) N 1s, and (d) O 1s of CQDs.	89
Figure 4.2	(a) FT-IR graph of CQDs, (b) Zeta potential, and (c) XRD spectra of CQDs.	90
Figure 4.3	(a) TEM image at 100 nm scale and (b) 50 nm scale inset showing size distribution histogram of CQDs.	91
Figure 4.4	(a) DLS size distribution, (b) Raman spectra of CQDs with inset showing 2D band, (c) UV-Vis absorption spectrum with inset showing CQDs exposed to visible and ultraviolet light, and (d) fluorescence emission spectrum of as-prepared CQDs.	92
Figure 4.5	(a) Spectra of PL emission at different excitation wavelengths, (b) impact of time (mins), (c) effect of storage duration (days) on CQDs PL stability, and (d) effect of pH (3-13) on the stability of CQDs.	93
Figure 4.6	CQDs selectivity tests using (a) various metal cations, and (b) metal anions.	94
Figure 4.7	Effect of pH on the performance of the sensors for the selective detection of Cr^{6+}.	94
Figure 4.8	(a) Variation in fluorescence intensity of CQDs with a distinct concentration of Cr^{6+} ions, (b) Stern-Volmer quenching plot of CQDs with Cr^{6+}, (c) linear relation among PL response (F_0-F/F_0) and Cr^{6+} ions (0-480 nM), and (d) B-H binding plot of CQDs with Cr^{6+}.	96
Figure 4.9	(a) Overlapping of absorption spectra of Cr^{6+} ions with the excitation and emission spectrum of CQDs, and (b) PL lifetime decay of CQDs with Cr^{6+}.	98
Figure 4.10	(a) Interference analysis of CQDs for 4-NP ions, and (b) effect of pH on the performance of the sensors for the selective detection of 4-NP.	100
Figure 4.11	(a) Change in PL intensity of CQDs with distinct concentrations of 4-NP ions, (b) linear relation between PL response (F_0-F/F_0) and concentrations of 4-NP ions (0-840 nM) with the inset image of F_0-F/F_0 vs conc. of 4-NP (0-90 nM), (c) linear relation amid PL response (F_0/F) and 4-NP concentrations, and (d) B-H binding plot of CQDs with 4-NP.	101

Figure 4.12	(a) Overlapping of 4-NP absorption spectrum with CQDs excitation and emission spectrum, and (b) PL lifetime decay of CQDs with 4-NP.	103

Chapter 5

Figure 5.1	(a) TEM image of LP-CQDs with inset representing size distribution histogram, (b) TEM image with inset showing lattice spacing, (c) XRD spectrum, and (d) FT-IR spectra of LP-CQDs.	115
Figure 5.2	(a) Survey graph of LP-CQDs, High resolution spectrum of (b) C 1s, (c) O 1s, and (d) N1s of LP-CQDs.	116
Figure 5.3	(a) Raman spectrum of LP-CQDs, (b) UV-Vis absorption spectra with inset showing LP-CQDs in UV and Visible light, and (c) excitation and emission spectra of LP-CQDs.	117
Figure 5.4	(a) PL emission spectra of LP-CQDs under various excitation wavelengths, (b) influence of pH (2-13) on PL emission behavior of LP-CQDs, (c) impact of irradiation time (in mins), and (d) effect of storage time (in days) on the fluorescence emission of LP-CQDs.	118
Figure 5.5	(a) Effect of temperature and (b) storage conditions on the fluorescence stability of LP-CQDs.	119
Figure 5.6	(a) Change in fluorescence intensity of LP-CQDs with the change in concentrations of TC, (b) Stern-Volmer plot of LP-CQDs, (c) linear relation between fluorescence response (F_0-F/F_0) and different concentrations of TC with inset image showing TC structure, and (d) B-H plot of TC with LP-CQDs.	120
Figure 5.7	(a) Selectivity studies of LP-CQDs towards different analytes, (b) selectivity studies of LP-CQDs with different metal ions, and (c) interreference study with and without TC with diverse analytes.	122
Figure 5.8	Selectivity photographs of LP-CQDs containing different analytes in UV light irradiation.	123
Figure 5.9	(a) Overlapping of absorption spectra of TC with excitation spectra of LP-CQDs, (b) Lifetime decay curves of LP-CQDs and LP-CQDs+ TC, and (c) UV-Vis absorption spectra of LP-CQDs, TC, and LP-CQDs+ TC.	124
Figure 5.10	Photographs of LP-CQDs in fluorescent characters of	126

handwritten (a) words and (b) images, (c) paper-based fluorescent strip of LP-CQDs, and (d) LP-CQDs in presence of TC.

LIST OF TABLES

Table No.	Title	Page No.
	Chapter 1	
Table 1.1	Detection of various analytes using quantum dots-based sensing probe.	16
	Chapter 2	
Table 2.1	Quantum yield (ϕ), Stern-Volmer quenching constant (K_{sv}), and binding constant (K) of A and B-GQDs with Mn^{2+} quencher and GSH[a].	43
Table 2.2	Quantum yield (ϕ), Stern-Volmer quenching constant (K_{sv}), and binding constant (K) of A and B-GQDs with Mn^{7+} quencher and GSH[a].	45
Table 2.3	Final turn on percentage of different systems after the GSH addition.	47
	Chapter 3	
Table 3.1	Summary of Quantum Yield of Rice husk-derived quantum dots.	64
Table 3.2	Analytical performance for Fe^{3+} by the developed sensor.	66
Table 3.3	Various sensing systems based on quantum dots for Fe^{3+} detection.	66
Table 3.4	Intraday and Inter day precision data for the estimation of Fe^{3+} by the developed sensor.	68
Table 3.5	Robustness evaluation of the developed sensor.	68
Table 3.6	Fluorescence lifetime parameters of RH-CQDs, RH-CQDs + Fe^{3+}.	70
Table 3.7	Different photophysical parameters for RH-CQDs in presence and absence of Fe^{3+}.	70
Table 3.8	Application of the developed sensor for the detection of Fe^{3+} in tablet dosage.	72
Table 3.9	Analytical performance data for OFX and CPX by the developed sensor.	73

Table 3.10	Intraday and Inter day precision data for the estimation of OFX and CPX by the developed sensor.	74
Table 3.11	Fluorescence lifetime parameters of RH-CQDs, RH-CQDs + OFX, and RH-CQDs + CPX.	74
Table 3.12	Application of the developed sensor for the detection of OFX and CPX in tablet dosage.	75

Chapter 4

Table 4.1	Sensing capabilities for Cr^{6+} ions by the prepared sensor.	95
Table 4.2	Different quantum dots-based sensing devices for Cr^{6+} detection.	96
Table 4.3	Intraday and Inter day precision data for estimating Cr^{6+} by the developed sensor.	97
Table 4.4	Fluorescence lifetime parameters of CQDs, and CQDs+Cr^{6+}.	98
Table 4.5	Application of developed nanosensor for the detection of Cr^{6+} ions in real samples.	99
Table 4.6	Analytical performance for 4-NP by the prepared sensor.	101
Table 4.7	Different sensors for 4-NP detection.	102
Table 4.8	Intraday and Inter day precision data for estimating 4-NP by the developed sensor.	102
Table 4.9	Fluorescence lifetime parameters of CQDs, and CQDs+4-NP.	103
Table 4.10	Application of the developed nanosensor for the detection of 4-NP in real samples.	104

Chapter 5

Table 5.1	Methodical sensing performance of developed sensor for TC.	121
Table 5.2	Comparison of CQDs as nanosensors for TC detection.	121
Table 5.3	Intraday and Inter day precision data for estimating TC by the	122

developed sensor.

Table 5.4	Fluorescence lifetime parameters of LP-CQDs in presence of TC.	125
Table 5.5	Application of the fabricated sensor for TC detection in real samples.	126

LIST OF SCHEMES

Scheme No.	Title	Page No.
	Chapter 2	
Scheme 2.1	Schematic representation of the synthesis of GQDs from Indian anthracite and bituminous coal.	33
Scheme 2.2	Figure showing mechanism of GQDs detecting GSH in presence of Mn^{n+}.	47
	Chapter 3	
Scheme 3.1	A pictorial illustration of the synthesis of RH-CQDs.	59
Scheme 3.2	Mechanism showing Fluorescence quenching of RH-CQDs on addition of Fe^{3+} ions.	71
Scheme 3.3	Plausible mechanism between RH-CQDs and CPX.	76
	Chapter 4	
Scheme 4.1	A pictorial illustration of the synthesis of RH-CQDs.	88
Scheme 4.2	Plausible sensing mechanism of Cr^{6+}.	99
Scheme 4.3	Plausible quenching mechanism of CQDs in presence of 4-NP.	103
	Chapter 5	
Scheme 5.1	Fabrication of LP-CQDs from *Citrus limon* peels.	114
Scheme 5.2	Plausible mechanism of TC sensing.	125

LIST OF ABBREVIATIONS

0D	Zero-dimensional
1D	One-dimensional
2D	Two-dimensional
3D	Three-dimensional
CNTs	Carbon nanotubes
CDs	Carbon dots
GQDs	Graphene quantum dots
CQDs	Carbon quantum dots
PL	Photoluminescence
CPDs	Carbonized polymer dots
QDs	Quantum dots
QCE	Quantum confinement effect
VB	Valence bands
CB	Conduction bands
HOMO	Highest occupied molecular orbital
LUMO	Lowest Unoccupied molecular orbital
CNTs	Carbon nanotubes
PET	Photoinduced electron transfer
IFE	Inner filter effect
FRET	Fluorescence resonance energy transfer
ES	Excited state
GS	Ground state
SERS	Surface-enhanced Raman spectroscopy
UV-Vis	Ultraviolet-Visible
TEM	Transmission electron microscopy
FTIR	Fourier transform infrared spectroscopy
XPS	X-ray photoelectron spectroscopy
XRD	X-ray diffraction
EDX	Energy dispersive X-ray analysis
LOD	Limit of detection

TCSPC	Time-correlated single-photon counting
LOQ	Limit of quantification
RSD	Relative standard deviation

LIST OF SYMBOLS

nm	Nano-meter
µM	Micro-Molar
mM	Milli-Molar
nM	Nano-Molar
µl	Micro-Litre
ml	Milli-Litre
ns	nanosecond
M	Molar
$\boldsymbol{\phi}$	Fluorescence quantum yield
τ_{av}	Average lifetime
k_r	Radiative rate constant
k_{nr}	Non-radiative rate constant
k_{ET}	Rate of electron transfer
ϕ_{EET}	Efficiency of the electron transfer
λ_{th}	Specific excitation wavelength threshold
λ_{ex}	Excitation wavelength
λ_{em}	Emission wavelength
K_{SV}	Stern-Volmer constant

ABSTRACT

The thesis entitled "**Synthesis of Graphene Quantum Dots (GQDs) and Carbon Quantum Dots (CQDs) for their Sensing Applications**" is divided into five Chapters.

Chapter-1. It describes the background of nanomaterials, carbon-based nanomaterials including graphene quantum dots (GQDs) and carbon quantum dots (CQDs) along with literature survey and scope of the work. This Chapter discusses the detailed information about GQDs and CQDs with their optical properties, synthesis methods, fluorescence quenching and restoration mechanisms. Importance of coal-derived GQDs and natural-resource derived CQDs were also described in this chapter. Various sensing applications for the detection of different analytes was also explained.

Chapter-2. Coal is an abundant, low-cost, and high carbon content energy source on the planet. Herein, water-soluble graphene quantum dots (GQDs) were prepared from Indian anthracite and bituminous coals labelled as A-GQDs and B-GQDs, respectively by the facile one-step wet chemical route. The size of B-GQDs (7.38 nm ± 0.13) was smaller than A-GQDs (10.25 nm ± 0.19) which was analysed from TEM. The effects of pH, temperature and irradiation time on the fluorescence of the GQDs have been studied which affirmed the stability of GQDs. Moreover, both the synthesized GQDs exhibited tunable photoluminescence (PL) properties and excitation wavelength dependency. The developed GQDs was high selective and sensitivity for Mn^{n+} (2+, 7+) ions. However, the as-prepared GQDs showed significant change in both the steady state absorption and fluorescence intensity but remain unaltered in the excited state lifetime values in the presence of different Mn^{n+} quenchers, which validated the static quenching mechanism between GQDs@Mn^{n+} nanoprobes. The prepared nanosensor showed high sensitivity for GSH sensing with a good detection limit of 27 μM for B-GQD@Mn^{7+}. Accrediting low-cost productivity and intriguing photoluminescence properties, the current study reveals new potential for sustainable synthesis of GQDs with novel ascribed attributes.

Chapter-3. Eco-friendly, water-soluble, and fluorescent carbon quantum dots (CQDs) with an average size of 8.3 nm were synthesized from rice husk (RH) using the hydrothermal method, and the CQDs were labelled as rice-husk carbon quantum dots (RH-CQDs). The composition and surface functionalities were studied using X-ray photoelectron spectroscopy, FT-IR, and Raman spectroscopy. A study on the impact of pH and irradiation time on fluorescence

affirmed the stability of RH-CQDs. The as-synthesized nanosensor has high selectivity and sensitivity for Fe^{3+} ions. Several photophysical studies were performed to investigate the interaction between RH-CQDs and Fe^{3+}. From the time-correlated single-photon technique (TCSPC), the average lifetime value of RH-CQDs significantly decreases in the presence of Fe^{3+} which supports a dynamic quenching mechanism. The developed sensor exhibited excellent sensitivity with a detection limit in the nanomolar range (149 nM) with a wide linear range of 0-1300 nM for Fe^{3+} ions. The prepared nanosensor was also used to detect Fe^{3+} in a tablet supplement with high recoveries. Moreover, the RH-CQDs nanoprobe was used to detect other analytes (fluoroquinolones) using the fluorescent enhancement technique. It showed high selectivity and sensitivity toward Ofloxacin (OFX) and Ciprofloxacin (CPX). The detection limit calculated was 150 nM and 127 nM with a linearity range of 50-1150 nM for OFX and CPX, respectively. The enhancement of average lifetime value and quantum yield in the presence of OFX and CPX favors the increased fluorescence property of RH-CQDs through hydrogen bonding and charge-transfer complex. In this work, integration of two different mechanisms (fluorescence quenching and fluorescence enhancement) was followed to construct a single sensing platform for accurate quantification of dual-mode nanosensors for the detection of metal ions and fluoroquinolones by excited state electron transfer and hydrogen bonding mechanism respectively. This strategy also stimulates the detection of more than one analyte.

Chapter-4. Green-emissive carbon quantum dots (CQDs) with exclusive chemosensing aspects were synthesized from orange pomace as a biomass-based precursor via a facile microwave method without using any chemicals. The synthesis of highly fluorescent CQDs with inherent Nitrogen was confirmed through X-ray diffraction, X-ray photoelectron, FT-IR, Raman, and Transmission electron microscopic techniques. The average size of synthesized CQDs was found to be 7.5 nm. These fabricated CQDs displayed excellent photostability, water solubility, and outstanding fluorescent quantum yield, i.e., 54.26%. The synthesized CQDs showed promising results for the detection of Cr^{6+} ions and 4-nitrophenol (4-NP). The sensitivity of CQDs towards Cr^{6+} and 4-NP was found up to the nanomolar range with the limit of detection (LOD) values 59.6 nM and 14 nM, respectively. Several analytical performances were thoroughly studied for high precision of dual analytes of the proposed nanosensor. Various photophysical parameters of CQDs (quenching efficiency, binding constant, etc.) were analyzed in the presence of dual analytes to gain more insight into the sensing mechanism. The synthesized CQDs exhibited fluorescence quenching towards incrementing the quencher

concentration, which was rationalized by the inner filter effect (IFE) through time-correlated single photon counting (TCSPC) measurements. The CQDs fabricated in the current work exhibited a lower detection limit and wide linear range through the simple, eco-friendly, and rapid detection of Cr^{6+} and 4-NP ions. To evaluate the feasibility of the detection approach, real sample analysis was conducted, demonstrating satisfactory recovery rates and relative standard deviations towards developed probes. This research paves the way for developing CQDs with superior characteristics utilizing orange pomace (biowaste precursor).

Chapter-5. A sustainable way was developed for the production of water-soluble carbon quantum dots employing green approach. The synthetic protocol was employed using microwave pyrolysis technique, while lemon peel was served as a carbon precursor. Fabrication of highly fluorescent lemon-peel derived CQDs (LP-CQDs) having inherent nitrogen functionality was validated by X-ray photoelectron spectroscopy, FT-IR, X-ray diffraction, Raman spectroscopic analysis, and TEM techniques. Average particle size of fabricated LP-CQDs was 4.46 nm. LP-CQDs yielded a remarkable quantum yield of 49.5%, which displayed excellent salinity, photostability, storage time, and pH stability. LP-CQDs displayed encouraging results for tetracycline (TC) detection using a PL turn-off approach. The sensitivity of LP-CQDs towards TC was seen in nanomolar range having detection limit of 50.4 nM. Method validation was comprehensively studied to ensure the precision of the nanosensor. A complete analysis of different photophysical parameters of LP-CQDs was performed with TC to gain deeper understanding of the sensing mechanism. Fabricated LP-CQDs showed fluorescence quenching towards TC, elucidated by inner filter effect (IFE) mechanism. The synthesized nanoprobe demonstrated a lesser detection limit with broad linear range enabling facile, cheap, environmentally friendly, and fast detection of TC. Practicality of the detection method was assessed through the analysis of real samples, resulting in satisfactory recovery percentage and relative standard deviation with respect to the developed probes. Furthermore, LP-CQDs were used as a fluorescent ink and to fabricate the paper-based fluorescent strips. This study lays the door for the sensing platform of LP-CQDs towards detection of TC, which may impact potential role for environmental sustainability.

CHAPTER-1

Introduction and Literature

1.1 Background

1.1.1 Nanomaterials

Nanomaterials are the substances characterized by having one of their dimensions (length, width, or height) within the range of 100 nm. These can be classified into 0D, 1D, 2D, and 3D on the basis of their dimensions. Zero-dimensional nanomaterials (0D) exhibits nanoscopic dimensions (no dimension greater than 100 nm) in all the three axis i.e., Lx, Ly, and Lz (length along X, Y, and Z axis). Illustrative examples include quantum dots, nanospheres, etc. One-dimensional nanomaterials (1D) are defined as linear structure in the nanoscopic range with diameter less than 100 nm, including nanotubes, nanorods and nanowires. Two-dimensional materials (2D) encompass the characteristic where any two-dimensions exceed the nanoscopic range, such as: nanosheets, graphene, etc.[1] In three-dimensional nanomaterials (3D) all the three dimensions are outside the nanoscopic range (>100 nm), for example: nanoprism, etc.[2] Nanomaterials offers the advantages of possessing elevated specific surface area, increased porosity, and surface to volume ratio which enables their usage in plethora of applications such as electronics, biomedicine, catalysis, and fluorescent nanosensors, etc.[3] Recently, carbon-based nanomaterials have gained prominence as remarkable fluorescent probes utilized in various sensing applications, owing to their exceptional properties.

1.1.2 Carbon-Based Nanomaterials

Carbon-based nanomaterials play crucial role in advancing the field of material science. The realm of carbon-based nanomaterials, extending from conventional industrial carbon like carbon black and activated carbon to newer variants like graphene and carbon nanotubes (CNTs), continues to captivate researchers and find wide-ranging applications such as photocatalysis,[4] medical diagnosis,[5] biomolecular imaging,[6] pollution management,[7] sensing,[8] hydrogen evolution,[9] and various interdisciplinary domains due to their environment friendly nature,[10] increased adsorption capacity, and greater number of active sites.[4] Nevertheless, macroscopic carbon materials suffers from a lack of suitable band gap, which poses challenge to their effectiveness as a fluorescent material.[11] Carbon dots (CDs), an emerging and highly intriguing member of the carbon family, have garnered significant attention.

1.1.3 Carbon Dots (CDs)

CDs are zero-dimensional carbon nanomaterials having fluorescence property.[12] CDs possess outstanding biocompatibility, tunable photoluminescence, excellent water solubility, and photostability, making them a highly effective alternative to other fluorescent nanomaterials. CDs are classified into graphene quantum dots (GQDs), carbon quantum dots (CQDs), and carbonized polymer dots (CPDs) on the basis of distinct formation mechanism, properties, and core structure.[11,13]

1.1.3.1 Graphene Quantum Dots (GQDs)

Graphene quantum dots (GQDs) were first discovered in 2008 by Ponomarenko and Geim.[14,15] GQDs are 0D fluorescent material having size typically less than 20 nm.[16] GQDs are single or few layers of π-conjugated nanostructures primarily made by the fragmentation of large graphene sheets.[17] They contains functional groups on their edges, which provide several functionalization sites (Figure 1.1).[18] GQDs are anisotropic in nature. GQDs exhibits quantum confinement of conjugated π-domains, presence of more active sites (such as functional groups, edges, and dopants), excellent photostability, biocompatibility, and water dispersibility. The quantum confinement effect and size dependence significantly impacts the electronic bandgap structures of GQDs.[19]

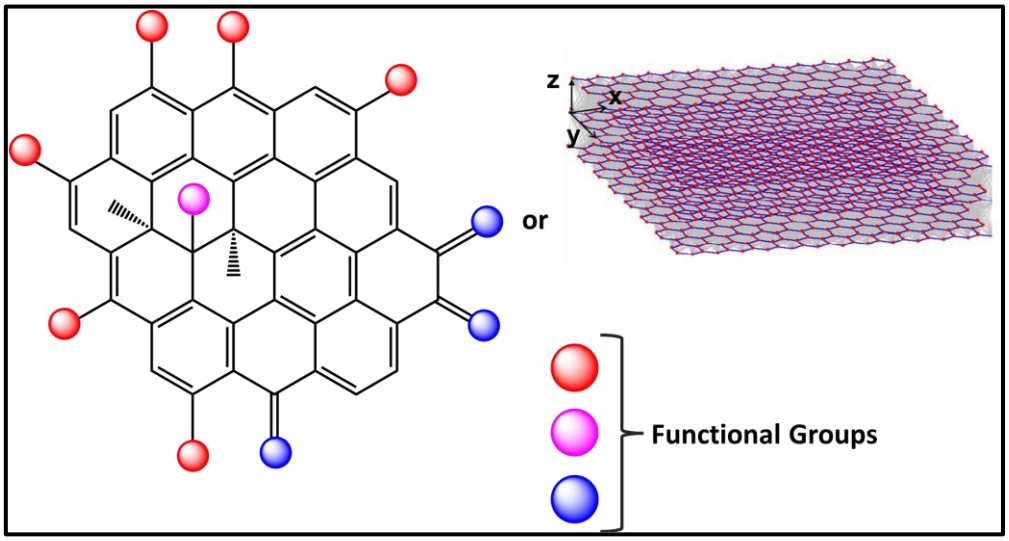

Figure 1.1. Structural depiction of GQDs.

1.1.3.2 Carbon Quantum Dots (CQDs)

In 2004, accidental discovery of CQDs while purifying single-walled carbon nanotubes by *Xu et al.* led to further investigations aimed at harnessing the fluorescence characteristics of

CQDs, giving rise to a novel category of promising fluorescent nanomaterials.[20] In 2006, *Sun et al.* coined the term "carbon quantum dots" to refer to fluorescent carbon nanoparticles.[21] CQDs are 0D fluorescent material having size typically less than 10 nm.[22] CQDs consist of amorphous to nanocrystalline cores with both sp^2 and sp^3 hybridised carbon networks and exhibit a quasi-spherical nanoparticle structure.[23,24] CQDs have a carbon based skeleton (carbon core) and functional groups on its surface (Figure 1.2).[25]

Furthermore, their surfaces can be readily functionalized with carboxyl, amino, hydroxyl, carbonyl, and epoxy groups, offering additional benefits for binding with both organic and inorganic moieties.[26] The functionalities permit the CQDs surface to adopt either hydrophobic or hydrophilic characteristics, leading to the essential thermodynamic stability in various solvents, particularly water.[27] When compared to conventional semiconductor quantum dots, CQDs exhibit a range of distinctive features that make them highly attractive for plethora of applications. These features include their innocuous chemical composition, economical, ease of functionalization, tunable fluorescence, easy synthesis, excellent biocompatibility, and exceptional physicochemical, photochemical stability (no-photobleaching).[28] GQDs and CQDs exhibit great potential as a highly effective nanosensor in various sensing applications.

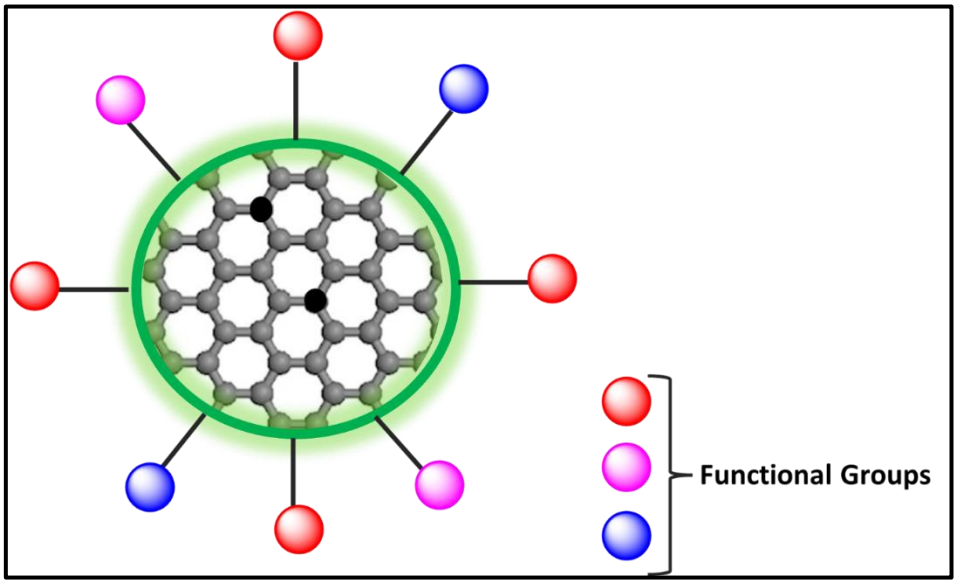

Figure 1.2. Structure of CQDs.

1.1.4 Nanosensor

A sensor is a device capable of detecting physical property of substance (i.e., mass, optical, mechanical, electrical) and converting them into measurable signals.[29] Sensors can be primarily categorized according to the types of transducers employed. A transducer is described as a device that transforms one form of energy into a signal that can be interpreted or read. In

other words, the transducer serves as an interface between the physical parameter being measured by the sensor and the signal processing system, enabling the sensor to generate an output that represents the measured data. The transducers used in sensors can be broadly classified into three types: electrochemical, optical, and mechanical.[30] Figure 1.3 illustrates the working scheme of nanosensor.[31]

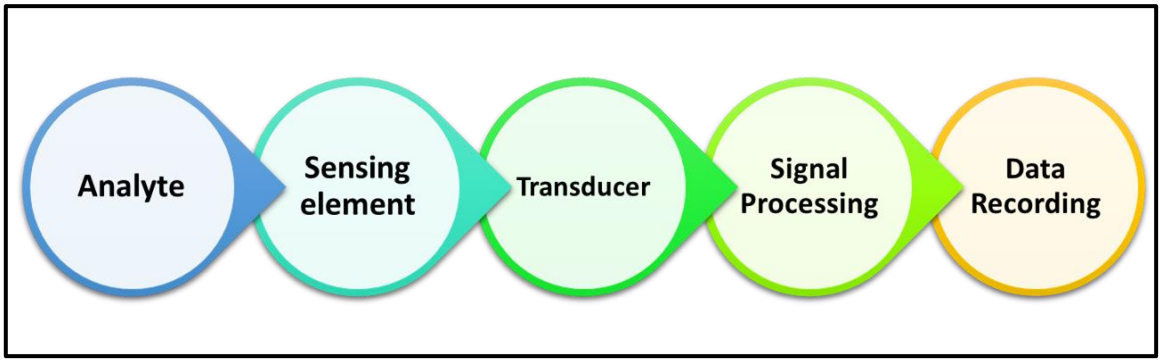

Figure 1.3. Working scheme of nanosensor.

Nanosensor are the sensing devices that possess at least one sensing dimension within 100 nm range.[32] The specificity of nanosensors is achieved through targeting ligands, which are directly attached to the nanoparticles. These ligands selectively attract specific markers of interest (analytes), while the nanoparticles provide sensitivity and facilitate the conversion of signals or serve as detectors for the generated signals.[30] Nanosensors are classified on the basis of structure into electrochemical and optical.[33] Optical nanosensors are utilised for the qualitative and quantitative detection of the sensitivity of optically fluorescent active materials.[33] They can measure fluorescence, absorbance, reflectance, luminescence, and delay time. The fluorescent nanosensor which is based on fluorescence optical detection method has garnered growing interest for the real-time detection of various analytes such as, biomolecules/metal ions/organic pollutants etc. This is primarily due to its remarkable attributes, including high sensitivity, selectivity, simple operations, and quick response time.[34] Numerous nanomaterials are utilised in the fabrication of fluorescent nanosensor, including gold/platinum nanoparticles, organic dyes, quantum dots, etc.[34] Metal nanoparticles, such as gold or platinum are both less stable and expensive. Organic dyes like fluorescein, coumarin have drawbacks including poor biocompatibility, less solubility, and high photobleaching.[35] Semiconductor quantum dots (QDs) like CdSe have limitations like high toxicity because of heavy metal contents, less biocompatibility which limits its biological application.[36] Also, due to their intrinsic blinking, semiconductor QDs cannot be employed to trace a single molecule for long time monitoring.[37] Hence, there is a need for the advancement of environmentally

friendly materials that exhibit outstanding fluorescence properties, affordability, high stability, and favourable biocompatibility, for the fabrication of fluorescent nanosensors. GQDs and CQDs serves as a potential fluorescent probe for sensing applications.

GQDs and CQDs of diverse electronic transitions typically exhibit very similar fluorescence mechanism and optical properties, encompassing optical absorption, fluorescence, etc.

1.1.5 Optical Properties of GQDs and CQDs

Because of electronic transitions from π to π* of the C=C bonds and phenyl rings or n to π* of C=O bonds or related functional groups, GQDs and CQDs predominantly demonstrate absorption in the near-ultraviolet region, while displaying broad tail in the visible region.[22,38] Under optical excitation, photoluminescence (PL) is the spontaneous emission of light from a material. The PL emission mechanism can be ascribed to factors: band-gap transitions of conjugated π-π bonds or surface defects that arise from non-perfect sp^2 domains.[23,39] One significant aspect is the occurrence of the quantum confinement effect (QCE), which becomes apparent when the GQDs/CQDs are reduced in size to below the exciton Bohr radius. The effect (QCE) involves a change in the valence (VB) and conduction band (CB), transitioning from a continuous energy band to distinct energy levels. As the 3-D size of the material reduce to nanometer scale, there is an increase in the band gap. This results in a shift in the band gap into the ultraviolet-visible range, resulting in a substantial improvement in the quantum yield (QY).[40]

The dominant source of fluorescence arises from the interplay of the QCE and the band gap associated with conjugated π-domains in GQDs/CQDs featuring substantial conjugated sp^2-domains and a surface functional groups.[19,41] As the size of GQDs/CQDs conjugated π-domains increases, the band gap decreases, resulting in a noticeable redshift in the emission peak as shown in Figure 1.4. Surface defect states are another factor responsible for the fluorescence of GQDs/CQDs. Surface defects refer to the distinct regions that lie at the boundary or surface mainly contains many functional groups, which are different from the carbon core.[42] The fluorescence arising from surface defect states exhibits excitation-dependent luminescence due to the diverse and intricate nature of these surface defect states.[40] Surface defects primarily originate from surface oxidation and act as trapping sites for excitons, leading to fluorescence associated with surface defect states.[43] As the degree of surface oxidation on GQDs/CQDs increases, there is a corresponding rise in surface defects and emission sites, which leads to a red-shift in the emission wavelength (Figure 1.4).

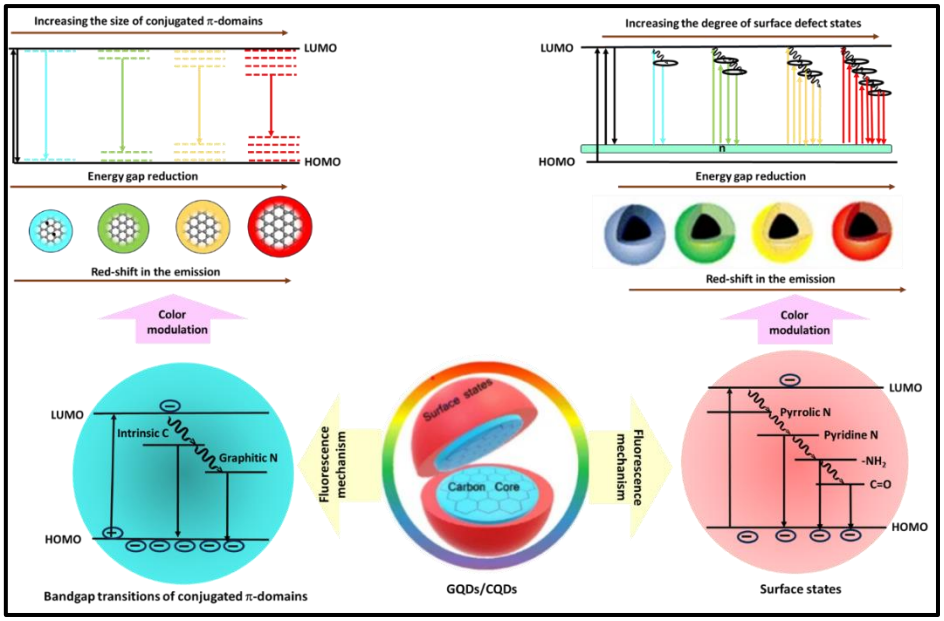

Figure 1.4. The PL mechanism of GQDs/CQDs based on band-gap transitions of conjugated π-π bonds or surface defects.

The excitation-dependent and excitation-independent photoluminescence (PL) behaviour remains a topic of ongoing debate. Excitation-independent emission refers to a phenomenon where the fluorescence emission intensity remains constant or shows minimal variation regardless of changes in the excitation wavelength or energy.[44] While, in excitation-dependent emission, fluorescence emission characteristics of GQDs/CQDs vary with changes in the excitation wavelength or energy. In other words, the emitted light's properties, such as intensity and wavelength, are influenced by the specific wavelength or energy of light used to excite the GQDs/CQDs.[45] The initial ideas focused on quantum size effects, aiming to clarify the excitation-dependent emission. This was done on the basis of selective excitation of diverse sizes correlating to distinct dominant bandgaps.[46] Nevertheless, it became evident shortly after that the observed excitation-dependent emission cannot be solely explained by size differences.[47,48] The excitation-dependent emission vary depending on factors such as their surface states, charge transfer mechanism, zig-zag edge sites, quantum confinement effect (QCE), different sizes, and conjugated sp^2 π-domains.[49,50] The distinction between excitation energy dependence and independence is marked by a specific excitation wavelength threshold (λ_{th}). When the GQDs/CQDs are stimulated with energy below λ_{th}, their emission shows no dependence on the excitation. However, once the excitation energy exceeds λ_{th}, the emission becomes excitation dependent.[51] Excitation-independent emissions arise from the recombination of electrons and holes via transitions over the band edges or the HOMO-LUMO

gap. When electron is excited to CB or above LUMO, it undergoes non-radiative relaxation to the conduction band edge or LUMO before eventually experiencing radiative recombination with a hole situated close to the valence band edge. As a consequence, excitation independent emission arises when excitation energy surpasses the bandgap energy (Figure 1.5). Carbogenic core size likely to influence this bandgap. Conversely, size-independent interface/surface and edge states found within the bandgap become more significant when excitation energy is insufficient to propel the electrons into the CB. The radiative emission resulting from recombination of electron and holes, facilitated by these surface and edge states, is accountable for the excitation-dependent emissions.[51]

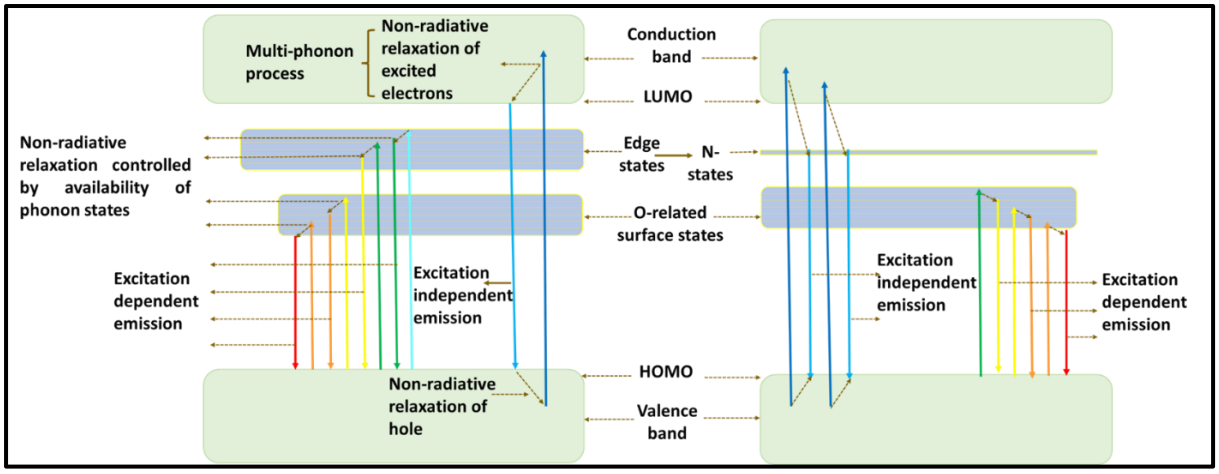

Figure 1.5. PL mechanism showing excitation-dependent and excitation-independent emission.

The fluorescence quantum yield and average lifetime parameters are among the notable characteristics of GQDs and CQDs. The quantum yield for fluorescence quantifies the efficiency of a process by expressing the proportion of emitted photons to absorbed photons. Value of quantum yield ranges between zero and one. Zero implies that no absorbed photons led to a fluorescence, whereas a quantum yield of one show that every absorbed photon resulted in a fluorescence. A higher quantum yield will result in a more noticeably brighter emission. In the context of the kinetic model, it represents a ratio of rate constants. The quantum yield was calculated with respect to reference solution using equation 1.1:

$$\phi_S = \phi_R \times \frac{A_S}{A_R} \times \frac{(Abs)_R}{(Abs)_S} \times \frac{\eta_S^2}{\eta_R^2} \qquad (1.1)$$

In this context, "*S*" subscripts represent the sample parameters, and "*R*" subscripts represent the reference parameters. "*Abs*" refers to absorbance, while "*A*" and "η" correspond to area and refractive index, respectively.

Lifetime is a significant factor in fluorescence, representing how long a molecules stays in the excited state on average after being excited.[52] The average lifetime of the entire fluorescent molecule population is determined by the lifetimes of its excited states. If processes like vibrational relaxation, solvent collision, fluorescence, or phosphorescence reduce the excited state population, the average fluorescence lifetime will decrease. Average lifetime (τ_{av}) values can give information regarding energy transfer rates, such as average time a molecule remains in an excited state before transitioning back to its ground state through both radiative and non-radiative processes. The obtained lifetime value was modelled using a double-exponential equation (equation 1.2). Subsequently, the average lifetime was computed using equation 1.3.[53]

$$Y(t) = a_i \exp\left(\frac{-t}{\tau_i}\right) \tag{1.2}$$

$$\tau^* = \frac{\sum_i a_i \tau_i^2}{\sum_i a_i \tau_i} \tag{1.3}$$

Where, "a_i" is the fractional contributions of time-resolved fluorescence decay lifetimes "τ_i", while "τ^*" is the average lifetime.

Radiative and non-radiative rate constants can be determined using equation 1.4 and equation 1.5:

$$k_r = \frac{\phi_f}{\tau^*} \tag{1.4}$$

$$\frac{1}{\tau^*} = k_r + k_{nr} \tag{1.5}$$

The parameters "k_r" and "k_{nr}" correspond to the radiative and non-radiative rate constants, respectively, while "ϕ_f" and "τ^*" quantify the fluorescence quantum yield and average lifetime value, respectively.

1.1.6 Synthesis Methods

Synthesis of GQDs and CQDs can be broadly classified into two approaches: top-down and bottom-up methods.[54] Synthetic methods and precursor used determine the properties of GQDs/CQDs such as their physiochemical and optical properties, i.e., particle size, dopants, surface functional groups, and PL emission. The top-down method involves cutting large carbonaceous resources like coal, carbon nanotubes (CNTs), carbon black, graphite, and numerous others into small size nanoparticles using various techniques, including physical, chemical, and electrochemical approaches.[55] Bottom-up method involves the pyrolysis or

carbonization of small carbon sources or organic molecules such as carbohydrates, citrates, and other green precursors utilizing microwave, hydrothermal, and high-temperature treatments.[35] Typically in this approach, organic molecules undergo four stages in the formation of GQDs/CQDs: condensation, polymerization, carbonization, and passivation.[56] The top-down approach enables the production on a large scale, but it is associated with several limitations, including non-uniform size, complex synthesis methods, low yield, and the requirement for special conditions. Bottom-up synthesized GQDs/CQDs have gained significant interest owing to their superior flexibility and improved optical performance, which sets them apart from top-down methods. Furthermore, in bottom-up approach it has been discovered that the characteristics, such as particle size, surface functionality, and photoluminescence emission, can be controlled by carefully choosing the starting precursor, solvents, and synthesis conditions. Nevertheless, the fluorescent products obtained from small carbon molecules impose limitations on the mass production of GQDs/CQDs and hinder quality control due to their inherent heterogeneity.[57]

To enhance their PL properties and expand their applications, additional passivation of GQDs/CQDs using tailored organic coating materials can result in brighter, improved biocompatibility, and long-term stability. Also, the surface passivation and functionalization of GQDs/CQDs serves as a crucial link, connecting them to intriguing biological applications like in vivo bioimaging.[58]

1.1.7 Fluorescence Quenching Mechanism

The sensing application of GQDs/CQDs relies on the interactions between them and various analytes, leading to the modulation of fluorescence intensity through quenching or enhancement effects by suppressing quenching.[59] Various fluorescence quenching mechanisms exist for GQDs/CQDs, including static, dynamic quenching, photoinduced electron transfer (PET), inner filter effect (IFE), and fluorescence resonance energy transfer (FRET) (Figure 1.6).[22]

Static quenching occurs when there is an interaction between a quencher and GQDs/CQDs, resulting in the generation of a nonfluorescent ground-state complex. In static quenching, ground-state complex causes a modification in the absorption spectrum of the GQDs/CQDs.[60] Dynamic quenching pertains to the quenching mechanism wherein the excited state (ES) of the GQDs/CQDs returns to its ground state (GS) due to collisions between the GQDs/CQDs and the quencher, involving charge transfer or energy transfer mechanisms. In contrast to static quenching, dynamic quenching does not exhibit changes in the absorption

spectra of the GQDs/CQDs, and its impact is limited to the excited state.[22] Dynamic quenching can be expressed by a straightforward equation 1.6:

$$M + hv' \rightarrow M^* \ (excitation),$$
$$M^* + Q \rightarrow M + Q + hv''(emission) \qquad (1.6)$$

Where, M^* denoted GQDs/CQDs, Q represents quencher and * denotes excited state. This process follows the Stern–Volmer relationship in terms of its kinetics (equation 1.7).[61]

$$\frac{F_0}{F} = 1 + K_{SV}[Q] \qquad (1.7)$$

In the above equation, F_0 and F denotes PL intensity without and with quencher, K_{sv} is Stern-Volmer quenching constant, $[Q]$ tells the quencher concentration. Here, $K_{sv} = K_q \tau_0$, K_q denotes the biomolecular quencher rate coefficient and τ_0 signifies the lifetime of emissive ES of GQDs/CQDs in absence of quencher.[62] Moreover, in order to comprehend the interaction strength and stoichiometry between the GQDs/CQDs and the quencher, values of binding constant were determined by assessing the changes in PL intensity using the 1:1 linear Benesi-Hildebrand equation 1.8:[63]

$$\frac{1}{F_0 - F} = \frac{1}{F_0 - F_1} + \frac{1}{K[Q](F_0 - F)} \qquad (1.8)$$

In above equation, F_0 and F represent the PL intensities absence and presence of the quencher, respectively. F_1 corresponds to the PL intensity for the 1:1 stoichiometric GQDs/CQDs-quencher complex. Parameter K signifies the binding constant values for the GQDs/CQDs and the quencher. For energy transfer, the rate of electron transfer (k_{ET}) is determined by the following equation:

$$k_{ET} = \frac{1}{\tau_{DA}} - \frac{1}{\tau_D} \qquad (1.9)$$

τ_{DA} and τ_D denotes the average lifetime values of GQDs/CQDs with and without the addition of the quencher, respectively.

The electron transfer efficiency (ϕ_{EET}) is calculated using equation 1.10:

$$\phi_{EET} = 1 - \frac{\phi_{DA}}{\phi_D} = 1 - \frac{\tau_{DA}}{\tau_D} \qquad (1.10)$$

Where ϕ_{DA} and ϕ_D depicts the quantum yields of the GQDs/CQDs with and without quencher.

PET (Photoinduced Electron Transfer) can be elucidated as the occurrence of electron transfer between the GQDs/CQDs (acting as electron donors or electron receptors) and the

quencher (acting as electron receptor or electron donor), leading to the formation of cation radicals and anion radicals, respectively.[64] During this process, a complex is formed between the electron donor and the electron receptor, which can return to the ground state without emitting a photon. PET is categorised into reductive PET and oxidative PET (Figure 1.6). Reductive PET involves GQDs/CQDs acting as electron receptors, receiving electrons from the electron donor. On the other hand, oxidative PET is the opposite of reductive PET, where GQDs/CQDs act as electron donors, transferring electrons to the electron acceptor.[59] The energy gap between the quencher's lowest unoccupied molecular orbitals (LUMO) and the GQDs/CQDs highest occupied molecular orbitals (HOMO) served as the driving force for reductive electron transfer. Conversely, for oxidative electron transfer, the driving force originated from energy gap between the LUMO of the CQDs/GQDs and the LUMO of the quencher.[65]

IFE (Inner Filter Effect) happens when the absorption spectrum of the quencher in the detection system overlaps with the excitation or emission spectrum of GQDs/CQDs. IFE, at times referred to as "apparent quenching," is not an actual quenching process. Rather, it arises from the reduction of the excitation beam or the absorption of emitted radiation caused by an excessive concentration of GQDs/CQDs or the quencher in the solution.[66] This phenomenon also takes place if the distances among the emitted and re-absorber is more than 10 nm. Since the IFE process does not fall under static/dynamic quenching, the absorption peaks of the GQDs/CQDs remain unchanged, indicating that there is no new substance formed in this process. As a result, the fluorescence lifetime of GQDs/CQDs remains unaffected.

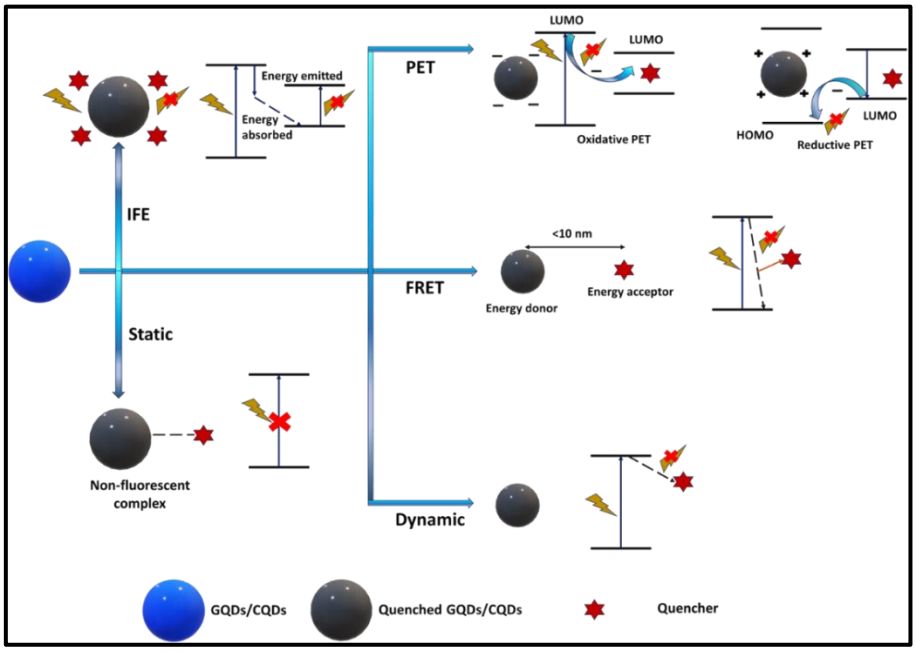

Figure 1.6. Quenching mechanism of GQDs/CQDs.

FRET (Fluorescence Resonance Energy Transfer) is an electrodynamics process that relies on long-range dipole-dipole interactions occurring between the GQDs/CQDs and the quencher.[59] FRET takes place when the GQDs/CQDs emissions spectrum overlaps with the quencher's absorption spectrum, and it occurs between GQDs/CQDs in the excited state and the quencher in the ground state. Therefore, (a) when the fluorescence spectra of CQDs/GQDs coincides with the absorbance spectra of the quencher, (b) there is a decrease in the fluorescence lifetime of GQDs/CQDs, and (c) the distance between GQDs/CQDs and the quencher falls within the range of 10Å–100Å, it indicates that the quenching mechanism between GQDs/CQDs and the quencher is likely to be Förster resonance energy transfer (FRET).[64]

1.1.8 Fluorescence Restoration Mechanism

The fluorescence restoration mechanism is a phenomenon used in fluorescence-based sensors and molecular probes. It involves the reversible interaction between a fluorophore (a molecule that emits light when excited by certain wavelengths of light) and an analyte of interest. When the analyte binds to the fluorophore or interacts with it in a specific way, it brings changes in the fluorescence emission of the fluorophore, leading to a measurable signal. This interaction results in either an increase or restoration of fluorescence intensity, hence the term "fluorescence restoration." The general mechanism of fluorescence restoration is shown in Figure 1.7.

The process of fluorescence restoration typically follows these steps:

a. Initial Fluorescence Quenching: In the absence of the analyte, the fluorophore exhibits reduced fluorescence intensity due to a phenomenon called fluorescence quenching. The quenching can be caused by various factors, such as interactions with surrounding molecules or energy transfer to non-radiative pathways.
b. Analyte Binding: When the analyte of interest is present in the sample, it interacts with the fluorophore in a specific manner. This interaction can be based on molecular recognition, conformational changes, or chemical reactions.
c. Conformational Change: Upon binding to the analyte, the fluorophore may undergo a conformational change that alters its electronic and/or steric properties. This change prevents or reduces the quenching interactions and allows the fluorophore to regain its fluorescence properties.
d. Fluorescence Restoration: As a result of the analyte-induced conformational change, the fluorophore's fluorescence is restored, leading to an increase in fluorescence intensity. This

change in fluorescence can be detected and quantified by appropriate instrumentation, such as a fluorescence spectrometer or a fluorescence microscope.

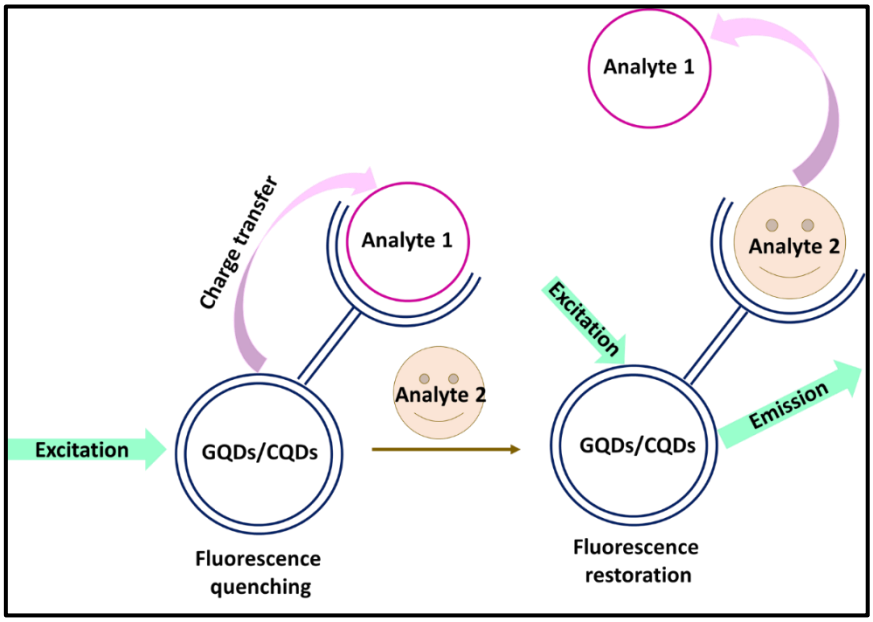

Figure 1.7. Representation of fluorescence restoration mechanism.

Fluorescence restoration mechanisms have been widely applied in various sensing and imaging applications.[67] They offer high sensitivity, selectivity, and real-time monitoring capabilities, making them valuable tools in modern research and technology. Different fluorescent molecules and strategies can be employed to design sensors with specific detection capabilities for a wide range of analytes, making fluorescence restoration an important technique in molecular sensing and imaging fields.

1.1.9 Coal-Derived GQDs

Coal, being an ubiquitous energy resource composed of large aromatic rings and aliphatic chains, is renowned for its affordability, abundant availability on Earth, and high carbon content.[68] It is Coal is rich in small sp^2 carbon crystallites that can be readily exfoliated.[69] In the coal structure, the crystalline carbon is more susceptible to oxidative displacement compared to pure sp^2-carbon structures. The small crystalline domains within coal offer benefits compared to simple exfoliation of graphite-like materials, such as improved functionalization, chemical cutting, and dispersion properties. This leads to the formation of nanometer-sized GQDs with amorphous carbon addends along the edges. Furthermore, the GQDs from coal presents several advantages, including feasibility, non-toxicity, ease of operation, and low cost. The GQDs synthesized from coal exhibit excellent solubility and fluorescence in aqueous solutions, showing great potential for applications in various fields

like bioimaging, biomedicine, photovoltaics, and optoelectronics.[70] Additionally, these GQDs can serve as cost-effective additives for structural composites.[71]

1.1.10 Importance of Natural Resources-Derived CQDs

Carbon quantum dots (CQDs) can be fabricated using different carbon sources, including inorganic materials like graphene, carbon black, and wax, as well as organic materials like polymers, plant extracts, food, and food waste. However, there is a growing preference for organic materials as the carbon source due to their economic affordability, ready availability, and environmentally friendly characteristics in the synthesis of CDs compared to inorganic materials. The carbon-containing organic sources used in CQDs synthesis have been recognized as environmentally friendly or "green" precursors. In the majority of preparation methods, CQDs are synthesized through the carbonization of these organic precursors.[72] Opting for CQD synthesis from "green" precursors offers several advantages, like reduced chemical exposure, minimized waste generation, cost-effectiveness, eco-friendliness, and the abundance of biomass. Biomass is a plentiful and non-toxic feedstock with a significant carbon and oxygen content.[73] It consists mainly of cellulose (40%-50%), hemicellulose (20%-30%), lignin (20%-25%), and a little proportion of inorganic substances (1%-10%) that are highly water-soluble. Due to these characteristics, biomass presents itself as an intriguing source for the production of carbon quantum dots (CQDs).[74]

Variety of forestry, agricultural, and food waste materials have been utilized in the production of luminescent carbon quantum dots, including rice husk,[75] wheat straw,[76] sugarcane bagasse,[77] orange peels,[78] lemon peels,[79] coffee grounds,[80] banana peels,[81] peanut shell,[82] and soybean[83] etc. Transforming biomass into high-value products serves a dual purpose: effectively managing solid waste disposal and alleviating the escalating resource, environmental, and energy challenges.[84] Natural biomass inherently possesses a substantial amount of oxygen, carbon, and different heteroatoms such as nitrogen (N), sulfur (S), and silica (Si), which impart self-passivation or self-doping properties to carbon quantum dots (CQDs). The abundant presence of various functional oxygenic groups like hydroxyl, alkyl, epoxide, carboxyl, and carbonyl on biomass-derived CQDs surface contributes to their remarkable water-soluble characteristics.[85] The incorporation of amorphous heteroatoms into the carbon framework through covalent decoration leads to broad light absorption and strong photoluminescence (PL) in self-doped CQDs. Choosing the synthetic pathway allows for the regulation of carbonization level, morphology, and size in CQDs produced from biomass.

1.1.11 Sensing Application (Detection of Various Analytes)

Owing to unique properties of GQDs/CQDs, they have the potential to function as sensors for a diverse range of analytes, including small molecules, macromolecules, organic compounds, and cells etc.

The most prevalent utilization of GQDs/CQDs is in the detection of metal ions. They can be used for various targets, such as Fe^{3+}, Hg^{2+}, Cr^{6+}, Cu^{2+}, Ag^{+}, and more. Iron plays a vital role in our lives, and its deficiency is considered one of the three global micronutrient deficiencies.[86] Fe^{3+} ions play a vital role in numerous biochemical processes, including oxygen storage, oxygen transfer to tissues, red blood cell development, and enzyme catalysis.[87] $Hg^{2+}$and Cr^{6+} is among the most dangerous and widespread pollutants, raising environmental and health concerns.[88] But improper amount of these metal ions can cause various disorders like DNA damage, mitosis impairment, hereditary gene defects, allergic reactions, kidney damage, and many more. Numerous biomolecules including carbohydrates, lipids, proteins, and nucleic acids, such as glutathione (GSH), ascorbic acid (AA), glucose, dopamine (DA), glucose, choline, cysteine (Cys), etc. play vital roles in sustaining the human body's metabolism.[89] For instance, low-molecular weight cellular thiols (GSH and Cys) contribute to upholding the biological redox balance and cellular functions.[64] GSH participates in various cellular functions, including intracellular redox homeostasis, gene regulation, facilitating intracellular signal transduction, and detoxification.[90] Ascorbic acid (AA), widely recognized as vitamin C, functions as an antioxidant and holds a vital role in numerous biochemical processes i.e. oxidation and reduction within living organisms. It also contributes in bolstering the body's immune function and supporting the synthesis of collagen and mucopolysaccharides.[91]

Likewise, DA is a neurotransmitter crucial for the proper functioning of the central nervous and cardiovascular systems.[92] However, an imbalance in the levels of these biomolecules in the human body can lead to various diseases, including but not limited to AIDS, mental disorders, cardiovascular diseases, cancer, Parkinson's, and numerous others. GQDs/CQDs can also be used for the sensing of noxious pollutants like 4-nitrophenol etc. which are responsible for methemoglobinemia and have carcinogenic capacity.[93] Further, GQDs/CQDs can be utilized for the detection of different antibiotics, such as ofloxacin (OFX), ciprofloxacin (CPX), tetracycline (TC), etc. TC is a broad-spectrum antibiotic renowned for its exceptional sterilization and disinfection capabilities, and antimicrobial activity. This cost-effective option is widely employed in animal husbandry to effectively combat various disease-causing bacteria, including rickettsia, chlamydia, and mycoplasma.[94] Fluoroquinolone is a

commonly used medication to prevent and treat a variety of infectious illnesses in both humans and animals.[95] OFX and CPX are among the most extensively utilized fluoroquinolones. However, improper use poses significant risks to human health, including liver damage, visual problems, and bacterial resistance. Hence, the sensing of different metal ions/biomolecules/organic compounds holds significant importance in diverse applications, including medical analysis, drug delivery, environmental science, and the food industry. This has resulted in an increased demand for the fabrication of easy, highly sensitive, selective, and cost-efficacious biosensors. Currently, numerous techniques are available for detecting various analytes, such as colorimetry,[96] chromatography,[97] surface-enhanced Raman spectroscopy (SERS),[98] spectroscopy,[99] electrochemical method,[100,101] electrochemiluminescence,[102] high-performance liquid chromatography,[103] and more. These techniques are constrained in their practical applicability for routine analysis due to their heavy instrumentation, lower sensitivity, time-consuming nature, the costliness of biological reagents, and complex handling. Nevertheless, fluorescence spectroscopy has garnered significant interest due to its notable advantages, including high sensitivity, non-destructive nature, fast analysis, low cost, good reproducibility, and simplicity.[104] Several sensing probes based on quantum dots for the detection of analytes are reported in Table 1.1

Table 1.1: Detection of various analytes using quantum dots-based sensing probe.

Sensing Probe	**Precursor used**	**Analyte**	**Detection range**	**LOD**	**Quantum yield**	**Ref.**
C-GQDs	Anthracite coal	Cu^{2+}	0-8 μM	0.29 μM	5.98%	69
S-CQDs	Vitamin B1	Fe^{3+}	0.1- 3.3 mM	177 nM	4.4%	105
P-CQDs	Pine wood	Fe^{3+}	0-2000 μM	355.4 nM	4.69%	106
N-CQDs	Methyl Glycine Diacetic acid trisodium salt & ethylenediamine	ClO^- Cr^{6+}	0-300 μM 0-500 μM	5.0 μM 2.1 μM	22.14%	107
S,N-CQDs	Citric acid & thiamine hydrocholride	Ag^+ Cysteine	0-250 μM 0-120 μM	0.40 μM 0.35 μM	63.8%	108
GQDs	Citric acid	Dopamine	0.25-50 μM	0.09 μM	-	92

Cu-CQDs	*Citrus limetta* waste pulp	Histidine	10-100 mM	17.82 mM	-	[109]
BCQDs	Hydroquinone & BBr_3	Glucose	0-80 μM	8.0 μM	14.8%	[110]
N,P-CQDs	Beer	AA	1-200 μM	0.84 μM	21.7%	[111]
GQDs-Cu^{2+}	Ginkgo biloba leaves	GSH	20-500 μM	3.4 μM	1.4%	[112]
2,3-CQDs	2,3-Diaminonaphthalene	Ofloxacin	1-120 μM	0.46 μM	20%	[95]
CdSe QDs	Cadmium chloride, thioglycolic acid & SeO_2	Ciprofloxacin	0-120 μM	0.6 μM	-	[113]
Eu-CQDs	Citric acid & $Eu(NO_3)_3$	TC	0.5-200 μM	0.3 μM	4.7%	[114]
N-CQDs	Glucose & ethylenediamine	TC	0-100 μM	0.344 μM	10.97%	[115]
CDs	Ethyleneglycol bis-(2-aminoethyl ether)-N,N,N',N'-tetraacetic acid (EGTA) and tris(hydroxymethyl)aminomethane (Tris)	4-nitrophenol	0.1-50 μM	28 nM	28%	[116]
B,N-CDs	3-aminophenylboronic acid	4-nitrophenol	0.5-200 μM	0.2 μM	7.0%	[117]

1.2 Research Gaps

Through a comprehensive literature review, following research gaps are identified:

- Limited literature is available concerning the utilization of GQDs and CQDs derived from coal/bio-waste via simple and cost-effective methods for the sensing of metal ions/biomolecules/organic compounds.
- The exploration of the selective and sensitive detection of biomolecules in relation to the variable oxidation state of the quencher remains unexplored.
- The study of all photophysical parameters of GQDs and CQDs is limited to only a few available studies.
- Carbon Quantum Dots-Based Dual-Mode Nanoprobe has not been explored yet.
- No significant work has been carried out till now for application of CQDs as fluorescent ink.

1.3 Objectives

The main motive of the present research work is to synthesize graphene quantum dots and carbon quantum dots from different precursors for the selective detection of metal ions/biomolecules/organic compounds. The specific objectives are as follows:

- Synthesis and characterization of graphene quantum dots (GQDs) and carbon quantum dots (CQDs) from coals and bio-waste respectively.
- To study the effect of various precursors on the sensing efficiency of metal ions/biomolecules/organic compounds.
- Validation of the proposed method for real samples.

References

(1) Baig, N. Two-Dimensional Nanomaterials: A Critical Review of Recent Progress, Properties, Applications, and Future Directions. *Compos. Part A Appl. Sci. Manuf.* **2023**, *165*, 107362. https://doi.org/10.1016/j.compositesa.2022.107362.

(2) Byakodi, M.; Shrikrishna, N. S.; Sharma, R.; Bhansali, S.; Mishra, Y.; Kaushik, A.; Gandhi, S. Emerging 0D, 1D, 2D, and 3D Nanostructures for Efficient Point-of-Care Biosensing. *Biosens. Bioelectron.X* **2022**, *12*, 100284. https://doi.org/10.1016/j.biosx.2022.100284.

(3) Kolahalam, L. A.; Kasi Viswanath, I. V.; Diwakar, B. S.; Govindh, B.; Reddy, V.; Murthy, Y. L. N. Review on Nanomaterials: Synthesis and Applications. *Mater. Today Proc.* **2019**, *18*, 2182–2190. https://doi.org/10.1016/j.matpr.2019.07.371.

(4) Ahmed, S. F.; Kumar, P. S.; Ahmed, B.; Mehnaz, T.; Shafiullah, G. M.; Nguyen, V. N.; Duong, X. Q.; Mofijur, M.; Badruddin, I. A.; Kamangar, S. Carbon-Based Nanomaterials: Characteristics, Dimensions, Advances and Challenges in Enhancing Photocatalytic Hydrogen Production. *Int. J. Hydrogen Energy* **2023**. https://doi.org/10.1016/j.ijhydene.2023.03.185.

(5) Maiti, D.; Tong, X.; Mou, X.; Yang, K. Carbon-Based Nanomaterials for Biomedical Applications: A Recent Study. *Front. Pharmacol.* **2019**, *9*, 1401. https://doi.org/10.3389/fphar.2018.01401.

(6) Zhang, Y.; Wu, M.; Wu, M.; Zhu, J.; Zhang, X. Multifunctional Carbon-Based Nanomaterials: Applications in Biomolecular Imaging and Therapy. *ACS Omega* **2018**, *3*, 9126–9145. https://doi.org/10.1021/acsomega.8b01071.

(7) Liu, Z.; Ling, Q.; Cai, Y.; Xu, L.; Su, J.; Yu, K.; Wu, X.; Xu, J.; Hu, B.; Wang, X. Synthesis of Carbon-Based Nanomaterials and Their Application in Pollution Management. *Nanoscale Adv.* **2022**, *4*, 1246–1262. https://doi.org/ 10.1039/d1na00843a.

(8) Pan, M.; Yin, Z.; Liu, K.; Du, X.; Liu, H.; Wang, S. Carbon-Based Nanomaterials in Sensors for Food Safety. *Nanomaterials* **2019**, *9*, 1330. https://doi.org/10.3390/nano9091330.

(9) Jana, J.; Chung, J. S.; Hur, S. H. Carbon Dot Supported Bimetallic Nanocomposite for the Hydrogen Evolution Reaction. *J. Alloys Compd.* **2021**, *859*, 157895. https://doi.org/10.1016/j.jallcom.2020.157895.

(10) Patel, K. D.; Singh, R. K.; Kim, H. W. Carbon-Based Nanomaterials as an Emerging Platform for Theranostics. *Mater. Horizons* **2019**, *6*, 434–469. https://doi.org/10.1039/c8mh00966j.

(11) Liu, J.; Li, R.; Yang, B. Carbon Dots: A New Type of Carbon-Based Nanomaterial with Wide Applications. *ACS Cent. Sci.* **2020**, *6*, 2179–2195. https://doi.org/10.1021/acscentsci.0c01306.

(12) Nayak, S.; Das, P.; Singh, M. K. Carbon Dot with Aggregation Induced Emission and PH Triggered Disintegration. *Colloid Interface Sci. Commun.* **2021**, *45*, 100537. https://doi.org/10.1016/j.colcom.2021.100537.

(13) Mansuriya, B. D.; Altintas, Z. Carbon Dots: Classification, Properties, Synthesis, Characterization, and Applications in Health Care-an Updated Review (2018–2021). *Nanomaterials* **2021**, *11*, 2525. https://doi.org/10.3390/nano11102525.

(14) Ponomarenko, L. A.; Schedin, F.; Katsnelson, M. I.; Yang, R.; Hill, E. W.; Novoselov, K. S.; Geim, A. K. Chaotic Dirac Billiard in Graphene Quantum Dots. *Science (80-.).* **2008**, *320*, 356–358. https://doi.org/10.1126/science.1154663.

(15) Tian, P.; Tang, L.; Teng, K. S.; Lau, S. P. Graphene Quantum Dots from Chemistry to

Applications. *Mater. Today Chem.* **2018**, *10*, 221–258. https://doi.org/10.1016/j.mtchem.2018.09.007.

(16) Bacon, M.; Bradley, S. J.; Nann, T. Graphene Quantum Dots. *Part. Part. Syst. Charact.* **2014**, *31*, 415–428. https://doi.org/10.1002/ppsc.201300252.

(17) Ji, C.; Zhou, Y.; Leblanc, R. M.; Peng, Z. Recent Developments of Carbon Dots in Biosensing: A Review. *ACS sensors* **2020**, *5*, 2724–2741. https://doi.org/10.1021/acssensors.0c01556.

(18) Faridbod, F.; Sanati, A. L. Graphene Quantum Dots in Electrochemical Sensors/Biosensors. *Curr. Anal. Chem.* **2018**, *15*, 103–123. https://doi.org/10.2174/1573411014666180319145506.

(19) Sk, M. A.; Ananthanarayanan, A.; Huang, L.; Lim, K. H.; Chen, P. Revealing the Tunable Photoluminescence Properties of Graphene Quantum Dots. *J. Mater. Chem. C* **2014**, *2*, 6954–6960. https://doi.org/10.1039/c4tc01191k.

(20) Xu, X.; Ray, R.; Gu, Y.; Ploehn, H. J.; Gearheart, L.; Raker, K.; Scrivens, W. A. Electrophoretic Analysis and Purification of Fluorescent Single-Walled Carbon Nanotube Fragments. *J. Am. Chem. Soc.* **2004**, *126*, 12736–12737. https://doi.org/10.1021/ja040082h.

(21) Sun, Y.-P.; Zhou, B.; Lin, Y.; Wang, W.; Fernando, K. A. S.; Pathak, P.; Meziani, M. J.; Harruff, B. A.; Wang, X.; Wang, H. Quantum-Sized Carbon Dots for Bright and Colorful Photoluminescence. *J. Am. Chem. Soc.* **2006**, *128*, 7756–7757. https://doi.org/10.1021/ja062677d.

(22) Molaei, M. J. Principles, Mechanisms, and Application of Carbon Quantum Dots in Sensors: A Review. *Anal. Methods* **2020**, *12*, 1266–1287. https://doi.org/10.1039/c9ay02696g.

(23) Lim, S. Y.; Shen, W.; Gao, Z. Carbon Quantum Dots and Their Applications. *Chem. Soc. Rev.* **2015**, *44*, 362–381. https://doi.org/10.1039/c4cs00269e.

(24) Gayen, B.; Palchoudhury, S.; Chowdhury, J. Carbon Dots: A Mystic Star in the World of Nanoscience. *J. Nanomater.* **2019**, *2019*, 1–19. https://doi.org/10.1155/2019/3451307.

(25) Kumar, P.; Dua, S.; Kaur, R.; Kumar, M.; Bhatt, G. A Review on Advancements in Carbon Quantum Dots and Their Application in Photovoltaics. *RSC Adv.* **2022**, *12*, 4714–4759. https://doi.org/10.1039/D1RA08452F.

(26) Ding, C.; Zhu, A.; Tian, Y. Functional Surface Engineering of C-Dots for Fluorescent Biosensing and in Vivo Bioimaging. *Acc. Chem. Res.* **2014**, *47*, 20–30. https://doi.org/10.1021/ar400023s.

(27) Zuo, J.; Jiang, T.; Zhao, X.; Xiong, X.; Xiao, S.; Zhu, Z. Preparation and Application of Fluorescent Carbon Dots. *J. Nanomater.* **2015**, *2015*, 10-10.

https://doi.org/10.1155/2015/787862.

(28) Manikandan, V.; Lee, N. Y. Green Synthesis of Carbon Quantum Dots and Their Environmental Applications. *Environ. Res.* **2022**, *212*, 113283. https://doi.org/10.1016/j.envres.2022.113283.

(29) Mousavi, S. M.; Hashemi, S. A.; Zarei, M.; Amani, A. M.; Babapoor, A. Nanosensors for Chemical and Biological and Medical Applications. *Med Chem (Los Angeles)* **2018**, *8*, 444–2161. https://doi.org/10.47277/AANBT/2(3)45.

(30) Munawar, A.; Ong, Y.; Schirhagl, R.; Tahir, M. A.; Khan, W. S.; Bajwa, S. Z. Nanosensors for Diagnosis with Optical, Electric and Mechanical Transducers. *RSC Adv.* **2019**, *9*, 6793–6803. https://doi.org/10.1039/c8ra10144b.

(31) Sohal, N.; Maity, B.; Shetti, N. P.; Basu, S. Biosensors Based on MnO2 Nanostructures: A Review. *ACS Appl. Nano Mater.* **2021**, *4,* 2285–2302. https://doi.org/10.1021/acsanm.0c03380.

(32) Abdel-Karim, R.; Reda, Y.; Abdel-Fattah, A. Nanostructured Materials-Based Nanosensors. *J. Electrochem. Soc.* **2020**, *167*, 37554. https://doi.org/10.1149/1945-7111/ab67aa.

(33) Denizli, A.; Nguyen, T. A.; Rajendran, S.; Yasin, G.; Nadda, A. K. *Nanosensors for Smart Agriculture*; Elsevier, **2021**. https://doi.org/10.1016/C2019-0-05461-1.

(34) Sargazi, S.; Fatima, I.; Kiani, M. H.; Mohammadzadeh, V.; Arshad, R.; Bilal, M.; Rahdar, A.; Díez-Pascual, A. M.; Behzadmehr, R. Fluorescent-Based Nanosensors for Selective Detection of a Wide Range of Biological Macromolecules: A Comprehensive Review. *Int. J. Biol. Macromol.* **2022**, *206*, 115–147. https://doi.org/10.1016/j.ijbiomac.2022.02.137.

(35) Yoo, D.; Park, Y.; Cheon, B.; Park, M. H. Carbon Dots as an Effective Fluorescent Sensing Platform for Metal Ion Detection. *Nanoscale Res. Lett.* **2019**, *14*, 1–13. https://doi.org/10.1186/s11671-019-3088-6.

(36) Winnik, F. M.; Maysinger, D. Quantum Dot Cytotoxicity and Ways to Reduce It. *Acc. Chem. Res.* **2013**, *46*, 672–680. https://doi.org/10.1021/ar3000585.

(37) Shimizu, K. T.; Neuhauser, R. G.; Leatherdale, C. A.; Empedocles, S. A.; Woo, W. K.; Bawendi, M. G. Blinking Statistics in Single Semiconductor Nanocrystal Quantum Dots. *Phys. Rev. B* **2001**, *63*, 205316. https://doi.org/10.1103/PhysRevB.63.205316.

(38) Gao, X.; Du, C.; Zhuang, Z.; Chen, W. Carbon Quantum Dot-Based Nanoprobes for Metal Ion Detection. *J. Mater. Chem. C* **2016**, *4*, 6927–6945. https://doi.org/10.1039/C6TC02055K.

(39) Rawat, P.; Nain, P.; Sharma, S.; Sharma, P. K.; Malik, V.; Majumder, S.; Verma, V. P.; Rawat, V.; Rhyee, J. S. An Overview of Synthetic Methods and Applications of Photoluminescence Properties of Carbon Quantum Dots. *Luminescence* **2022**, *38*, 845-866. https://doi.org/10.1002/bio.4255.

(40) Yan, F.; Sun, Z.; Zhang, H.; Sun, X.; Jiang, Y.; Bai, Z. The Fluorescence Mechanism of Carbon Dots, and Methods for Tuning Their Emission Color: A Review. *Microchim. Acta* **2019**, *186*, 1–37. https://doi.org/10.1007/s00604-019-3688-y.

(41) Kwon, W.; Lee, G.; Do, S.; Joo, T.; Rhee, S. Size-controlled Soft-template Synthesis of Carbon Nanodots toward Versatile Photoactive Materials. *Small* **2014**, *10*, 506–513. https://doi.org/10.1002/smll.201301770.

(42) Shen, J.; Zhu, Y.; Yang, X.; Li, C. Graphene Quantum Dots: Emergent Nanolights for Bioimaging, Sensors, Catalysis and Photovoltaic Devices. *Chem. Commun.* **2012**, *48*, 3686–3699. https://doi.org/10.1039/C2CC00110A.

(43) Du, J.; Wang, H.; Wang, L.; Zhu, S.; Song, Y.; Yang, B.; Sun, H. Insight into the Effect of Functional Groups on Visible-Fluorescence Emissions of Graphene Quantum Dots. *J. Mater. Chem. C* **2016**, *4*, 2235–2242. https://doi.org/10.1039/C6TC00548A.

(44) Joffrion, J. B.; Clower, W.; Wilson, C. G. Tunable Excitation-Independent Emissions from Graphene Quantum Dots through Microplasma-Assisted Electrochemical Synthesis. *Nano-Structures and Nano-Objects* **2019**, *19*, 100341. https://doi.org/10.1016/j.nanoso.2019.100341.

(45) Gan, Z.; Xu, H.; Hao, Y. Mechanism for Excitation-Dependent Photoluminescence from Graphene Quantum Dots and Other Graphene Oxide Derivates: Consensus, Debates and Challenges. *Nanoscale* **2016**, *8*, 7794–7807. https://doi.org/10.1039/c6nr00605a.

(46) Barman, M. K.; Patra, A. Current Status and Prospects on Chemical Structure Driven Photoluminescence Behaviour of Carbon Dots. *J. Photochem. Photobiol. C Photochem. Rev.* **2018**, *37*, 1–22. https://doi.org/10.1016/j.jphotochemrev.2018.08.001.

(47) Maiti, S.; Kundu, S.; Roy, C. N.; Das, T. K.; Saha, A. Synthesis of Excitation Independent Highly Luminescent Graphene Quantum Dots through Perchloric Acid Oxidation. *Langmuir* **2017**, *33*, 14634–14642. https://doi.org/10.1021/acs.langmuir.7b02611.

(48) Xu, Q.; Zhou, Q.; Hua, Z.; Xue, Q.; Zhang, C.; Wang, X.; Pan, D.; Xiao, M. Single-Particle Spectroscopic Measurements of Fluorescent Graphene Quantum Dots. *ACS Nano* **2013**, *7*, 10654–10661. https://doi.org/10.1021/nn4053342.

(49) Ding, H.; Yu, S. B.; Wei, J. S.; Xiong, H. M. Full-Color Light-Emitting Carbon Dots with a Surface-State-Controlled Luminescence Mechanism. *ACS Nano* **2016**, *10*, 484–491.

https://doi.org/10.1021/acsnano.5b05406.

(50) Langer, M.; Paloncýová, M.; Medveď, M.; Pykal, M.; Nachtigallová, D.; Shi, B.; Aquino, A. J. A.; Lischka, H.; Otyepka, M. Progress and Challenges in Understanding of Photoluminescence Properties of Carbon Dots Based on Theoretical Computations. *Appl. Mater. Today* **2021**, *22*, 100924. https://doi.org/10.1016/j.apmt.2020.100924.

(51) Siddique, A. B.; Hossain, S. M.; Pramanick, A. K.; Ray, M. Excitation Dependence and Independence of Photoluminescence in Carbon Dots and Graphene Quantum Dots: Insights into the Mechanism of Emission. *Nanoscale* **2021**, *13*, 16662–16671. https://doi.org/10.1039/d1nr04301c.

(52) Sahoo, D. K.; Dasgupta, S.; Kistwal, T.; Datta, A. Fluorescence Monitoring of Binding of a Zn (II) Complex of a Schiff Base with Human Serum Albumin. *Int. J. Biol. Macromol.* **2023**, *226*, 1515–1522. https://doi.org/10.1016/j.ijbiomac.2022.11.263.

(53) Xu, N.; Gao, S.; Xu, C.; Fang, Y.; Xu, L.; Zhang, W. Carbon Quantum Dots Derived from Waste Acorn Cups and Its Application as an Ultraviolet Absorbent for Polyvinyl Alcohol Film. *Appl. Surf. Sci.* **2021**, *556*, 149774. https://doi.org/10.1016/j.apsusc.2021.149774.

(54) Vibhute, A.; Patil, T.; Gambhir, R.; Tiwari, A. P. Fluorescent Carbon Quantum Dots: Synthesis Methods, Functionalization and Biomedical Applications. *Appl. Surf. Sci. Adv.* **2022**, *11*, 100311. https://doi.org/10.1016/j.apsadv.2022.100311.

(55) Zhang, L.; Yang, X.; Yin, Z.; Sun, L. A Review on Carbon Quantum Dots: Synthesis, Photoluminescence Mechanisms and Applications. *Luminescence* **2022**, *37*, 1612–1638. https://doi.org/10.1002/bio.4351.

(56) Liu, M. L.; Chen, B. Bin; Li, C. M.; Huang, C. Z. Carbon Dots: Synthesis, Formation Mechanism, Fluorescence Origin and Sensing Applications. *Green Chem.* **2019**, *21*, 449–471. https://doi.org/10.1039/C8GC02736F.

(57) Yoo, D.; Park, Y.; Cheon, B.; Park, M.-H. Carbon Dots as an Effective Fluorescent Sensing Platform for Metal Ion Detection. *Nanoscale Res. Lett.* **2019**, *14*, 1–13. https://doi.org/10.1186/s11671-019-3088-6.

(58) Wolfbeis, O. S. An Overview of Nanoparticles Commonly Used in Fluorescent Bioimaging. *Chem. Soc. Rev.* **2015**, *44*, 4743–4768. https://doi.org/10.1039/C4CS00392F.

(59) Zu, F.; Yan, F.; Bai, Z.; Xu, J.; Wang, Y.; Huang, Y.; Zhou, X. The Quenching of the Fluorescence of Carbon Dots: A Review on Mechanisms and Applications. *Microchim. Acta* **2017**, *184*, 1899–1914. https://doi.org/10.1007/s00604-017-2318-9.

(60) Iqbal, A.; Tian, Y.; Wang, X.; Gong, D.; Guo, Y.; Iqbal, K.; Wang, Z.; Liu, W.; Qin, W. Carbon Dots Prepared by Solid State Method via Citric Acid and 1,10-Phenanthroline for

Selective and Sensing Detection of Fe^{2+} and Fe^{3+}. *Sensors Actuators, B Chem.* **2016**, *237*, 408–415. https://doi.org/10.1016/j.snb.2016.06.126.

(61) Lakowicz, J. R. *Principles of Fluorescence Spectroscopy*; Springer, **2006,** 27-61. https://doi.org/10.1007/978-0-387-46312-4.

(62) Gehlen, M. H. The Centenary of the Stern-Volmer Equation of Fluorescence Quenching: From the Single Line Plot to the SV Quenching Map. *J. Photochem. Photobiol. C Photochem. Rev.* **2020**, *42*, 100338. https://doi.org/10.1016/j.jphotochemrev.2019.100338.

(63) Benesi, H. A.; Hildebrand, J. H. A Spectrophotometric Investigation of the Interaction of Iodine with Aromatic Hydrocarbons. *J. Am. Chem. Soc.* **1949**, *71*, 2703–2707. https://doi.org/10.1021/ja01176a030.

(64) Sun, X.; Lei, Y. Fluorescent Carbon Dots and Their Sensing Applications. *TrAC - Trends Anal. Chem.* **2017**, *89*, 163–180. https://doi.org/10.1016/j.trac.2017.02.001.

(65) Fan, Y. Z.; Zhang, Y.; Li, N.; Liu, S. G.; Liu, T.; Li, N. B.; Luo, H. Q. A Facile Synthesis of Water-Soluble Carbon Dots as a Label-Free Fluorescent Probe for Rapid, Selective and Sensitive Detection of Picric Acid. *Sensors Actuators, B Chem.* **2017**, *240*, 949–955. https://doi.org/10.1016/j.snb.2016.09.063.

(66) Panigrahi, S. K.; Mishra, A. K. Inner Filter Effect in Fluorescence Spectroscopy: As a Problem and as a Solution. *J. Photochem. Photobiol. C Photochem. Rev.* **2019**, *41*, 100318. https://doi.org/10.1016/j.jphotochemrev.2019.100318.

(67) Majumder, P., Sarkar, R., Shaw, A.K., Chakraborty, A. and Pal, S.K. Ultrafast dynamics in a nanocage of enzymes: Solvation and fluorescence resonance energy transfer in reverse micelles. *Journal of colloid and interface science* **2005**, *290*, 462-474. https://doi.org/10.1016/j.jcis.2005.04.053.

(68) He, Z.; Liu, S.; Zhang, C.; Fan, L.; Zhang, J.; Chen, Q.; Sun, Y.; He, L.; Wang, Z.; Zhang, K. Coal Based Carbon Dots: Recent Advances in Synthesis, Properties, and Applications. *Nano Sel.* **2021**, *2*, 1589–1604. https://doi.org/10.1002/nano.202100019.

(69) Zhang, Y.; Li, K.; Ren, S.; Dang, Y.; Liu, G.; Zhang, R.; Zhang, K.; Long, X.; Jia, K. Coal-Derived Graphene Quantum Dots Produced by Ultrasonic Physical Tailoring and Their Capacity for Cu(II) Detection. *ACS Sustain. Chem. Eng.* **2019**, *7*, 9793–9799. https://doi.org/10.1021/acssuschemeng.8b06792.

(70) Saikia, B. K.; Benoy, S. M.; Bora, M.; Tamuly, J.; Pandey, M.; Bhattacharya, D. A Brief Review on Supercapacitor Energy Storage Devices and Utilization of Natural Carbon Resources as Their Electrode Materials. *Fuel* **2020**, *282*, 118796. https://doi.org/10.1016/j.fuel.2020.118796.

(71) Ye, R.; Xiang, C.; Lin, J.; Peng, Z.; Huang, K.; Yan, Z.; Cook, N. P.; Samuel, E. L. G.; Hwang, C.-C.; Ruan, G. Coal as an Abundant Source of Graphene Quantum Dots. *Nat. Commun.* **2013**, *4*, 1–7. https://doi.org/10.1038/ncomms3943.

(72) Alas, M. O.; Alkas, F. B.; Aktas Sukuroglu, A.; Genc Alturk, R.; Battal, D. Fluorescent Carbon Dots Are the New Quantum Dots: An Overview of Their Potential in Emerging Technologies and Nanosafety. *J. Mater. Sci.* **2020**, *55*, 15074–15105. https://doi.org/10.1007/s10853-020-05054-y.

(73) Shen, J.; Shang, S.; Chen, X.; Wang, D.; Cai, Y. Facile Synthesis of Fluorescence Carbon Dots from Sweet Potato for Fe^{3+} Sensing and Cell Imaging. *Mater. Sci. Eng. C* **2017**, *76*, 856–864. https://doi.org/10.1016/j.msec.2017.03.178.

(74) Mahat, N. A.; Shamsudin, S. A. Transformation of Oil Palm Biomass to Optical Carbon Quantum Dots by Carbonisation-Activation and Low Temperature Hydrothermal Processes. *Diam. Relat. Mater.* **2020**, *102*, 107660. https://doi.org/10.1016/j.diamond.2019.107660.

(75) Abidin, N. H. Z.; Wongso, V.; Hui, K. C.; Cho, K.; Sambudi, N. S.; Ang, W. L.; Saad, B. The Effect of Functionalization on Rice-Husks Derived Carbon Quantum Dots Properties and Cadmium Removal. *J. Water Process Eng.* **2020**, *38*, 101634. https://doi.org/10.1016/j.jwpe.2020.101634.

(76) Shi, J.; Zhou, Y.; Ning, J.; Hu, G.; Zhang, Q.; Hou, Y.; Zhou, Y. Prepared Carbon Dots from Wheat Straw for Detection of Cu^{2+} in Cells and Zebrafish and Room Temperature Phosphorescent Anti-Counterfeiting. *Spectrochim. Acta Part A Mol. Biomol. Spectrosc.* **2022**, *281*, 121597. https://doi.org/10.1016/j.saa.2022.121597.

(77) S., T.; D., R. S. Green Synthesis of Highly Fluorescent Carbon Quantum Dots from Sugarcane Bagasse Pulp. *Appl. Surf. Sci.* **2016**, *390*, 435–443. https://doi.org/10.1016/j.apsusc.2016.08.106.

(78) Olmos-Moya, P. M.; Velazquez-Martinez, S.; Pineda-Arellano, C.; Rangel-Mendez, J. R.; Chazaro-Ruiz, L. F. High Added Value Functionalized Carbon Quantum Dots Synthetized from Orange Peels by Assisted Microwave Solvothermal Method and Their Performance as Photosensitizer of Mesoporous TiO_2 Photoelectrodes. *Carbon N. Y.* **2022**, *187*, 216–229. https://doi.org/10.1016/j.carbon.2021.11.003.

(79) Su, A.; Wang, D.; Shu, X.; Zhong, Q.; Chen, Y.; Liu, J.; Wang, Y. Synthesis of Fluorescent Carbon Quantum Dots from Dried Lemon Peel for Determination of Carmine in Drinks. *Chem. Res. Chinese Univ.* **2018**, *34*, 164–168. https://doi.org/10.1007/s40242-018-7286-z.

(80) Yao, L.; Zhao, M.-M.; Luo, Q.-W.; Zhang, Y.-C.; Liu, T.-T.; Yang, Z.; Liao, M.; Tu,

P.; Zeng, K.-W. Carbon Quantum Dots-Based Nanozyme from Coffee Induces Cancer Cell Ferroptosis to Activate Antitumor Immunity. *ACS Nano* **2022**, *16*, 9228–9239. https://doi.org/10.1021/acsnano.2c01619.

(81) Atchudan, R.; Edison, T. N. J. I.; Shanmugam, M.; Perumal, S.; Somanathan, T.; Lee, Y. R. Sustainable Synthesis of Carbon Quantum Dots from Banana Peel Waste Using Hydrothermal Process for in Vivo Bioimaging. *Phys. E Low-dimensional Syst. Nanostructures* **2021**, *126*, 114417. https://doi.org/10.1016/j.physe.2020.114417.

(82) Zhu, J.; Zhu, F.; Yue, X.; Chen, P.; Sun, Y.; Zhang, L.; Mu, D.; Ke, F. Waste Utilization of Synthetic Carbon Quantum Dots Based on Tea and Peanut Shell. *J. Nanomater.* **2019**, *2019*. https://doi.org/10.1155/2019/7965756.

(83) Li, W.; Yue, Z.; Wang, C.; Zhang, W.; Liu, G. An Absolutely Green Approach to Fabricate Carbon Nanodots from Soya Bean Grounds. *RSC Adv.* **2013**, *3*, 20662–20665. https://doi.org/10.1039/C3RA43330G.

(84) Liu, Y.; Zhu, C.; Gao, Y.; Yang, L.; Xu, J.; Zhang, X.; Lu, C.; Wang, Y.; Zhu, Y. Biomass-Derived Nitrogen Self-Doped Carbon Dots via a Simple One-Pot Method: Physicochemical, Structural, and Luminescence Properties. *Appl. Surf. Sci.* **2020**, *510*, 145437. https://doi.org/10.1016/j.apsusc.2020.145437.

(85) Jones, S. S.; Sahatiya, P.; Badhulika, S. One Step, High Yield Synthesis of Amphiphilic Carbon Quantum Dots Derived from Chia Seeds: A Solvatochromic Study. *New J. Chem.* **2017**, *41*, 13130–13139. https://doi.org/10.1039/C7NJ03513F.

(86) Zhou, M.; Zhou, Z.; Gong, A.; Zhang, Y.; Li, Q. Synthesis of Highly Photoluminescent Carbon Dots via Citric Acid and Tris for Iron(III) Ions Sensors and Bioimaging. *Talanta* **2015**, *143*, 107–113. https://doi.org/10.1016/j.talanta.2015.04.015.

(87) Das, R.; Sugimoto, H.; Fujii, M.; Giri, P. K. Quantitative Understanding of Charge-Transfer-Mediated Fe^{3+} Sensing and Fast Photoresponse by N-Doped Graphene Quantum Dots Decorated on Plasmonic Au Nanoparticles. *ACS Appl. Mater. Interfaces* **2020**, *12*, 4755–4768. https://doi.org/10.1021/acsami.9b19067.

(88) Bogireddy, N. K. R.; Sotelo Rios, S. E.; Agarwal, V. Simple One Step Synthesis of Dual-Emissive Heteroatom Doped Carbon Dots for Acetone Sensing in Commercial Products and Cr (VI) Reduction. *Chem. Eng. J.* **2021**, *414*, 128830. https://doi.org/10.1016/j.cej.2021.128830.

(89) Hou, J.; Zhang, F.; Yan, X.; Wang, L.; Yan, J.; Ding, H.; Ding, L. Sensitive Detection of Biothiols and Histidine Based on the Recovered Fluorescence of the Carbon Quantum Dots-Hg(II) System. *Anal. Chim. Acta* **2015**, *859*, 72–78. https://doi.org/10.1016/j.aca.2014.12.021.

(90) Ma, Y.; Chen, A. Y.; Huang, Y. Y.; He, X.; Xie, X. F.; He, B.; Yang, J. H.; Wang, X. Y. Off-on Fluorescent Switching of Boron-Doped Carbon Quantum Dots for Ultrasensitive Sensing of Catechol and Glutathione. *Carbon N. Y.* **2020**, *162*, 234–244. https://doi.org/10.1016/j.carbon.2020.02.048.

(91) Wang, T.; Luo, H.; Jing, X.; Yang, J.; Huo, M.; Wang, Y. Synthesis of Fluorescent Carbon Dots and Their Application in Ascorbic Acid Detection. *Molecules* **2021**, *26*, 1246. https://doi.org/10.3390/molecules26051246.

(92) Zhao, J.; Zhao, L.; Lan, C.; Zhao, S. Graphene Quantum Dots as Effective Probes for Label-Free Fluorescence Detection of Dopamine. *Sensors Actuators, B Chem.* **2016**, *223*, 246–251. https://doi.org/10.1016/j.snb.2015.09.105.

(93) Hao, T.; Wei, X.; Nie, Y.; Xu, Y.; Yan, Y.; Zhou, Z. An Eco-Friendly Molecularly Imprinted Fluorescence Composite Material Based on Carbon Dots for Fluorescent Detection of 4-Nitrophenol. *Microchim. Acta* **2016**, *183*, 2197–2203. https://doi.org/10.1007/s00604-016-1851-2.

(94) Zhu, T.; Cao, L.; Kou, X.; Liu, Y.; Dong, W.-F.; Ge, M.; Li, L. Nitrogen-Doped Cyan-Emissive Carbon Quantum Dots for Fluorescence Tetracycline Detection and Lysosome Imaging. *RSC Adv.* **2022**, *12*, 33761–33771. https://doi.org/10.1039/D2RA04945G.

(95) Rateb, A.; Ghubish, Z.; Abdel Hakiem, A. F.; El-Kemary, M. A Multifunctional Sensing of Two Carbon Dots Based on Diaminonaphthalenes for Detection of Ofloxacin Drug. *J. Photochem. Photobiol. A Chem.* **2023**, *443*, 114867. https://doi.org/10.1016/j.jphotochem.2023.114867.

(96) Khani, H.; Abbasi, S.; Yaraki, M. T.; Tan, Y. N. A Naked-Eye Colorimetric Assay for Detection of Hg^{2+} Ions in Real Water Samples Based on Gold Nanoparticles-Catalyzed Clock Reaction. *J. Mol. Liq.* **2022**, *345*, 118243. https://doi.org/10.1016/j.molliq.2021.118243.

(97) Molineau, J.; Hideux, M.; West, C. Chromatographic Analysis of Biomolecules with Pressurized Carbon Dioxide Mobile Phases–A Review. *J. Pharm. Biomed. Anal.* **2021**, *193*, 113736. https://doi.org/10.1016/j.jpba.2020.113736.

(98) Yan, S.; Chu, F.; Zhang, H.; Yuan, Y.; Huang, Y.; Liu, A.; Wang, S.; Li, W.; Li, S.; Wen, W. Rapid, One-Step Preparation of SERS Substrate in Microfluidic Channel for Detection of Molecules and Heavy Metal Ions. *Spectrochim. Acta Part A Mol. Biomol. Spectrosc.* **2019**, *220*, 117113. https://doi.org/10.1016/j.saa.2019.05.018.

(99) Mohan, B.; Xing, T.; Kumar, S.; Kumar, S.; Ma, S.; Sun, F.; Xing, D.; Ren, P. A Chemosensing Approach for the Colorimetric and Spectroscopic Detection of Cr^{3+}, Cu^{2+}, Fe^{3+}, and Gd^{3+} Metal Ions. *Sci. Total Environ.* **2022**, *845*, 157242.

https://doi.org/10.1016/j.scitotenv.2022.157242.
(100) Yence, M.; Cetinkaya, A.; Çorman, M. E.; Uzun, L.; Caglayan, M. G.; Ozkan, S. A. Fabrication of Molecularly Imprinted Electrochemical Sensors for Sensitive Codeine Detection. *Microchem. J.* **2023**, *193*, 109060. https://doi.org/10.1016/j.microc.2023.109060.
(101) Singh, M.; Kapur, A.; Chauhan, M.; Kaur, G.; Kaushik, A.; Chaudhary, G. R. Green Arginine Capped Hafnium Oxide Nanoparticles, a Computationally Designed Framework, for Electrochemical Sensing of Mercury (II) Ion. *Chem. Eng. J.* **2023**, *469,* 144075. https://doi.org/10.1016/j.cej.2023.144075.
(102) Kurup, C. P.; Lim, S. A.; Ahmed, M. U. Nanomaterials as Signal Amplification Elements in Aptamer-Based Electrochemiluminescent Biosensors. *Bioelectrochemistry* **2022**, *147*, 108170. https://doi.org/10.1016/j.bioelechem.2022.108170.
(103) Galyautdinova, G. G.; Egorov, V. I.; Saifutdinov, A. M.; Rakhmetova, E. R.; Malanev, A. V; Aleyev, D. V; Semenov, E. I.; Smolentsev, S. Y. Detection of Tetracycline Antibiotics in Honey Using High-Performance Liquid Chromatography. *Int. J. Res. Pharm. Sci.* **2020**, *11*, 311–314. https://doi.org/10.26452/ijrps.v11i1.1822.
(104) Singh, J.; Kaur, S.; Lee, J.; Mehta, A.; Kumar, S.; Kim, K. H.; Basu, S.; Rawat, M. Highly Fluorescent Carbon Dots Derived from Mangifera Indica Leaves for Selective Detection of Metal Ions. *Sci. Total Environ.* **2020**, *720*, 137604. https://doi.org/10.1016/j.scitotenv.2020.137604.
(105) Wu, F.; Yang, M.; Zhang, H.; Zhu, S.; Zhu, X.; Wang, K. Facile Synthesis of Sulfur-Doped Carbon Quantum Dots from Vitamin B1 for Highly Selective Detection of Fe3+ Ion. *Opt. Mater. (Amst).* **2018**, *77*, 258–263. https://doi.org/10.1016/j.optmat.2018.01.048.
(106) Zhao, S.; Song, X.; Chai, X.; Zhao, P.; He, H.; Liu, Z. Green Production of Fluorescent Carbon Quantum Dots Based on Pine Wood and Its Application in the Detection of Fe3+. *J. Clean. Prod.* **2020**, *263*, 121561. https://doi.org/10.1016/j.jclepro.2020.121561.
(107) Wang, G.; Zhang, S.; Cui, J.; Gao, W.; Rong, X.; Lu, Y.; Gao, C. Preparation of Nitrogen-Doped Carbon Quantum Dots from Chelating Agent and Used as Fluorescent Probes for Accurate Detection of ClO^- and Cr(VI). *Anal. Chim. Acta* **2022**, *1195*, 339478. https://doi.org/10.1016/j.aca.2022.339478.
(108) Liao, S.; Zhao, X.; Zhu, F.; Chen, M.; Wu, Z.; song, X.; Yang, H.; Chen, X. Novel S, N-Doped Carbon Quantum Dot-Based "off-on" Fluorescent Sensor for Silver Ion and Cysteine. *Talanta* **2018**, *180*, 300–308. https://doi.org/10.1016/j.talanta.2017.12.040.
(109) Thakur, A.; Chopra, T.; Devi, P. Green Synthesized Cu@ Carbon Quantum Dots for Histidine and Arsenate Sensing. *IEEE Sens. J.* **2021**, *21*, 16464–16468.

https://doi.org/10.1109/JSEN.2021.3081634.

(110) Shan, X.; Chai, L.; Ma, J.; Qian, Z.; Chen, J.; Feng, H. B-Doped Carbon Quantum Dots as a Sensitive Fluorescence Probe for Hydrogen Peroxide and Glucose Detection. *Analyst* **2014**, *139*, 2322–2325. https://doi.org/10.1039/C3AN02222F.

(111) Li, X.; Wang, C.; Li, P.; Sun, X.; Shao, Z.; Xia, J.; Liu, Q.; Shen, F.; Fang, Y. Beer-Derived Nitrogen, Phosphorus Co-Doped Carbon Quantum Dots: Highly Selective on–off-on Fluorescent Probes for the Detection of Ascorbic Acid in Fruits. *Food Chem.* **2023**, *409*, 135243. https://doi.org/10.1016/j.foodchem.2022.135243.

(112) Xin-Yu, L. I.; ZHANG, Q.; Ni, W.; Jia-Jun, L. I. U.; Jian, W. Cu2+-Mediated Fluorescence Switching of Graphene Quantum Dots for Highly Selective Detection of Glutathione. *Chinese J. Anal. Chem.* **2020**, *48*, 339–346. https://doi.org/10.1016/S1872-2040(20)60003-2.

(113) Xia, H.; Peng, M.; Li, N.; Liu, L. CdSe Quantum Dots-Sensitized FRET System for Ciprofloxacin Detection. *Chem. Phys. Lett.* **2020**, *740*, 137085. https://doi.org/10.1016/j.cplett.2019.137085.

(114) Liu, M. L.; Chen, B. Bin; Yang, T.; Wang, J.; Liu, X. D.; Huang, C. Z. One-Pot Carbonization Synthesis of Europium-Doped Carbon Quantum Dots for Highly Selective Detection of Tetracycline. *Methods Appl. Fluoresc.* **2017**, *5*, 15003. https://doi.org/10.1016/j.cplett.2019.137085.

(115) Wang, C.; Sun, Q.; Yang, M.; Liu, E.; Xue, W.; Fan, J. Preparation of Highly Luminescent Nitrogen-Doped Carbon Quantum Dots and Their Detection of Tetracycline Antibiotics. *Colloids Surfaces A Physicochem. Eng. Asp.* **2022**, *653*, 129982. https://doi.org/10.1016/j.colsurfa.2022.129982.

(116) Ahmed, G. H. G.; Laíño, R. B.; Calzón, J. A. G.; García, M. E. D. Highly Fluorescent Carbon Dots as Nanoprobes for Sensitive and Selective Determination of 4-Nitrophenol in Surface Waters. *Microchim. Acta* **2015**, *182*, 51–59. https://doi.org/10.1007/s00604-014-1302-x.

(117) Xiao, N.; Liu, S. G.; Mo, S.; Li, N.; Ju, Y. J.; Ling, Y.; Li, N. B.; Luo, H. Q. Highly Selective Detection of P-Nitrophenol Using Fluorescence Assay Based on Boron, Nitrogen Co-Doped Carbon Dots. *Talanta* **2018**, *184*, 184–192. https://doi.org/10.1016/j.talanta.2018.02.114.

CHAPTER-2

Coal-derived Graphene Quantum Dots with Mn^{2+}/Mn^{7+} Nanosensor for Selective Detection of Glutathione

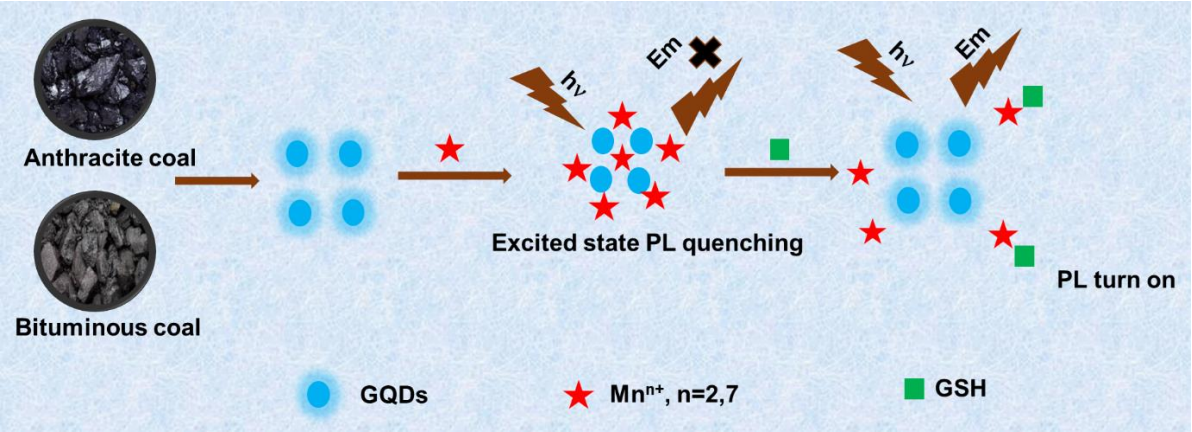

Highlights

- Water-soluble graphene quantum dots (GQDs) were prepared from both Indian anthracite and bituminous coals labelled as A-GQDs and B-GQDs, respectively.
- The role of different oxidation states of Mn i.e., Mn^{2+} and Mn^{7+} as a quencher was studied.
- Examination of different GQDs-Mn^{n+} nanoprobe as turn-off-on sensor to detect GSH.
- Study of all the photophysical parameters including binding efficiency.

2.1 Introduction

Glutathione (GSH) is a non-proteinaceous thiol, crucial antioxidant, and a free radical scavenger [1] in the body that helps to keep cellular functions running smoothly.[2] GSH has a noteworthy impact on both pathological and physiological processes, like regulating cell proliferation, preserving the proper thiol-disulfide balance of proteins, xenobiotic metabolism, and many others.[3] An imbalance in GSH levels has been associated with a wide range of disorders.[4] Therefore, assessing GSH content in cells is important for human health monitoring. Hence, the detection of GSH has been subjected to a lot of interest in recent years. Various technologies like colorimetry,[5] high-performance liquid chromatography, mass spectroscopy, electrochemical,[6] etc. have been developed in recent years but are limited in their practical applicability for the routine analysis of GSH. Currently, extensive research is being conducted to develop a fluorescent sensor for GSH detection as they have merits like rapid response, easy operation, and excellent sensitivity.

Fluorescent nanomaterials i.e., quantum dots have found extensive application in GSH detection. GQDs are ideal biosensors because of their enticing superiorities and promising utilization. Toxic transition metal quantum dots have been replaced by GQDs as a green alternative. GQDs can be synthesized using different chemical precursors such as pyrene,[7] citric acid,[8] ethylene diamine tetra acetic acid (EDTA),[9] thiourea,[10] ammonium citrate,[11] graphite,[12] etc. However, attempts to replace the chemical precursors have been made, owing to their perceived toxicity.[13] Meanwhile, the synthesis of GQDs from coal offers various advantages like feasibility, low cost, non-toxic, easy operations, and ubiquitous source of energy.[14]

Zhang and co-workers synthesized GQDs from anthracite coal using the physical tailoring method and used them for the Cu^{2+} detection.[15] Ye et al., synthesized graphene quantum dots by anthracite coal by chemical oxidative treatment followed by separation using cross-flow ultrafiltration.[16] Kovalchuk et al., synthesized GQDs using bituminous coal by oxidative treatment and further prepared a polymer composite material taking polyvinyl alcohol (PVA) as a matrix.[17] Zhang et al., used anthracite coal for the synthesis of GQDs and then treated with α–Fe_2O_3 by electrodeposition method and the synthesized C-GQDs/ α–Fe_2O_3 nanocomposite was used for the lithium-ion storage properties.[18] Singamaneni et al., demonstrated a chemical oxidative technique for synthesis of GQDs at large scale using inexpensive and readily available coal, paving the path for more efficient coal resource utilisation.[19] Although, there are several studies reported regarding the GQDs synthesis from

coal but the role of different types of coal on the synthesis of GQDs and their sensing application has not been studied yet. GQDs have conjugated π-domains, -OH, and -COOH groups on their surfaces which have tendency to simply interact with the metal ions. Further, introduction of metal ions as a quencher to GQDs promotes the detection of GSH. Among several metal ions, studies of Mn ion as a quencher are not reported yet. However, it has a stable variable oxidation state which may affect the quenching efficiency.

In the current work, a simplistic method was employed for GQDs synthesis using Indian anthracite and bituminous coal. The stability studies i.e., the effect of pH, temperature, and irradiation time on fluorescence of GQDs was also studied. The effect of the different oxidation states of Mn ion (2+ and 7+) on the fluorescence quenching of the synthesized GQDs was analysed. Further, the developed sensor was used for the rapid detection of GSH by fluorescence turn off-on mechanism. The selectivity and sensitivity of the developed system were also studied. Also, the quenching mechanism was proposed by time-resolved lifetime analysis.

2.2 Experimental Section

2.2.1 Materials

Potassium permanganate ($KMnO_4$) and manganese (II) nitrate tetrahydrate ($MnN_2O_6.4H_2O$) (99%) were procured from Sigma-Aldrich and Loba Chemie Pvt. Ltd., respectively. The chemicals were used to study the role of different oxidation states of Mn. GSH was acquired from HiMedia and was used for sensing. Dialysis membrane-110 was purchased from HiMedia Laboratories Pvt. Ltd. Anthracite and bituminous coals were purchased from S V ISPAT Pvt Ltd, Pune, Maharashtra, India. Double distilled water was utilized for stock solutions preparation. All chemicals used were pure and utilized without any further purification.

2.2.2 Synthesis of GQDs

Initially, coal (300 mg) was dispersed in conc. H_2SO_4 (60 mL) and HNO_3 (20 mL) followed by ultrasonication (Antech GT-1860QTS) for 2 hrs. The reaction mixture was subjected to stirring and heating (24 hrs) in an oil bath at 100 °C. The above solution was chilled to room temperature before being placed in an ice-filled beaker, after which the pH was adjusted with NaOH until it reached ~7. After filtering the neutral mixture via a 0.45-μm polytetrafluoroethylene membrane, for 5 days the filtrate was dialyzed in a dialysis bag (Scheme 2.1). The obtained GQDs were stored in a glass vial. The same protocol was followed

for the GQDs preparation from both anthracite and bituminous coals and abbreviated as A-GQDs and B-GQDs, respectively.

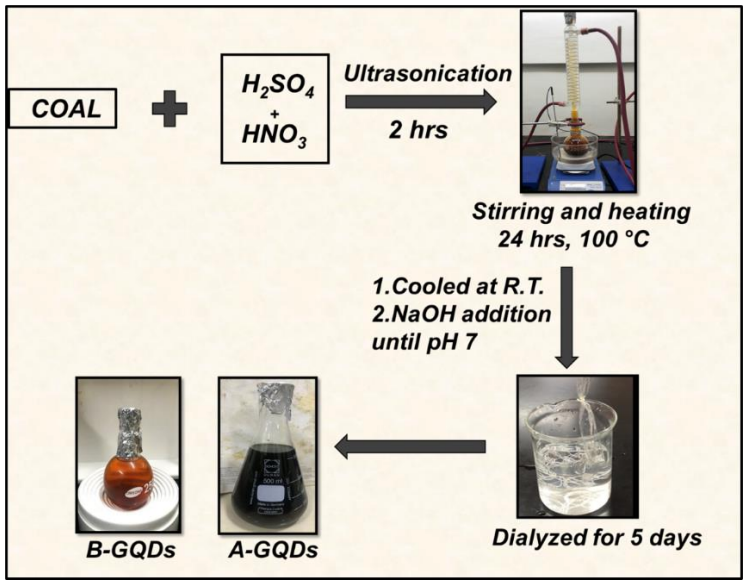

Scheme 2.1. Schematic representation of the synthesis of GQDs from Indian anthracite and bituminous coal.

2.2.3 Characterizations

UV-Visible spectrophotometer (Analytik Jena, Specord, India) and spectrofluorometer instrument (Perkin Elmer LS-55, USA) were used to study the emission spectra of absorption and fluorescence of the synthesized GQDs, respectively. The size and morphology of the synthesized A-GQDs and B-GQDs were scrutinized by transmission electron microscopy (TEM, Jeol 2100 plus). The occurrence of different functionalities on the GQDs surface was studied using FT-IR spectroscopy (Agilent Resolution Pro-carry 660). XPS spectrometer (PHI 5000 VersaProbe III) was used to know the elemental compositions. The amorphous structure of the synthesized GQDs was studied by X-ray diffraction studies (XRD, SmartLab SE) with Cu Kα (λ=1.540 Å) as the radiation source ($0 \leq 2\theta \leq 70°$).

2.2.4 Preparation of the Sample Solutions

The stock solution of manganese nitrate (Mn^{2+}), potassium permanganate (Mn^{7+}), and GSH of particular concentrations were prepared. For investigating the quenching studies of A-GQDs and B-GQDs with Mn^{2+} and Mn^{7+} at neutral pH, GQDs stock solution (1000 µL) was pipetted out in a cuvette containing 1000 µL of deionized water. Further, addition of Mn^{2+} (0-0.90 mM) and Mn^{7+} (0-1.50 mM) was done in the respective cuvette. GSH detection was done by adding the specific concentration of GSH (0-0.50 mM) to the cuvette containing GQDs and

Mn ion (Mn^{2+} and Mn^{7+}). The cuvette was kept as such for 5-7 mins after the addition of GSH, and then the PL spectra was recorded. The excitation wavelength used for the studies was 345 nm. The quantum yield (ϕ) of GQDs in the presence of Mn ion and GSH was assessed using quinine sulfate (reference solution $\phi_R = 0.546$)[20] using the equation 1.1.

2.3 Results and Discussions

2.3.1 Characterizations

The size and morphology of the synthesized A-GQDs and B-GQDs were analyzed by TEM analysis. Figure 2.1(a-b) displays the TEM image of A-GQDs and B-GQDs, respectively which are disc-like in shape.[13] The inset image of Figures 2.1a and 2.1b represent the HRTEM images of A-GQDs and B-GQDs which signifies the lattice spacing *i.e.,* 0.34 nm and 0.36 nm, respectively, corresponding to the (002) lattice fringe of graphene.[15] Histogram distribution shows that B-GQDs (Figure 2.1 (d)) within a range of 4-11 nm having an average diameter of 7.38 ± 0.13 nm, are smaller in size than the A-GQDs, which range from 7-14 nm having an average diameter of 10.25 ± 0.19 nm (Figure 2.1(c)).

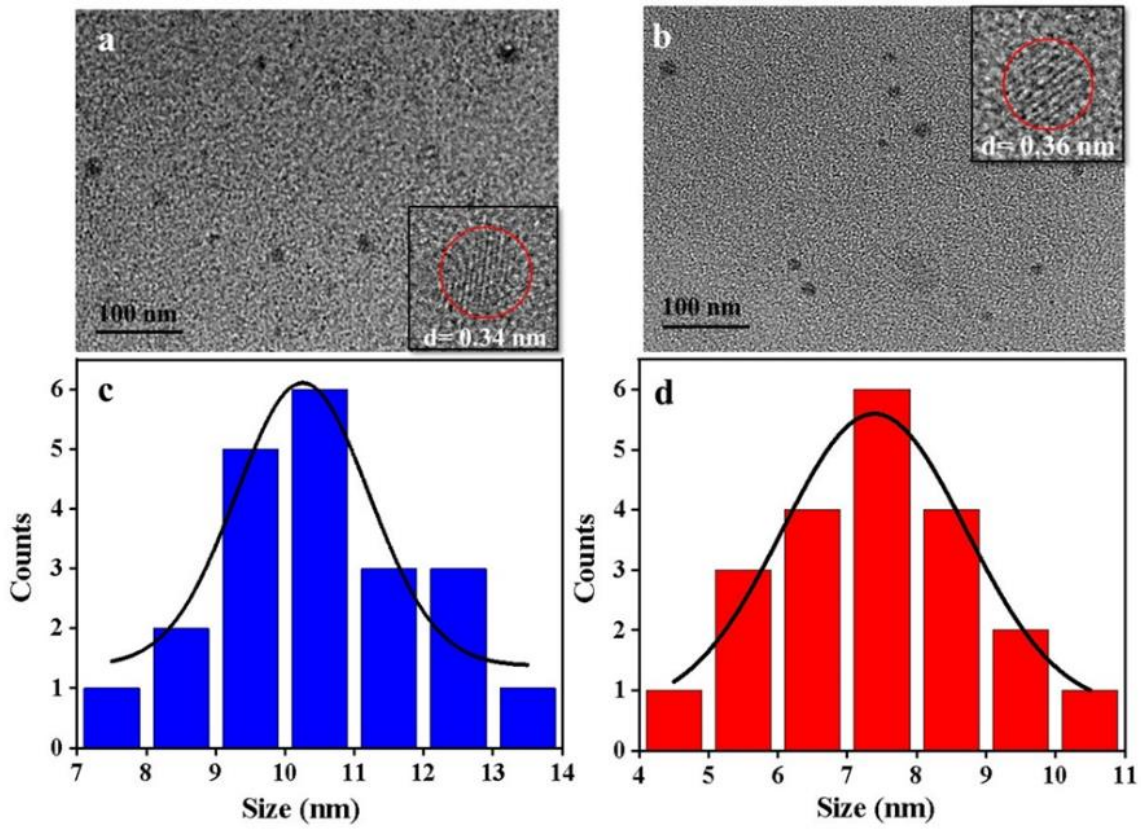

Figure 2.1. TEM and inset HR-TEM image of (a) A-GQDs, (b) B-GQDs; the size distribution histogram of (c) A-GQDs, and (d) B-GQDs.

XRD measurements of the synthesized GQDs are shown in Figure 2.2(a-b). The diffraction peak for the A-GQDs and B-GQDs appears at 2θ= 26.2° (Figure 2.2(a)) and 2θ= 25.5°(Figure 2.2(b)) corresponding to the (002) plane with the d-spacing of 0.34 nm and 0.36 nm,[21] respectively which is also validated by the HR-TEM results. The functionalization of the synthesized GQDs is confirmed by FTIR spectra. A-GQDs exhibits absorption peaks (Figure 2.2c) at 3367 cm^{-1} (O-H, COOH), 1695 cm^{-1} (C=O), 1344 cm^{-1} (C-H), 1091 (C-O), and 650 (C=C bending).[22] Similarly, the B-GQDs surface contains the same functional groups with a slight shift in the peak positions. The additional band at 2081 cm^{-1} was allocated to N-H stretching vibration (Figure 2.2(d)).[23] The broad band at 3300 cm^{-1} implies stretching vibration of O-H and N-H.[24]

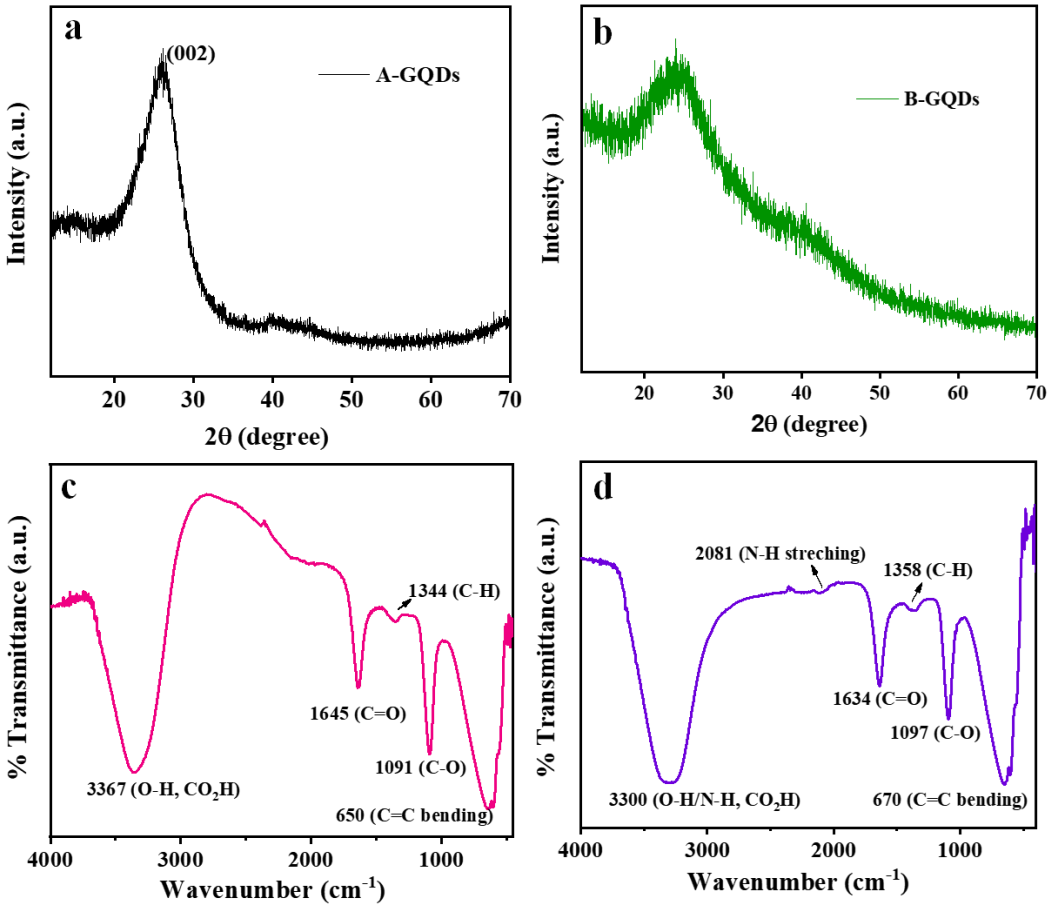

Figure 2.2. XRD spectra of (a)A-GQDs, (b) B-GQDs, FTIR spectra of (c) A-GQDs and (d) B-GQDs.

XPS analysis was used to study the surface chemical compositions of the synthesized GQDs. The survey scan of A-GQDs is composed of Al, Si, C, O (Figure 2.3(a)).[22] The high-resolution XPS data of C1s (Figure 2.3(b)) was bifurcated at 284.4, 286.4, and 288.3 eV, conforming to C-C/C=C, C-O, and COOH.[13,25] The O1s spectra (Figure 2.3(c)) displayed peaks

at 531.2 eV and 533.0 eV which implies C-O and C=O.[23] Figure 2.3(d) shows the survey scan of B-GQDs indicating the occurrence of Al, Si, O, N, C. The high-resolution C 1s XPS spectra of B-GQDs show peaks at 284.8, 286.1, and 288.5 eV which is allocated to C=C/C-C, C-N/C-O, and C=O/-CONH- (Figure 2.3(e)).[23] The O1s spectra (Figure 2.3(c)) show peaks at 531.2 eV and 533.0 eV which denotes C-O and C=O.[23] N 1s exhibits 2 peaks at 398.8 eV and 399.9 eV corresponds to pyridinic N and pyrrolic N, respectively (Figure 2.3(f)).[26]

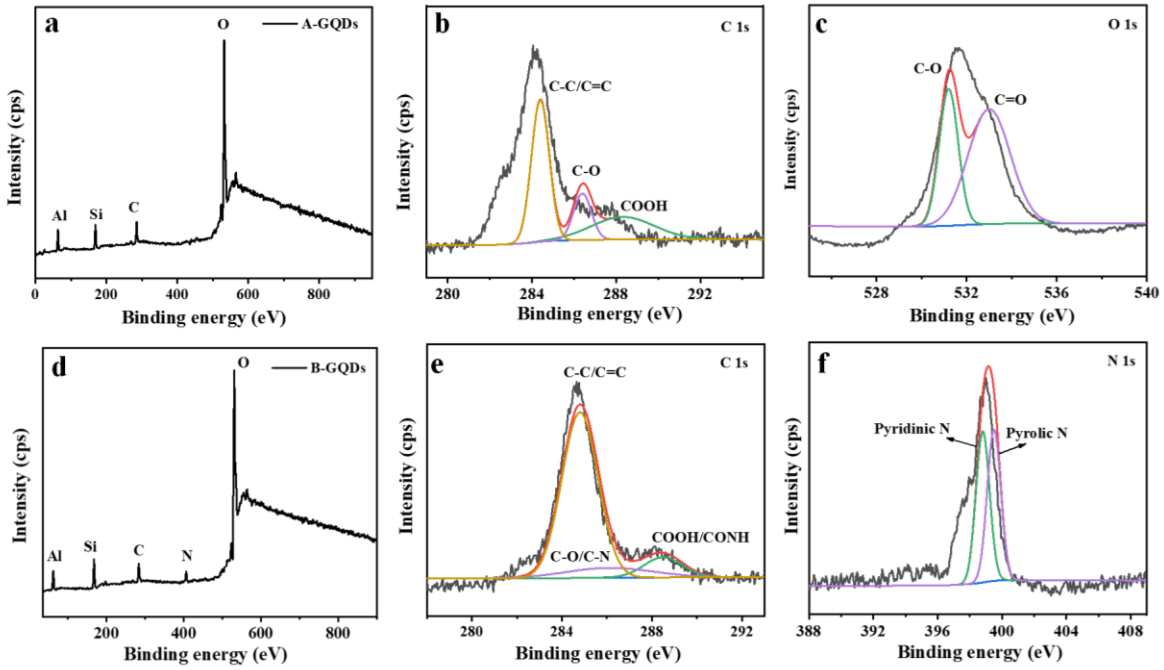

Figure 2.3. (a) XPS survey scan of A-GQDs, (b) high-resolution spectra of C 1s of A-GQDs, (c) O 1s of A-GQDs and B-GQDs, (d) survey spectrum of B-GQDs, (e) C 1s of B-GQDs, and (f) N 1s of B-GQDs.

EDX (energy dispersive X-ray analysis) of A-GQDs and B-GQDs is displayed in Figure 2.4(a, b). It validates that Al, Si, C, O are present in A-GQDs while, in B-GQDs, N is also present along with Al, Si, C, O which is in accordance with XPS spectra.

2.3.2 Optical Properties

The UV-Visible absorption spectra depict the optical characteristics of the synthesized GQDs (Figure 2.4(c)). The absorption peak of both the GQDs was observed at 345 nm[22] corresponding to n-π^* transition due to C=O of GQDs.[27] The additional peak shoulder at 270 nm corresponds to π- π^* transition of aromatic C=C bond.[28] The inset image of Figure 2.4(c) shows that GQDs in water medium show a brown color in visible light and green luminescence in presence of UV light. Figures 2.4(d) and 2.4(e) exhibit the PL excitation and emission spectra

of A and B-GQDs, respectively excited at 345 nm. The PL intensity of A-GQDs > B-GQDs is because of the quantum confinement effect, signifying a size-dependent consequence on the PL properties. Small size quantum dots generally give rise to blue-shifted emission.[22]

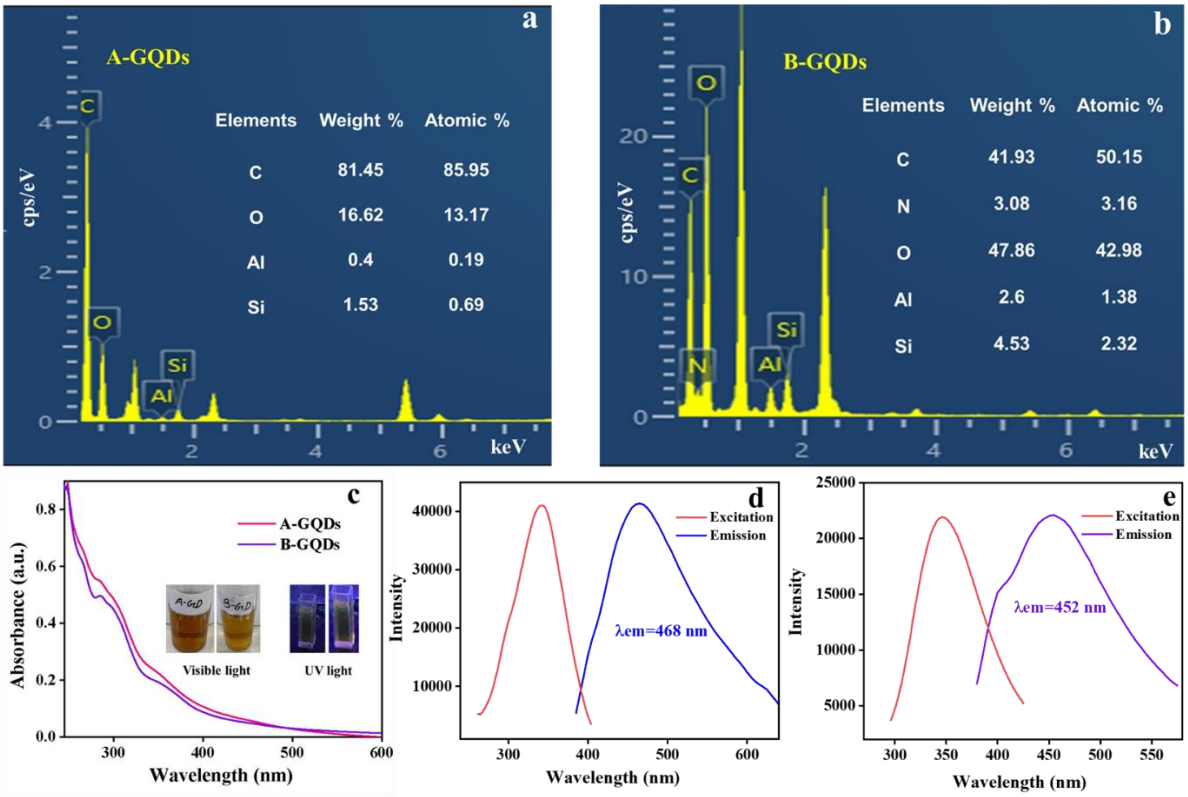

Figure 2.4. (a) EDX spectra of A-GQDs, (b) B-GQDs, (c) UV-Visible spectra of A-GQDs and B-GQDs, (d) PL excitation and emission spectra of A-GQDs, and (e) B-GQDs.

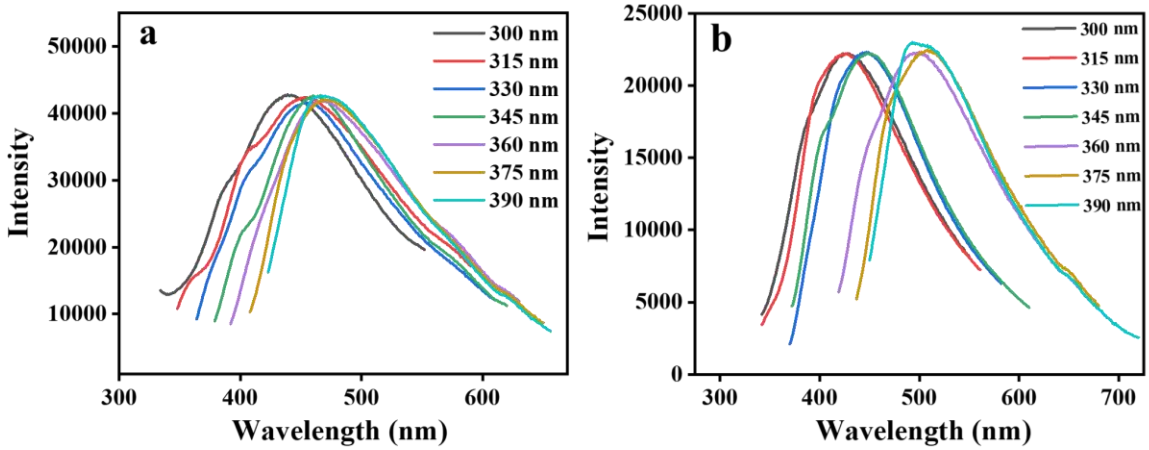

Figure 2.5. PL spectra of (a) A-GQDs, (b) B-GQDs at different excitation wavelength.

The synthesized GQDs exhibited excitation wavelength dependency behaviour and tunable photoluminescence properties. The fluorescence spectra at different excitation

wavelengths ranging from 300-390 nm are shown in Figure 2.5(a-b). The optimal excitation wavelength was selected at 345 nm. The emission maxima observed for A-GQDs and B-GQDs was 468 nm and 452 nm, respectively. A shift was observed in the emission wavelengths with the change in excitation wavelength. This excitation dependent emission properties of the synthesized GQDs are dependent on different factors like quantum confinement effect, zigzag edge sites, size variations, surface edge defects, and conjugated sp^2 π-domains.[29]

2.3.3 Effect of Irradiation Time, pH, Temperature

To investigate the photostability of the synthesized GQDs the irradiation time studies were performed. It was observed that there is no significant change in PL intensity of the GQDs with a change in irradiation time up to 90 mins (Figure 2.6 (a, b)).

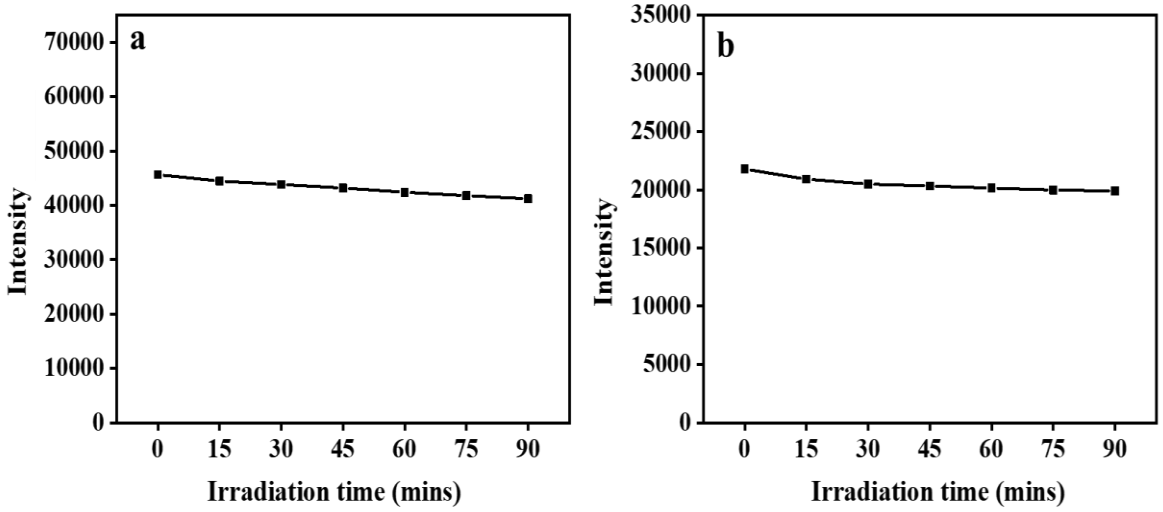

Figure 2.6. The effect of irradiation time on the PL intensity of (a) A-GQDs, and (b) B-GQDs.

The fluorescence emission of the synthesized A-GQDs and B-GQDs was observed to be pH-dependent. PL intensity change of A-GQDs and B-GQDs with the change in pH is shown in Figure 2.7(a, b). The maximum PL intensity was observed at pH 7. A bathochromic shift was observed when the pH changed from 7 to 1. Blueshift (hypsochromic shift) was noticed when the pH increased from 7 to 13 (Figure 2.7a, 2.7b) corresponds to the non-aggregated state which was due to the deprotonation of the carboxyl group of the as-prepared GQDs in basic solution enhancing the electrostatic repulsions between them and hence overcomes the trend of aggregation via layer-layer stacking. Also, the aggregation in neutral and acidic solution decreases the bandgap and hence bathochromic shift was observed.[22]

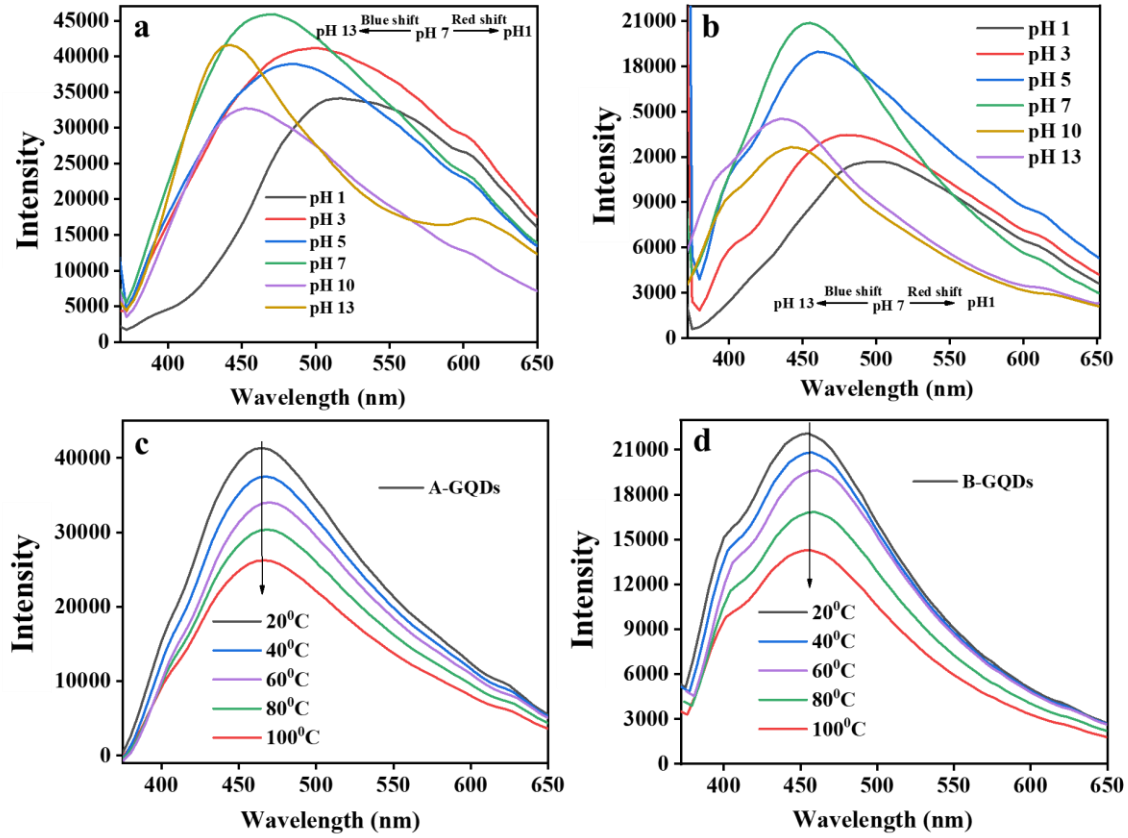

Figure 2.7. Effect of pH on (a) A-GQDs, (b) B-GQDs, effect of temperature on the fluorescence of (c) A-GQDs, and (d) B-GQDs.

The temperature dependence of the PL fluorescence spectrum of A-GQDs and B-GQDs at 345 nm excitation is shown in Figure 2.7c, 2.7d. The PL intensity of the synthesized GQDs decreases with increase in temperature as the stability of complex decreased.[30] This may be attributed to the reason that the non-radiative decay rate increases as the temperature increase which led to a decrease in quantum efficiency along with the PL intensity.[31]

2.3.4 Selectivity Studies of Different Metal Ions

The fluorescence studies were executed to check the selectivity of different metal ions with the synthesized GQDs. The metal cations studied were Pb^{2+}, Zn^{2+}, Hg^{2+}, Cu^{2+}, Co^{2+}, Ni^{2+}, Fe^{3+}, Mn^{2+}, and Mn^{7+} with the 0.5 mM concentration of each metal ion. The result showed a significant fluorescence response after adding Fe^{3+}, Mn^{2+}, and Mn^{7+}, while the remaining metal ions displayed minimal responses (Figure 2.8(a,b)). To validate the selectivity of the as-prepared quantum dots, its PL response in presence of various anions (F^-, S^{2-}, PO_4^{3-}, ClO_3^-, NO_2^-, Cl^-, OH^-, SO_4^{2-}, NO_3^-) were also studied. The results showed that there is minimal effect on the fluorescence intensity of quantum dots on changing anions (Figure 2.8(c,d)). Though,

Mn ion (2+ and 7+) exhibited the maximum decrease in fluorescence intensity, which confirms that both the synthesized A-GQDs and B-GQDs are selective for Mn ions.

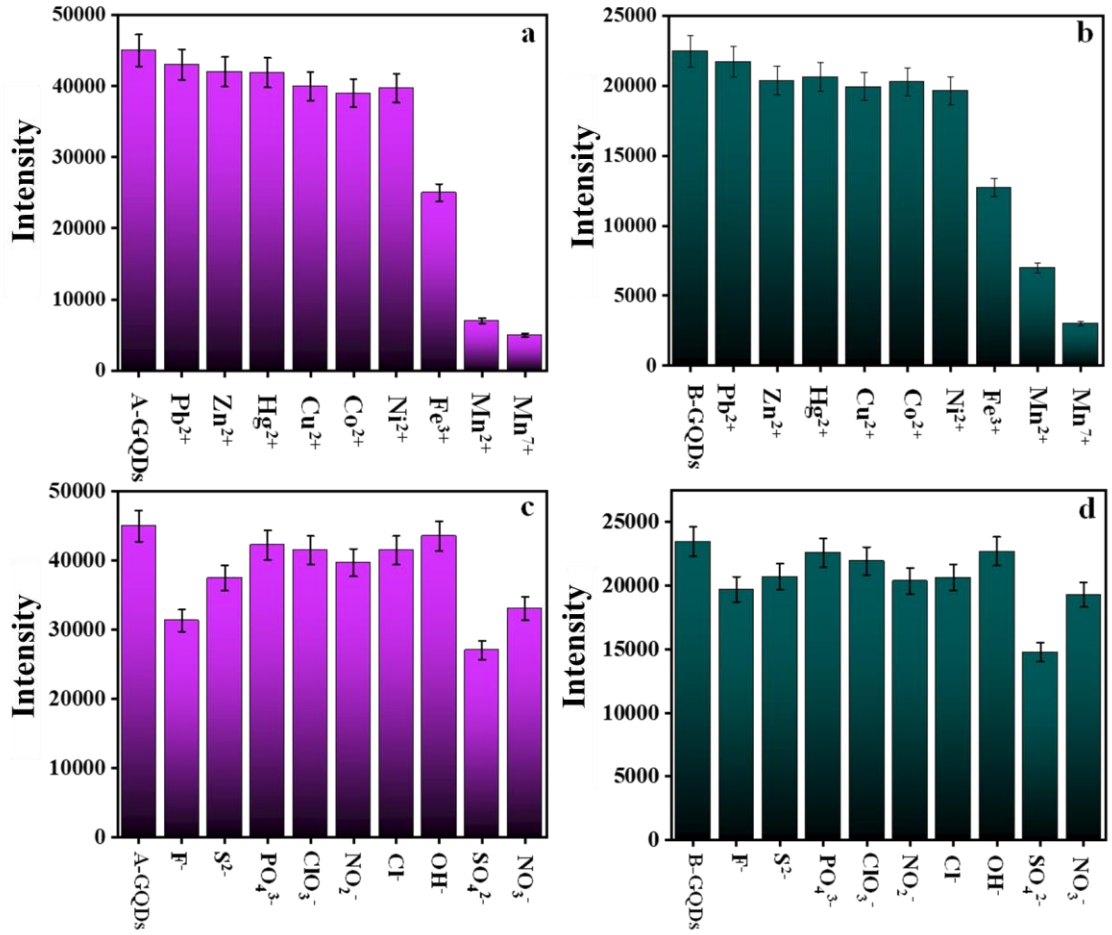

Figure 2.8. Fluorescence response studies of (a) A-GQDs, (b) B-GQDs with cations, (c) A-GQDs, and (d) B-GQDs with anions.

2.3.5 Fluorescence Quenching of GQDs by Mn^{n+} Ions (n=2,7)

The fluorescence intensity of the prepared A-GQDs and B-GQDs was effectually quenched by adding the different oxidation states of Mn (2+ and 7+) (Figure 2.9).

The quenching percentage was different for A-GQDs and B-GQDs in the presence of Mn (2+) and Mn (7+). The fluorescence quenching of the GQDs by Mn ion is accredited to multisite coordination among Mn ion and the electron-rich groups present in the synthesized GQDs. Metal ions can have interaction with GQDs via chelation with O functional moieties present on GQDs along with the π system of graphene domain in GQDs.[32]

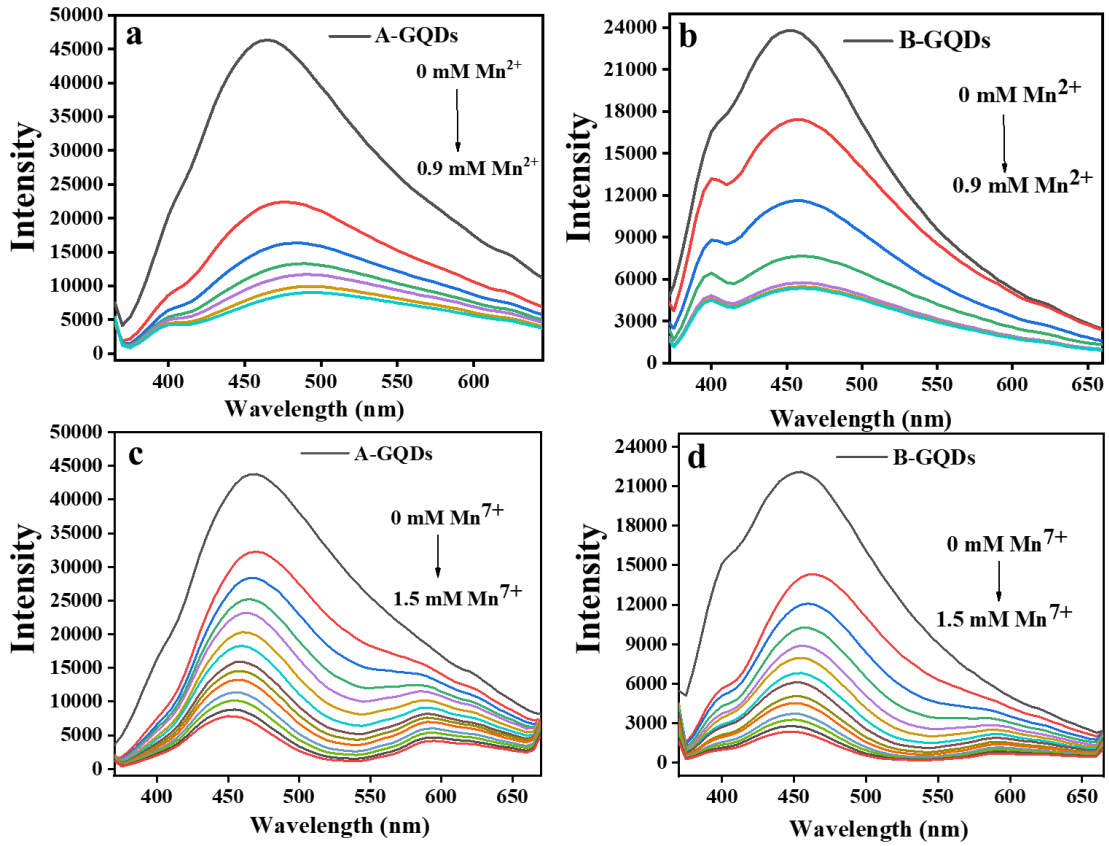

Figure 2.9. Fluorescence quenching spectra of (a) A-GQDs in the presence of Mn^{2+}, (b) B-GQDs in the presence of Mn^{2+}, (c) A-GQDs in presence of Mn^{7+}, and (d) B-GQDs in the presence of Mn^{7+}.

Moreover, the GQDs contain more oxygen-containing groups that serve as electron donors to make non-fluorescence complexes.[33] From UV-Visible absorption spectrum (Figure 2.10(a,b)), it was clearly observed that gradual addition of the quenchers (Mn^{n+}) results ground state complex formation. As a result, we have found the fluorescence quenching in the excited state in presence of the quenchers (Figure 2.9).

The quenching mechanism was further confirmed by time-correlated single photon counting (TCSPC) measurement, which showed that addition of the quencher, the lifetime value of the synthesized GQDs remains unaltered (Figure 2.10(c-d)). Moreover, we have also evaluated the rate of quenching constant of the quencher with variation of the temperature. The results validated that the rate of quenching gradually decreases, which also confirms the static quenching mechanism.

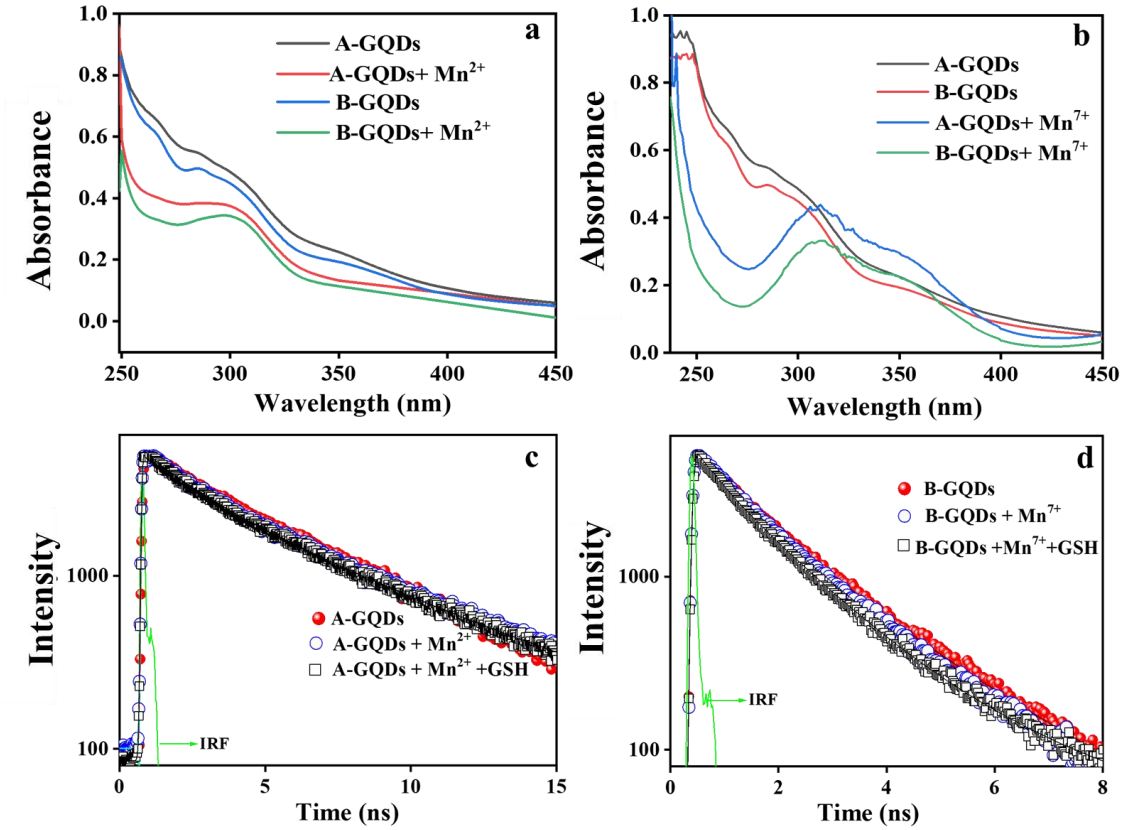

Figure 2.10. UV-Visible absorption spectrum of A-GQDs and B-GQDs before and after the addition of (a) Mn^{2+}, (b) Mn^{7+}, Time-resolved fluorescence emission decays of (c) A-GQDs with Mn^{2+} and GSH, and (d) B-GQDs with Mn^{7+} and GSH.

2.3.6 Fluorescence Quenching of A and B-GQDs by Mn^{2+}

To comprehend the fluorescence quenching of A-and B-GQDs in Mn^{2+}, the concentration of Mn^{2+} varies from 0 mM to 0.90 mM (Figure 2.9(a,b)). To understand the quenching efficiency of Mn^{2+}, the graph between F_0/F vs. Mn^{2+} concentration was plotted according to the Stern-Volmer equation (1.7). The calculated K_{sv} values are 4.85 mM^{-1} and 4.27 mM^{-1} for A-GQDs (Figure 2.11(a)) and B-GQDs (Figure 2.11(b)) with $Mn^{2+,}$ respectively. The quenching efficacy of A-GQDs and B-GQDs with Mn^{2+} is 81.4% and 76.1%, respectively. Additionally, to know the stoichiometry and interaction between the A and B-GQDs with Mn^{2+}, the binding constant values were estimated using fluorescence intensity data by the 1:1 linear Benesi-Hildebrand equation (1.8). The graph between ($1/ F_0$-F) versus 1/[Q] displays a linear curve (Figure 2.11(c, d)). From this graph, value of binding constant (K) of A-GQDs and B-GQDs with Mn^{2+} are 3.77×10^5 mM^{-1} and 5.08×10^4 mM^{-1}, respectively. Table 2.1 shows the fluorescence quantum yields which were estimated using equation 1.1. The quantum yields of A and B-GQDs are quenched ~2.67 and ~ 2.56 times in the presence of Mn^{2+}, respectively.

Table 2.1. Quantum yield (ϕ), Stern-Volmer quenching constant (K_{sv}), and binding constant (K) of A and B-GQDs with Mn^{2+} quencher and GSH[a].

Systems	Φ (λ_{exi} = 345 nm)	$K_{S\text{-}V}$ (mM^{-1})	Binding constant (*K*) (mM^{-1})
A-GQDs	33.54%	-	-
A-GQDs+ Mn^{2+}	12.57%	4.85	3.77×10^{5}
A-GQDs+ Mn^{2+}+ GSH	29.20%	-	6.42×10^{4}
B-GQDs	30.72%	-	-
B-GQDs+ Mn^{2+}	12.02%	4.27	5.08×10^{4}
B-GQDs+ Mn^{2+}+ GSH	26.42%	-	6.85×10^{3}

[a]Experimental error ±5%

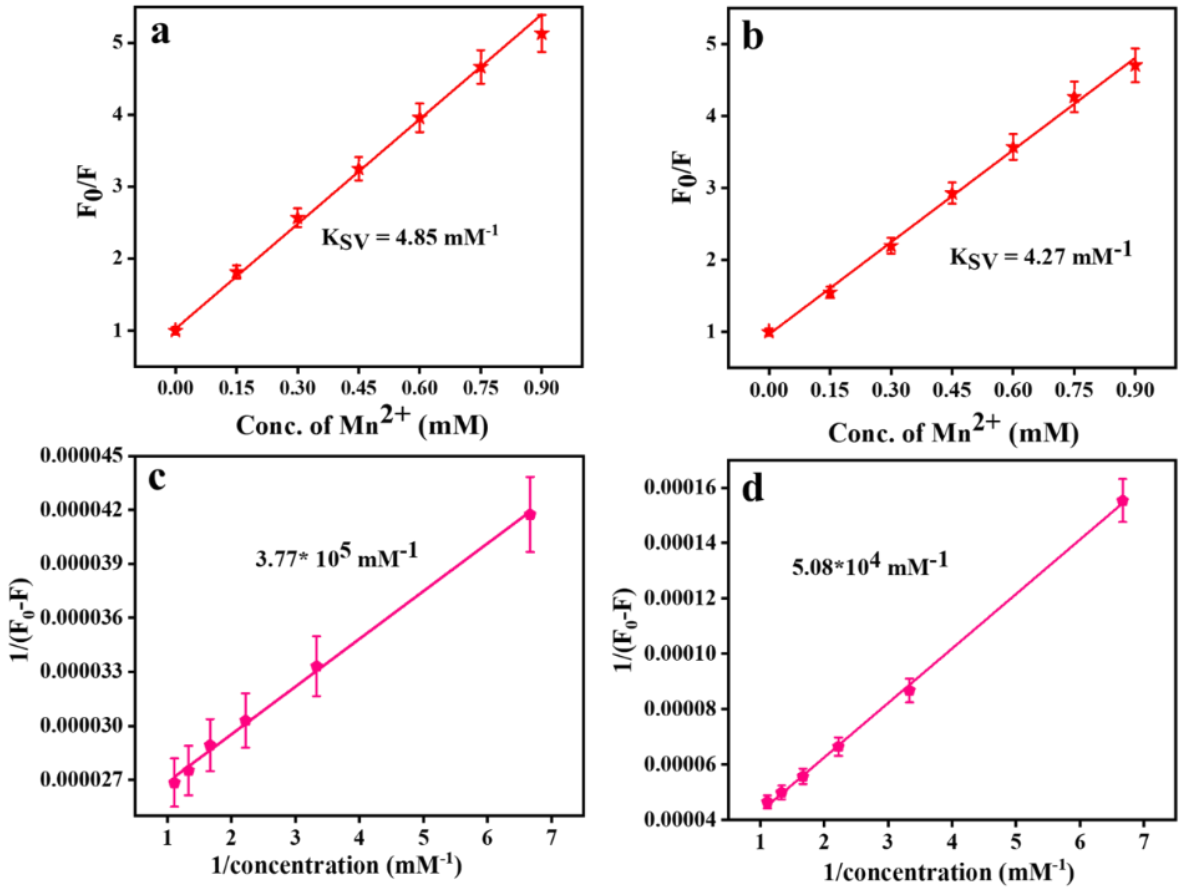

Figure 2.11. Stern-Volmer quenching plot of (a) A-GQDs with Mn^{2+} quencher, (b) B-GQDs with Mn^{2+}, B-H binding plot of (c) A-GQDs with Mn^{2+}, and (d) B-GQDs with Mn^{2+}.

2.3.7 Fluorescence Quenching of A and B-GQDs by Mn^{7+} Ions

To understand the interaction between A and B-GQDs with Mn^{7+}, the concentration of Mn^{7+} varies from 0 mM to 1.50 mM (Figure 2.9(c,d)). To understand the quenching efficiency of Mn^{7+}, the plot between F_0/F vs. the quencher [Q] concentration was drawn according to equation (1.7). Figure 2.12(a,b) shows the plot of F_0/F versus Mn^{7+} concentration. From the slope values, the individual K_{sv} for both the GQDs was assessed. The K_{sv} values are 2.42 mM^{-1} and 3.95 mM^{-1} for A-GQDs (Figure 2.12a) and B-GQDs (Figure 2.12b) with $Mn^{7+,}$ respectively. The quenching efficiency of A-GQDs and B-GQDs with Mn^{7+} is 83.1% and 90.3%, respectively. Also, to assess the stoichiometry and interaction between the A and B-GQDs with Mn^{7+}, the binding constant values were estimated using fluorescence intensity data using equation (1.8). The graph between $(1/F_0\text{-}F)$ versus 1/[Q] displays a linear curve (Figure 2.12 (c,d)). From this graph, the binding constant values (K) of A-GQDs and B-GQDs are 9.63×10^4 mM^{-1} and 7.88×10^5 $mM^{-1,}$ respectively. The fluorescence quantum yield was calculated using equation 1.1 and is shown in Table 2.2. From the table, we observed that the fluorescence quantum yields of A and B-GQDs are quenched ~27.04 and ~27.18 times in the presence of $Mn^{7+,}$ respectively.

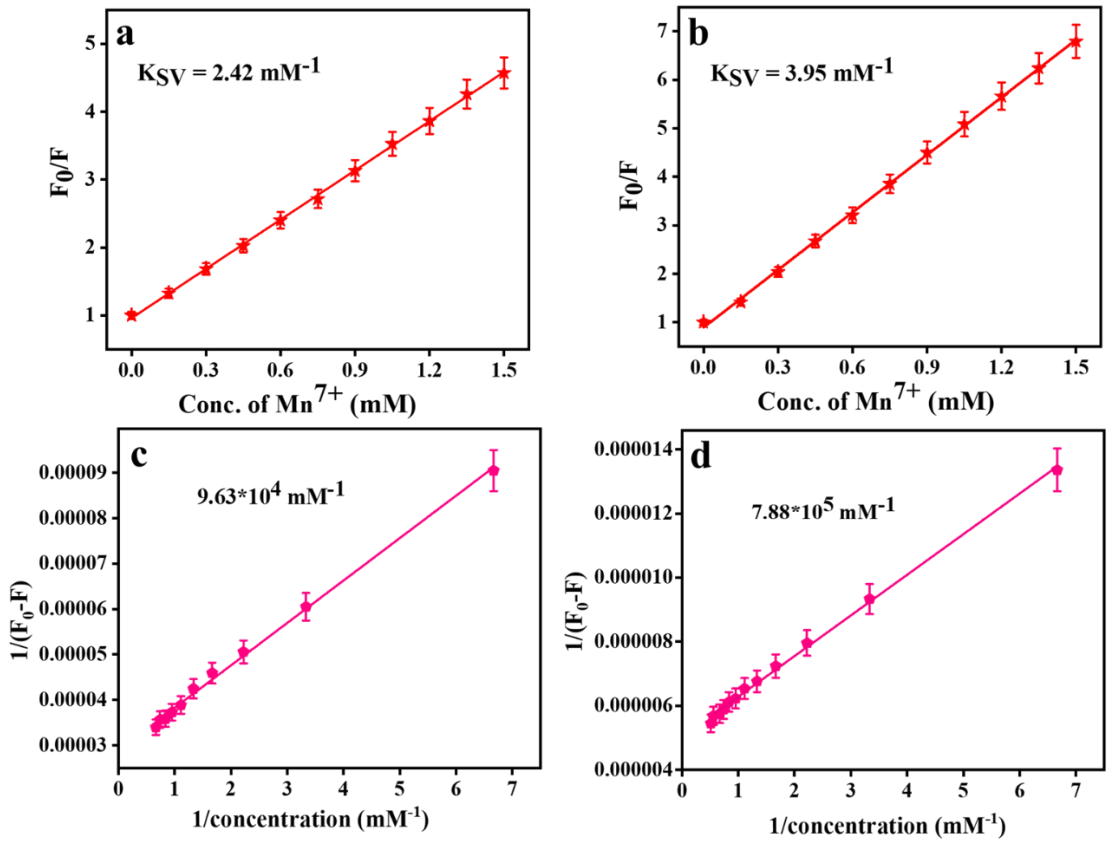

Figure 2.12. Stern-Volmer quenching plot of (a) A-GQDs with Mn^{7+} quencher, (b) B-GQDs with Mn^{7+}, B-H binding plot of (c) A-GQDs with Mn^{7+}, and (d) B-GQDs with Mn^{7+}.

Table 2.2. Quantum yield (ϕ), Stern-Volmer quenching constant (K_{sv}), and binding constant (K) of A and B-GQDs with Mn^{7+} quencher and GSH[a].

Systems	Φ (λ_{exi} = 345 nm)	$K_{S\text{-}V}$ (mM^{-1})	Binding constant (*K*) (mM^{-1})
A-GQDs	33.54%	-	-
A-GQDs+ Mn^{7+}	1.24%	2.42	9.63×10^4
A-GQDs+ Mn^{7+}+ GSH	26.40%	-	4.05×10^4
B-GQDs	30.72%	-	-
B-GQDs+ Mn^{7+}	1.13%	3.95	7.88×10^5
B-GQDs+ Mn^{7+}+ GSH	27.96%	-	5.43×10^4

[a]Experimental error ±5%

The comparison of the fluorescence turn-off efficiency of the synthesized GQDs in Mn^{2+} and Mn^{7+} presence is shown in Figure 2.13(a) and Figure 2.13(b), respectively.

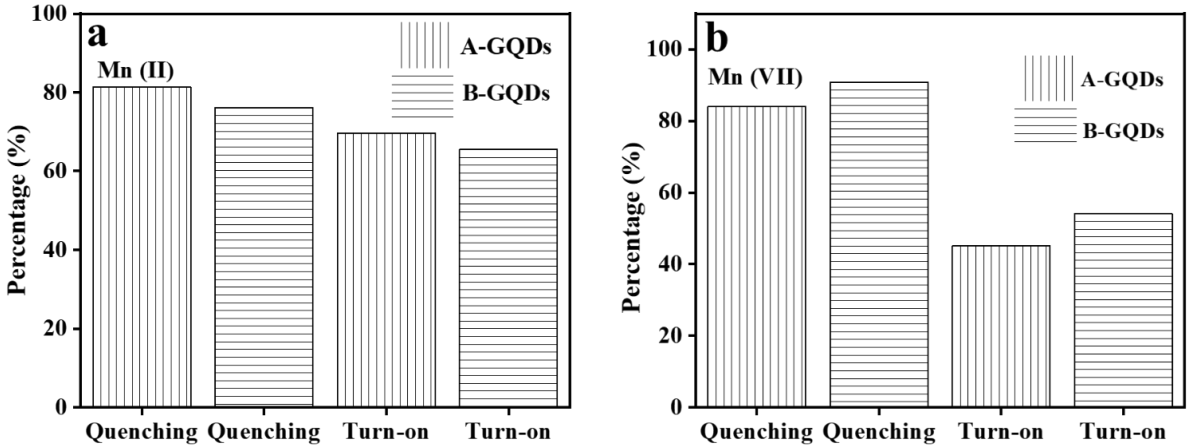

Figure 2.13. Bar graph showing comparison study of quenching and turn-on of (a) A-GQDs and B-GQDs with Mn^{2+}, (b) A-GQDs and B-GQDs with Mn^{7+}.

2.3.8 Fluorescence Restoration of GQDs and GSH Detection

The GSH addition to the different systems of A and B-GQDs with Mn^{2+} and Mn^{7+} nanoprobes consequences the recovery of the fluorescence properties of GQDs (Figure 2.14 (a-d)). This fluorescence turn-on/ restoration of A and B-GQDs in the case of Mn^{2+} quencher is majorly accredited to the stable complex formation formed by reduced GSH with Mn^{2+}. Here, Mn^{2+} is bi-coordinated with O atoms from the carboxyl group of glycine residue and N

atom from the amine group of glutamyl[34] (Scheme 2.2). The fluorescence recovery of A and B-GQDs in the presence of Mn^{7+} quencher is because of the redox reaction amid $KMnO_4$ (7+) and GSH (Scheme 2.2) by the equation below:

$$2\ GSH + KMnO_4 + 5H^+ \longrightarrow GSSG + Mn^{2+} + 3H_2O + KOH \qquad (2.1)$$

In the above equation, reduction of Mn^{7+} to Mn^{2+}, and oxidation of GSH give glutathione disulfide (GSSG). The GSH detection and the fluorescence recovery were investigated by varying concentrations of GSH with fixed conc. of different systems i.e., A and B-GQDs- Mn^{2+} and A and B-GQDs-$Mn^{7+,}$ respectively. It was seen that on gradually increasing the GSH concentration, the fluorescence intensity also increases (Figure 2.14(a-d)).

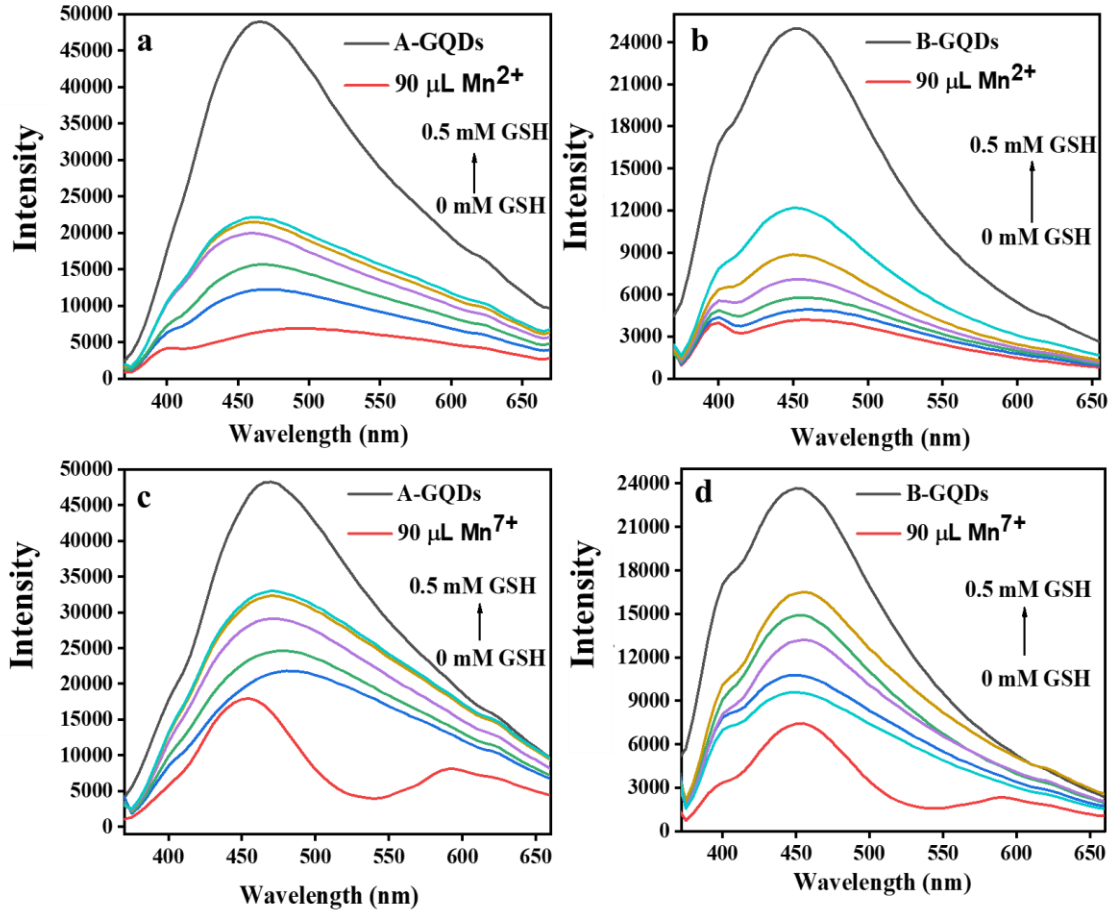

Figure 2.14. Fluorescence restoration of (a) A-GQDs with Mn^{2+}, (b) B-GQDs with Mn^{2+}, c) A-GQDs with Mn^{7+}, and (d) B-GQDs with Mn^{7+} upon addition of GSH.

The comparison of the fluorescence turn-on efficacy of the synthesized GQDs with Mn^{2+} and Mn^{7+} in the GSH presence is represented in Figure 2.13(a) and Figure 2.13(b), respectively.

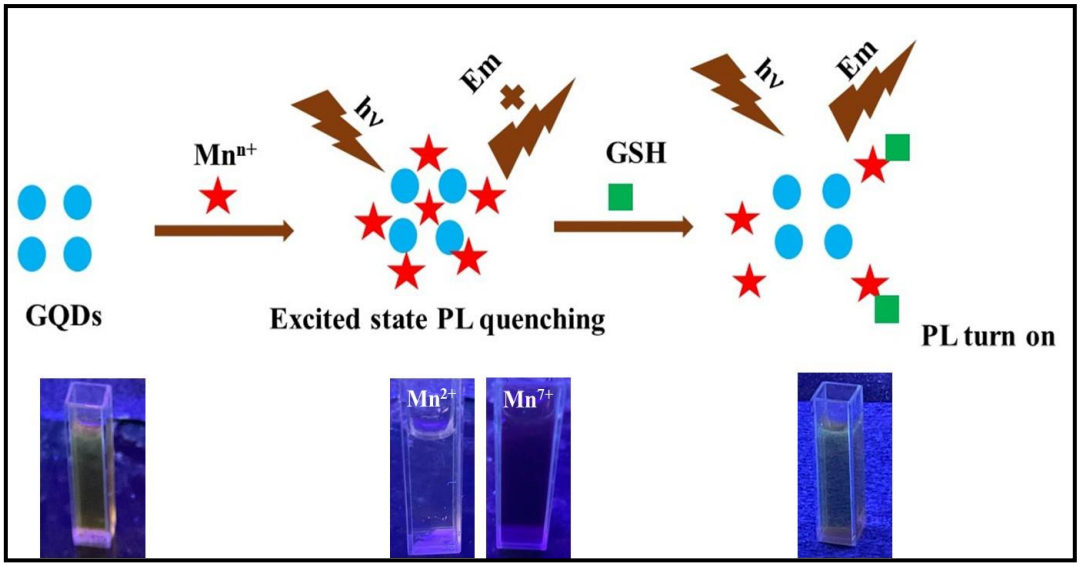

Scheme 2.2. Figure showing mechanism of GQDs detecting GSH in presence of Mn^{n+}.

The final turn on percentage i.e., the effect of GSH on fluorescence recovery of A-GQDs and B-GQDs in presence of different systems is shown in Table 2.3.

Table 2.3. Final turn on percentage of different systems after the GSH addition.

	A-GQDs+Mn^{2+}	**B-GQDs+Mn^{7+}**	**A-GQDs+Mn^{2+}**	**B-GQDs+Mn^{7+}**
GSH	69.6%	65.5%	45.1%	54.1%

Further, the binding constant values of A and B-GQDs- Mn^{2+} and A and B-GQDs-Mn^{7+} by adding GSH were calculated using the Benesi-Hildebrand method.[35] The B-H values for A-GQDs-Mn^{2+}(Figure 2.15(a)), B-GQDs-Mn^{2+} (Figure 2.15(b)), A-GQDs-Mn^{7+} (Figure 2.15(c)), and B-GQDs-Mn^{7+} (Figure 2.15(d)) in the presence of GSH are 6.42×10^4 mM^{-1}, 6.85×10^3 mM^{-1}, 4.05×10^4 mM^{-1}, and 5.43×10^4 mM^{-1}, respectively. It was seen that the GSH presence leads to a decrease in the binding constant values. This result implies that GSH addition leads to the removal of GQDs from the quencher surface. The fluorescence quantum yield in the GSH presence was shown in Table 2.1 and Table 2.2. It was observed that the restoration of the Φ values for A-GQDs-Mn^{2+}, B-GQDs-Mn^{2+}, A-GQDs-Mn^{7+}, B-GQDs-Mn^{7+} in GSH presence are ~2.32, ~2.19, ~21.29, ~24.74 times respectively.

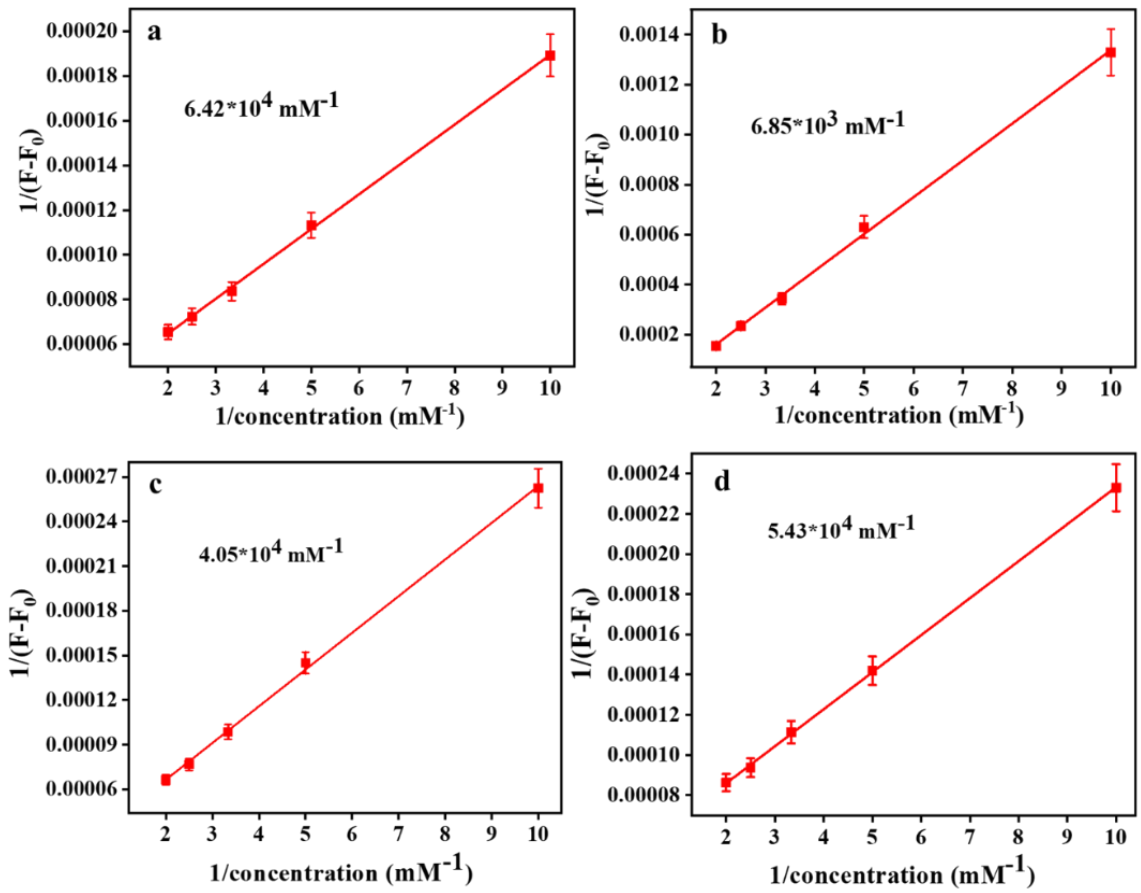

Figure 2.15. B-H binding plot of (a) A-GQDs with Mn^{2+}, (b) B-GQDs with Mn^{2+}, c) A-GQDs with Mn^{7+}, and (d) B-GQDs with Mn^{7+} in presence of GSH.

2.3.9 Selectivity and Sensitivity Studies of Different Analytes for Fluorescence Restoration

To know the selectivity of the anticipated facile sensor for GSH detection, fluorescence studies were done over various competitive analytes. A specific concentrations of amino acids like lysine (Lys), aspartic acid (Asp), cysteine (Cys), ascorbic acid (AA), methionine (Met), tryptophan (Trp), alanine (Ala), arginine (Arg), tyrosine (Tyr), leucine (Leu), glucose, glycine (Gly), glutamic acid (GA), and glutathione (GSH) was mixed with different systems i.e. A-GQDs-Mn^{2+}(Figure 2.16(a)), B-GQDs-Mn^{2+}(Figure 2.16(b)), A-GQDs-Mn^{7+}(Figure 2.16(c)), and B-GQDs-Mn^{7+}(Figure 2.16(d)).

The results confirmed that the GSH exhibited a significant response in comparison to other analytes (Figure 2.16(a-d)). This confirms that the developed sensing platform was very selective and sensitive for the detection of GSH.

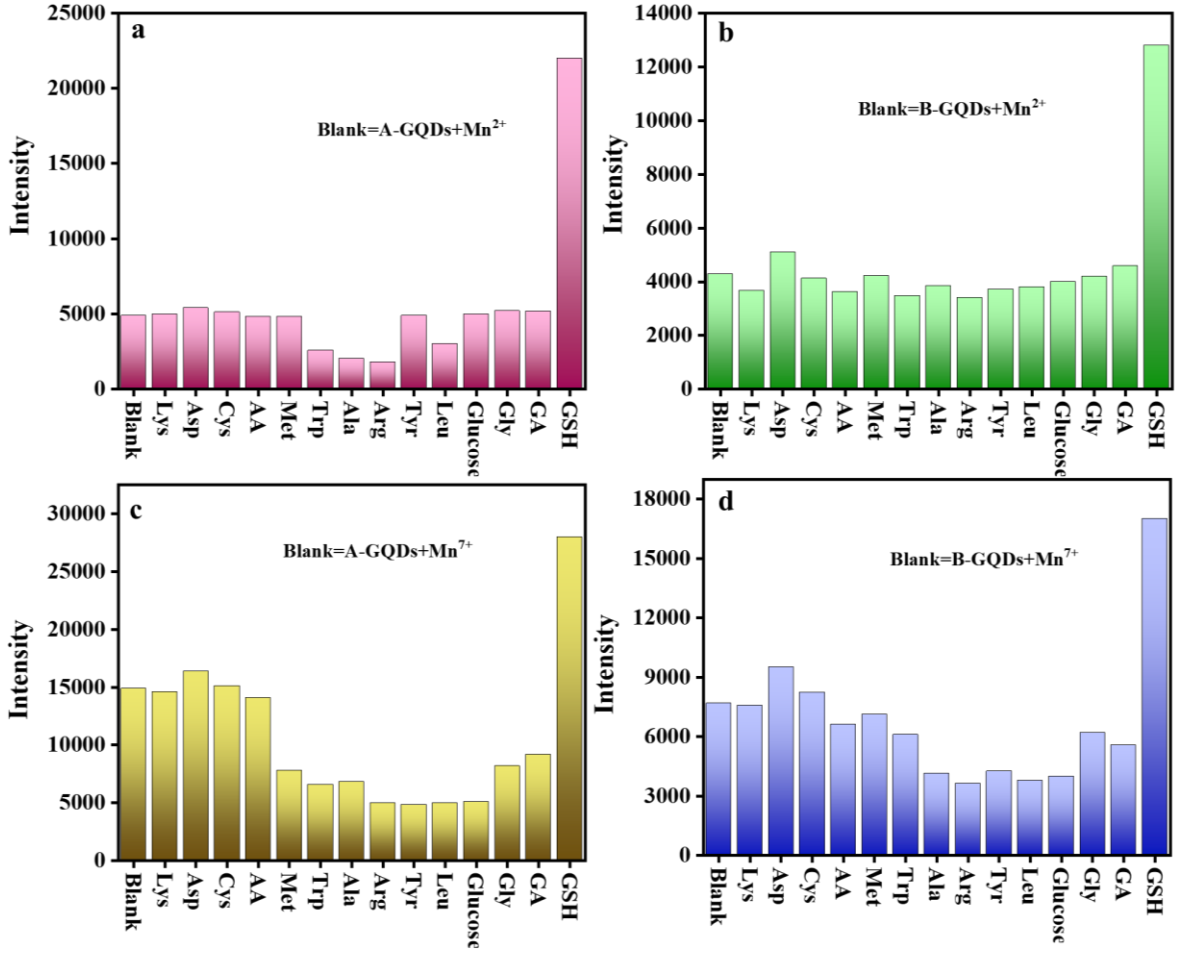

Figure 2.16. Fluorescence response of (a) A-GQDs with Mn^{2+}, (b) B-GQDs with Mn^{2+}, c) A-GQDs with Mn^{7+}, and (d) B-GQDs with Mn^{7+} as a sensing system towards various analytes.

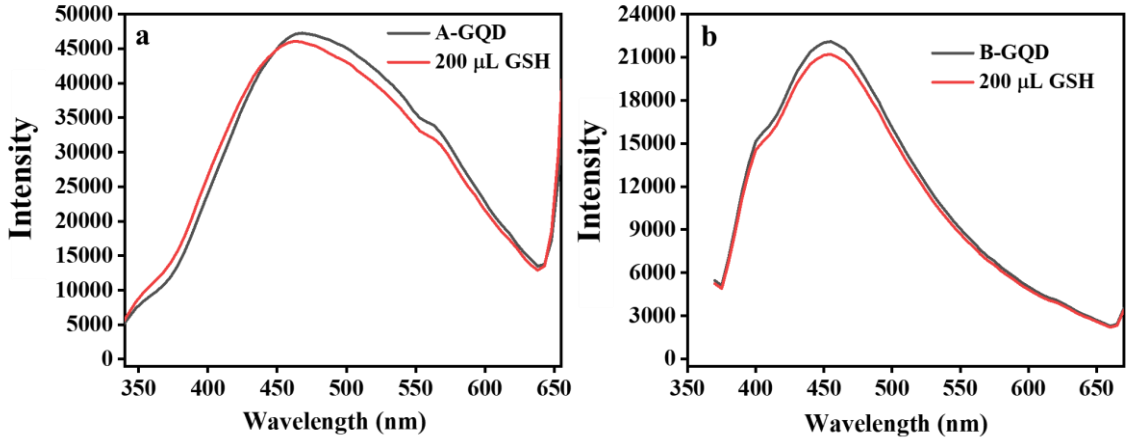

Figure 2.17. Fluorescence response of (a) A-GQDs, (b) B-GQDs in presence of GSH.

Also, a control experiment was performed which showed that GQDs are not directly associated with the selectivity in GSH detection (Figure 2.17(a, b)) as there are minimal changes in fluorescence intensity.

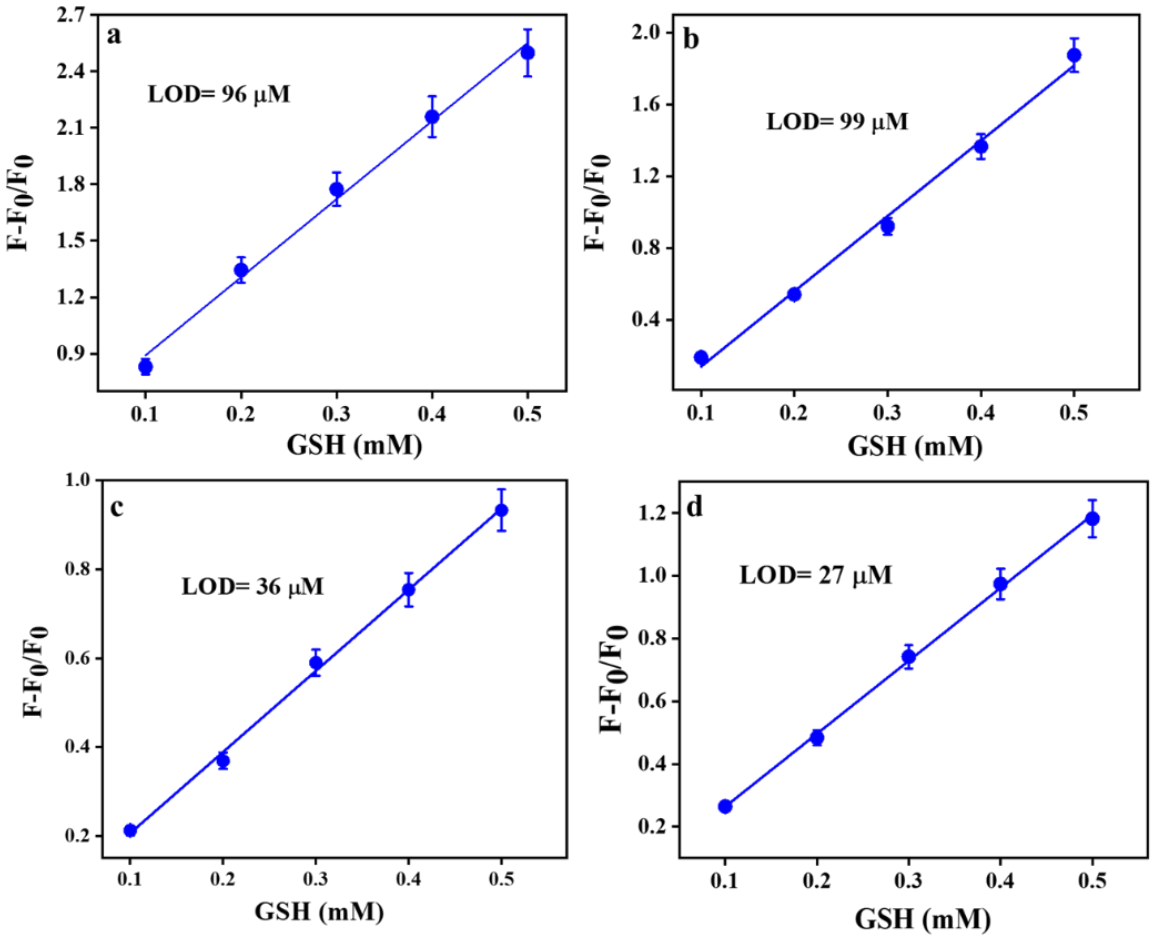

Figure 2.18. A plot of fluorescence response of (a) A-GQDs-Mn^{2+}, (b) B-GQDs-Mn^{2+}, (c) A-GQDs-Mn^{7+}, and (d) B-GQDs-Mn^{7+} systems [$(F-F_0)/F_0$] vs. GSH concentration.

For all the systems of A-GQDs-Mn^{2+}, B-GQDs-Mn^{2+}, A-GQDs-Mn^{7+}, B-GQDs-Mn^{7+}, a decent linear range was seen from the graph of $(F-F_0/F_0)$ vs. GSH concentration, in which F corresponds to fluorescence intensity in GSH presence, F_0 signifies the fluorescence intensity in the absence of GSH. The limit of detection (LOD) values for A-GQDs-Mn^{2+}, B-GQDs-Mn^{2+}, A-GQDs-Mn^{7+}, B-GQDs-Mn^{7+} upon GSH addition are 96 µM, 99 µM, 36 µM, and 27 µM, respectively (Figure 2.18 (a-d)). These studies displayed that the developed sensing platform is facile, green, and cost-effective in comparison to other techniques.

Conclusions

In this chapter, a unique strategy was successfully established to synthesize GQDs from coal which is a ubiquitous energy resource. An efficient fluorometric nanosensor is fabricated using Indian anthracite and bituminous coal-derived GQDs and different oxidation state of Mn ion (2+ and 7+) for the GSH detection. A simple wet chemical route via a top-down technique was employed for the highly water-soluble GQDs synthesis using different coals. The surface functionality and morphology of GQDs were observed by TEM, XPS, EDX, XRD, and FT-IR analysis. The size of synthesized B-GQDs (7.38 nm ± 0.13) was smaller than A-GQDs (10.25 nm ± 0.19) as confirmed through TEM analysis. The PL intensity of the A-GQDs is greater than B-GQDs which is attributed to the quantum confinement effect, signifying a size-dependent outcome on the PL properties. Small size quantum dots generally give rise to hypsochromic shift (blue shift). This study confirmed that the distinctive coal structure is superior for synthesizing GQDs. Along with that, the effect of pH, temperature, and irradiation time on the stability of GQDs has also been studied. With the increase in pH hypsochromic shift was observed and with the increase in temperature the fluorescence intensity of GQDs decreases. The as-prepared GQDs demonstrated excellent selectivity and sensitivity towards Mn^{n+} (2+, 7+) ions. Nevertheless, the GQDs produced exhibited a substantial alteration in both their steady-state absorption and fluorescence intensity when exposed to various Mn^{n+} quenchers. However, the excited state lifetime values remained consistent, confirming the validity of the static quenching mechanism between the GQDs@Mn^{n+} nanoprobes. With the help of fluorescence intensity data, quantum yield (ϕ), Stern-Volmer quenching constant (K_{sv}), and binding constant values (K) were calculated. Furthermore, experiments were conducted to assess fluorescence restoration in the presence of GSH. The synthesized nanoprobe (GQDs-Mn system) is effective for the sensitive and selective analysis of GSH by fluorescence "turn-off-on" mechanism with the detection limit of 96 μM, 99 μM, 36 μM, and 27 μM for A-GQDs-Mn^{2+}, B-GQDs-Mn^{2+}, A-GQDs-Mn^{7+}, B-GQDs-Mn^{7+} in presence of GSH, respectively. In short, the above findings showed that the developed fluorescent probes are inexpensive and simplified method for GSH detection to practical claims.

References

(1) Yan, X.; Song, Y.; Zhu, C.; Song, J.; Du, D.; Su, X.; Lin, Y. Graphene Quantum Dot–MnO_2 Nanosheet Based Optical Sensing Platform: A Sensitive Fluorescence "Turn off–on" Nanosensor for Glutathione Detection and Intracellular Imaging. *ACS Appl. Mater. Interfaces* **2016**, *8*, 21990–21996. https://doi.org/10.1021/acsami.6b05465.

(2) Xin-Yu, L. I.; ZHANG, Q.; Ni, W.; Jia-Jun, L. I. U.; Jian, W. Cu2+-Mediated Fluorescence Switching of Graphene Quantum Dots for Highly Selective Detection of Glutathione. *Chinese J. Anal. Chem.* **2020**, *48*, 339–346. https://doi.org/10.1016/S1872-2040(20)60003-2.

(3) Sohal, N.; Maity, B.; Basu, S. Carbon Dot-MnO2Nanosphere Composite Sensors for Selective Detection of Glutathione. *ACS Appl. Nano Mater.* **2020**, *3*, 5955–5964. https://doi.org/10.1021/acsanm.0c01088..

(4) Lee, S.; Li, J.; Zhou, X.; Yin, J.; Yoon, J. Recent Progress on the Development of Glutathione (GSH) Selective Fluorescent and Colorimetric Probes. *Coord. Chem. Rev.* **2018**, *366*, 29–68. https://doi.org/10.1016/j.ccr.2018.03.021.

(5) Ni, P.; Sun, Y.; Dai, H.; Hu, J.; Jiang, S.; Wang, Y.; Li, Z. Highly Sensitive and Selective Colorimetric Detection of Glutathione Based on Ag [I] Ion-3,3',5,5'-Tetramethylbenzidine (TMB). *Biosens. Bioelectron.* **2015**, *63*, 47–52. https://doi.org/10.1016/j.bios.2014.07.021.

(6) Wang, Y.; Jiang, L.; Leng, Q.; Wu, Y.; He, X.; Wang, K. Electrochemical Sensor for Glutathione Detection Based on Mercury Ion Triggered Hybridization Chain Reaction Signal Amplification. *Biosens. Bioelectron.* **2016**, *77*, 914–920. https://doi.org/10.1016/j.bios.2015.10.071.

(7) Lin, R.; Zhang, J.; Shu, L.; Zhu, J.; Fu, B.; Song, C.; Shang, W.; Tao, P.; Deng, T. Self-Dispersible Graphene Quantum Dots in Ethylene Glycol for Direct Absorption-Based Medium-Temperature Solar-Thermal Harvesting. *RSC Adv.* **2020**, *10*, 45028–45036. https://doi.org/10.1039/d0ra08128k.

(8) Alizadeh, T.; Shokri, M. A New Humidity Sensor Based upon Graphene Quantum Dots Prepared via Carbonization of Citric Acid. *Sensors Actuators, B Chem.* **2016**, *222*, 728–734. https://doi.org/10.1016/j.snb.2015.08.122.

(9) Ma, C. B.; Zhu, Z. T.; Wang, H. X.; Huang, X.; Zhang, X.; Qi, X.; Zhang, H. L.; Zhu, Y.; Deng, X.; Peng, Y.; Han, Y.; Zhang, H. A General Solid-State Synthesis of Chemically-Doped Fluorescent Graphene Quantum Dots for Bioimaging and Optoelectronic Applications. *Nanoscale* **2015**, *7*, 10162–10169. https://doi.org/10.1039/c5nr01757b.

(10) Jovanović, S. P.; Syrgiannis, Z.; Budimir, M. D.; Milivojević, D. D.; Jovanovic, D. J.; Pavlović, V. B.; Papan, J. M.; Bartenwerfer, M.; Mojsin, M. M.; Stevanović, M. J. Graphene Quantum Dots as Singlet Oxygen Producer or Radical Quencher-The Matter of Functionalization with Urea/Thiourea. *Mater. Sci. Eng. C* **2020**, *109*, 110539. Jovanović, S. P.; Syrgiannis, Z.; Budimir, M. D.; Milivojević, D. D.; Jovanovic, D. J.; Pavlović, V. B.; Papan,

J. M.; Bartenwerfer, M.; Mojsin, M. M.; Stevanović, M. J. Graphene Quantum Dots as Singlet Oxygen Producer or Radical Quencher-The Matter of Functionalization with Urea/Thiourea. *Mater. Sci. Eng. C* **2020**, *109*, 110539.

(11) Fang, L.; Zhang, L.; Chen, Z.; Zhu, C.; Liu, J.; Zheng, J. Ammonium Citrate Derived Carbon Quantum Dot as On-off-on Fluorescent Sensor for Detection of Chromium(VI) and Sulfites. *Mater. Lett.* **2017**, *191*, 1–4. https://doi.org/10.1016/j.matlet.2016.12.098.

(12) Sun, Y.; Wang, S.; Li, C.; Luo, P.; Tao, L.; Wei, Y.; Shi, G. Large Scale Preparation of Graphene Quantum Dots from Graphite with Tunable Fluorescence Properties. *Phys. Chem. Chem. Phys.* **2013**, *15*, 9907–9913. https://doi.org/10.1039/c3cp50691f.

(13) Nilewski, L.; Mendoza, K.; Jalilov, A. S.; Berka, V.; Wu, G.; Sikkema, W. K. A.; Metzger, A.; Ye, R.; Zhang, R.; Luong, D. X.; Wang, T.; McHugh, E.; Derry, P. J.; Samuel, E. L.; Kent, T. A.; Tsai, A. L.; Tour, J. M. Highly Oxidized Graphene Quantum Dots from Coal as Efficient Antioxidants. *ACS Appl. Mater. Interfaces* **2019**, *11*, 16815–16821. https://doi.org/10.1021/acsami.9b01082.

(14) Das, T.; Saikia, B. K.; Dekaboruah, H. P.; Bordoloi, M.; Neog, D.; Bora, J. J.; Lahkar, J.; Narzary, B.; Roy, S.; Ramaiah, D. Blue-Fluorescent and Biocompatible Carbon Dots Derived from Abundant Low-Quality Coals. *J. Photochem. Photobiol. B Biol.* **2019**, *195*, 1–11. https://doi.org/10.1016/j.jphotobiol.2019.04.004.

(15) Zhang, Y.; Li, K.; Ren, S.; Dang, Y.; Liu, G.; Zhang, R.; Zhang, K.; Long, X.; Jia, K. Coal-Derived Graphene Quantum Dots Produced by Ultrasonic Physical Tailoring and Their Capacity for Cu(II) Detection. *ACS Sustain. Chem. Eng.* **2019**, *7*, 9793–9799. https://doi.org/10.1021/acssuschemeng.8b06792.

(16) Ye, R.; Peng, Z.; Metzger, A.; Lin, J.; Mann, J. A.; Huang, K.; Xiang, C.; Fan, X.; Samuel, E. L. G.; Alemany, L. B.; Martí, A. A.; Tour, J. M. Bandgap Engineering of Coal-Derived Graphene Quantum Dots. *ACS Appl. Mater. Interfaces* **2015**, *7*, 7041–7048. https://doi.org/10.1021/acsami.5b01419.

(17) Kovalchuk, A.; Huang, K.; Xiang, C.; Martí, A. A.; Tour, J. M. Luminescent Polymer Composite Films Containing Coal-Derived Graphene Quantum Dots. *ACS Appl. Mater. Interfaces* **2015**, *7*, 26063–26068. https://doi.org/10.1021/acsami.5b06057.

(18) Zhang, Y.; Zhang, K.; Jia, K.; Liu, G.; Ren, S.; Li, K.; Long, X.; Li, M.; Qiu, J. Preparation of Coal-Based Graphene Quantum Dots/A-Fe2O3 Nanocomposites and Their Lithium-Ion Storage Properties. *Fuel* **2019**, *241*, 646–652. https://doi.org/10.1016/j.fuel.2018.12.030.

(19) Singamaneni, S. R.; Van Tol, J.; Ye, R.; Tour, J. M. Intrinsic and Extrinsic Defects in a Family of Coal-Derived Graphene Quantum Dots. *Appl. Phys. Lett.* **2015**, *107* (21), 212402. https://doi.org/10.1063/1.4936204.

(20) Crosby, G. A.; Demas, J. N. Measurement of Photoluminescence Quantum Yields. *Chem. Int.* **2015**, *37*, 991–1024. https://doi.org/10.1515/ci-2015-0521.

(21) Kumar, S.; Ojha, A. K.; Ahmed, B.; Kumar, A.; Das, J.; Materny, A. Tunable (Violet to Green) Emission by High-Yield Graphene Quantum Dots and Exploiting Its Unique Properties towards Sun-Light-Driven Photocatalysis and Supercapacitor Electrode Materials. *Mater. Today Commun.* **2017**, *11*, 76–86. https://doi.org/10.1016/j.mtcomm.2017.02.009.

(22) Ye, R.; Xiang, C.; Lin, J.; Peng, Z.; Huang, K.; Yan, Z.; Cook, N. P.; Samuel, E. L. G.; Hwang, C.-C.; Ruan, G. Coal as an Abundant Source of Graphene Quantum Dots. *Nat. Commun.* **2013**, *4*, 1–7. 10.1038/ncomms3943.

(23) Kainth, S.; Maity, B.; Basu, S. Label-Free Detection of Creatinine Using Nitrogen-Passivated Fluorescent Carbon Dots. *RSC Adv.* **2020**, *10*, 36253–36264. https://doi.org/10.1039/D0RA06512A.

(24) Xu, Y.; Wang, S.; Hou, X.; Sun, Z.; Jiang, Y.; Dong, Z.; Tao, Q.; Man, J.; Cao, Y. Coal-Derived Nitrogen, Phosphorus and Sulfur Co-Doped Graphene Quantum Dots: A Promising Ion Fluorescent Probe. *Appl. Surf. Sci.* **2018**, *445*, 519–526. https://doi.org/10.1016/j.apsusc.2018.03.156.

(25) Zhang, S.; Zhu, J.; Qing, Y.; Fan, C.; Wang, L.; Huang, Y.; Sheng, R.; Guo, Y.; Wang, T.; Pan, Y. Construction of Hierarchical Porous Carbon Nanosheets from Template-Assisted Assembly of Coal-Based Graphene Quantum Dots for High Performance Supercapacitor Electrodes. *Mater. today energy* **2017**, *6*, 36–45. https://doi.org/10.1016/j.mtener.2017.08.003.

(26) Sun, L.; Luo, Y.; Li, M.; Hu, G.; Xu, Y.; Tang, T.; Wen, J.; Li, X.; Wang, L. Role of Pyridinic-N for Nitrogen-Doped Graphene Quantum Dots in Oxygen Reaction Reduction. *J. Colloid Interface Sci.* **2017**, *508*, 154–158. https://doi.org/10.1016/j.jcis.2017.08.047.

(27) Kaczmarek, A.; Hoffman, J.; Morgiel, J.; Mościcki, T.; Stobiński, L.; Szymański, Z.; Małolepszy, A. Luminescent Carbon Dots Synthesized by the Laser Ablation of Graphite in Polyethylenimine and Ethylenediamine. *Materials (Basel).* **2021**, *14*, 1–13. https://doi.org/10.3390/ma14040729.

(28) Abbas, A.; Tabish, T. A.; Bull, S. J.; Lim, T. M.; Phan, A. N. High Yield Synthesis of Graphene Quantum Dots from Biomass Waste as a Highly Selective Probe for Fe^{3+} Sensing. *Sci. Rep.* **2020**, *10*, 1–16. https://doi.org/10.1038/s41598-020-78070-2.

(29) Sohal, N.; Bhatia, S. K.; Basu, S.; Maity, B. Nanomolar Level Detection of Metal Ions by Improving the Monodispersity and Stability of Nitrogen-Doped Graphene Quantum Dots. *New J. Chem.* **2021**, *45*, 19941–19949. https://doi.org/10.1039/D1NJ04551B.

(30) Zhang, J.; Na, L.; Jiang, Y.; Lou, D.; Jin, L. Graphene Quantum Dots as a Fluorescence-Quenching Probe for Quantitative Analysis of Ponceau 4R Solution. *Anal. Methods* **2016**, *8*, 7242–7246. https://doi.org/10.1039/C6AY02203K.

(31) Li, C.; Yue, Y. Fluorescence Spectroscopy of Graphene Quantum Dots: Temperature Effect at Different Excitation Wavelengths. *Nanotechnology* **2014**, *25*, 435703. 10.1088/0957-4484/25/43/435703.

(32) Huang, H.; Liao, L.; Xu, X.; Zou, M.; Liu, F.; Li, N. The Electron-Transfer Based Interaction between Transition Metal Ions and Photoluminescent Graphene Quantum Dots (GQDs): A Platform for Metal Ion Sensing. *Talanta* **2013**, *117*, 152–157. https://doi.org/10.1016/j.talanta.2013.08.055.

(33) Wang, F.; Gu, Z.; Lei, W.; Wang, W.; Xia, X.; Hao, Q. Graphene Quantum Dots as a Fluorescent Sensing Platform for Highly Efficient Detection of Copper (II) Ions. *Sensors Actuators B Chem.* **2014**, *190*, 516–522. https://doi.org/10.1016/j.snb.2013.09.009.

(34) Liu, J.; Liu, H.; Li, Y.; Wang, H. Probing the Coordination Properties of Glutathione with Transition Metal Ions (Cr^{2+}, Mn^{2+}, Fe^{2+}, Co^{2+}, Ni^{2+}, Cu^{2+}, Zn^{2+}, Cd^{2+}, Hg^{2+}) by Density Functional Theory. *J. Biol. Phys.* **2014**, *40*, 313–323. 10.1007/s10867-014-9350-3.

(35) Benesi, H. A.; Hildebrand, J. H. A Spectrophotometric Investigation of the Interaction of Iodine with Aromatic Hydrocarbons. *J. Am. Chem. Soc.* **1949**, *71*, 2703–2707. https://doi.org/10.1021/ja01176a030.

CHAPTER-3

Rice-Husk Derived Carbon Quantum Dots-Based Dual-Mode Nanoprobe for Selective and Sensitive Detection of Fe^{3+} and Fluoroquinolones

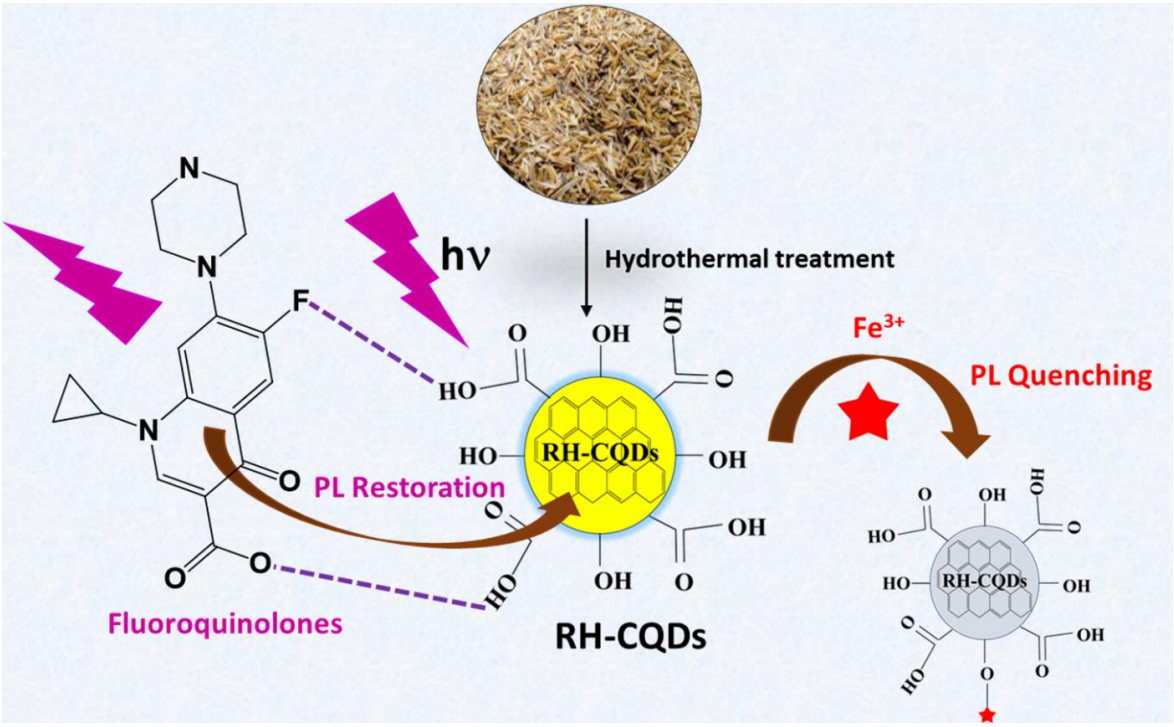

Highlights

- Synthesis of carbon quantum dots from rice husk using the hydrothermal method.
- Study of several photophysical parameter to investigate the interaction between RH-CQDs and Fe^{3+}.
- Comparative photophysical studies were performed to investigate the interaction between RH-CQDs and Ofloxacin/Ciprofloxacin.
- Integration of two different mechanisms (fluorescence quenching and fluorescence enhancement) to construct a single sensing platform for accurate quantification of dual-mode nanosensors.

3.1 Introduction

Energy scarcity, the steady depletion of non-renewable resources, and environmental conditions are humans global concerns.[1–3] Biomass conversion has a lot of potential to solve these problems because of its abundance of renewable, eco-friendly, sustainable, and clean resources.[4] Moreover, it's a promising "waste to wealth" technique in today's era. Green and sustainable synthesis of carbon-derived materials from biomass has recently sparked an extensive study.[5] Rice (*Oryza sativa*), a rich source of carbohydrates, is one of the most significant cultivated harvests in the world.[6] Every year, around 156 million tonnes of rice husk (RH) are produced worldwide.[7] Most husk is wasted as agricultural waste or burned to emit greenhouse gases. Also, in addition to silica, RH constitutes a high quantity of organic components such as lignin, hemicellulose, and cellulose (72-85 wt%).[8] Because of its high carbon content and readily accessible raw materials for mass production and scale-up, RH is selected as the precursor for synthesizing optically distinct CQDs. Different studies have looked into the production of CQDs from rice husks. *Pandey et al.* described the synthesis of bio-compatible mesoporous silica oxide/ carbon-dots complex. The as-prepared complex was used in biological imaging.[9] *Ngu et al.* synthesized carbon dots using thermally-assisted carbonization from rice husk, and further used them to sense Sn^{2+} ions.[10] *Wang et al.* reported the synthesis of photoluminescent carbon dot grafted silica nanoparticles from rice husk.[11] The promising properties of carbon quantum dots endorse them as a suitable sensor for detecting metal ions in both biological and environmental systems and have attracted considerable attention.[12]

Carbon quantum dots contain -COOH groups, -OH groups on the surface, and conjugated π-domains that can interact with metal ions.[13,14] The chelation tends to occur fast when transition metals come into contact with an electron donor group because of empty d-orbitals. Since, CQDs have oxygen-containing functional groups which serve as electron donors, combining with ions to generate non-fluorescent complexes.[15] As a result, CQDs are efficient sensors for some transition metal ions. Fe^{3+} is the most abundant essential trace element in biological systems and the atmosphere. It is the most frequent heavy metal pollutant found in natural water bodies.[16] Fe^{3+} ions play a crucial role in various biochemical processes.[17] The abnormal level of ferric ions can cause several disorders, such as malaria, anaemia, Parkinson's, and Alzheimer's disease.[18] Hence, the sensitive detection of Fe^{3+} has a lot of significance.[19]

Continued use of antibiotics results in serious environmental concerns. Ofloxacin (OFX) and Ciprofloxacin (CPX) are one of the most widely used fluoroquinolones. The human body cannot wholly metabolize fluoroquinolone, which is excreted in pharmacologically active form. Also, it has poor degradability and thus polluting surface and sewage water.[20] Their residue in the environment have been shown to cause the formation of novel antibiotic resistance bacteria, which could constitute a public health risk.[21] Detection of OFX and CPX in food samples, pharmaceutical preparations, and the environment is essential and has attracted much research interest.

For metal ion sensing and fluoroquinolone detection, different equipment and electrochemical approaches have been utilized. However, they are costly, time-consuming, and complex. Fluorescence spectroscopy is accessible, highly sensitive, and inexpensive for detecting metal ions[22] and antibiotics.[23,24] *Zhao et al.* synthesized carbon quantum dots from pine wood and used them for the detection of the Fe^{3+} ions.[25] *Zhang et al.* used the hydrothermal method for the synthesis of carbon quantum dots from corncob residues and used for Fe^{3+} sensors.[26] *Khan et al.* fabricated carbon quantum dots from red lentils using the hydrothermal method and used it for sensitive detection of Fe^{3+}.[27] *Suanchan et al.* synthesized hierarchical porous carbon, and graphene quantum dots and this probe was used for the detection of ofloxacin.[24] *Shan et al.* fabricated CdS quantum dots for the determination of ciprofloxacin in biological fluids.[28]

In the present work, rice husk (RH) as a bio-waste precursor was used for the facile and eco-friendly synthesis of CQDs. Stability studies like pH effect, irradiation time (mins), and storage days on the fluorescence of RH-CQDs were performed. The as-prepared RH-CQDs were successfully tried as a fluorescent nanoprobe for the sensing of Fe^{3+} with desirable sensitivity and selectivity over other metal ions. Furthermore, the fabricated sensor was utilized as a sensing probe for the detection of Fe^{3+} in tablet supplements. Also, the synthesized nanosensor was simultaneously investigated for the detection of fluoroquinolone (OFX and CPX) using a fluorescent restoration technique with excellent sensitivity and selectivity over different analytes. Fluorescence restoration of RH-CQDs with OFX/CPX is affirmed using lifetime studies. To the best of our knowledge this is the first report in which the carbon quantum dots act as a dual-mode nanoprobe simultaneously for selective and sensitive detection of Fe^{3+} and Ofloxacin/Ciprofloxacin.

3.2 Experimental Section

3.2.1 Materials and Reagents

Rice husk was procured from rice sailors in Patiala, India. Reagents such as sodium hydroxide (NaOH), sulphuric acid (H_2SO_4), and nitric acid (HNO_3) used for the synthesis of RH-CQDs were purchased from Loba Chemie Pvt. Ltd., India. Chemicals used for metal ions stock solutions like $Hg(NO_3)_2$, $Zn(NO_3)_2$, $Cu(NO_3)_2$, $Mn(NO_3)_2$, $Co(NO_3)_2$, $Cr(NO_3)_3$, $Fe(NO_3)_2$, $Pb(NO_3)_2$, $Ni(NO_3)_2$, and $Fe(NO_3)_3$ were purchased from Loba Chemie Pvt. Ltd., India. Double-distilled water was used for the preparation of stock solutions.

3.2.2 Synthesis of Rice Husk-Carbon Quantum Dots (RH-CQDs)

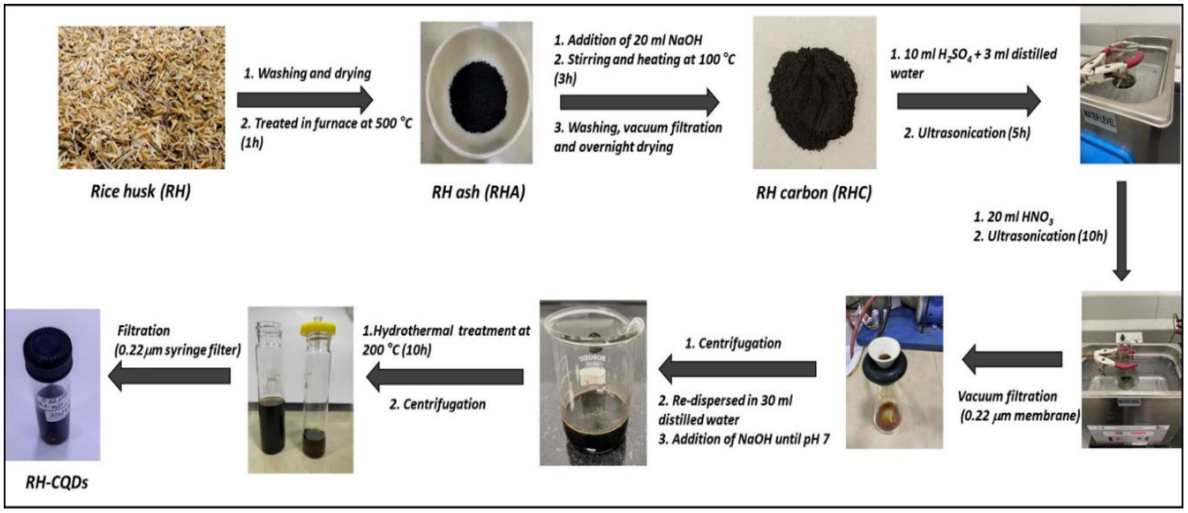

Scheme 3.1. A pictorial illustration of the synthesis of RH-CQDs.

Firstly, rice husk was thoroughly washed with double distilled water and dried in an oven at 90 °C. The dried sample was kept in a furnace at 500 °C for 1 hr to obtain rice husk ash (RHA). NaOH (1.0 N, 20 mL) was added to the measured amount of RHA, which was then stirred and heated at 100 °C for 3 hr. The solution was thoroughly washed with distilled water, vacuum filtered, and dried overnight to obtain rice husk carbon (RHC). Now, RHC (50 mg) was dissolved in distilled water (3 mL) and H_2SO_4 (10 mL), ultrasonicated (Labman scientific instruments, Ultrasonic cleaner) for 5 hrs. HNO_3 (20 mL) was gradually added and ultrasonicated for 10 hrs. The obtained solution was further vacuum filtered with 0.22 μm microporous membrane and centrifuged for 10 mins at 5000 rpm (REMI PR-24). Further, the solution was re-dispersed in distilled water (30 mL) and NaOH (1.0 M) was added until pH 7. The dispersion was transferred to a Teflon-lined autoclave, and the hydrothermal treatment was done at 200 °C for 10 hr. The solution was cooled at room temperature, centrifuged, and filtered using a 0.22 μm syringe filter leading to brown-coloured RH-CQDs as shown in Scheme 3.1.

3.2.3 Characterizations

The UV-Visible absorption spectra of the as-prepared RH-CQDs were recorded using UV-Vis spectrophotometer (Shimadzu UV 2600). The emission spectra were studied using a spectrofluorometer instrument (Shimadzu, RF-6000). The morphology and size of the prepared CQDs were examined with transmission electron microscopy (TEM, FEI Tecnai G2 F20). Elemental composition was examined through X-ray photoelectron spectroscopy (XPS) (PHI 5000 Versa Probe III) and Energy dispersive X-ray spectroscopy (EDX) (Oxford INCA-XACT). The fluorescence lifetime decays were recorded using time-correlated single-photon counting (TCSPC) measurements from Edinburgh instrument (Model: Lifespec-II, U.K.) with an excitation source at 340 nm (nano-LED). Raman spectrometer (HORIBA LabRAM HR Evolution) was used to analyse the structural defects and purity of the sample in the range 1000-1800 cm^{-1} with a 532 nm laser. Functional groups were determined by infrared (IR) spectra through FT-IR spectroscopy (Shimadzu IRTracer-100).

3.2.4 Methodology of Metal ion Sensing

The stock solution of various metal ions (1 mM) such as Hg^{2+}, Zn^{2+}, Cu^{2+}, Mn^{2+}, Co^{2+}, Cr^{3+}, Fe^{2+}, Pb^{2+}, Ni^{2+}, and Fe^{3+} were prepared in aqueous medium (distilled water) to evaluate the selectivity studies of the prepared RH-CQDs. The measured amount (0.1 mM) of stock solution of respective metal ion solution was added to 100 μL of RH-CQDs in 2 mL distilled water, and the respective fluorescence emission spectra were recorded at the specific excitation wavelength. Furthermore, stock solution of Fe^{3+} (1μM) was prepared to validate the sensitivity studies.

3.2.5 Sensing of Tablet Supplement

To evaluate the sensing efficacy of the as-prepared sensor in tablet dosage, the iron supplement (Abbott, Ferric Saccharate chewable tablets), ofloxacin tablet (Microbid), and ciprofloxacin tablet (Floxip) was purchased form a local market. Three tablets of each of the supplement were weighed separately. They were further homogeneously grounded using mortar and pestle. An accurate weighing of the powder corresponds to 9.0 mg of OFX, 8.3 mg of CPX, and 17. 0 mg of iron supplement which was transferred to volumetric flask of 25 mL to prepare 1mM stock solution. Sonication for 10 mins was performed to completely dissolve the tablets in distilled water. The solution was further diluted to obtain 1μM stock solution of the tablet supplement. To record the photoluminescence (PL) spectra, 100 μL of as prepared stock solution was successively added to the prepared sensing system for further study.

3.3 Results and Discussions

3.3.1 Characterizations

To know the surface chemical compositions of the as-prepared RH-CQDs, XPS analysis was carried out. The survey spectrum shows two peaks at 285 eV and 530 eV corresponds to C 1s and O1s (Figure 3.1(a)). The high-resolution C1s spectra (Figure 3.1b) was deconvoluted into three peaks at 284.96, 287.56, and 289.1 eV conforming to C=C/C-C, C=O, and O=C-O, respectively.[7,15] The O 1s spectra (Figure 3.1c) show peaks at 530.6 and 533.6 eV corresponding to C=O and O=C-O.[7] The spectrum (Figure 3.1d) showed signals at 3260 cm^{-1} of O-H, small band at 2829 cm^{-1} corresponds to C-H, signals at 1723 cm^{-1} (C=O) and 1612 cm^{-1} confirms the presence of C=C. This affirmed the presence of graphitic carbon and hydroxyl group in the synthesized RH-CQDs.[14,29] The absence of any signal at ~400-1100 cm^{-1} confirmed that there is no contamination of silica in the synthesized RH-CQDs.[29]

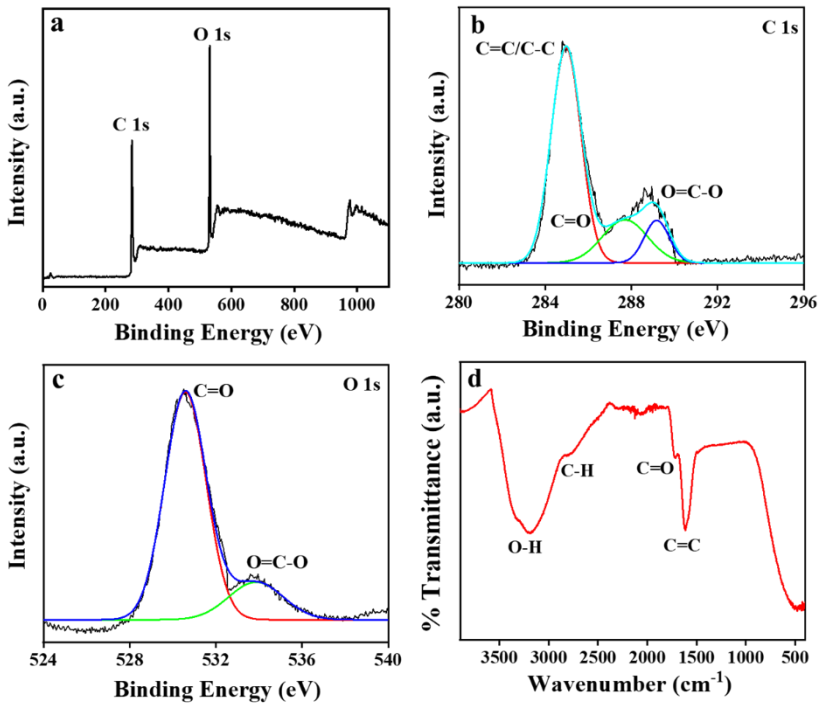

Figure 3.1. (a) XPS survey spectrum of RH-CQDs, (b) High-resolution C 1s spectrum, (c) O1s, and (d) FT-IR spectra of RH-CQDs.

The elemental analysis of the synthesized RH-CQDs shows the weight concentration (%) and atomic concentration (%) of the elements present that is C (28.21%, 34.31%) and O (71.79%, 65.69%). The elemental components of rice husk (RH) and rice husk carbon were also detected using EDX which were shown in Figure 3.2 (a, b). Rice husk contains C (31.66%, 38.90%), O (61.71%, 57.55%), Na (0.16%, 0.10%), Al (0.10%, 0.06%), Si (6.36%, 3.39%),

and P (0.01%, 0.00%) (Figure 3.2(a)), while, rice husk carbon (RHC) contains C (55.83%, 64.11%), O (36.82%, 31.88%), and Na (7.35%, 4.01%) (Figure 3.2(b)).

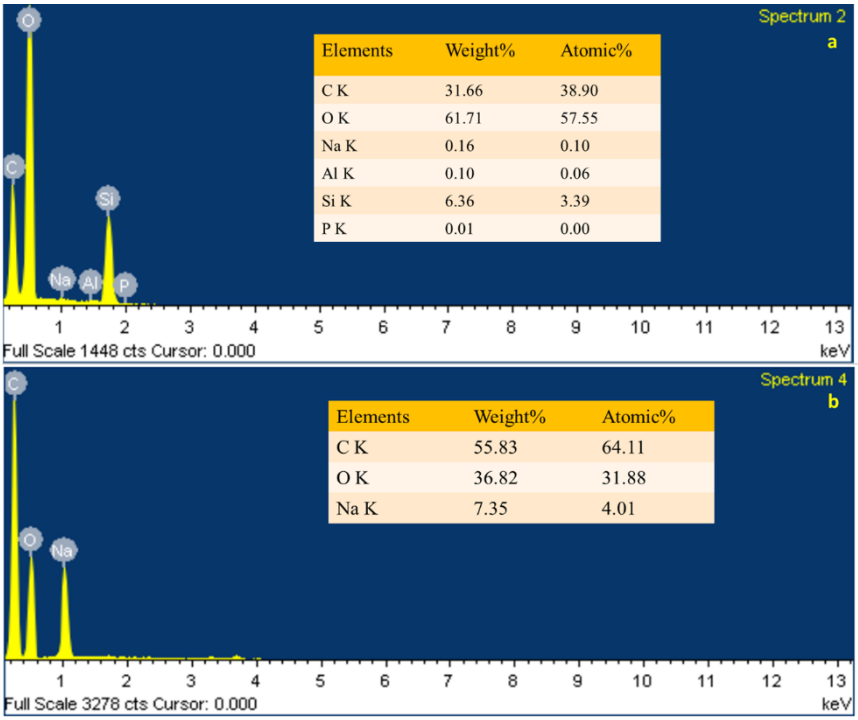

Figure 3.2. EDX Spectra of (a) rice husk (RH), and (b) rice husk carbon (RHC).

The morphology and size of the synthesized RH-CQDs were analysed from TEM. Figure 3.3a shows the spherical quantum dots with inset HR-TEM image showing the lattice spacing (0.24 nm), corresponds to (1120) lattice fringes of graphene.[30] Figure 3.3b and 3.3c shows the agglomerated particles with size distribution range from 4-18 nm having an average particle diameter of 8.3 ± 0.44 nm. The as-prepared carbon quantum dots are present in agglomerated clusters which could be caused by the high surface energy of RH-CQDs leading to significant attraction in-between the nanoparticles.[31]

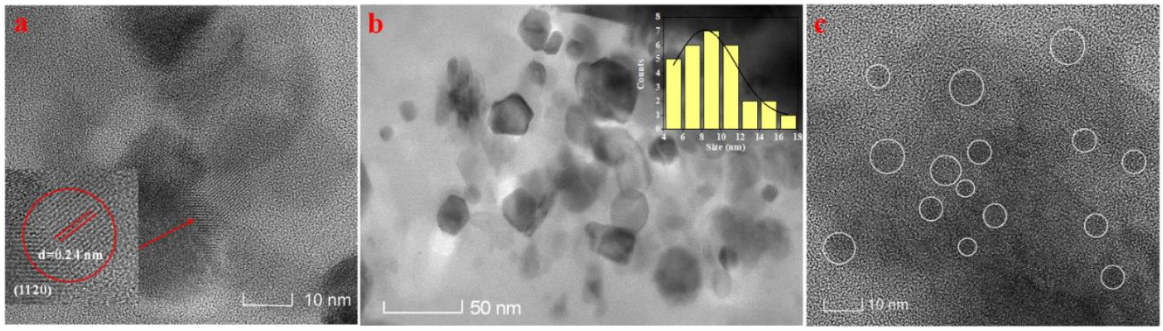

Figure 3.3. (a) HR-TEM image of RH-CQDs with inset showing lattice spacing, (b) TEM image of agglomerated particles with inset size distribution histogram, and (c) lattice fringes in the synthesized RH-CQDs.

Figure 3.4a shows a Raman spectrum exhibiting G band at 1594 cm^{-1} and a broad D band at 1200-1500 cm^{-1} with a peak centred at 1374 cm^{-1} having an intensity ratio of ID/IG of 0.86, confirming the high number of defects. Raman results confirms the occurrence of sp^2 carbon (G band) and sp^3 defects (D band) within the RH-CQDs.[29,32,33]

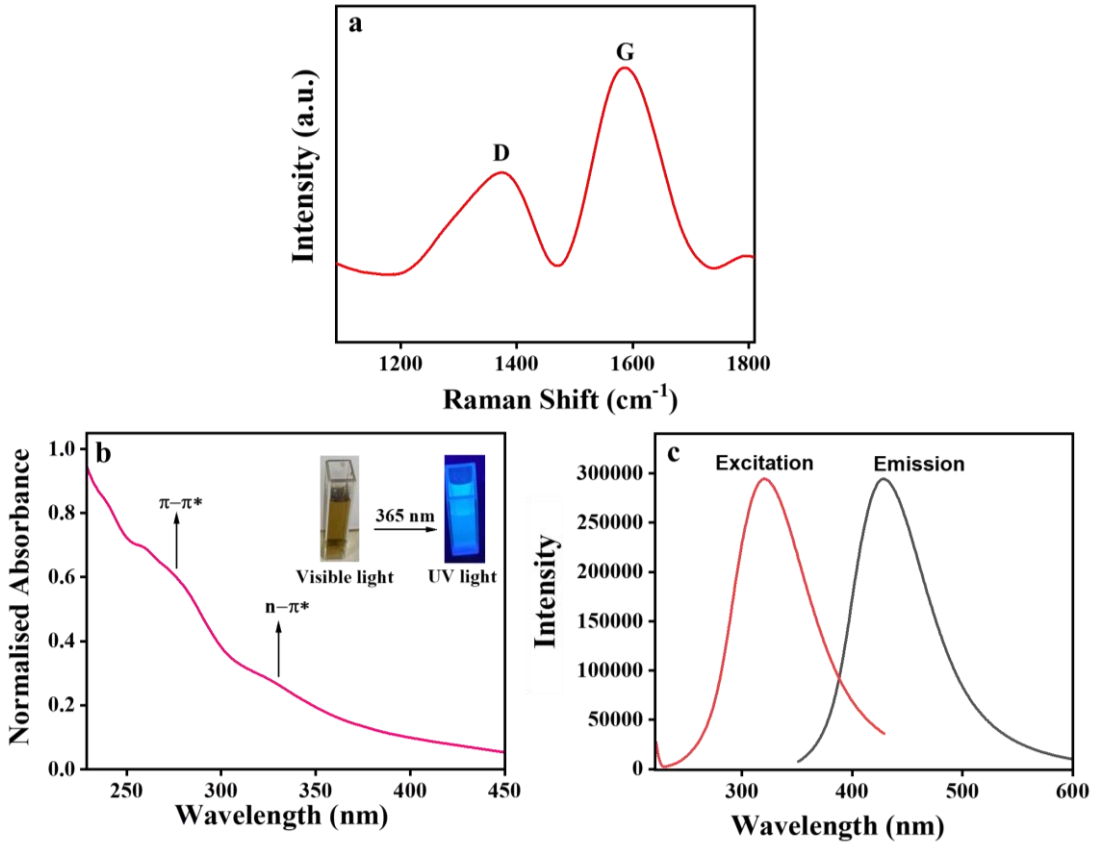

Figure 3.4. (a) Raman spectrum of RH-CQDs exhibiting D and G bands, (b) UV-Visible absorption spectrum of RH-CQDs with inset image showing RH-CQDs under visible and UV light illumination, and (c) PL excitation and emission spectra of RH-CQDs.

3.3.2 Optical properties of RH-CQDs

The optical properties were analysed using UV-Visible absorption spectra and fluorescence spectra of the synthesized RH-CQDs. Figure 3.4b exhibits a small shoulder at 270 nm corresponds to the π–π*transition of the sp^2 domains.[34] A broad band at 280-320 nm was due to n-π*transition of C=O of RH-CQDs.[29] The inset image shows that RH-CQDs in aqueous medium exhibits a brown colour in visible light, and blue emission upon irradiation in UV light of 365 nm. It is possibly due to the radiative recombination between holes and electrons, caused by the photoinduced charge separation and trapping at surface sites, is thought to contribute to the fluorescence emission of the synthesized RH-CQDs.[35–37]

Figure 3.4c shows the PL excitation and emission spectra upon excitation at 320 nm with maximum emission centred at 428 nm. The PL quantum yield of 56.2% w.r.t. quinine sulfate was observed for the synthesized RH-CQDs. Table 3.1 compares the high quantum yield of the RH-CQDs prepared in this study with the previous works reported in the literature.

Table 3.1. Summary of Quantum Yield of Rice husk-derived quantum dots.

S.No.	Precursor	Synthesis Method	Quantum Yield	Ref.
1	Rice husk	Hydrothermal	20.80%	[38]
2	Rice husk Ash	Thermal hydrosilylation	34.6%	[39]
3	Rice husk	Hydrothermal & calcination	3%	[29]
4	Rice husk	One-pot hydrothermal method	8.8%	[15]
5	Rice Straw	Hydrothermal-carbonization	24.03%	[40]
6	Rice husk	Hydrothermal	56.2%	Present work

The fluorescence spectra at distinct excitation wavelengths (280 nm- 410 nm) are exhibited in Figure 3.5 (a). A shift was noticed in the emission wavelengths from 404 nm to 490 nm under the change in λ_{ex}. This confirms that PL emission spectra is related to the PL excitation energy which are reliant on different factors like surface edge defects, quantum confinement effect, aromatic sp^2 bonds, size variation, and zigzag edge effects.[41]

3.3.3 Stability Studies of RH-CQDs

The effect of pH, irradiation time on the fluorescence intensity of the synthesized RH-CQDs was evaluated. The increase in PL intensity was observed as pH changes from 1 to 7 (Figure 3.5 (b)). The maximum intensity was observed at pH 7, then the slight decrease in PL intensity was observed with the change in pH (7 to 13). This is attributed to protonation and deprotonation of the emissive sites in the RH-CQDs, consequently leading to change in PL intensity.[14] It was seen that there is no significant change in PL intensity of RH-CQDs with the irradiation time up to 60 mins (Figure 3.5 (c)). Also, the prepared RH-CQDs were incubated for 30 days and PL spectra was noted at regular interval showing no notable change in fluorescence intensity with incubation period (Figure 3.5(d)). This confirms that the synthesized RH-CQDs have high stability and are suitable for various analytical applications.

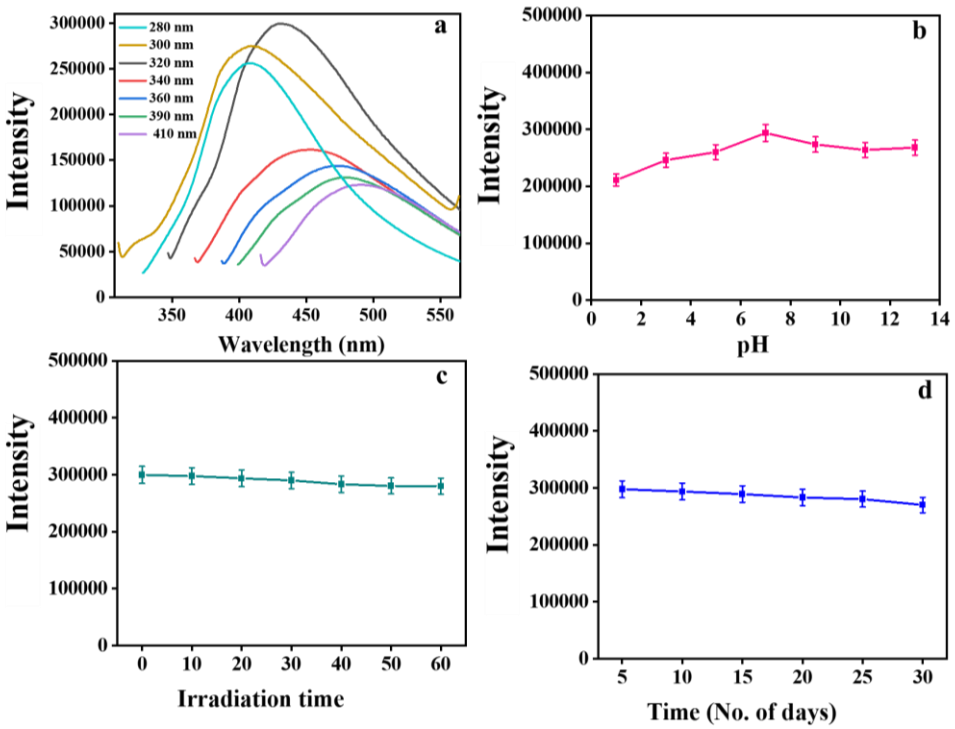

Figure 3.5. (a) PL emission spectra of RH-CQDs at different excitation wavelengths (280-410 nm), (b) effect of pH (1-13) on PL intensity, (c) effect of irradiation time (mins), and (d) impact of storage time (days) on the fluorescence stability of RH-CQDs.

3.3.4 Method Validation

The developed method was validated according to ICHQ2(R1) guidelines.[42]

3.3.4.1 Linearity and Range

To evaluate the sensitivity of the developed sensor, the impact of fluorescence intensity of different concentrations of Fe^{3+}(nM) with RH-CQDs was studied. The fluorescence intensity of RH-CQDs was quenched gradually with various concentrations of Fe^{3+} as shown in Figure 3.6 (a).

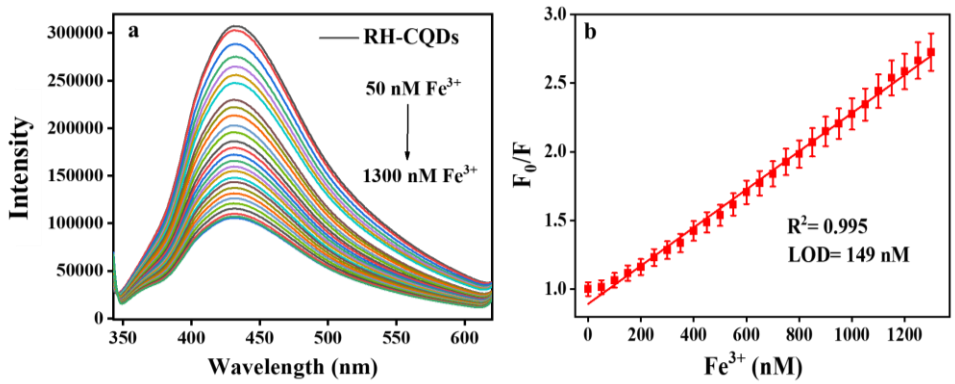

Figure 3.6. (a) PL quenching spectrum of RH-CQDs with different concentration of Fe^{3+}, and (b) linear plot of F_0/F with Fe^{3+} ions (0-1300 nM).

To comprehend the quenching efficiency, the graph between F_0/F vs. the quencher [Q] concentration was plotted according to the Stern-Volmer equation 1.7. Figure 3.6 b depicts a linear relation between F_0/F and concentrations of Fe^{3+} (0-1300 nM) with a linear regression equation shown as:

$$F_0/F = 0.00139\ [Fe^{3+}] + 0.89291\ (R^2 = 0.995) \quad (3.1)$$

Values of correlation coefficient (R^2) reaching approximate unity indicates the acceptable linearity of the proposed system (Table 3.2).

Table 3.2. Analytical performance for Fe^{3+} by the developed sensor.

Parameters	**Fe^{3+}**
Linearity range (nM)	0-1300
Limit of Detection (LOD)[a] (nM)	149
Limit of Quantification (LOQ) [b] (nM)	497
Regression equation	$F_0/F = 0.00139\ [Fe^{3+}] + 0.89291$
Correlation coefficient	0.995
Binding Efficacy (nM^{-1})	95

[a]LOD =3σ/K, [b]LOQ =10σ/K, σ is standard deviation of intercept and K is the slope.

3.3.4.2 Limit of Detection and Limit of Quantification

The LOD and LOQ values were calculated using 3σ/K and 10σ/K (Table 3.2), respectively where σ is standard deviation of intercept and K corresponds to the slope of linear line. The LOD values calculated from Figure 3.6b is 149 nM (Table 3.2). Table 3.3 shows the prepared sensor exhibits the high sensitivity towards Fe^{3+} and a low detection limit in comparison to other sensor systems reported in the literature.

Table 3.3. Various sensing systems based on quantum dots for Fe^{3+} detection.

Sr. No.	**Sensor's system**	**Linear range**	**LOD**	**Ref.**
1	P-CQDs	0-2000 μM	355.4 nM	[25]
2	CQDs	0-300 μM	19 μM	[43]
3	S-CDs	0-500 μM	0.1 μM	[44]
4	N-CQDs	50-300 μM	10.8 μM	[45]
5	GQDs	0.004-1.8 mM	1.2 μM	[46]
6	Carbon dots	30-600 μM	9.55 μM	[47]

7	NA-GQDs	0.5 µM-0.5 mM	0.1 µM	[48]
8	Carbon dots	0-50 µM	0.8 µM	[49]
9	RH-CQDs	0-1300 nM	149 nM	Present work

3.3.4.3 Binding Efficacy

The value of excited state binding constant has been evaluated using 1:1 linear Benesi-Hildebrand (B-H) equation 1.8[50] to better understand the stoichiometry and binding interaction between the RH-CQDs and Fe^{3+}. The graph between ($1/F_0$-F) versus 1/[Q] shows a linear plot with binding constant value K = 95 nM^{-1} and R^2 = 0.992 (Figure 3.7a, Table 3.2).

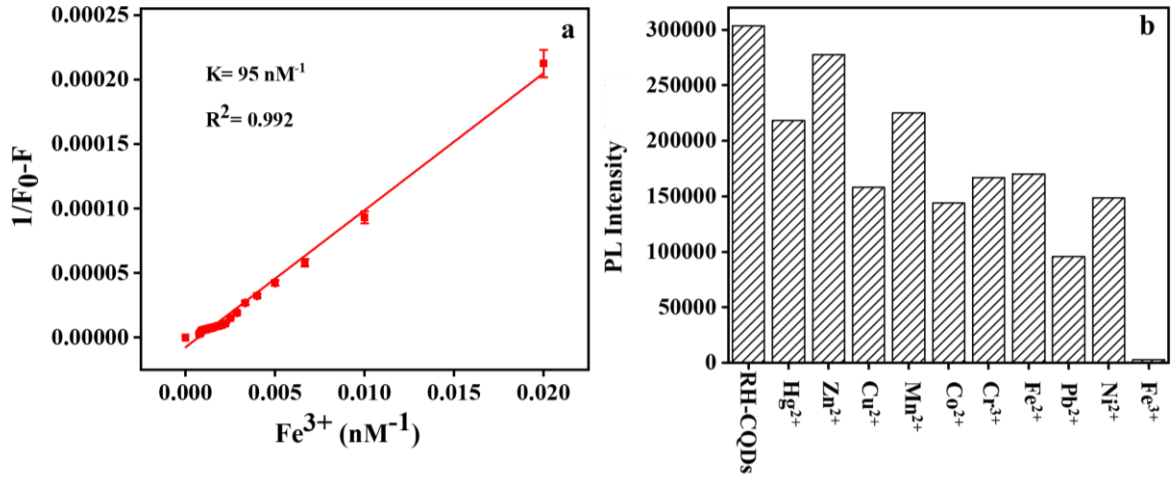

Figure 3.7. (a) B-H binding plot of RH-CQDs with quencher (Fe^{3+}), and (b) selectivity study of RH-CQDs on addition of different metal ions.

3.3.4.4 Precision and Accuracy

This was carried out to assess the intra-day and inter-day precisions. This was carried out using three different concentrations and the three replicates of every concentration. Acceptable %RSD value was displayed which is less than 2% which signifies an acceptable precision of the developed method (Table 3.4).

3.3.4.5 Robustness

It is an important validation parameter. This signifies the influence of minute changes in factors affecting the fluorescence sensing. The effect of volume added of RH-CQDs (100.0 µL±1) and pH (7±0.1) was studied showing no noticeable effect on recovery percentage and %RSD values as shown in Table 3.5.

Table 3.4. Intraday and Inter day precision data for the estimation of Fe^{3+} by the developed nanosensor.

Analyte	Conc. taken (nM)	Intra Day[a]			Inter Day[b]		
		Conc. found ± S.D. (nM)	%RSD	%Error[c]	Conc. found ± S.D. (nM)	%RSD	%Error[c]
Fe^{3+}	200	199.3±0.95	0.95	0.55	199.0±1.15	1.15	0.66
	600	604.2±0.91	0.30	0.17	598.8±1.60	0.55	0.31
	1000	1000.3±1.37	0.27	0.15	1002.4±1.75	0.35	0.20

Each result is the average of three separate determinations

[a]Within a day [b]Three consecutive days [c]%Error=%RSD/√n

Table 3.5. Robustness evaluation of the developed sensor.

Variation			
Volume (100.0 µL±1)	**Recovery error (%)**	**Recovery rate (%)**	**RSD (%)**
99.0 µL	1.05	101.07	1.39
100.0 µL	1.96	98.07	1.43
101.0 µL	0.22	100.77	1.53
pH (7±0.1)			
6.9	1.00	101.01	1.61
7	0.14	99.85	1.50
7.1	0.42	100.42	1.70

3.3.5 Selectivity Studies for Detection of Fe^{3+} Ions

Selectivity is a critical component to investigate while developing an effective sensor. For this study, the change in PL intensity of RH-CQDs by the addition of different metal ions was studied. The stock solution of 1mM of Hg^{2+}, Zn^{2+}, Cu^{2+}, Mn^{2+}, Co^{2+}, Cr^{3+}, Fe^{2+}, Pb^{2+}, Ni^{2+}, and Fe^{3+} ions were prepared. The measured amount of respective metal ion solution was added to 100 µL of RH-CQDs in 2 mL distilled water. Among all the metal ions, Fe^{3+} ions showed a high selectivity and quenching effect with RH-CQDs as shown in Figure 3.7b. The further sensitivity studies were performed using 1 µM stock solution of Fe^{3+} ions. The

fluorescence quenching of RH-CQDs by the Fe^{3+} ions addition is due to the coordination between the phenolic hydroxyl groups and Fe^{3+} ions which facilitated charge transfer. This results into the restraining of exciton recombination and the fluorescence quenching take place.[51]

3.3.6 Plausible Reason of High Selectivity of RH-CQDs with Fe^{3+} Ions

The plausible mechanism for PL quenching by the addition of Fe^{3+} is because of the functional groups (-OH, -COOH) present on the surface of RH-CQDs. These surface functional groups exhibits significant interaction with metal ions towards coordination complex formation.[52] Fe^{3+} binds with -OH group of RH-CQDs resulting into formation of Fe(III) chelate complex. Electrons get transferred from the excited state of RH-CQDs to half-filled 3d orbitals of Fe (III) leading to non-radiative e^--h^+ recombination ultimately resulting in PL quenching as shown in equation 3.2.[53]

$$6\ \text{CQDs-OH} + Fe^{3+} \rightarrow [Fe(OCQDs)_6]^{3+} + 6H^+ \qquad (3.2)$$

Also, Fe(III) displayed fast chelating speed for the formation of coordination or chelation complexes in comparison to other metal ions because of high thermodynamic affinity.[54]

3.3.7 Sensitivity Studies for Detection of Fe^{3+} Ions

To understand the quenching mechanism i.e., static or dynamic between the RH-CQDs and Fe^{3+}, time resolved emission measurements were executed Figure 3.8. The lifetime components along with their relative populations are tabulated in Table 3.6. The average lifetime value of RH-CQDs was observed to be τ_{av} = 5.00 ns and upon addition of Fe^{3+} it was decreased to τ_{av} = 0.63 ns (Table 3.6) which shows that fluorescence quenching is based on transfer of electrons from RH-CQDs to Fe^{3+}. Due to non-radiative electron-hole recombination, electrons from excited state are transferred from RH-CQDs to the half-filled 3d orbitals of Fe^{3+}.[55] As a result of these findings, dynamic quenching occurred in between the surface functional groups of both the donor (RH-CQDs) and the acceptor (Fe^{3+}). Additionally, to comprehend the quenching mechanism in detail, we have calculated the radiative (K_r) and non-radiative (K_{nr}) rate constants with average lifetime (τ^*) and quantum yield (ϕ) using the equations 1.4, 1.5.[56]

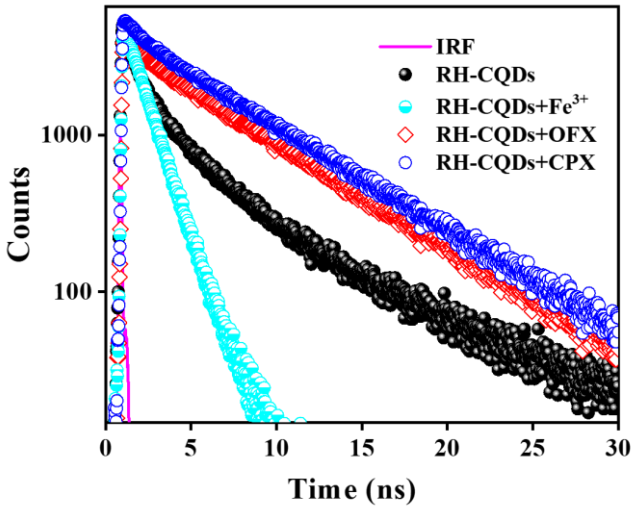

Figure 3.8. Time-resolved fluorescence emission decays of RH-CQDs in presence of Fe^{3+}, OFX, CPX.

Table 3.6. Fluorescence lifetime parameters of RH-CQDs in absence and presence of Fe^{3+}.

System	**τ_1 (ns)**	**a_1**	**τ_2 (ns)**	**a_2**	**#<τ_{av}>(ns)**	**χ^2**
RH-CQDs	2.44	0.60	8.84	0.40	5.00	1.16
RH-CQDs + Fe^{3+}	0.25	0.90	4.12	0.10	0.63	1.07

Table 3.7 exhibits the k_r and k_{nr} values. The value of k_r reduced, whereas k_{nr} value get increased in presence of Fe^{3+} in RH-CQDs. This shows that fluorescence quenching mechanism relies on the excited state electron transfer.[14] The electron transfer rate (k_{ET}) was calculated to know the excited state dynamics of RH-CQDs with Fe^{3+} ions using the equation 1.9.

The efficiency of electron transfer (ϕ_{EET}) is evaluated using equation 1.10. The values of k_{ET} and ϕ_{EET} augments the transfer of electrons in excited state, which conform to the dynamic quenching (Table 3.7).

Table 3.7. Different photophysical parameters for RH-CQDs in presence and absence of Fe^{3+}.

Systems	ϕ	**τ_{av} (ns)**	**k_r ($\times 10^9$ s^{-1})**	**k_{nr} ($\times 10^9$ s^{-1})**	**k_{ET} ($\times 10^9$ s^{-1})**	$\phi_{EET}(\tau_D)$	$\phi_{EET}(\phi_D)$	**PL quenching (%)**
RH-CQDs	0.562	5.00	0.112	0.088	-	-	-	-
RH-CQDs + Fe^{3+}	0.050	0.63	0.079	1.501	1.387	0.874	0.911	66.40

3.3.8 Fluorescence Quenching Mechanism

With the addition of inhibitory molecules, the fluorescence quenching mechanism of a fluorescent moiety is largely dynamic or static quenching.[57] The PL intensity of RH-CQDs was steadily decreased in presence of Fe^{3+} (quencher). Dynamic quenching is due to the collision between fluorescent probe in excited state and the quencher, which is then reverted to ground state due to charge transfer. The Stern-Volmer quenching constant (K_{SV}) along with binding constant (K) values were calculated using equation 1.7 and equation 1.8, respectively. Moreover, the decrease in average lifetime values of RH-CQDs upon addition of Fe^{3+} ions using time-resolved lifetime measurements (Figure 3.8) confirmed the dynamic quenching mechanism. The plausible reason for dynamic quenching is due to excited state charge transfer from surface of RH-CQDs to half-filled (3d) orbital of Fe^{3+} (Scheme 3.2). This results into conversion of fluorescent RH-CQDs to non-fluorescent complex in presence of quencher (Fe^{3+}) in excited state collision path and then return to ground state. Also, we have calculated the electron transfer rate (K_{ET}) and electron transfer efficiency (ϕ_{EET}) to validate that the dynamic fluorescence quenching mechanism take place between the RH-CQDs and Fe^{3+} ions.

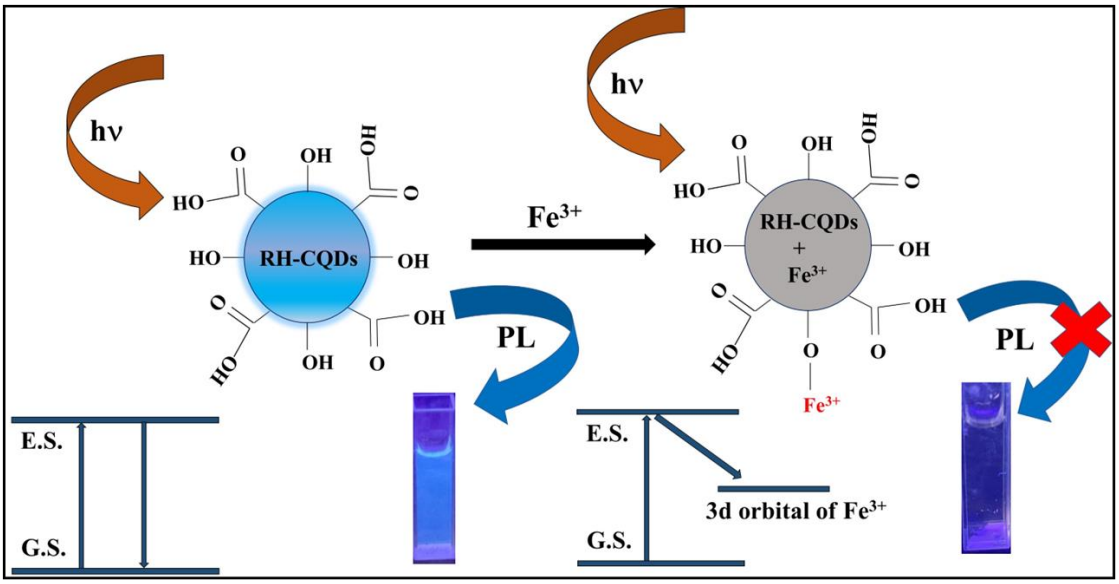

Scheme 3.2. Mechanism showing Fluorescence quenching of RH-CQDs on addition of Fe^{3+} ions.

3.3.9 Detection of Fe^{3+} in Tablet Supplement

The as-prepared RH-CQDs were used as a fluorescent probe for the detection of Fe^{3+} in tablet dosage. The fluorescence intensity of the RH-CQDs upon addition of different concentrations of Fe^{3+} in sample was shown in Figure 3.9a. The plot clearly shows that the PL intensity gradually decreases as the concentration of Fe^{3+} increases. The standard curve for Fe^{3+}

detection in the sample was displayed in Figure 3.9b. A linear plot was noticed among F_0/F and various concentrations of Fe^{3+} in tablet supplement (50-1300 nM) with R^2= 0.992 (Figure 3.9(b)). The values of recovery rate (%), recovery error (%), relative standard deviation (RSD) (%) are summarized in Table 3.8 and the results confirmed that the RH-CQDs can be utilized as a sensing probe in the tablet supplements.

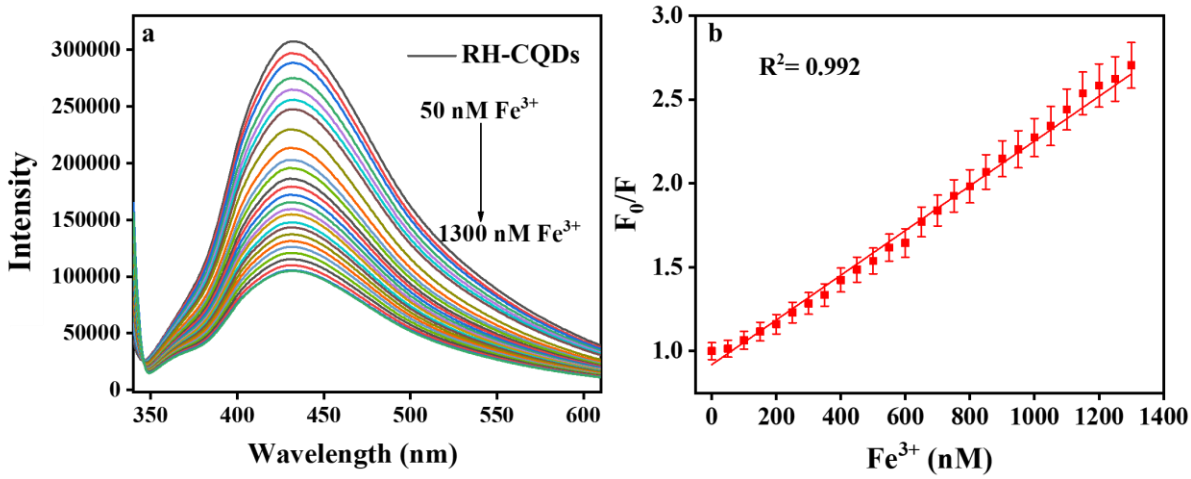

Figure 3.9. (a) Fluorescence quenching spectra with distinct concentrations of Fe^{3+}, and (b) linear plot of F_0/F and Fe^{3+}concentrations in tablet supplement.

Table 3.8. Application of the developed sensor for the detection of Fe^{3+} in tablet dosage.

Sample	**Amount added to our system (nM)**	**Amount detected by our system (nM)**	**Recovery error (%)**	**Recovery rate (%)**	**RSD (%)**
Iron supplement	100	101.6	1.57	101.6	1.03
	200	202.5	1.23	101.25	1.58
	400	396.6	0.85	99.15	0.77

3.3.10 Detection of Fluoroquinolone with Fluorescence Enhancement Technique

The fluorescence intensity of the as-prepared RH-CQDs was eventually enhanced by adding different concentrations of OFX and CPX (Figure 3.10a, 3.10b). This enhancement in PL intensity is mainly credited to the hydrogen bond formation between the carboxyl of RH-CQDs and amine of the piperazine ring.[58] Linearity range, detection limit (LOD), limit of quantification (LOQ), regression equation, and other analytical performance parameters for the detection of OFX and CPX were given in Table 3.9. The LOD values calculated for OFX and

CPX from Figure 3.10c, 3.10d are 150 nM (R^2= 0.994) and 127 nM (R^2= 0.996), respectively. B-H values for OFX and CPX in presence of RH-CQDs are 191 nM^{-1} (Figure 3.11a) and 694 nM^{-1} (Figure 3.11b), respectively. The high binding constant values verified the strong interaction between RH-CQDs and OFX and CPX.

Table 3.9. Analytical performance data for OFX and CPX by the developed sensor.

Parameters	**OFX**	**CPX**
Linearity range (nM)	50-1150	50-1150
Limit of Detection (LOD)[a] (nM)	150	127
Limit of Quantification (LOQ) [b] (nM)	497	424
Regression equation	$F_0/F = 9.054\times10^{-4}$ [OFX] + 0.0026	$F_0/F = 9.123\times10^{-4}$ [CPX] + 0.1033
Correlation coefficient	0.994	0.996
Binding Efficacy (nM^{-1})	191	694

[a]LOD =3σ/K, [b]LOQ =10σ/K, σ is standard deviation of intercept and K is the slope.

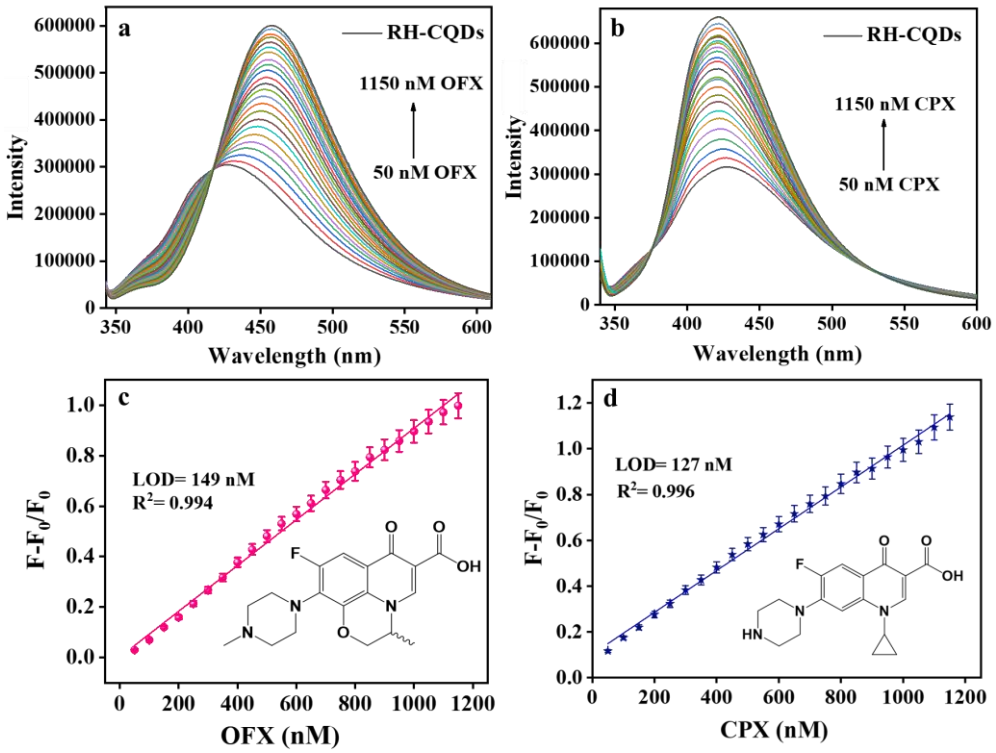

Figure 3.10. Fluorescence enhancement spectra of RH-CQDs in presence of (a) OFX, (b) CPX, (c) linear plot of F_0-F/F_0 with OFX (0-1150 nM), and (d) linear relationship of F_0-F/F_0 with different concentrations of CPX.

Precision calculations were performed with three different concentrations and replicates of each concentration of both OFX and CPX to test intra and inter day precision as given in Table 3.10.

Table 3.10. Intraday and Inter day precision data for the estimation of OFX and CPX by the developed nanosensor.

Analytes	**Conc. taken (nM)**	**Intra Day[a]**			**Inter Day[b]**		
		Conc. found ± S.D. (nM)	**%RSD**	**%Error[c]**	**Conc. found ± S.D. (nM)**	**%RSD**	**%Error[c]**
OFX	200	198.69±0.65	0.65	0.37	199.4±1.51	1.52	0.87
	600	602.2±1.55	0.51	0.29	600.03±1.43	0.47	0.27
	1000	1003.1±1.32	0.26	0.15	996.40±1.66	0.33	0.19
CPX	200	196.19±0.63	0.64	0.37	199.06±1.40	1.41	0.81
	600	600.6±1.01	0.33	0.19	594.03±1.95	0.66	0.38
	1000	1004±1.51	0.30	0.17	997.73±1.05	0.21	0.12

Each result is the average of three separate determinations.

[a]Within a day [b]Three consecutive days [c]%Error=%RSD/√n

Also, time-resolved measurements were performed. The average lifetime of RH-CQDs is 5.00 ns and after the addition of OFX and CPX, the τ_{av} was 6.07 ns and 6.40 ns, respectively (Table 3.11, Figure 3.8).

Table 3.11. Fluorescence lifetime parameters of RH-CQDs, RH-CQDs + OFX, and RH-CQDs + CPX.

Systems	**τ_1 (ns)**	**a_1**	**τ_2 (ns)**	**a_2**	**#<τ_{av}>(ns)**	**χ^2**
RH-CQDs	2.44	0.60	8.84	0.40	5.00	1.16
RH-CQDs + OFX	0.66	0.04	6.30	0.96	6.07	1.11
RH-CQDs + CPX	1.21	0.03	6.57	0.97	6.40	1.12

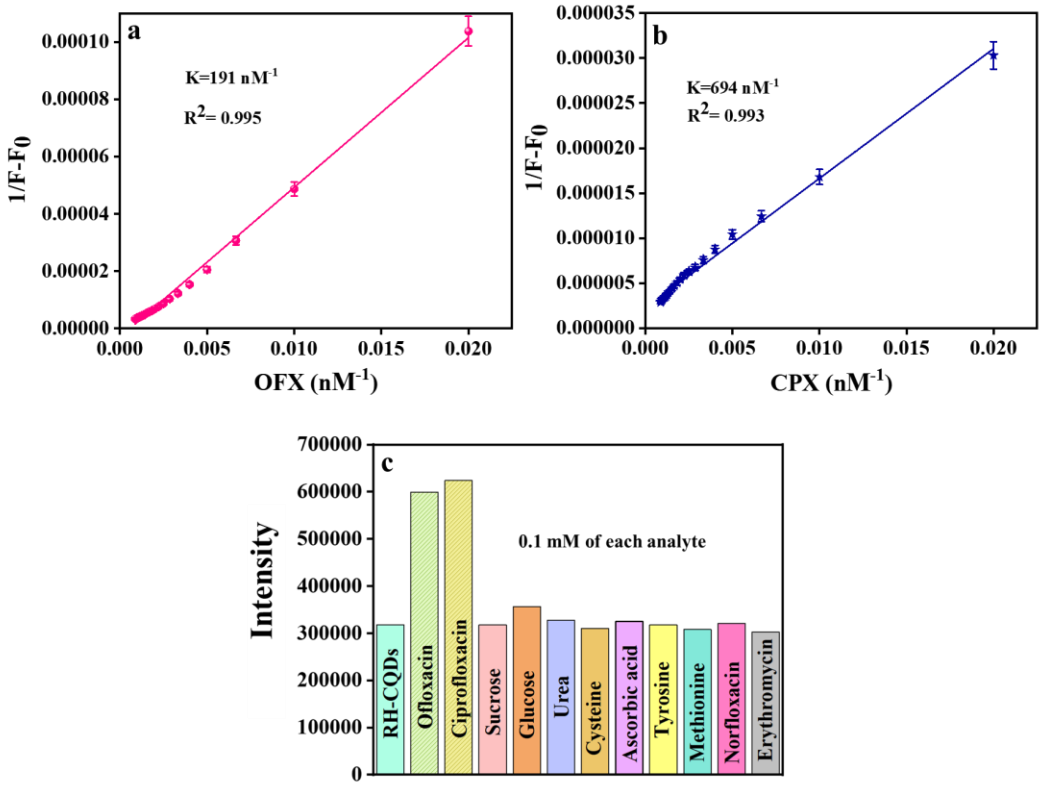

Figure 3.11. B-H binding plot of RH-CQDs with (a) OFX, (b) CPX, and (c) selectivity studies of RH-CQDs with different analytes.

The analytical performance parameters (recovery rate (%), recovery error (%), relative standard deviation (RSD) (%)) evidenced that the developed method is used for detecting OFX and CPX at trace levels as summarized in Table 3.12.

Table 3.12. Application of the developed sensor for the detection of OFX and CPX in tablet dosage.

Samples	Amount added to our system (nM)	Amount detected by our system (nM)	Recovery error (%)	Recovery rate (%)	RSD (%)
OFX	150	151.5	0.99	101	1.18
	300	295.7	1.45	98.56	1.48
	450	445.7	0.96	99.0	1.10
CPX	150	147.8	1.48	98.53	1.52
	300	302.8	0.92	100.93	0.84
	150	445.2	1.07	98.93	1.07

3.3.11 Selectivity Measurements

To examine the selectivity of the proposed sensor, PL studies were done with various analytes. A specific concentration of ofloxacin (OFX), ciprofloxacin (CPX), sucrose, glucose, urea, cysteine (Cys), ascorbic acid (AA), tyrosine (Tyr), norfloxacin (NFX), erythromycin (ERM), and methionine (Met) were mixed with RH-CQDs. OFX and CPX exhibited high selectivity in comparison to others (Figure 3.11(c)). The plausible reason of high selectivity is attributed to unique structure of fluoroquinolones.[21] These are fluorinated 4-quinolone rings with carboxylic acid, fluorine, and a piperazine ring substitution on position 3,7,8. The carboxyl of RH-CQDs preferentially forms a strong hydrogen bond with amine of the piperazine ring.[58] Furthermore, this hydrogen bond is crucial for all H-bond bridges. Also, the quinolone ring is an important conjugation system for fluoroquinolone, with charge transfer occurring between the quinolone ring and RH-CQDs.

3.3.12 Plausible Mechanism for Fluorescence Restoration

The enhancement in fluorescence may assigned to the important phenomenon of hydrogen bonding and charge transfer complex between RH-CQDs and OFX/CPX. The existence of numerous hydroxyl and carboxyl moieties offers strong hydrogen bonds formation between the carboxyl/hydroxyl groups of RH-CQDs and fluorine/nitrogen of OFX/CPX (Scheme 3.3).[21] Strong intermolecular hydrogen bonding creates centre that connects two adjacent molecules. The delocalization of π-electrons within intermolecular hydrogen-bonded systems has an impact on the ring stabilisation parameters, hence these bonds were credited as resonance assisted systems.[59]

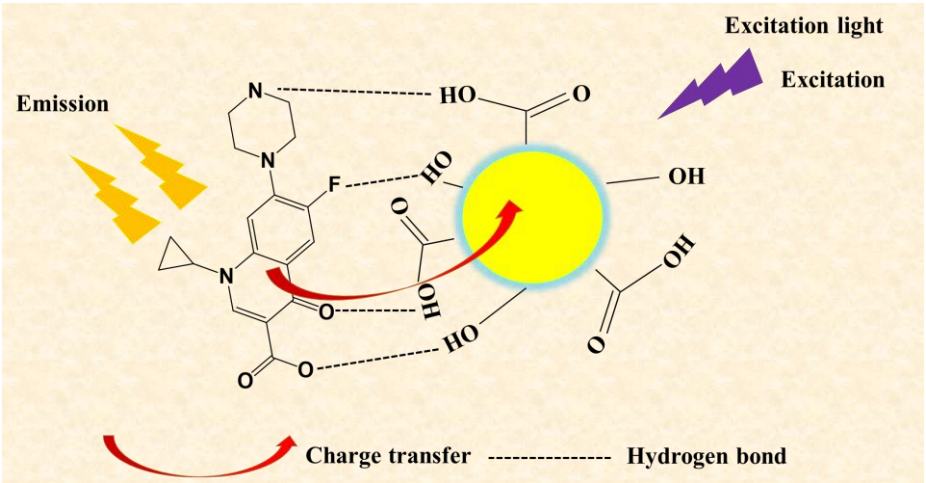

Scheme 3.3. Plausible mechanism between RH-CQDs and CPX.

Ar-H-O hydrogen bonds can be generated because the carbon on the aromatic ring has a comparatively strong electron withdrawing capacity. Also, the amount of resonance and the

strength of hydrogen bond in the H-bonded systems is associated with the molecular symmetry and the interaction type (O-H.N/O-H.F).[60] Also, the property of electron donation of OFX/CPX contribute in donor-π-acceptor system via charge transfer may foster the C=C bonds conjugation. The addition of OFX/CPX noticeably enhance the PL intensity of RH-CQDs as shown in Figure 3.10a and 3.10b. The average lifetime of values of RH-CQDs significantly increases in presence of OFX and CPX (Figure 3.8). From the lifetime studies, it was clearly evident that radiative decay rate enhanced and non-radiative decay rate declined in the presence of OFX and CPX. This result also confirms the enhancement of fluorescence emission of RH-CQDs. The collaborative effect of hydrogen bonding and charge transfer promotes the fluorescence restoration mechanism.

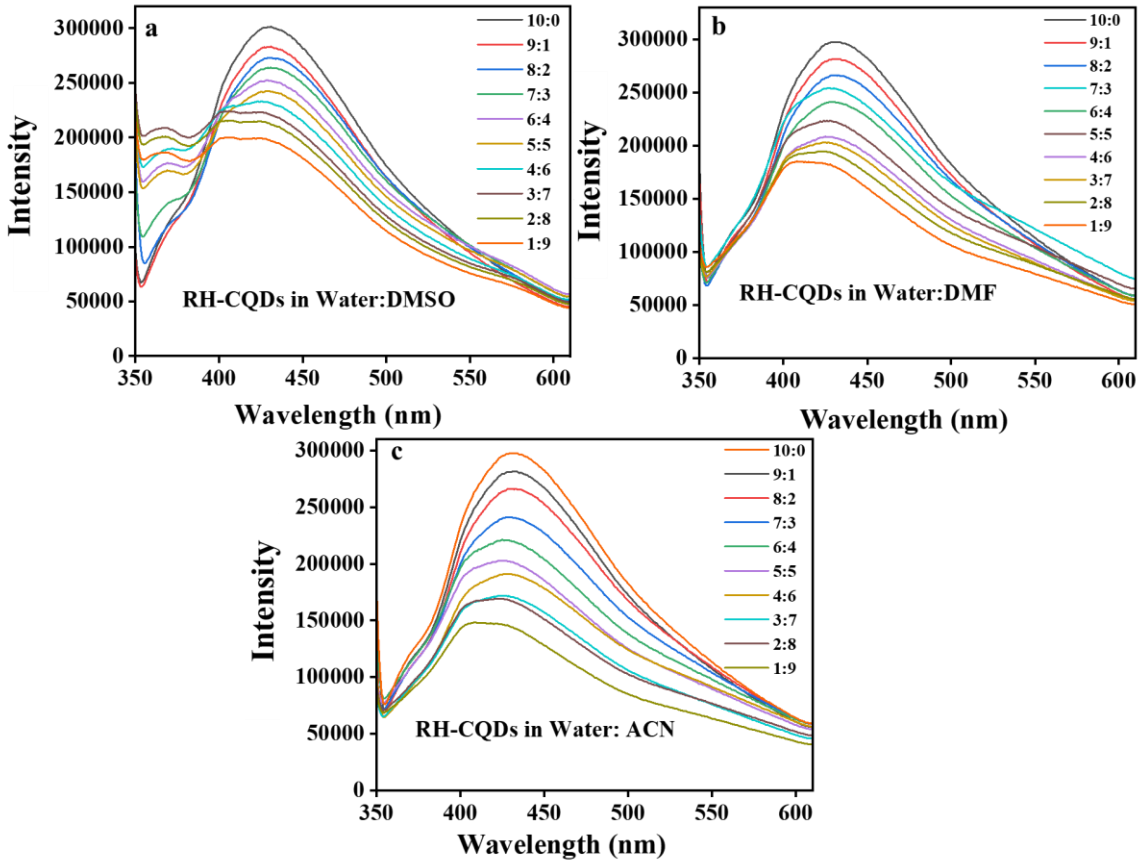

Figure 3.12. Interaction of test system with increasing the proportion of aprotic solvent (a) DMF, (b) DMSO, (c) ACN.

To prove the fluorescence enhancement due hydrogen bonding phenomenon, the experiment was performed. The effect of increasing the proportion of aprotic solvents i.e., DMF, DMSO, and Acetonitrile in test systems on the fluorescence was studied (Figure 3.12(a-c)). As the proportion of polar aprotic solvent increased hydrogen bonding tendency with RH-

CQDs gradually decreased and ultimately the fluorescence decreased. As the concentration of these solvents increased, RH-CQDs exhibits a bathochromic shift in emission spectra as compared to water as shown in Figure 3.12(a-c). The hypsochromic shift in water (less conc. of aprotic solvent) was due to solvent induced change of electronic ground state from less dipolar to more dipolar chromophore.[61] Also in water, extensive hydrogen bonding, dipole-dipole and solute-solvent interactions are present. But, in aprotic solvents these are less prominent and ultimately reduced fluorescence is observed. Therefore, it can be concluded that hydrogen bonding plays an important role for the interaction between OFX/CPX and RH-CQDs.

Conclusions

Highly water soluble, strong fluorescent (56.2%), and stable RH-CQDs with an average size of 8.3 nm were prepared through hydrothermal treatment of rice-husk (biowaste). This approach is non-toxic, economical, and eco-friendly that can be used for macroscale production. The synthesized RH-CQDs exhibited excitation dependence within range of 280 nm-410 nm and are blue fluorescent. RH-CQDs act as nanosensor for highly sensitive and selective detection of Fe^{3+} with 66.4% quenching and detection limit of 149 nM. High chelating speed of Fe^{3+} for the formation of coordination complexes results in fluorescence quenching. The lifetime values confirmed the occurrence of charge transfer from RH-CQDs to Fe^{3+} in excited state, confirming dynamic quenching. Also, RH-CQDs were used for the detection of OFX and CPX by fluorescence enhancement technique. The reason for high selectivity and sensitivity among various analytes towards fluoroquinolones is because of hydrogen bond formation between the carboxyl of RH-CQDs and amine of piperazine ring. The interference free detection is because of hydrogen bonding and charge transfer between RH-CQDs and OFX/CPX. The detection limit calculated was 150 nM and 127 nM for OFX and CPX, respectively. Full validation of the developed method was carried out in accordance with ICH recommendations. This environment-friendly approach comes out to be efficacious technique for the synthesis of biocompatible RH-CQDs for sensing of Fe^{3+} and OFX/CPX leading to substantial economic and environmental benefits. Here, integration of two different mechanisms (fluorescence quenching and fluorescence enhancement) was followed to construct a single sensing platform for accurate quantification of dual-mode nanosensors.

References

(1) Kundu, A.; Sharma, S.; Basu, S. Modulated BiOCl Nanoplates with Porous g-C_3N_4 Nanosheets for Photocatalytic Degradation of Color/Colorless Pollutants in Natural Sunlight.

J. Phys. Chem. Solids **2021**, *154*, 110064. https://doi.org/10.1016/j.jpcs.2021.110064.

(2) Kundu, A.; Shetti, N. P.; Basu, S.; Reddy, K. R.; Nadagouda, M. N.; Aminabhavi, T. M. Identification and Removal of Micro-and Nano-Plastics: Efficient and Cost-Effective Methods. *Chem. Eng. J.* **2021**, *421*, 129816. https://doi.org/10.1016/j.cej.2021.129816.

(3) Sharma, S.; Kundu, A.; Basu, S.; Shetti, N. P.; Aminabhavi, T. M. Sustainable Environmental Management and Related Biofuel Technologies. *J. Environ. Manage.* **2020**, *273*, 111096. https://doi.org/10.1016/j.jenvman.2020.111096.

(4) Hu, B.; Wang, K.; Wu, L.; Yu, S.; Antonietti, M.; Titirici, M. Engineering Carbon Materials from the Hydrothermal Carbonization Process of Biomass. *Adv. Mater.* **2010**, *22*, 813–828. https://doi.org/10.1002/adma.200902812.

(5) Son, B. T.; Long, N. V.; Hang, N. T. N. The Development of Biomass-Derived Carbon-Based Photocatalysts for the Visible-Light-Driven Photodegradation of Pollutants: A Comprehensive Review. *RSC Adv.* **2021**, *11*, 30574–30596. https://doi.org/10.1039/D1RA05079F.

(6) Ray, D. K.; Ramankutty, N.; Mueller, N. D.; West, P. C.; Foley, J. A. Recent Patterns of Crop Yield Growth and Stagnation. *Nat. Commun.* **2012**, *3*, 1–7. https://doi.org/10.1038/ncomms2296.

(7) Hui, K. C.; Ang, W. L.; Sambudi, N. S. Nitrogen and Bismuth-Doped Rice Husk-Derived Carbon Quantum Dots for Dye Degradation and Heavy Metal Removal. *J. Photochem. Photobiol. A Chem.* **2021**, *418*, 113411. https://doi.org/10.1016/j.jphotochem.2021.113411.

(8) Chen, H.; Wang, W.; Martin, J. C.; Oliphant, A. J.; Doerr, P. A.; Xu, J. F.; DeBorn, K. M.; Chen, C.; Sun, L. Extraction of Lignocellulose and Synthesis of Porous Silica Nanoparticles from Rice Husks: A Comprehensive Utilization of Rice Husk Biomass. *ACS Sustain. Chem. Eng.* **2013**, *1*, 254–259. https://doi.org/10.1021/sc300115r.

(9) Pandey, S.; Mewada, A.; Thakur, M.; Pillai, S.; Dharmatti, R.; Phadke, C.; Sharon, M. Synthesis of Mesoporous Silica Oxide/C-Dot Complex (Meso-SiO_2/C-Dots) Using Pyrolysed Rice Husk and Its Application in Bioimaging. *RSC Adv.* **2014**, *4*, 1174–1179. https://doi.org/10.1039/C3RA45227A.

(10) Ngu, P. Z. Z.; Chia, S. P. P.; Fong, J. F. Y.; Ng, S. M. Synthesis of Carbon Nanoparticles from Waste Rice Husk Used for the Optical Sensing of Metal Ions. *New Carbon Mater.* **2016**, *31*, 135–143. https://doi.org/10.1016/S1872-5805(16)60008-2.

(11) Wang, Z.; Liu, J.; Wang, W.; Wei, Z.; Wang, F.; Gong, P.; Wang, J.; Li, N.; Liu, B.; Zhang, Z. Photoluminescent Carbon Quantum Dot Grafted Silica Nanoparticles Directly Synthesized from Rice Husk Biomass. *J. Mater. Chem. B* **2017**, *5*, 4679–4689.

https://doi.org/10.1039/C7TB00811B.

(12) Mandal, S.; Pal, J.; Subramanian, R.; Das, P. Amplified Fluorescence of Mg^{2+} Selective Red-Light Emitting Carbon Dot in Water and Direct Evaluation of Creatine Kinase Activity. *Nano Res.* **2020**, *13*, 2770–2776. https://doi.org/10.1007/s12274-020-2927-1.

(13) Molaei, M. J. Carbon Quantum Dots and Their Biomedical and Therapeutic Applications: A Review. *RSC Adv.* **2019**, *9*, 6460–6481. https://doi.org/10.1039/C8RA08088G.

(14) Sohal, N.; Bhatia, S. K.; Basu, S.; Maity, B. Nanomolar Level Detection of Metal Ions by Improving the Monodispersity and Stability of Nitrogen-Doped Graphene Quantum Dots. *New J. Chem.* **2021**, *45*, 19941–19949. https://doi.org/10.1039/D1NJ04551B.

(15) Wang, W.; Wang, Z.; Liu, J.; Peng, Y.; Yu, X.; Wang, W.; Zhang, Z.; Sun, L. One-Pot Facile Synthesis of Graphene Quantum Dots from Rice Husks for Fe^{3+} Sensing. *Ind. Eng. Chem. Res.* **2018**, *57*, 9144–9150. https://doi.org/10.1021/acs.iecr.8b00913.

(16) Zhu, L.; Shen, D.; Liu, Q.; Wu, C.; Gu, S. Sustainable Synthesis of Bright Green Fluorescent Carbon Quantum Dots from Lignin for Highly Sensitive Detection of Fe^{3+} Ions. *Appl. Surf. Sci.* **2021**, *565*, 150526. https://doi.org/10.1016/j.apsusc.2021.150526.

(17) Das, R.; Sugimoto, H.; Fujii, M.; Giri, P. K. Quantitative Understanding of Charge-Transfer-Mediated Fe^{3+} Sensing and Fast Photoresponse by N-Doped Graphene Quantum Dots Decorated on Plasmonic Au Nanoparticles. *ACS Appl. Mater. Interfaces* **2020**, *12*, 4755–4768. https://doi.org/10.1021/acsami.9b19067.

(18) Li, S.; Li, Y.; Cao, J.; Zhu, J.; Fan, L.; Li, X. Sulfur-Doped Graphene Quantum Dots as a Novel Fluorescent Probe for Highly Selective and Sensitive Detection of Fe^{3+}. *Anal. Chem.* **2014**, *86*, 10201–10207. https://doi.org/10.1021/ac503183y.

(19) Wang, R.; Jiao, L.; Zhou, X.; Guo, Z.; Bian, H.; Dai, H. Highly Fluorescent Graphene Quantum Dots from Biorefinery Waste for Tri-Channel Sensitive Detection of Fe^{3+} Ions. *J. Hazard. Mater.* **2021**, *412*, 125096. https://doi.org/10.1016/j.jhazmat.2021.125096.

(20) Wang, Y.; Wang, F.; Feng, Y.; Xie, Z.; Zhang, Q.; Jin, X.; Liu, H.; Liu, Y.; Lv, W.; Liu, G. Facile Synthesis of Carbon Quantum Dots Loaded with Mesoporous GC_3N_4 for Synergistic Absorption and Visible Light Photodegradation of Fluoroquinolone Antibiotics. *Dalt. Trans.* **2018**, *47*, 1284–1293. https://doi.org/10.1039/C7DT04360K.

(21) Ali, H. R. H.; Hassan, A. I.; Hassan, Y. F.; El-Wekil, M. M. Mannitol Capped Magnetic Dispersive Micro-Solid-Phase Extraction of Polar Drugs Sparfloxacin and Orbifloxacin from Milk and Water Samples Followed by Selective Fluorescence Sensing Using Boron-Doped Carbon Quantum Dots. *J. Environ. Chem. Eng.* **2021**, *9*, 105078. https://doi.org/10.1016/j.jece.2021.105078.

(22) Zhu, X.; Zhang, Z.; Xue, Z.; Huang, C.; Shan, Y.; Liu, C.; Qin, X.; Yang, W.; Chen, X.; Wang, T. Understanding the Selective Detection of Fe^{3+} Based on Graphene Quantum Dots as Fluorescent Probes: The K Sp of a Metal Hydroxide-Assisted Mechanism. *Anal. Chem.* **2017**, *89*, 12054–12058. https://doi.org/10.1021/acs.analchem.7b02499.

(23) Magdy, G.; Abdel Hakiem, A. F.; Belal, F.; Abdel-Megied, A. M. Green One-Pot Synthesis of Nitrogen and Sulfur Co-Doped Carbon Quantum Dots as New Fluorescent Nanosensors for Determination of Salinomycin and Maduramicin in Food Samples. *Food Chem.* **2021**, *343*, 128539. https://doi.org/10.1016/j.foodchem.2020.128539.

(24) Suanchan, K.; Chansud, N.; Sa-nguanprang, S.; Bunkoed, O. A Nanocomposite Optosensing Probe Based on Hierarchical Porous Carbon and Graphene Quantum Dots Incorporated in Selective Polymer for the Detection of Trace Ofloxacin. *Colloids Surfaces A Physicochem. Eng. Asp.* **2021**, *628*, 127376. https://doi.org/10.1016/j.colsurfa.2021.127376.

(25) Zhao, S.; Song, X.; Chai, X.; Zhao, P.; He, H.; Liu, Z. Green Production of Fluorescent Carbon Quantum Dots Based on Pine Wood and Its Application in the Detection of Fe3+. *J. Clean. Prod.* **2020**, *263*, 121561. https://doi.org/10.1016/j.jclepro.2020.121561.

(26) Zhang, L.; Wang, Y.; Liu, W.; Ni, Y.; Hou, Q. Corncob Residues as Carbon Quantum Dots Sources and Their Application in Detection of Metal Ions. *Ind. Crops Prod.* **2019**, *133*, 18–25. https://doi.org/10.1016/j.indcrop.2019.03.019.

(27) Khan, Z. M. S. H.; Rahman, R. S.; Shumaila; Islam, S.; Zulfequar, M. Hydrothermal Treatment of Red Lentils for the Synthesis of Fluorescent Carbon Quantum Dots and Its Application for Sensing Fe^{3+}. *Opt. Mater. (Amst).* **2019**, *91*, 386–395. https://doi.org/10.1016/j.optmat.2019.03.054.

(28) Shan, J.; Li, R.; Yan, K.; Zhu, Y.; Zhang, J. In Situ Anodic Stripping of Cd(II) from CdS Quantum Dots for Electrochemical Sensing of Ciprofloxacin. *Sensors Actuators, B Chem.* **2016**, *237*, 75–80. https://doi.org/10.1016/j.snb.2016.06.066.

(29) Thongsai, N.; Tanawannapong, N.; Praneerad, J.; Kladsomboon, S.; Jaiyong, P.; Paoprasert, P. Real-Time Detection of Alcohol Vapors and Volatile Organic Compounds via Optical Electronic Nose Using Carbon Dots Prepared from Rice Husk and Density Functional Theory Calculation. *Colloids Surfaces A Physicochem. Eng. Asp.* **2019**, *560*, 278–287. https://doi.org/10.1016/j.colsurfa.2018.09.077.

(30) Wang, Z.; Yu, J.; Zhang, X.; Li, N.; Liu, B.; Li, Y.; Wang, Y.; Wang, W.; Li, Y.; Zhang, L. Large-Scale and Controllable Synthesis of Graphene Quantum Dots from Rice Husk Biomass: A Comprehensive Utilization Strategy. *ACS Appl. Mater. Interfaces* **2016**, *8*, 1434–1439. https://doi.org/10.1021/acsami.5b10660.

(31) Ashraf, M. A.; Peng, W.; Zare, Y.; Rhee, K. Y. Effects of Size and Aggregation/Agglomeration of Nanoparticles on the Interfacial/Interphase Properties and Tensile Strength of Polymer Nanocomposites. *Nanoscale Res. Lett.* **2018**, *13*, 1–7. https://doi.org/10.1186/s11671-018-2624-0.

(32) Souza da Costa, R.; Ferreira da Cunha, W.; Simenremis Pereira, N.; Marti Ceschin, A. An Alternative Route to Obtain Carbon Quantum Dots from Photoluminescent Materials in Peat. *Materials (Basel).* **2018**, *11*, 1492. https://doi.org/10.3390/ma11091492.

(33) Wongso, V.; Sambudi, N. S.; Sufian, S.; Abdullah, B. The Effect of PH in the Synthesis of Carbon Quantum Dots from Rice Husk on Their Photoluminescence Properties. In *IOP Conference Series: Earth and Environmental Science* **2019**, *268*, 12087. 10.1088/1755-1315/268/1/012087.

(34) Supchocksoonthorn, P.; Thongsai, N.; Wei, W.; Gopalan, P.; Paoprasert, P. Highly Sensitive and Stable Sensor for the Detection of Capsaicin Using Electrocatalytic Carbon Dots Grafted onto Indium Tin Oxide. *Sensors Actuators B Chem.* **2021**, *329*, 129160. https://doi.org/10.1016/j.snb.2020.129160.

(35) Ding, H.; Yu, S. B.; Wei, J. S.; Xiong, H. M. Full-Color Light-Emitting Carbon Dots with a Surface-State-Controlled Luminescence Mechanism. *ACS Nano* **2016**, *10*, 484–491. https://doi.org/10.1021/acsnano.5b05406.

(36) Strauss, V.; Margraf, J. T.; Dolle, C.; Butz, B.; Nacken, T. J.; Walter, J.; Bauer, W.; Peukert, W.; Spiecker, E.; Clark, T. Carbon Nanodots: Toward a Comprehensive Understanding of Their Photoluminescence. *J. Am. Chem. Soc.* **2014**, *136*, 17308–17316. https://doi.org/10.1021/ja510183c.

(37) Xu, J.; Sahu, S.; Cao, L.; Bunker, C. E.; Peng, G.; Liu, Y.; Fernando, K. A. S.; Wang, P.; Guliants, E. A.; Meziani, M. J. Efficient Fluorescence Quenching in Carbon Dots by Surface-Doped Metals-Disruption of Excited State Redox Processes and Mechanistic Implications. *Langmuir* **2012**, *28*, 16141–16147. https://doi.org/10.1021/la302506e.

(38) Wongso, V.; Sambudi, N. S.; Sufian, S.; Isnaeni. The Effect of Hydrothermal Conditions on Photoluminescence Properties of Rice Husk-Derived Silica-Carbon Quantum Dots for Methylene Blue Degradation. *Biomass Convers. Biorefinery* **2021**, *11*, 2641–2654. https://doi.org/10.1007/s13399-020-00662-9.

(39) Le, T. H.; Le, D. T. T.; Tung, N. Van. Synthesis of Colloidal Silicon Quantum Dot from Rice Husk Ash. *J. Chem.* **2021**, *2021*, 1–9. https://doi.org/10.1155/2021/6689590.

(40) Mogharbel, A. T.; Pashameah, R. A.; Alluhaybi, A. A.; Almahri, A.; Abumelha, H. M.; Habeebullah, T. M.; El-Metwaly, N. M. Development of a “Turn-off” Fluorescent Sensor for

Acetone from Rice Straw-Derived Carbon Dots Immobilized onto Textile Cotton Mask. *J. Mol. Liq.* **2022**, *362*, 119666. https://doi.org/10.1016/j.molliq.2022.119666.

(41) Gan, Z.; Xu, H.; Hao, Y. Mechanism for Excitation-Dependent Photoluminescence from Graphene Quantum Dots and Other Graphene Oxide Derivates: Consensus, Debates and Challenges. *Nanoscale* **2016**, *8*, 7794–7807. https://doi.org/10.1039/c6nr00605a.

(42) Guideline, I. C. H. H. T. Validation of Analytical Procedures: Text and Methodology. *Q2* **2005**, *1*, 5.

(43) Khan, W. U.; Wang, D.; Zhang, W.; Tang, Z.; Ma, X.; Ding, X.; Du, S.; Wang, Y. High Quantum Yield Green-Emitting Carbon Dots for Fe (III) Detection, Biocompatible Fluorescent Ink and Cellular Imaging. *Sci. Rep.* **2017**, *7*, 1–9. 10.1038/s41598-017-15054-9.

(44) Xu, Q.; Pu, P.; Zhao, J.; Dong, C.; Gao, C.; Chen, Y.; Chen, J.; Liu, Y.; Zhou, H. Preparation of Highly Photoluminescent Sulfur-Doped Carbon Dots for Fe (III) Detection. *J. Mater. Chem. A* **2015**, *3*, 542–546. https://doi.org/10.1039/C4TA05483K.

(45) Li, G.; Lv, N.; Bi, W.; Zhang, J.; Ni, J. Nitrogen-Doped Carbon Dots as a Fluorescence Probe Suitable for Sensing Fe^{3+} under Acidic Conditions. *New J. Chem.* **2016**, *40*, 10213–10218. https://doi.org/10.1039/C6NJ02088G.

(46) Xuan, W.; Ruiyi, L.; Saiying, F.; Zaijun, L.; Guangli, W.; Zhiguo, G.; Junkang, L. D-Penicillamine-Functionalized Graphene Quantum Dots for Fluorescent Detection of Fe^{3+} in Iron Supplement Oral Liquids. *Sensors Actuators B Chem.* **2017**, *243*, 211–220. https://doi.org/10.1016/j.snb.2016.11.150.

(47) Zulfajri, M.; Gedda, G.; Chang, C.-J.; Chang, Y.-P.; Huang, G. G. Cranberry Beans Derived Carbon Dots as a Potential Fluorescence Sensor for Selective Detection of Fe^{3+} Ions in Aqueous Solution. *ACS omega* **2019**, *4*, 15382–15392. https://doi.org/10.1021/acsomega.9b01333.

(48) Li, L.; Li, L.; Wang, C.; Liu, K.; Zhu, R.; Qiang, H.; Lin, Y. Synthesis of Nitrogen-Doped and Amino Acid-Functionalized Graphene Quantum Dots from Glycine, and Their Application to the Fluorometric Determination of Ferric Ion. *Microchim. Acta* **2015**, *182*, 763–770. 10.1007/s00604-014-1383-6.

(49) Pang, S.; Liu, S. Dual-Emission Carbon Dots for Ratiometric Detection of Fe^{3+} Ions and Acid Phosphatase. *Anal. Chim. Acta* **2020**, *1105*, 155–161. https://doi.org/10.1016/j.aca.2020.01.033.

(50) Benesi, H. A.; Hildebrand, J. H. A Spectrophotometric Investigation of the Interaction of Iodine with Aromatic Hydrocarbons. *J. Am. Chem. Soc.* **1949**, *71*, 2703–2707. https://doi.org/10.1021/ja01176a030.

(51) Zhang, Y.-L.; Wang, L.; Zhang, H.-C.; Liu, Y.; Wang, H.-Y.; Kang, Z.-H.; Lee, S.-T. Graphitic Carbon Quantum Dots as a Fluorescent Sensing Platform for Highly Efficient Detection of Fe^{3+} Ions. *Rsc Adv.* **2013**, *3*, 3733–3738. https://doi.org/10.1039/C3RA23410J.

(52) Deng, X.; Feng, Y.; Li, H.; Du, Z.; Teng, Q.; Wang, H. N-Doped Carbon Quantum Dots as Fluorescent Probes for Highly Selective and Sensitive Detection of Fe^{3+} Ions. *Particuology* **2018**, *41*, 94–100. https://doi.org/10.1016/j.partic.2017.12.009.

(53) Lv, P.; Yao, Y.; Zhou, H.; Zhang, J.; Pang, Z.; Ao, K.; Cai, Y.; Wei, Q. Synthesis of Novel Nitrogen-Doped Carbon Dots for Highly Selective Detection of Iron Ion. *Nanotechnology* **2017**, *28*, 165502. https://doi.org/10.1088/1361-6528/aa6320.

(54) Wang, R.; Fan, H.; Jiang, W.; Ni, G.; Qu, S. Amino-Functionalized Graphene Quantum Dots Prepared Using High-Softening Point Asphalt and Their Application in Fe^{3+} Detection. *Appl. Surf. Sci.* **2019**, *467*, 446–455. https://doi.org/10.1016/j.apsusc.2018.10.104.

(55) Song, Y.; Zhu, C.; Song, J.; Li, H.; Du, D.; Lin, Y. Drug-Derived Bright and Color-Tunable N-Doped Carbon Dots for Cell Imaging and Sensitive Detection of Fe^{3+} in Living Cells. *ACS Appl. Mater. Interfaces* **2017**, *9*, 7399–7405. https://doi.org/10.1021/acsami.6b13954.

(56) Zu, F.; Yan, F.; Bai, Z.; Xu, J.; Wang, Y.; Huang, Y.; Zhou, X. The Quenching of the Fluorescence of Carbon Dots: A Review on Mechanisms and Applications. *Microchim. Acta* **2017**, *184*, 1899–1914. https://doi.org/10.1007/s00604-017-2318-9.

(57) Qi, H.; Teng, M.; Liu, M.; Liu, S.; Li, J.; Yu, H.; Teng, C.; Huang, Z.; Liu, H.; Shao, Q.; Umar, A.; Ding, T.; Gao, Q.; Guo, Z. Biomass-Derived Nitrogen-Doped Carbon Quantum Dots: Highly Selective Fluorescent Probe for Detecting Fe^{3+} Ions and Tetracyclines. *J. Colloid Interface Sci.* **2019**, *539*, 332–341. https://doi.org/10.1016/j.jcis.2018.12.047.

(58) Hua, J.; Jiao, Y.; Wang, M.; Yang, Y. Determination of Norfloxacin or Ciprofloxacin by Carbon Dots Fluorescence Enhancement Using Magnetic Nanoparticles as Adsorbent. *Microchim. Acta* **2018**, *185*, 1–9. https://doi.org/10.1007/s00604-018-2685-x.

(59) Samant, V.; Singh, A. K.; Ramakrishna, G.; Ghosh, H. N.; Ghanty, T. K.; Palit, D. K. Ultrafast Intermolecular Hydrogen Bond Dynamics in the Excited State of Fluorenone. *J. Phys. Chem. A* **2005**, *109*, 8693–8704. https://doi.org/10.1021/jp050848f.

(60) Grabowski, S. J. [FHF]−—The Strongest Hydrogen Bond under the Influence of External Interactions. *Crystals* **2015**, *6*, 3. https://doi.org/10.3390/cryst6010003.

(61) Kainth, S.; Maity, B.; Basu, S. Deciphering the Interaction of Solvents with Dual Emissive Carbon Dots: A Photoluminescence Study and Its Response for Different Metal Ions. *Mater. Sci. Eng. C* **2020**, *108*, 110443. https://doi.org/10.1016/j.msec.2019.110443.

CHAPTER-4

Orange Pomace Derived Fluorescent Carbon Quantum Dots: Detection of Cr (VI) and 4-Nitrophenol in Nanomolar Range

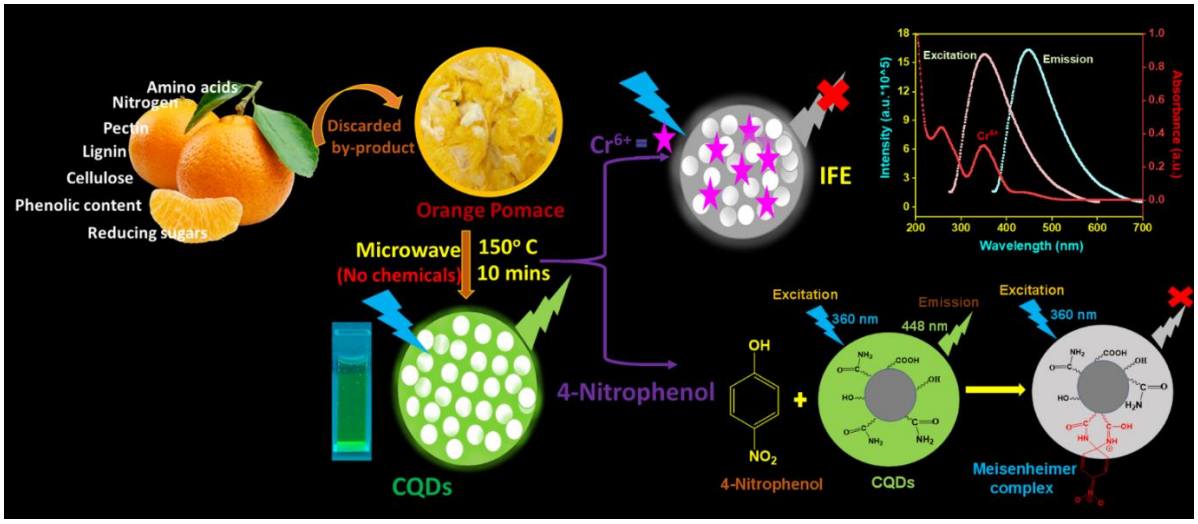

Highlights

- Synthesis of green-emissive carbon quantum dots (CQDs) from orange pomace via microwave method.
- Fabricated CQDs displayed excellent photostability, water solubility, and outstanding fluorescent quantum yield, i.e., 54.26%.
- The synthesized CQDs showed promising results for the detection of Cr^{6+} ions and 4-nitrophenol (4-NP) up to nanomolar range.
- Various photophysical parameters were analysed to gain more insight into the sensing mechanism
- The PL quenching was attributed to IFE for the detection of Cr^{6+} while, for 4-NP it is due to formation of zwitterionic spirocyclic Meisenheimer complex and IFE.

4.1 Introduction

Carbon Quantum dots (CQDs) are a distinct group of fluorescent nanomaterials, which have gained prominence in recent years.[1] A thorough review of the available literature found that organic compounds and natural precursors (biomass and biowaste) were employed to synthesize CQDs.[2] Organic compounds like citric acid, glycerol, and chitosan have been used to produce CQDs but have limitations like toxicity, post-surface passivation, and harsh reaction conditions.[2] Therefore, it is preferable to synthesize CQDs through eco-friendly, affordable, and facile pathways from biomass.[3] Biomass-derived CQDs have high C content (45-55wt%).[4] Also, this is the cost-efficacious and convenient method for the mass production of CQDs without involving any refractory solvents.[4]

Despite progress in selecting green carbon precursors like apple juice,[5] garlic,[6] orange juice,[7] lemon juice,[8], the use of edible products continues to be a challenge.[9] The more favourable choice is to use the agro-industrial waste that comes from the consumption of primary products.[10,11] The beverage and juice industries generate ~125 million tonnes of by-products.[12] *Citrus sinensis* (Orange) is the typical citrus fruit with a global production of ~73 million tonnes used for non-culinary and culinary purposes.[9] After juice production, the by-product formed is known as pomace, often discarded. Each year, ~ 15 million tonnes of orange juice by-products are generated globally.[13] Orange pomace contains amino acids, Nitrogen, reducing sugars, fat (low content), pectin, cellulose, lignin, moisture, nucleic acid, and phenolic content.[12] Interestingly, pomace can be an effective green precursor for CQDs synthesis. The inherent N functionalities and surface-bound functional groups like phenolic, carboxyl, etc., in the as-prepared CQDs were responsible for the sensing of different analytes.

Meanwhile, Chromium (Cr) is one of the heavy metal pollutants affecting human health and the environment.[14] Among all the forms, Cr (VI) has drawn attention in recent times as it causes hereditary gene defects, allergic reactions, nasal mucosal irritation, and cancers.[15] The United States Environmental Protection Agency identified it as a heavy metal pollutant in the atmosphere.[16] Therefore, rapid and accurate Cr (VI) detection is of utmost importance. Also, 4-Nitrophenol (4-NP) is one of the refractory and noxious pollutants in the effluents produced from the manufacture of pharmaceutical dyes, explosives, and agrochemicals. The ingestion of 4-NP could lead to disorders like headache, kidney and liver damage, and methemoglobinemia.[17] Owing to its carcinogenic capacity and toxicity, the U.S. EPA has listed it in “Primary Pollutant list”.[18] Hence it is vital to create a very specific and sensitive detection system for the detection of 4-NP to save the environment and public health. Fluorescence spectroscopy is a widely used technique for the detection. *Wang and co-workers* fabricated N-

doped CQDs from a chelating agent and used it for detecting Cr (VI) ions.[19] *Xu et al.* prepared N-doped CQDs from D-glucose and L-arginine, which were used to detect Fe (III) and Cr (VI).[20] *Guo et al.* described the hydrothermal preparation of N- and B-doped carbon dots for sensing Cr (VI) through a fluorescence quenching mechanism.[21] *Mondal et al.* prepared CQDs using citric acid and lanthanide to detect Cr (VI).[22] *Li et al.* employed apple peels for CQDs synthesis and utilized it for the detection of Cr (VI) having detection limit i.e., 0.73 μM.[23] Das and Dutta synthesized N-doped carbon dots with ethylene glycol and β-alanine for the detection of 4-nitrophenol and Cr (VI) with the 0.4 μM and 0.29 μM detection limit, respectively.[24] Huang reported the sensitive detection of 4-NP having 0.05 μM detection limit using cuttlefish ink-based N and S co-doped CQDs.[25] Amjadi and Hallaj studied glucose-derived CQDs-$Ru(bpy)_3^{2+}$-Ce (IV) chemiluminescence sensor designed for determination of 4-NP.[26]

This study emphasizes on synthesizing CQDs using orange pomace through the one-pot facile, green, and microwave-assisted methods without the incorporation of any chemicals. The as-prepared CQDs showed green emission and highly fluorescence property. The developed sensor was used for the selective and sensitive detection of Cr^{6+} and 4-NP at the nanomolar level by inner filter mechanism. This study also validates the results of real sample analysis.

4.2 Experimental Section

4.2.1 Materials

Orange pomace was taken from local juice shop (Patiala, India). All the chemicals necessary to prepare metal ions stock solutions were acquired from Loba Chemie, India. Deionized (DI) water was utilized during the experiments.

4.2.2 Synthesis of Orange Pomace-Derived CQDs

To begin, the orange pomace was gently cleansed with DI water. Water (100 mL) was added to pomace and grinded in a mixer which was further filtered and juice was collected. The filtered juice was transferred to reaction vial and kept for heating at 150 °C (300 W) for 10 mins in microwave reactor. The obtained solution was filtered using a syringe filter (0.22 μm) to obtain brown-coloured CQDs as illustrated in Scheme 4.1.

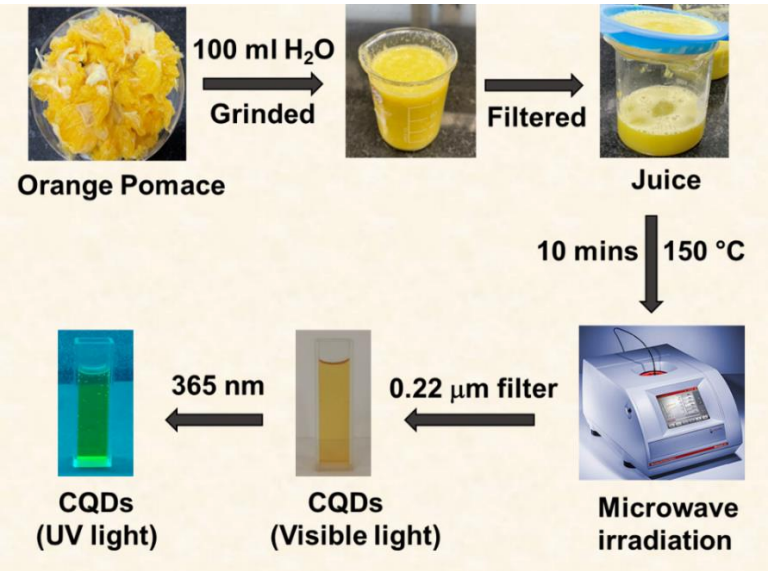

Scheme 4.1. Synthesis of CQDs from orange pomace.

4.2.3 Characterizations

The UV-Visible absorption spectrum was studied by UV-Vis spectrophotometer instrument (Shimadzu UV 2600). Photoluminescence spectra were recorded using a spectrofluorometer (Shimadzu, RF-6000) with light source i.e., xenon lamp. Time-resolved fluorescence measurements were carried by Deltaflex modular fluorescence lifetime spectrofluorometer (HORIBA Scientific) with a nano-LED pulse diode as excitation source at 340 nm. The size and morphology were explored through transmission electron microscopy (JEOL, JEM 2100 plus). Elemental composition was scrutinized using X-ray photoelectron spectroscopy (XPS) (PHI 5000 Versa Probe III). A Raman spectrometer (HORIBA LabRAM HR Evolution) with a 532 nm laser was used to assess the purity and structural defects of sample in the region 1100-1800 cm^{-1}. FT-IR spectrometer (Shimadzu IRTracer-100) were used to detect functional groups within a range of 400-4000 cm^{-1} with 100 numbers of scans. Monowave-300 microwave synthesis reactor (Anton Paar, USA) was used for the synthesis process.

4.2.4 Sample Solutions Preparation

The standard solution (1mM) of various metal (cations: Co^{2+}, Fe^{3+}, Cr^{6+}, Cu^{2+}, Ni^{2+}, Fe^{2+}, Zn^{2+}, Al^{3+}, Cr^{3+}, Hg^{2+}, Pb^{2+}, and Cd^{2+}) (anions: ClO_3^-, PO_4^{3-}, NO_2^-, SO_4^{2-}, Cl^-, NO_3^-, OH^-, F^-, S^{2-}) and analytes (glucose, hydroquinone, ascorbic acid, 4-Nitrophenol, 2-Nitrophenol, glycine, EDTA, alanine, glutathione, methoxy phenol, nitrobenzene, 1-Fluoro 2-nitrobenzene, and phenol were made in DI water to perform the selectivity experiments of synthesized CQDs. 0.1 mM of the solution was pipetted into the cuvette with the addition of 10 μL of CQDs in 2

ml of DI water. Further, the sensitivity studies validation was carried out using 1μM stock solution of Cr (VI) and 4-NP.

4.2.5 Real Sample Analysis

To examine the applicability of the present sensing method, the experiment was conducted with real samples (lake water and tap water). The water samples were collected from Patiala, India. Prior to analysis, the water samples underwent filtration using 0.45 μm nylon filters. After spiking the samples with different concentrations of Cr^{6+} and 4-NP, a solution of CQDs was added, and fluorescence measurements were recorded at a wavelength of 360 nm.

4.3 Results and Discussions

4.3.1 Characterizations

XPS study was done to know the surface chemical composition of the synthesized CQDs. The survey spectra exhibit peaks at 283.8, 398.5, and 531.6 eV corresponding to C1s (66.68%), N1s (2.45%), and O1s (30.87%), respectively (Figure 4.1a). The high-resolution C1s spectrum (Figure 4.1b) shows three major peaks at 284.8, 286.1, and 287.4 eV ascribing to C=C/C-C, C-O/C-N, and O=C-O, respectively.[27] The N1s spectrum (Figure 4.1c) exhibits peaks at 399.3 eV and 401.1 eV corresponds to N-H and C-N.[28] O1s spectrum (Figure 4.1d) showed peaks at 531.1 eV, 532.1 eV, and 533.0 eV assigned to C=O, C-O-C/C-OH, H-OH, respectively with the 25% water content in the sample.[29]

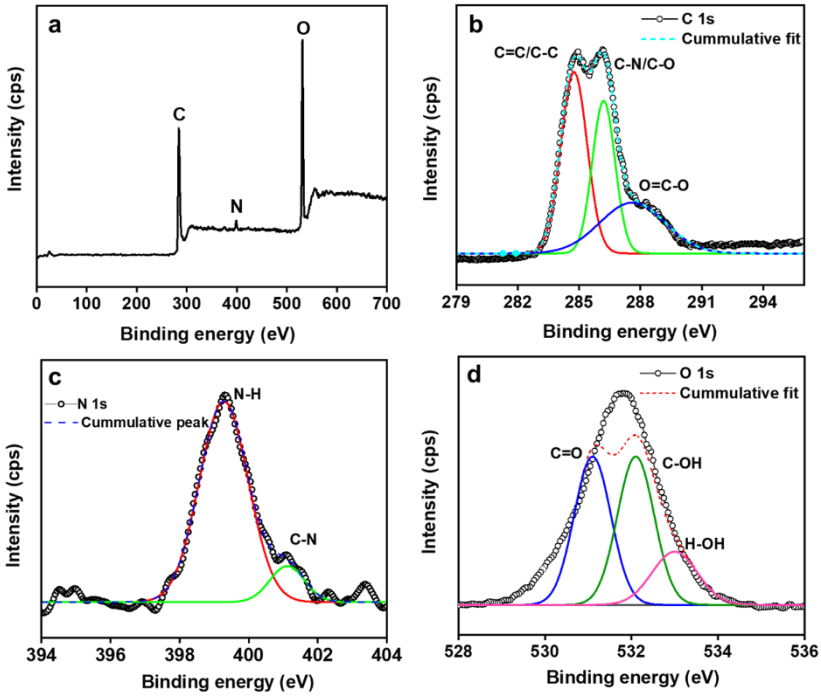

Figure 4.1. (a) Survey spectra of CQDs, (b) high-resolution spectra of C 1s, (c) N 1s, and (d) O 1s of CQDs.

Functional groups on CQDs surface were confirmed through FT-IR spectroscopy (Figure 4.2(a)). The FT-IR absorption bands were observed at 3352 cm^{-1} ascribed to stretching vibration of O-H/N-H group. Small band at 2961 cm^{-1} resembles to C-H stretching vibration, signals at 1737 cm^{-1} and 1622 cm^{-1} corresponds to C=O and C=C stretching, respectively. Additionally, peaks for amide II at 1571 cm^{-1} and amide I at 1618 cm^{-1} corresponds to the bending vibration of amide confirming the amide bonds.[30] The band at 1480 cm^{-1} corresponds to C-N stretching. Peaks at 1258 and 1087 cm^{-1} confirms the C-O stretching.[29] Signal at 1008 cm^{-1} corresponds to C=C bending vibrations. This affirmed the presence of hydroxyl, carboxyl, and amino groups on CQDs surface.

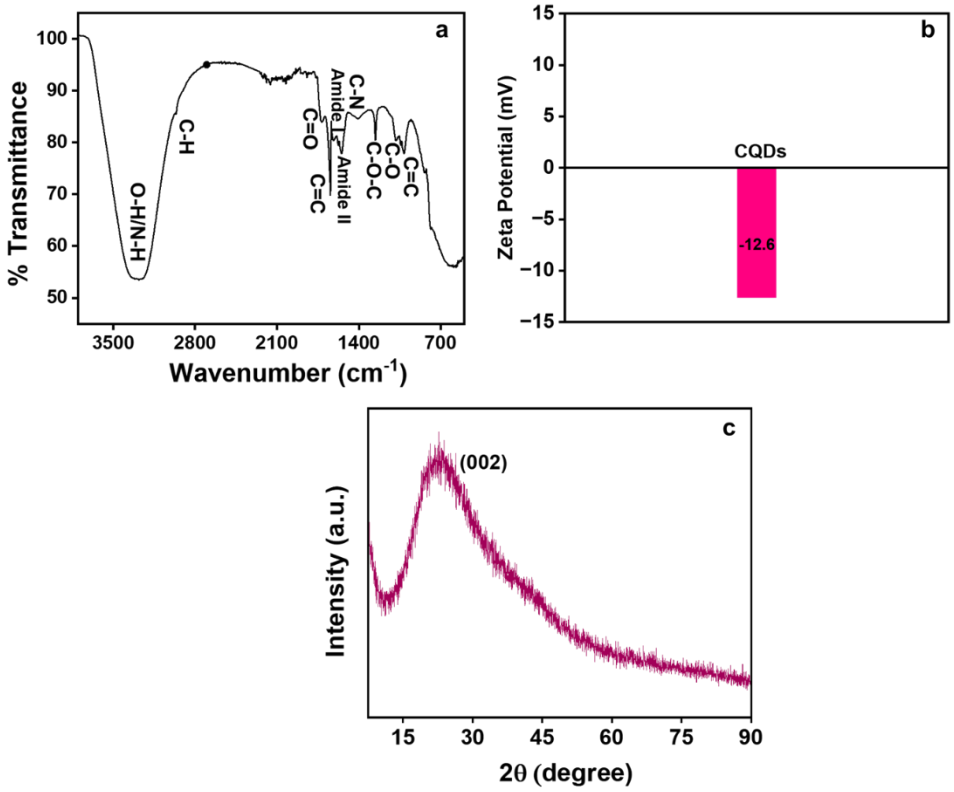

Figure 4.2. (a) FT-IR graph of CQDs, (b) Zeta potential, and (c) XRD spectra of CQDs.

Zeta potential was – 12.6 mV, confirming the abundance of negatively charge functional groups on CQDs (Figure 4.2(b)).[31] The XRD spectrum (Figure 4.2c) exhibited the broad amorphous peak at 2θ =23.5° was attributed to (002) graphitic carbon lattice spacing of the as-prepared CQDs.[23,31] The size and morphology of the orange pomace-derived CQDs were analysed using TEM. Figure 4.3a and 4.3b shows the as-prepared CQDs are nearly spherical in shape. The Inset of Figure 4.3b exhibits the particle size histogram distribution ranging from 3-11 nm, with a computed average particle size of 7.5 nm.

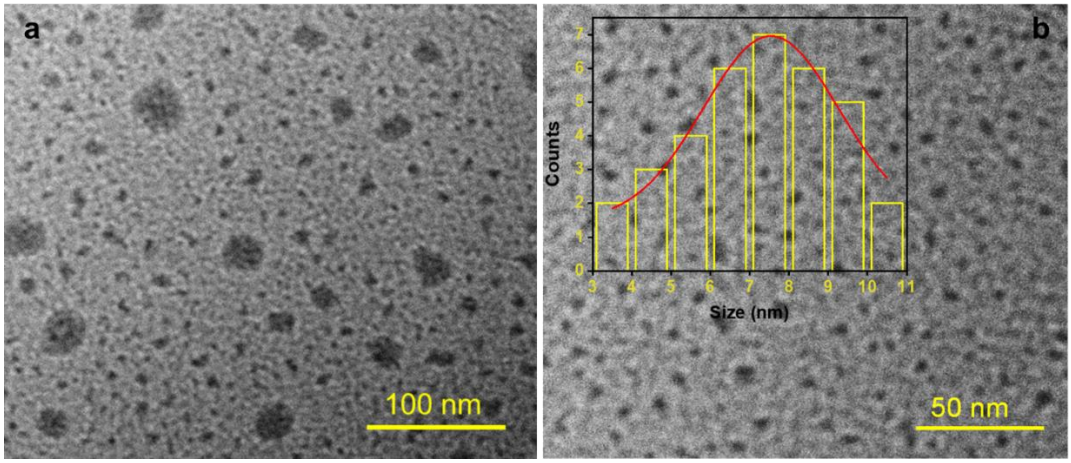

Figure 4.3. (a) TEM image at 100 nm scale and (b) 50 nm scale with inset showing size distribution histogram of CQDs.

Hydrodynamic particle size (~78 nm) was calculated using the DLS data (Figure 4.4(a)). Figure 4.4b exhibited Raman spectrum depicting two peaks at 1360 cm^{-1} (disordered-D) and 1568 cm^{-1} (graphite-G) bands.[32] The G band is a result of the 1st order scattering of E_2g phonons from carbon atoms that are sp^2-hybridized, while the D band arises due to a breathing motion of κ-point phonons with A_1g symmetry associated with defects in the sp^3 carbon bonds, like hydroxyl and/or epoxide bonds.[33] The higher intensity of the G band showed the presence of sp^2 carbons with fewer sp^3 hybridized carbons atoms in the synthesized CQDs. The additional wide 2D band was seen at around 2694 cm^{-1} showed the sp^2 hybridisation (IInd order phonon process).[34,35] The 2D band, historically known as G', represents an overtone of the D band.[36]

4.3.2 Optical Properties

The optical properties were studied using UV-Vis spectra and PL emission spectrum. Figure 4.4c depicts a predominant absorption band at 340 nm for C=O credited to n-π* and a weak absorption band at 275 nm was due to π-π* transition of sp^2 domains of the carbon core.[37] The inset image showed a brown colour during visible light irradiation and emits green fluorescence on irradiation of UV light (365 nm). This is ascribed to radiative recombination among electrons and holes, which is due to photoinduced separation of charge and surface site trapping leading to PL emission of the fabricated CQDs.[38] The PL emission spectra is shown in Figure 4.4d. The highest emission peak was observed at 448 nm upon excitation of 360 nm. The high PL quantum yield of 54.26% was noticed for the as-prepared CQDs. A bathochromic shift (Figure 4.5a) is noticed in the emission wavelength from 417-506 nm with a change in excitations 300-420 nm. This excitation-dependent fluorescence emission of CQDs is related

to fluorescence excitation energy and different factors like quantum confinement effect, surface edge defects, sp^2 π domains, zig-zag edge sites, and size variation.[38]

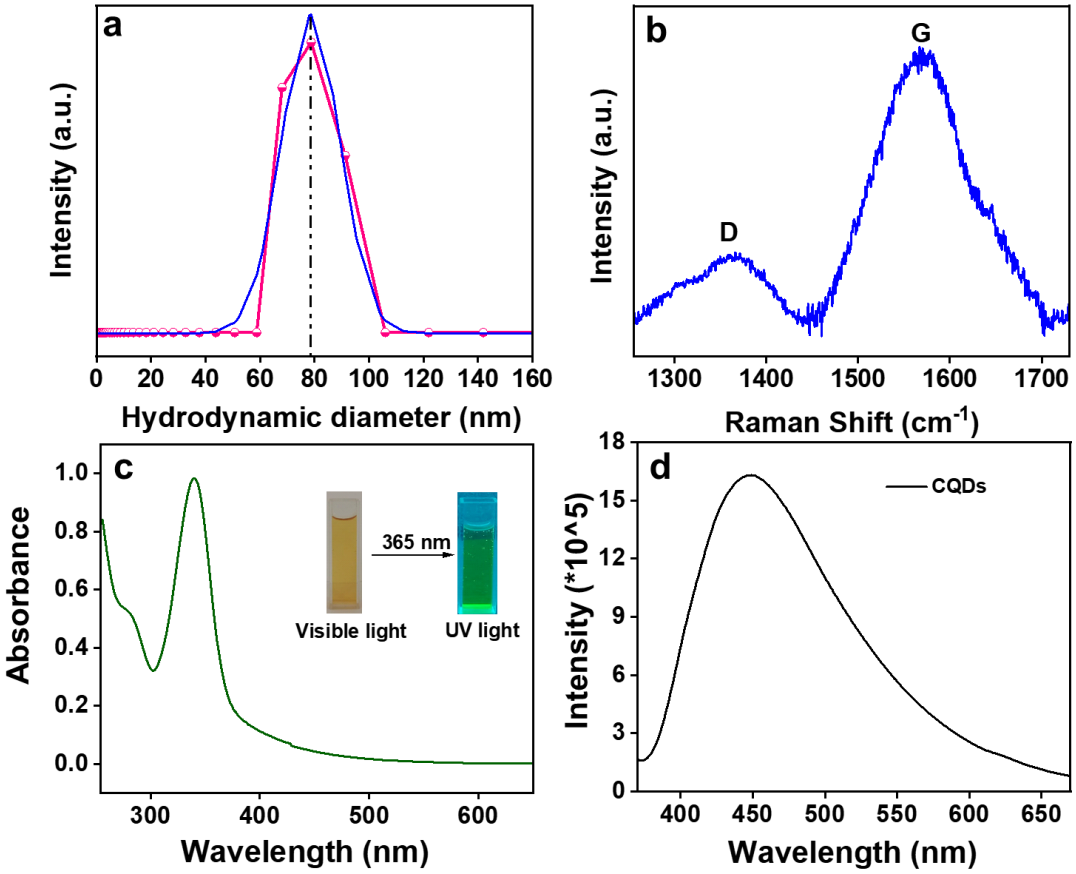

Figure 4.4. (a) DLS size distribution, (b) Raman spectra of CQDs with inset showing 2D band, (c) UV-Vis absorption spectrum with inset showing CQDs exposed to visible and ultraviolet light, and (d) fluorescence emission spectrum of as-prepared CQDs.

4.3.3 Stability Studies of CQDs

The stability of CQDs luminescence properties is a vital factor to be considered prior to further applications. The role of pH and irradiation time on the PL intensity of CQDs was studied. To know the photostability, as-prepared CQDs were irradiated under Xe lamp for 60 mins and no substantial change in intensity was seen (Figure 4.5(b)). CQDs were also stored for 45 days, and the fluorescence spectra were taken at regular intervals, revealing no discernible change in PL intensity over the course of time (Figure 4.5(c)). It affirms the high stability of CQDs. Additionally, the effect of pH (3-13) was investigated to know the pH interference with the PL intensity of CQDs. At various pH, almost same PL intensity of CQDs was observed, proving that CQDs can work effectively in both acidic and basic environments[39] (Figure 4.5(d)).

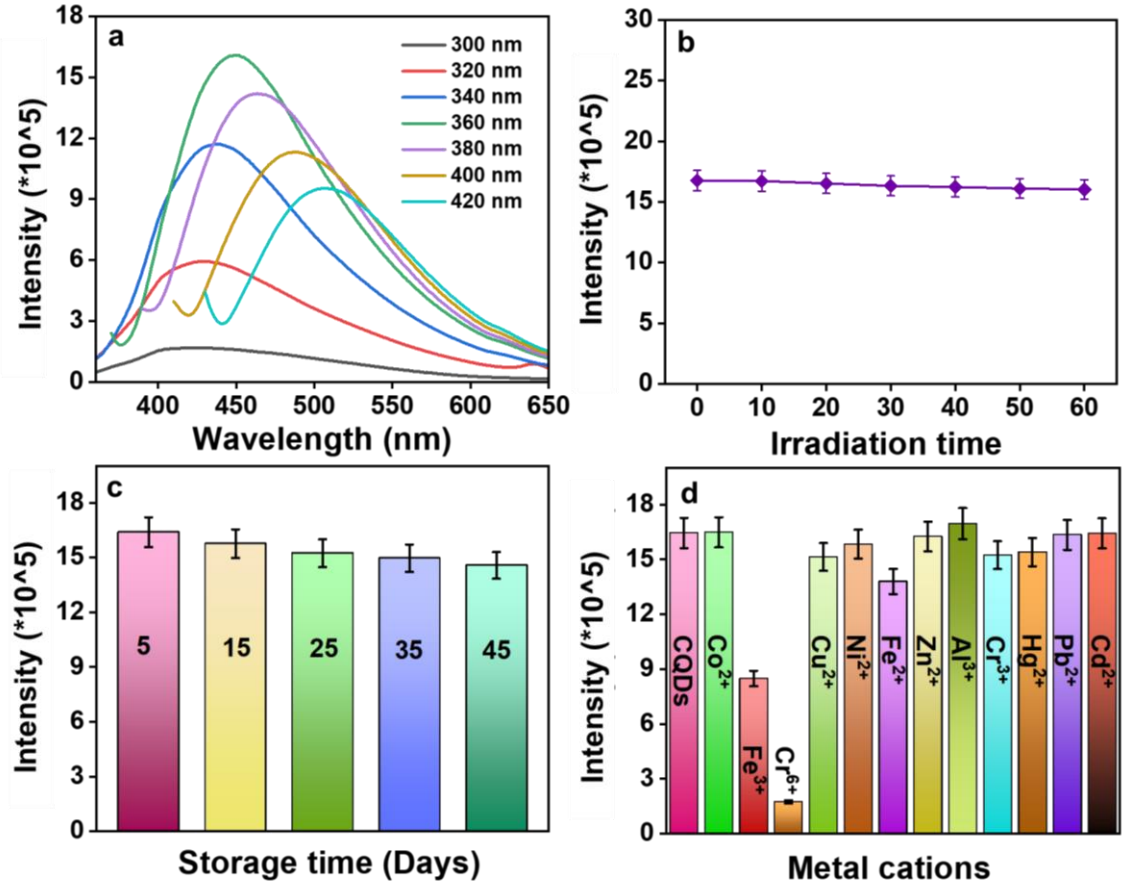

Figure 4.5. (a) Spectra of PL emission at different excitation wavelengths, (b) impact of time (mins), (c) effect of storage duration (days) on CQDs PL stability, and (d) effect of pH (3-13) on the stability of CQDs.

4.3.4 Selectivity Studies for Cr (VI)

This is an important parameter to study while developing a potent sensor. The variation in PL intensity of the CQDs with 0.1 mM concentration of the stock solution of different metal cations (Co^{2+}, Fe^{3+}, Cr^{6+}, Cu^{2+}, Ni^{2+}, Fe^{2+}, Zn^{2+}, Al^{3+}, Cr^{3+}, Hg^{2+}, Pb^{2+}, and Cd^{2+}) was studied. The result indicated a significant PL response after the addition of Fe^{3+} and Cr^{6+} ions, whiles all other cations show minimal response (Figure 4.6(a)). To further confirm the selectivity of the CQDs towards anions, its fluorescence behaviour in presence of different anions (ClO_3^-, PO_4^{3-}, NO_2^-, SO_4^{2-}, Cl^-, NO_3^-, OH^-, F^-, S^{2-}) was also considered. The results exhibited that there is negligeable response on the CQDs intensity on varying the anions (Figure 4.6(b)). Though, Cr^{6+} showed the maximum fluorescence quenching effect, which affirmed that the synthesized CQDs are selective for Cr^{6+} ions. Further sensitivity tests were carried out using 1 µM stock solution of Cr^{6+} ions.

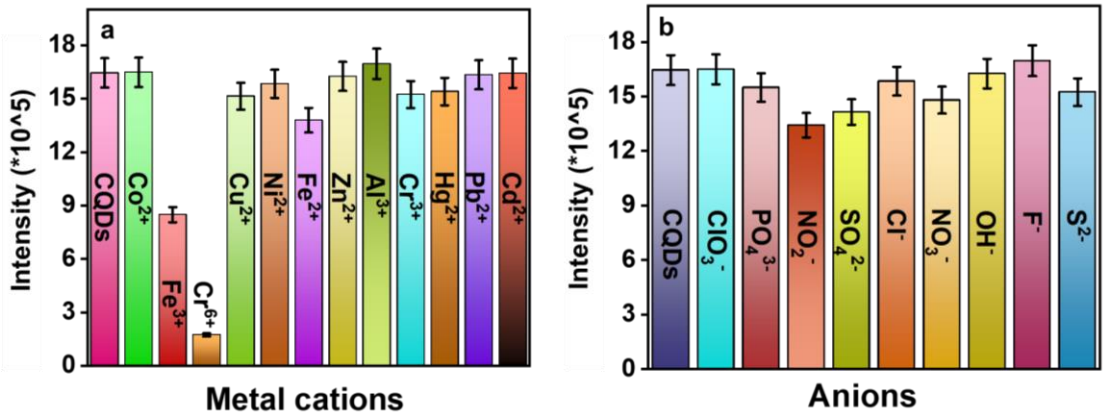

Figure 4.6. CQDs selectivity tests using (a) various metal cations, and (b) metal anions.

4.3.5 Plausible Reason for High Selectivity of Cr (VI) ions

The possible reason for the PL quenching of CQDs with addition of Cr^{6+} ions is because of high redox potential (~ +1.33 V) of Cr^{6+} (equation 4.3) at acidic pH (since the inherent pH of the CQDs is 3.5), making it strong oxidant which can be reduced in presence of electron donor moiety i.e., CQDs.[40] In water, Cr^{6+} exists in various anionic forms such as $Cr_2O_7^{2-}$, CrO_4^{2-}, and $HCrO_4^-$. These Cr^{6+} anionic forms are converted to each other as the pH of solution changes. $Cr_2O_7^{2-}$ and CrO_4^{2-} are in equilibrium in the solution, and as solution becomes acidic, the reaction equilibrium moves towards left (equation 4.1), and as shown in equation 4.2, $Cr_2O_7^{2-}$ is instantaneously converted to $HCrO_4^-$ as the primary constituent.

$$Cr_2O_7^{2-} + H_2O \leftrightarrow 2CrO_4^{2-} + 2H^+ \quad (4.1)$$

$$Cr_2O_7^{2-} + H^+ \rightarrow 2HCrO_4^- + 2H_2O \quad (4.2)$$

$$HCrO_4^- + 7H^+ + 3e^- \rightarrow Cr\ (III) + 4H_2O \qquad (E^0 = 1.33\ V) \quad (4.3)$$

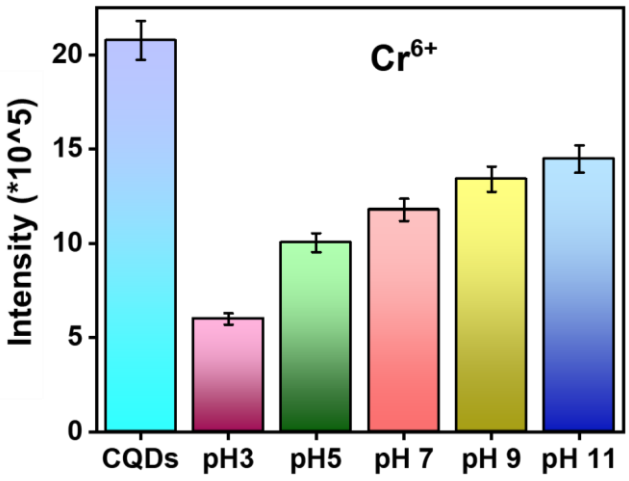

Figure 4.7. Effect of pH on the performance of the sensors for the selective detection of Cr^{6+}.

CQDs surface contains profuse number of functional groups like hydroxyl, carboxyl, amide and carbonyl some of which have reduced capabilities. As a result, Cr^{6+} directly reduced to Cr^{3+} in presence of CQDs.[41] The effect of pH on the performance of the sensors for the selective detection of Cr^{6+} was also studied. The sensor showed the maximum fluorescence quenching of Cr^{6+} in the acidic pH (Figure 4.7).

4.3.6 Method of Validation

This method was authenticated in accordance with ICHQ2(R1) recommendations.[42]

4.3.6.1 Linearity and Range

The interaction of PL intensity of varied Cr^{6+} ions concentrations (nM range) with CQDs was tested to determine sensitivity of the as-prepared sensor. The CQDs PL intensity was gradually quenched with different concentrations of Cr^{6+} ions, as exhibited in Figure 4.8a. To know quenching efficacy, the Stern-Volmer plot was drawn using the following equation 1.7. Figure 4.8b, Table 4.1 depicts the linear range of F_0/F and the Cr^{6+} concentrations (0-480 nM) with the regression equation as

$$F_0/F = 0.00626[Cr^{6+}] + 0.8914 \ (R^2 = 0.991) \quad (4.4)$$

The values of R^2 are approximate to unity indicating the satisfactory linearity of the developed method.

Table 4.1. Sensing capabilities for Cr^{6+} by the prepared sensor.

Parameters	**Cr^{6+}**
Range	0-480 nM
Limit of Detection[a]	59.6 nM
Limit of Quantification [b]	198.7 nM
Regression equation	$F_0/F = 0.00626\ [Cr^{6+}] + 0.8914$
Binding Efficacy	602 nM^{-1}
K_{sv}	0.00626 nM^{-1}

[a]LOD =3σ/K, [b]LOQ =10σ/K, σ is intercept's standard deviation and K represents slope.

4.3.6.2 Limit of Detection (LOD) and Limit of Quantification (LOQ)

The detection limit for Cr^{6+} ions were calculated using 3σ/K and LOQ using 10 σ/K, where σ denotes the intercept's standard deviation, K tells the slope of linear line. The LOD was calculated from Figure 4.8c i.e., 59.6 nM from a plot among PL responses (F_0-F/F_0) and

concentrations of Cr^{6+} ions (0 nM-480 nM) with R^2= 0.995. Table 4.1 shows the LOQ value of 198.7 nM.

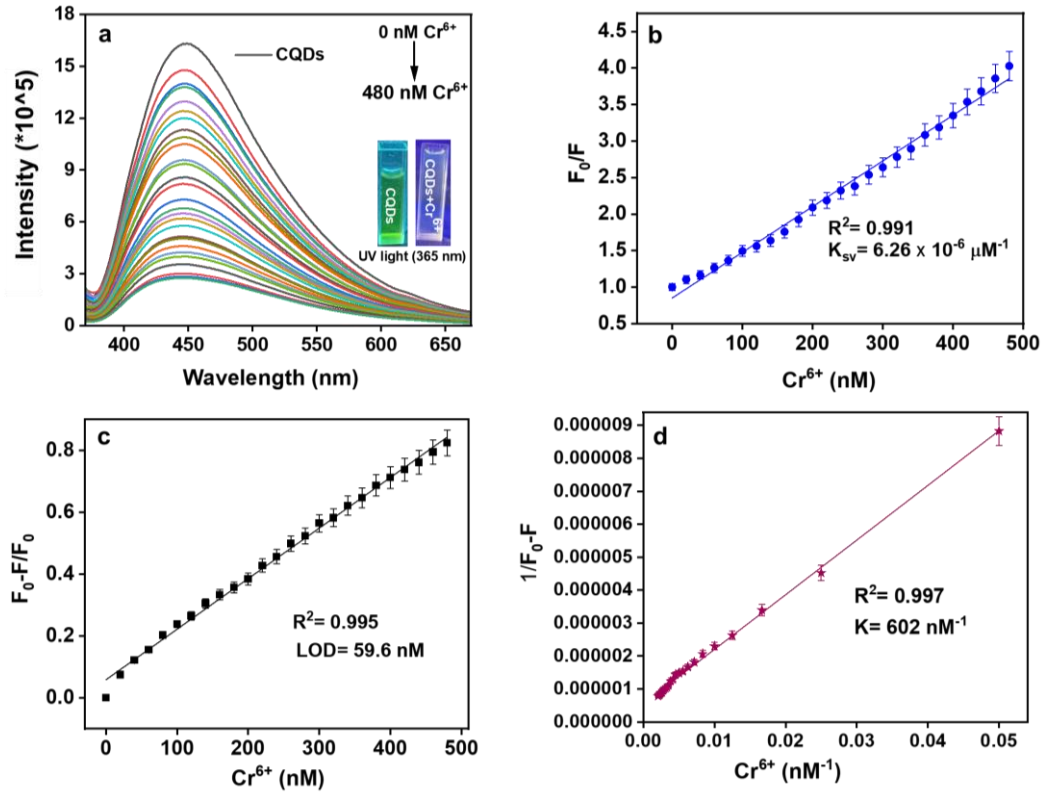

Figure 4.8. (a) Variation in fluorescence intensity of CQDs with a distinct concentration of Cr^{6+} ions, (b) Stern-Volmer quenching plot of CQDs with Cr^{6+}, (c) linear relation among PL response (F_0-F/F_0) and Cr^{6+} ions (0-480 nM), and (d) B-H binding plot of CQDs with Cr^{6+}.

Table 4.2 displays that the developed sensors have high sensitivity towards Cr^{6+} ions compared to other sensors mentioned in the literature.

Table 4.2. Different quantum dots-based sensing devices for Cr^{6+} detection.

Sr. No.	The Sensor system	Linearity range	Detection limit	Ref.
1	CQDs	0.5-200 µM	0.73 µM	[23]
2	N-CQDs	0-100 µM	2.1 µM	[19]
3	CQDs	1-20 µM	0.175 µM	[22]
4	N, S -CQDs	1-10 µM	0.2 µM	[43]
5	N, S-CQDs	1-40 µM	0.52 µM	[44]
6	B, N CDs	0.3-500 µM	0.24 µM	[45]
7	CQDs	0-480 nM	59.6 nM	Current work

4.3.6.3 Binding Efficiency

To determine the binding interaction and stoichiometry between CQDs and Cr^{6+}, excited-state binding constant was estimated with 1:1 linear Benesi-Hildebrand (B-H) equation 1.8. Plot between (1/ F_0-F) versus 1/[Q] exhibits a linear line with binding constant, K = 602 nM^{-1} and R^2 = 0.997 (Figure 4.8d, Table 4.1).

4.3.6.4 Analysis of Precision

An experiment was done to know the intra-day and inter-day precisions, which was carried out with three distinct concentrations along with three replicas of each concentration. Allowed %RSD value was < 2% demonstrating that the prepared method has acceptable precision (Table 4.3).

Table 4.3. Intraday and Inter day precision data for estimating Cr^{6+} by the developed sensor.

Analyte	Conc. taken (nM)	Intra Day[a]			Inter Day[b]		
		Conc. found ± S.D. (nM)	%RSD	%Error[c]	Conc. found ± S.D. (nM)	%RSD	%Error[c]
Cr^{6+}	100	100.73 ± 0.58	1.15	0.66	100.64 ±0.36	0.72	0.42
	200	198.73 ±1.38	1.38	0.80	199.4 ±0.70	0.71	0.41
	300	302.8 ±0.52	0.34	0.20	301.43 ±1.80	1.19	0.69

Each result is the average of three separate determinations.

[a]Within a day [b]Three consecutive days [c]%Error=%RSD/√n

4.3.7 Sensitivity Studies for Detection of Cr (VI) Ions

The linear response range and sensitivity of CQDs for Cr^{6+} ions were calculated by adding distinct concentrations of Cr^{6+} ions (0-480 nM) under optimized conditions. Figure 4.8a clearly shows that with a gradual increase in Cr^{6+}concentrations, the CQDs intensity was gradually decreased. Figure 4.8b showed the decent linear response of F_0/F with the concentration of Cr^{6+} by regression equation 1.8 having a 0.991 correlation coefficient. The detection limit was found to be 59.6 nM (Figure 4.8c) which is much lower than the reported sensitivity parameters value in the previous literature (Table 4.2). Since the average lifetime data of as-prepared CQDs remains constant in the existence of Cr^{6+} (Table 4.4), which clearly depicts that the developed inner filter effect (IFE) based fluorescence sensor has a high sensitivity to detect Cr^{6+} ions offering benefits like fast implementation, facile and expediency.

Table 4.4. Fluorescence lifetime parameters of CQDs, and CQDs+Cr^{6+}.

System	τ_1 (ns)	a_1	τ_2 (ns)	a_2	τ_3 (ns)	a_3	#<τ_{av}>(ns)	χ^2
CQDs	0.154	0.628	1.654	0.274	5.538	0.097	1.086	1.098
CQDs + Cr^{6+}	0.174	0.612	1.582	0.279	5.169	0.108	1.106	1.095

4.3.8 Possible Fluorescence Sensing Mechanism of Cr (VI) Ions

To examine the plausible interaction mechanism of Cr^{6+} ions and CQDs, optical properties spectra of Cr^{6+} and CQDs was first studied to know the quenching mechanism. Figure 4.9a showed the excitation and emission spectra of CQDs, and UV-Vis spectra of the Cr^{6+}. Here, the maximum absorption peak of quencher i.e., Cr^{6+} was overlapped with the excitation spectra of CQDs which is due to the IFE. It is an decent spectral overlay among the absorber's absorption band with fluorophore's excitation/emission band.[23] As showed in Figure 4.9a, the Cr^{6+} showed the broad absorption peak at 257, 352, and 444 nm. Simultaneously, CQDs displayed an excitation band at 360 nm with an emission peak centered at 448 nm demonstrating a great amount of effective overlapping between the excitation, emission, and absorption bands in the developed sensing system. Henceforth, the PL quenching can be credited to the IFE.[46] Also, the PL decay spectrum of CQDs without and with Cr^{6+} were further studied to validate the quenching mechanism. As depicted in Figure 4.9b, average lifetime of CQDs and CQDs+ Cr^{6+} were 1.086 ns and 1.106 ns, respectively (Table 4.4). The minimal change in the fluorescence lifetimes after the Cr^{6+} addition denotes that there was no substantial electron transfer between CQDs and Cr^{6+} and the mechanism was ascribed to IFE (Scheme 4.2).[47]

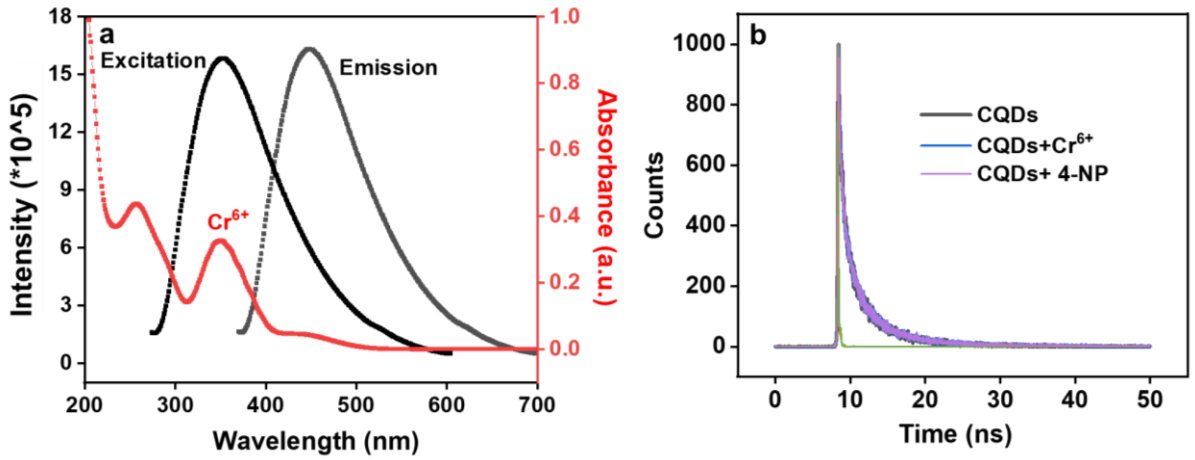

Figure 4.9. (a) Overlapping of absorption spectra of Cr^{6+} ions with the excitation and emission spectrum of CQDs, and (b) PL lifetime decay of CQDs with Cr^{6+}.

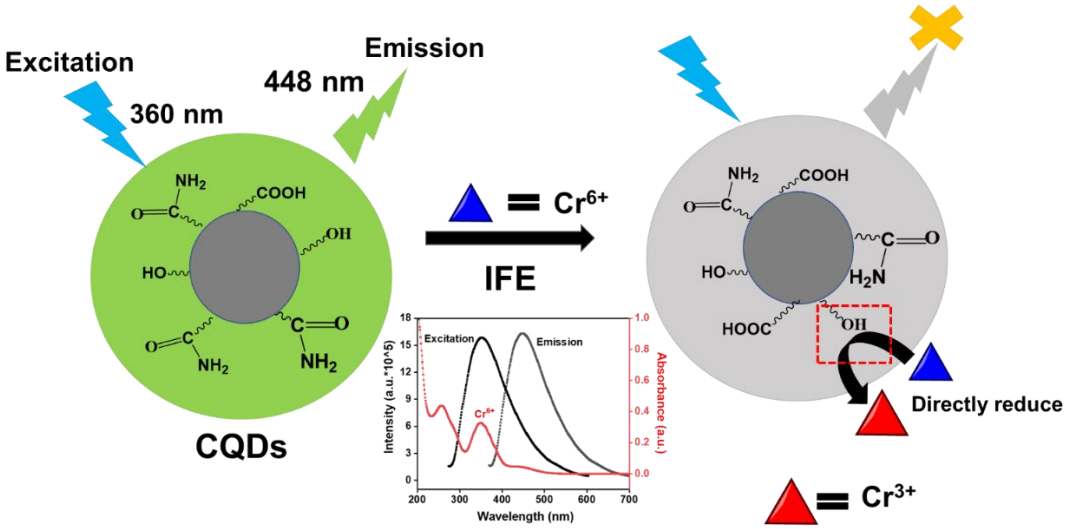

Scheme 4.2. Plausible sensing mechanism of Cr^{6+}.

4.3.9 Analysis of Real Samples

Table 4.5 depicts the practicability of CQDs towards sensing of Cr^{6+} ions in lake water and tap water. The data showed the good recovery percentage and relative standard deviation (%RSD). The observed values exhibited the acceptable precision values confirming the as-prepared CQDs can be successfully used for the sensing of Cr^{6+} in the real water samples.

Table 4.5. Application of developed nanosensor for the detection of Cr^{6+} ions in real samples.

Sample	Added (μM)	Found (μM)	Recovery (%)	RSD (%)
Lake water	0.5	0.47	94.80	1.23
	1.5	1.51	100.6	1.32
	2.5	2.48	99.20	1.06
	5	4.94	98.80	0.30
Tap Water	0.5	0.46	92.0	1.24
	1.5	1.48	98.6	0.67
	2.5	2.51	100.4	1.79
	5	4.93	98.6	0.42

4.3.10 Detection of 4-Nitrophenol (4-NP)

4.3.10.1 Selectivity Studies

To study the selectivity of fabricated CQDs towards 4-NP, changes in CQDs PL intensity were studied in the existence of various analytes like glucose, hydroquinone (HQ), ascorbic acid (AA), 4-NP, 2-NP, glycine, EDTA, alanine, glutathione (GSH) methoxy phenol (MP), nitrobenzene, 1-Fluoro 2- nitrobenzene (1-F-2NB), and phenol. Figure 4.10a depicts that

the PL quenching efficiency of CQDs was maximum in case of 4-NP than the remaining analytes. This displayed the excellent selectivity of synthesized CQDs towards 4-NP. The fluorescence quenching can be accredited to the energy transfer amid CQDS and 4-NP.[48] Also, overlap among the absorption spectra of 4-NP with the excitation and emission spectra of CQDs was responsible for PL quenching. As depicted in Scheme 4.3, the energy transfer could be eased by establishment of a zwitterionic spirocyclic Meisenheimer complex through CQDs and 4-NP combination. The negative charge gets delocalised across the cyclohexadienine ring and the nitro group as a consequence of the creation of a Meisenheimer complex, whilst positive charge will spread on iminium group. This transfer of energy produced by localisation of charges leads to fluorescence quenching of CQDs. Further sensitivity tests were carried out with 1μM stock solution of 4-NP. The effect of pH on the performance of the sensors for the selective detection of 4-NP was also carried out. The sensor showed the maximum fluorescence quenching of 4-NP in the basic pH (Figure 4.10b).

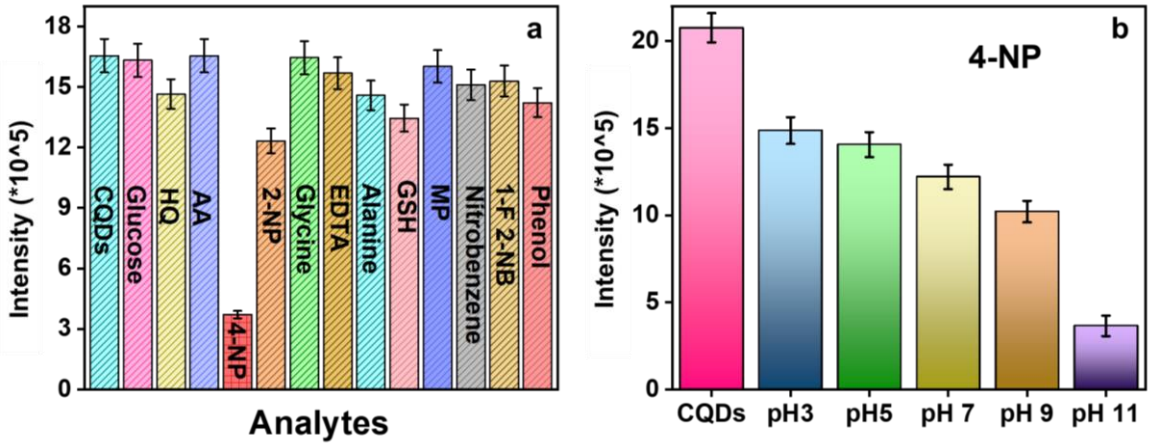

Figure 4.10. (a) Interference analysis of CQDs for 4-NP ions, and (b) effect of pH on the performance of the sensors for the selective detection of 4-NP.

4.3.10.2 Sensitivity Studies of 4-NP

PL intensity of the fabricated CQDs were eventually quenched by gradually adding various concentrations of 4-NP (0-840 nM) (Figure 4.11(a)). The detection limit (LOD), linearity range, LOQ, and further analytical parameters were tabulated in Table 4.6. Figure 4.11b showed the linear relation among PL responses (F_0-F/F_0) and different concentrations of 4-NP (0-840 nM) with the inset figure showing the linear calibration curve between F_0-F/F_0 and concentration of 4-NP (0-90 nM) having correlation coefficient of 0.991. The limit of detection was 14 nM which was calculated using IUPAC criterion (3σ/K), that is lower as compared to the values stated in the previous literatures (Table 4.7).

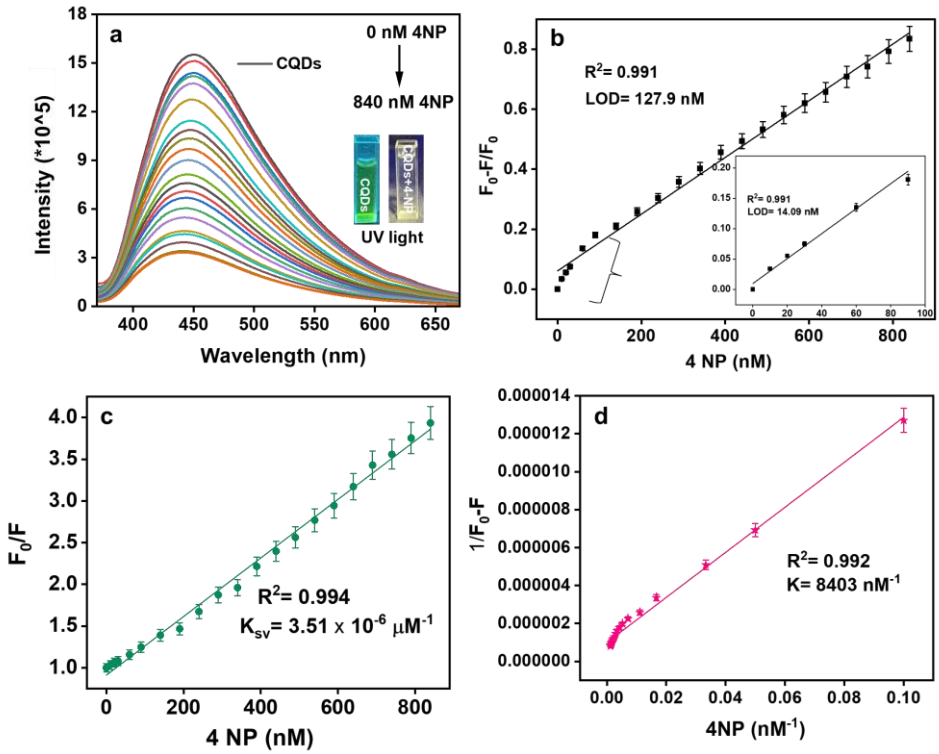

Figure 4.11. (a) Change in PL intensity of CQDs with distinct concentrations of 4-NP ions, (b) linear relation between PL response (F_0-F/F_0) and concentrations of 4-NP ions (0-840 nM) with the inset image of F_0-F/F_0 vs conc. of 4-NP (0-90 nM), (c) linear relation amid PL response (F_0/F) and 4-NP concentrations, and (d) B-H binding plot of CQDs with 4-NP.

The linear calibration curve was derived from Stern-Volmer graph with regression equation $F_0/F=0.00351[4\text{-NP}] + 0.91171$, here F_0 and F are PL intensity of CQDs without and with 4-NP with the high correlation coefficient (R^2=0.994) (Figure 4.11(c)). The Binding efficacy was also calculated using equation 1.8. The graph between (1/ F_0-F) vs. 1/[Q] depicts a linear line showing binding constant, K = 8403 nM^{-1} and R^2 = 0.992 (Figure 4.11d, Table 4.6).

Table 4.6. Analytical performance for 4-NP by the prepared sensor.

Parameters	**4-NP**
Linearity range	0-90 nM
Limit of Detection[a]	14 nM
Limit of Quantification[b]	63.8 nM
Regression equation	F_0/F = 0.00351 [4-NP] + 0.91171
Binding Efficacy	8403 nM^{-1}
K_{sv}	0.00351 nM^{-1}

[a]LOD =3σ/K, [b]LOQ =10σ/K, σ is intercept's standard deviation and K denotes the slope.

Table 4.7. Different sensors for 4-NP detection.

Sr. No.	The Sensors system	Linearity range	Detection limit	Ref.
1	Carbon dots (CDs)	0.1 μM -50 μM	0.028 μM	[49]
2	B, N-CDs	0.5 μM -200 μM	0.20 μM	[50]
3	β-CDs@ZnO QDs	1.0 μM-40 μM	0.34 μM	[51]
4	CdTe QDs	1.0 μM-30 μM	40 nM	[17]
5	CDs	0.001 μM-1 μM	60 nM	[39]
6	CQDs	0-90 nM	14 nM	Current work

Precision analysis were also performed with the acceptable %RSD value of less than 2% indicating that the developed method had an acceptable precision (Table 4.8).

Table 4.8. Intraday and Inter day precision data for estimating 4-NP by the developed sensor.

Analyte	Conc. taken (nM)	Intra Day[a]			Inter Day[b]		
		Conc. found ± S.D. (nM)	%RSD	%Error[c]	Conc. found ± S.D. (nM)	%RSD	%Error[c]
4-NP	200	199.02 ± 0.71	0.71	0.41	198.73 ± 1.22	1.23	0.71
	400	399.0 ±0.50	0.25	0.14	398.66 ±1.04	0.52	0.30
	600	600.93±0.55	0.18	0.10	601.26±0.80	0.26	0.15

Each result is the average of three separate determinations.

[a]Within a day [b]Three consecutive days [c]%Error=%RSD/√n

4.3.10.3 Quenching Mechanism

The PL quenching mechanism of CQDs in presence of 4-NP can be elucidated by the spectral overlapping of the absorption spectra of acceptor i.e., 4-NP with the excitation and emission spectrum of donor i.e., CQDs. This is because of the IFE as depicted in Figure 4.12a, absorption spectra of 4-NP is at 378 nm, which was overlapped with the excitation peak of CQDs that is cantered at 360 nm.[52] The PL decay spectra of CQDs with and without 4-NP were further evaluated to check the quenching mechanism. Figure 4.12b showed the average lifetime of CQDs and CQDs+ 4-NP were 1.086 ns and 1.078 ns, respectively (Table 4.9). Also, the zwitterionic spirocyclic Meisenheimer complex formation was responsible (Scheme 4.3). Here, nitro group and cyclohexadiene ring contains the negative charge and the iminium group

comprises the positive charge.[53] The transfer of energy created by the charges localization might leads to substantial fluorescence quenching of CQDs upon addition of 4-NP (contact quenching).[30]

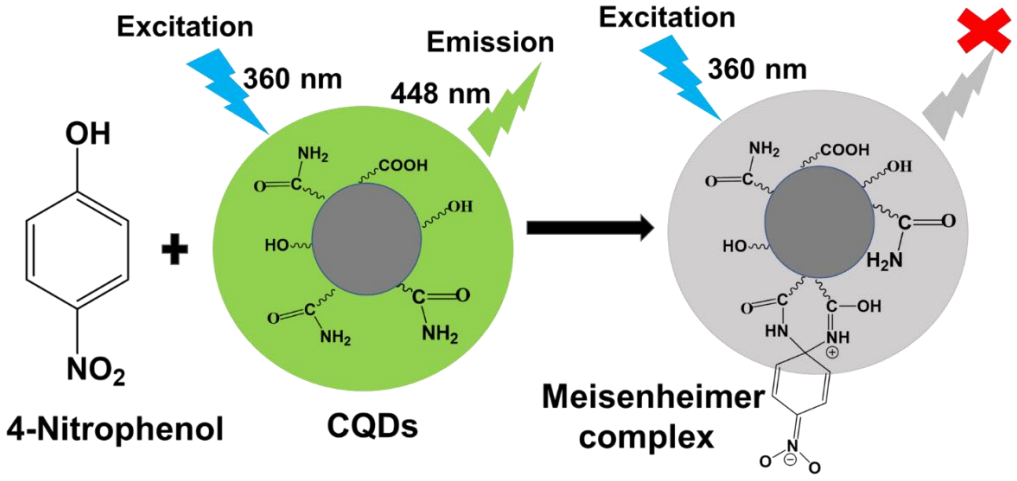

Scheme 4.3. Plausible quenching mechanism of CQDs in presence of 4-NP.

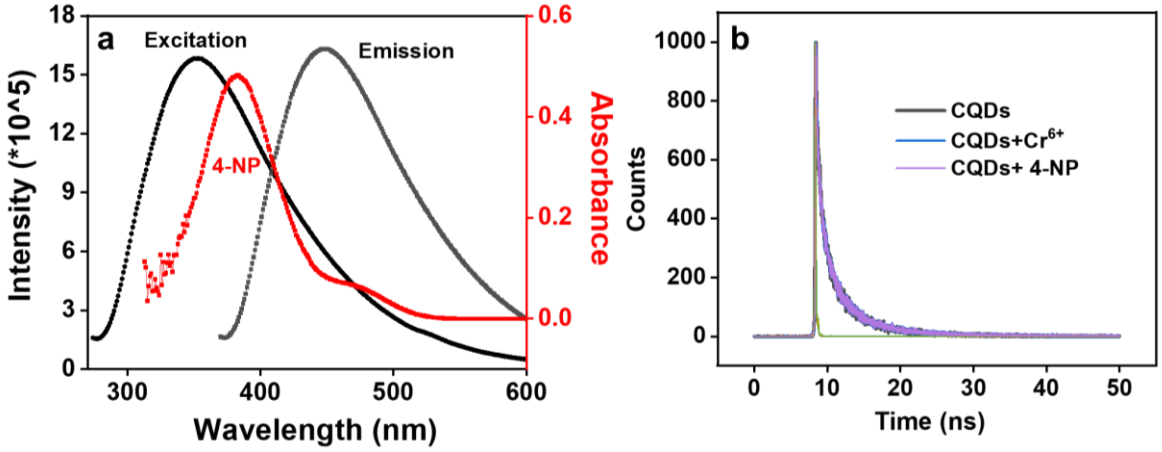

Figure 4.12. (a) Overlapping of 4-NP absorption spectrum with CQDs excitation and emission spectrum, and (b) PL lifetime decay of CQDs with 4-NP.

Table 4.9. Fluorescence lifetime parameters of CQDs, and CQDs+4-NP.

System	τ_1 (ns)	a_1	τ_2 (ns)	a_2	τ_3 (ns)	a_3	#<τ_{av}>(ns)	χ^2
CQDs	0.154	0.628	1.654	0.274	5.538	0.097	1.086	1.098
CQDs+4-NP	0.158	0.625	1.642	0.281	5.510	0.094	1.078	1.097

4.3.10.4 Real Sample Analysis for Method Validation

Real sample analysis was also carried out to confirm the practicability of the developed sensor against the detection of 4-NP in the real water samples. The result showed good %RSD and recoveries (Table 4.10).

Table 4.10. Application of the developed sensor for the detection of 4-NP in real samples.

Sample	Added (μM)	Found (μM)	Recovery (%)	RSD (%)
Lake water	1	1.07	107.0	2.47
	3	2.93	97.60	0.52
	5	4.92	98.40	0.31
	7	7.12	101.7	0.28
Tap Water	1	1.04	104.0	2.54
	3	2.92	97.30	0.19
	5	5.04	100.8	2.34
	7	6.96	99.40	0.46

Conclusions

In this work, eco-friendly, green methodology and cheaper approach was used for synthesis of fluorescent CQDs from biomass waste (orange pomace) by the microwave irradiation without incorporation of chemical substituents. The average size of synthesized CQDs was found to be 7.5 nm. These fabricated CQDs displayed excellent photostability, water solubility, and outstanding fluorescent quantum yield, i.e., 54.26%. The synthesized CQDs are stable, green luminescent showing excitation dependent emission ranging from 300-420 nm. CQDs acts as nanosensor for the sensitive detection of Cr^{6+} with 82% quenching and a detection limit of 59.6 nM within the concentration range of 0-480 nM. The PL quenching was attributed to IFE. Also, the prepared CQDs were applied for the detection of the extremely important mono-nitrophenols with respect to environmental concern. CQDs reacted well towards 4-NP with 14 nM limit of detection in the 0-90 nM concentration range. This is possibly because of formation of zwitterionic spirocyclic Meisenheimer complex and IFE. Validation of the as-prepared sensor was performed in accordance with ICH recommendations. Moreover, to evaluate the feasibility of the detection approach, the developed method was used to effectively detect chromium (Cr^{6+}) and 4-nitrophenol (4-NP) in real water samples with acceptable %RSD and precision. This current method and the detection strategy comes out to be a cheaper, easier, and environment-friendly approach for the detection of Cr^{6+} and 4-NP for various applications.

References

(1) Das, R.; Bandyopadhyay, R.; Pramanik, P. Carbon Quantum Dots from Natural Resource: A Review. *Mater. today Chem.* **2018**, *8*, 96–109. https://doi.org/10.1016/j.mtchem.2018.03.003

(2) Khan, Z. M. S. H.; Rahman, R. S.; Shumaila; Islam, S.; Zulfequar, M. Hydrothermal Treatment of Red Lentils for the Synthesis of Fluorescent Carbon Quantum Dots and Its Application for Sensing Fe^{3+}. *Opt. Mater. (Amst).* **2019**, *91*, 386–395. https://doi.org/10.1016/j.optmat.2019.03.054.

(3) Wang, C.; Shi, H.; Yang, M.; Yan, Y.; Liu, E.; Ji, Z.; Fan, J. Facile Synthesis of Novel Carbon Quantum Dots from Biomass Waste for Highly Sensitive Detection of Iron Ions. *Mater. Res. Bull.* **2020**, *124*, 110730. https://doi.org/10.1016/j.materresbull.2019.110730

(4) Thangaraj, B.; Solomon, P. R.; Chuangchote, S.; Wongyao, N.; Surareungchai, W. Biomass-derived Carbon Quantum Dots–A Review. Part 1: Preparation and Characterization. *ChemBioEng Rev.* **2021**, *8*, 265–301. https://doi.org/10.1002/cben.202000029.

(5) Borna, S.; Sabzi, R. E.; Pirsa, S. Synthesis of Carbon Quantum Dots from Apple Juice and Graphite: Investigation of Fluorescence and Structural Properties and Use as an Electrochemical Sensor for Measuring Letrozole. *J. Mater. Sci. Mater. Electron.* **2021**, *32*, 10866–10879. https://doi.org/10.1007/s10854-021-05745-5.

(6) Sun, C.; Zhang, Y.; Wang, P.; Yang, Y.; Wang, Y.; Xu, J.; Wang, Y.; Yu, W. W. Synthesis of Nitrogen and Sulfur Co-Doped Carbon Dots from Garlic for Selective Detection of Fe^{3+}. *Nanoscale Res. Lett.* **2016**, *11*, 1–9. https://doi.org/10.1186/s11671-016-1326-8.

(7) Li, Z.; Zhang, Y.; Niu, Q.; Mou, M.; Wu, Y.; Liu, X.; Yan, Z.; Liao, S. A Fluorescence Probe Based on the Nitrogen-Doped Carbon Dots Prepared from Orange Juice for Detecting Hg^{2+} in Water. *J. Lumin.* **2017**, *187*, 274–280. https://doi.org/10.1016/j.jlumin.2017.03.023.

(8) Schneider, E. M.; Bärtsch, A.; Stark, W. J.; Grass, R. N. Safe One-Pot Synthesis of Fluorescent Carbon Quantum Dots from Lemon Juice for a Hands-on Experience of Nanotechnology. *J. Chem. Educ.* **2019**, *96*, 540–545. http://dx.doi.org/10.1021/acs.jchemed.8b00114.

(9) Chatzimitakos, T.; Kasouni, A.; Sygellou, L.; Avgeropoulos, A.; Troganis, A.; Stalikas, C. Two of a Kind but Different: Luminescent Carbon Quantum Dots from Citrus Peels for Iron and Tartrazine Sensing and Cell Imaging. *Talanta* **2017**, *175*, 305–312. https://doi.org/10.1016/j.talanta.2017.07.053.

(10) Tovar, A. K.; Godínez, L. A.; Espejel, F.; Ramírez-Zamora, R. M.; Robles, I. Optimization of the Integral Valorization Process for Orange Peel Waste Using a Design of Experiments Approach: Production of High-Quality Pectin and Activated Carbon. *Waste Manag.* **2019**, *85*, 202–213. https://doi.org/10.1016/j.wasman.2018.12.029.

(11) Akhavan, O.; Bijanzad, K.; Mirsepah, A. Synthesis of Graphene from Natural and Industrial Carbonaceous Wastes. *RSC Adv.* **2014**, *4*, 20441–20448.

https://doi.org/10.1039/C4RA01550A.

(12) Gustavsson Cederberg Christel, Sonesson Ulf, J. Global Food Losses and Food Waste. *Unep*. FAO Rome **2011**, 1. https://doi.org/10.1155/2013/460215.

(13) Granucci, N.; Harris, P. J.; Villas-Boas, S. G. Chemical Compositions of Fruit and Vegetable Pomaces from the Beverage Industries. *Waste and Biomass Valorization* **2023**, 1–16. https://doi.org/10.1007/s12649-023-02095-7.

(14) Luo, X.; Bai, P.; Wang, X.; Zhao, G.; Feng, J.; Ren, H. Preparation of Nitrogen-Doped Carbon Quantum Dots and Its Application as a Fluorescent Probe for Cr (VI) Ion Detection. *New J. Chem.* **2019**, *43*, 5488–5494. https://doi.org/10.1039/C8NJ06305B.

(15) Lv, R.; Wang, J.; Zhang, Y.; Li, H.; Yang, L.; Liao, S.; Gu, W.; Liu, X. An Amino-Decorated Dual-Functional Metal–Organic Framework for Highly Selective Sensing of Cr (III) and Cr (VI) Ions and Detection of Nitroaromatic Explosives. *J. Mater. Chem. A* **2016**, *4*, 15494–15500. https://doi.org/10.1039/C6TA05965A.

(16) Services, U. S. D. of H. and H. Toxicological Profile for Chromium. *Public Heal. Serv. Agency Toxic Subst. Dis. Regist. Washington, DC* **1991**. *2013*, 460215. https://doi.org/10.1155/2013/460215

(17) Jiang, L.; Liu, H.; Li, M.; Xing, Y.; Ren, X. Surface Molecular Imprinting on CdTe Quantum Dots for Fluorescence Sensing of 4-Nitrophenol. *Anal. Methods* **2016**, *8*, 2226–2232. https://doi.org/10.1039/c5ay03160e.

(18) Wang, M.; Gao, M.; Deng, L.; Kang, X.; Yang, L.; Quan, T.; Xia, Z.; Gao, D. Composite Material Based on Carbon Dots and Molecularly Imprinted Polymers: A Facile Probe for Fluorescent Detection of 4-Nitrophenol. *Nano* **2020**, *15*, 2197–2203. https://doi.org/10.1142/S1793292020501052.

(19) Wang, G.; Zhang, S.; Cui, J.; Gao, W.; Rong, X.; Lu, Y.; Gao, C. Preparation of Nitrogen-Doped Carbon Quantum Dots from Chelating Agent and Used as Fluorescent Probes for Accurate Detection of ClO− and Cr (VI). *Anal. Chim. Acta* **2022**, *1195*, 339478. https://doi.org/10.1016/j.aca.2022.339478.

(20) Xu, Z.; Liu, J.; Wang, K.; Yan, B.; Hu, S.; Ren, X.; Gao, Z. Facile Synthesis of N-Doped Carbon Dots for Direct/Indirect Detection of Heavy Metal Ions and Cell Imaging. *Environ. Sci. Pollut. Res.* **2021**, *28* , 19878–19889. https://doi.org/10.1007/s11356-020-11880-z.

(21) Guo, Y.; Chen, Y.; Cao, F.; Wang, L.; Wang, Z.; Leng, Y. Hydrothermal Synthesis of Nitrogen and Boron Doped Carbon Quantum Dots with Yellow-Green Emission for Sensing Cr (VI), Anti-Counterfeiting and Cell Imaging. *RSC Adv.* **2017**, *7*, 48386–48393. https://doi.org/10.1039/C7RA09785A.

(22) Mondal, T. K.; Mondal, S.; Ghorai, U. K.; Saha, S. K. White Light Emitting Lanthanide Based Carbon Quantum Dots as Toxic Cr (VI) and PH Sensor. *J. Colloid Interface Sci.* **2019**, *553*, 177–185. https://doi.org/10.1016/j.jcis.2019.06.009.

(23) Li, L.; Shao, C.; Wu, Q.; Wang, Y.; Liu, M. Green Synthesis of Multifunctional Carbon Nanodots and Their Applications as a Smart Nanothermometer and Cr(VI) Ions Sensor. *Nano* **2018**, *13*, 1850147. https://doi.org/10.1142/S1793292018501473.

(24) Das, D.; Dutta, R. K. N-Doped Carbon Dots Synthesized from Ethylene Glycol and β-Alanine for Detection of Cr (VI) and 4-Nitrophenol via Photoluminescence Quenching. *ACS Appl. Nano Mater.* **2021**, *4*, 3444–3454. https://doi.org/10.1021/acsanm.0c03329.

(25) Huang, X.; Yang, C.; Chen, Y.; Zhu, Z.; Zhou, L. Cuttlefish Ink-Based N and S Co-Doped Carbon Quantum Dots as a Fluorescent Sensor for Highly Sensitive and Selective Para-Nitrophenol Detection. *Anal. Methods* **2021**, *13*, 5351–5359. https://doi.org/10.1039/D1AY01496J.

(26) Amjadi, M.; Hallaj, T. Dramatic Enhancement Effect of Carbon Quantum Dots on the Chemiluminescence of Ru (Bpy) 32+–Ce (IV) Reaction and Application to the Determination of 4-Nitrophenol. *J. Lumin.* **2016**, *171*, 202–207. https://doi.org/10.1016/j.jlumin.2015.11.019.

(27) Kainth, S.; Goel, N.; Basu, S.; Maity, B. Surfactant-Derived Water-Soluble Carbon Dots for Quantitative Determination of Fluoride via a Turn-off–on Strategy. *New J. Chem.* **2022**, *46*, 686–694. https://doi.org/10.1039/D1NJ04838D.

(28) Guo, Y.; Zhao, W. Hydrothermal Synthesis of Highly Fluorescent Nitrogen-Doped Carbon Quantum Dots with Good Biocompatibility and the Application for Sensing Ellagic Acid. *Spectrochim. Acta Part A Mol. Biomol. Spectrosc.* **2020**, *240*, 118580. https://doi.org/10.1016/j.saa.2020.118580.

(29) Hu, X.; Li, Y.; Xu, Y.; Gan, Z.; Zou, X.; Shi, J.; Huang, X.; Li, Z.; Li, Y. Green One-Step Synthesis of Carbon Quantum Dots from Orange Peel for Fluorescent Detection of Escherichia Coli in Milk. *Food Chem.* **2021**, *339*, 127775. https://doi.org/10.1016/j.foodchem.2020.127775.

(30) Dang, D. K.; Sundaram, C.; Ngo, Y. L. T.; Choi, W. M.; Chung, J. S.; Kim, E. J.; Hur, S. H. Pyromellitic Acid-Derived Highly Fluorescent N-Doped Carbon Dots for the Sensitive and Selective Determination of 4-Nitrophenol. *Dye. Pigment.* **2019**, *165*, 327–334. https://doi.org/10.1016/j.dyepig.2019.02.029.

(31) Singh, V. K.; Singh, V.; Yadav, P. K.; Chandra, S.; Bano, D.; Kumar, V.; Koch, B.; Talat, M.; Hasan, S. H. Bright-Blue-Emission Nitrogen and Phosphorus-Doped Carbon Quantum Dots as a Promising Nanoprobe for Detection of Cr (VI) and Ascorbic Acid in Pure Aqueous

Solution and in Living Cells. *New J. Chem.* **2018**, *42*, 12990–12997. https://doi.org/10.1039/c8nj02126k.

(32) Sahu, S.; Behera, B.; Maiti, T. K.; Mohapatra, S. Simple One-Step Synthesis of Highly Luminescent Carbon Dots from Orange Juice: Application as Excellent Bio-Imaging Agents. *Chem. Commun.* **2012**, *48*, 8835–8837. https://doi.org/10.1039/C2CC33796G.

(33) Akhavan, O. Bacteriorhodopsin as a Superior Substitute for Hydrazine in Chemical Reduction of Single-Layer Graphene Oxide Sheets. *Carbon N. Y.* **2015**, *81*, 158–166. https://doi.org/10.1016/j.carbon.2014.09.044.

(34) S., T.; D., R. S. Green Synthesis of Highly Fluorescent Carbon Quantum Dots from Sugarcane Bagasse Pulp. *Appl. Surf. Sci.* **2016**, *390*, 435–443. https://doi.org/10.1016/j.apsusc.2016.08.106.

(35) Mewada, A.; Pandey, S.; Shinde, S.; Mishra, N.; Oza, G.; Thakur, M.; Sharon, M.; Sharon, M. Green Synthesis of Biocompatible Carbon Dots Using Aqueous Extract of Trapa Bispinosa Peel. *Mater. Sci. Eng. C* **2013**, *33*, 2914–2917. https://doi.org/10.1016/j.msec.2013.03.018.

(36) Calizo, I.; Balandin, A. A.; Bao, W.; Miao, F.; Lau, C. N. Temperature Dependence of the Raman Spectra of Graphene and Graphene Multilayers. *Nano Lett.* **2007**, *7*, 2645–2649. https://doi.org/10.1021/nl071033g.

(37) Lv, P.; Yao, Y.; Zhou, H.; Zhang, J.; Pang, Z.; Ao, K.; Cai, Y.; Wei, Q. Synthesis of Novel Nitrogen-Doped Carbon Dots for Highly Selective Detection of Iron Ion. *Nanotechnology* **2017**, *28*, 165502. https://doi.org/10.1088/1361-6528/aa6320.

(38) Kundu, A.; Maity, B.; Basu, S. Rice Husk-Derived Carbon Quantum Dots-Based Dual-Mode Nanoprobe for Selective and Sensitive Detection of Fe^{3+} and Fluoroquinolones. *ACS Biomater. Sci. Eng.* **2022**. https://doi.org/10.1021/acsbiomaterials.2c00798.

(39) Qu, Y. Y.; Ren, G.; Yu, L.; Zhu, B.; Chai, F.; Chen, L. The Carbon Dots as Colorimetric and Fluorescent Dual-Readout Probe for 2-Nitrophenol and 4-Nitrophenol Detection. *J. Lumin.* **2019**, *207*, 589–596. https://doi.org/10.1016/j.jlumin.2018.12.017.

(40) Sun, Y.; Yue, Q.; Gao, B.; Gao, Y.; Li, Q.; Wang, Y. Adsorption of Hexavalent Chromium on Arundo Donax Linn Activated Carbon Amine-Crosslinked Copolymer. *Chem. Eng. J.* **2013**, *217*, 240–247. https://doi.org/10.1016/j.cej.2012.11.121.

(41) Yang, W.-M.; Liu, F.; Jin, Y.-T.; Dong, Z.-M.; Zhao, G.-C. Efficient Reduction of Cr (VI) with Carbon Quantum Dots. *ACS omega* **2022**, *7*, 23555–23565. https://doi.org/10.1021/acsomega.2c02063.

(42) Guideline, I. C. H. H. T. Validation of Analytical Procedures: Text and Methodology.

Q2 **2005**, *1*, 5.

(43) Zhang, H.; Huang, Y.; Hu, Z.; Tong, C.; Zhang, Z.; Hu, S. Carbon Dots Codoped with Nitrogen and Sulfur Are Viable Fluorescent Probes for Chromium (VI). *Microchim. Acta* **2017**, *184*, 1547–1553.

(44) Shen, J.; Shang, S.; Chen, X.; Wang, D.; Cai, Y. Highly Fluorescent N, S-Co-Doped Carbon Dots and Their Potential Applications as Antioxidants and Sensitive Probes for Cr (VI) Detection. *Sensors Actuators, B Chem.* **2017**, *248*, 92–100. https://doi.org/10.1016/j.snb.2017.03.123.

(45) Wang, Y.; Hu, X.; Li, W.; Huang, X.; Li, Z.; Zhang, W.; Zhang, X.; Zou, X.; Shi, J. Preparation of Boron Nitrogen Co-Doped Carbon Quantum Dots for Rapid Detection of Cr (VI). *Spectrochim. Acta Part A Mol. Biomol. Spectrosc.* **2020**, *243*, 118807. https://doi.org/10.1016/j.saa.2020.118807.

(46) Gong, X.; Liu, Y.; Yang, Z.; Shuang, S.; Zhang, Z.; Dong, C. An "on-off-on" Fluorescent Nanoprobe for Recognition of Chromium (VI) and Ascorbic Acid Based on Phosphorus/Nitrogen Dual-Doped Carbon Quantum Dot. *Anal. Chim. Acta* **2017**, *968*, 85–96. https://doi.org/10.1016/j.aca.2017.02.038.

(47) Feng, S.; Gao, Z.; Liu, H.; Huang, J.; Li, X.; Yang, Y. Feasibility of Detection Valence Speciation of Cr (III) and Cr (VI) in Environmental Samples by Spectrofluorimetric Method with Fluorescent Carbon Quantum Dots. *Spectrochim. Acta Part A Mol. Biomol. Spectrosc.* **2019**, *212*, 286–292. https://doi.org/10.1016/j.saa.2018.12.055.

(48) Hua, J.; Yang, J.; Zhu, Y.; Zhao, C.; Yang, Y. Highly Fluorescent Carbon Quantum Dots as Nanoprobes for Sensitive and Selective Determination of Mercury (II) in Surface Waters. *Spectrochim. Acta - Part A Mol. Biomol. Spectrosc.* **2017**, *187*, 149–155. https://doi.org/10.1016/j.saa.2017.06.058.

(49) Ahmed, G. H. G.; Laíño, R. B.; Calzón, J. A. G.; García, M. E. D. Highly Fluorescent Carbon Dots as Nanoprobes for Sensitive and Selective Determination of 4-Nitrophenol in Surface Waters. *Microchim. Acta* **2015**, *182*, 51–59. https://doi.org/10.1007/s00604-014-1302-x.

(50) Xiao, N.; Liu, S. G.; Mo, S.; Li, N.; Ju, Y. J.; Ling, Y.; Li, N. B.; Luo, H. Q. Highly Selective Detection of P-Nitrophenol Using Fluorescence Assay Based on Boron, Nitrogen Co-Doped Carbon Dots. *Talanta* **2018**, *184*, 184–192. https://doi.org/10.1016/j.talanta.2018.02.114.

(51) Geng, S.; Lin, S. M.; Liu, S. G.; Li, N. B.; Luo, H. Q. A New Fluorescent Sensor for Detecting: P -Nitrophenol Based on β-Cyclodextrin-Capped ZnO Quantum Dots. *RSC Adv.*

2016, *6*, 86061–86067. https://doi.org/10.1039/c6ra17378k.

(52) Tammina, S. K.; Yang, Y. Highly Sensitive and Selective Detection of 4-Nitrophenol, and on-off-on Fluorescence Sensor for Cr (VI) and Ascorbic Acid Detection by Glucosamine Derived n-Doped Carbon Dots. *J. Photochem. Photobiol. A Chem.* **2020**, *387*, 112134. https://doi.org/10.1016/j.jphotochem.2019.112134.

(53) Bogale, R. F.; Chen, Y.; Ye, J.; Yang, Y.; Rauf, A.; Duan, L.; Tian, P.; Ning, G. Highly Selective and Sensitive Detection of 4-Nitrophenol and Fe^{3+} Ion Based on a Luminescent Layered Terbium (III) Coordination Polymer. *Sensors Actuators, B Chem.* **2017**, *245*, 171–178. https://doi.org/10.1016/j.snb.2017.01.177.

CHAPTER-5

Upcycling Waste: *Citrus limon* peels derived Carbon Quantum Dots for Sensitive Detection of Tetracycline in Nanomolar Range

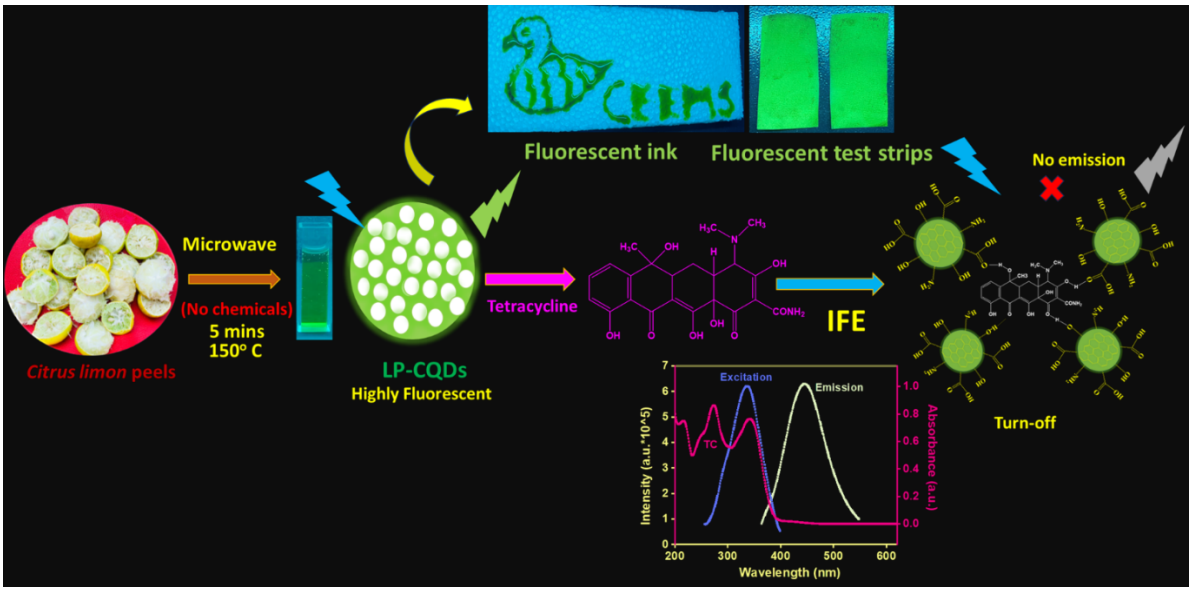

Highlights

- Synthesis of carbon quantum dots from lemon peels (LP-CQDs) using microwave pyrolysis technique.
- Fabricated LP-CQDs displayed encouraging results for tetracycline (TC) detection using a PL turn-off approach.
- A complete analysis of different photophysical parameters of LP-CQDs was performed with TC to gain deeper understanding of the sensing mechanism.
- LP-CQDs were used as a fluorescent ink and to fabricate the paper-based fluorescent strips.

5.1 Introduction

The emerging science of nanotechnology has a substantial influence on a number of disciplines, including chemistry, optics, medicine, thermology, and electricity. Recently, nanomaterials research has captivated the interest of scientists and engineers worldwide.[1] Carbon quantum dots have garnered considerable attention as a unique fluorescent zero-dimensional nanomaterial and regarded as excellent nanoprobe for a variety of applications.[2] Generally, CQDs have been synthesized using organic compounds and naturally available precursors, including biomass. *Citrus limon*, commonly known as lemon, is the most significant citrus fruit in the world, serving both culinary and non-culinary purposes.[3] However, once the juice is extracted; the peels are frequently discarded away and allowed to biodegrade, which potentially pollutes air by forming the dust.[4] Therefore, it is essential need to research low-cost strategies for transforming lemon peel into value-added products. Remarkably, the lemon peels are rich in proteins and fibers, which can serve as potential carbon source for synthesizing CQDs.

Tetracycline (TC), a broad-spectrum antibiotic with excellent sterilisation, and disinfection efficiency, antimicrobial activity, and low toxicity, is a cost-effective option. It is extensively utilized in animal husbandry to effectively combat various bacteria that cause diseases including rickettsia, chlamydia, and mycoplasma.[5] However, improper use of TC in veterinary medication along with food products has led to its presence in common food such as milk, meat, and honey.[6] This causes a major risk to human health including liver damage, visual problem, bacterial resistance, and affecting human teeths.[7] Due to these side effects, various techniques have been developed to identify tetracycline antibiotics. Nevertheless, these techniques necessitate time-consuming sample preparation stages, costly equipment, and professional operators, becoming considerable hurdles for real detection. To overcome these disadvantages, fluorescence-based technique has gained attention as a viable alternative for the quantification and detection of TCs. These methods offer operational convenience, affordability, real-time detection capabilities, high sensitivity and selectivity, fast analysis time.[2,8,9] *Liu et al.,* synthesized blue emissive europium-doped carbon quantum dots using carbonization, used them for the TC detection with 0.3 μM limit of detection.[10] *Fan et al.,* fabricated S, N-doped CQDs for the detection of TC antibiotic with 0.56 μmol/L detection limit in the range of 1.88–60 μmol/L.[11] *Wang et al.,* prepared of N-CQDs with quantum yield of 10.97% from ethylenediamine and glucose for the detection of TC antibiotics such as, chlortetracycline, oxytetracycline, and tetracycline with 0.117 μM, 0.265 μM, and 0.344 μM,

respectively.[6] *Qi et al.,* utilized rice residue and glycine as a biomass precursors for fabrication of N-doped CQDs using hydrothermal method, used it for the detection of Fe^{3+} and TC.[12] Zhang and Fan fabricated Ce-N co-doped CQDs with low cytotoxicity for TC residues and bioimaging with the detection limit of 0.25 μM.[13] *John at al.,* utilized R. *graveolens* leaves for the preparation of CQDs with 18% quantum yield. The probe was used for the electrochemical sensing of TC.[14]

In this work, biomass derived CQDs was synthesized as a fluorescent nanoprobe (quantum yield 49.5%) from dried peels of *Citrus limon* abbreviated as LP-CQDs. The synthesis methodology was purely maintained in green protocol without use of any chemicals. The intrinsic fluorescent nanoprobe was sustainable, simple and inexpensive. The formation of LP-CQDs was stable and displayed excellent selectivity towards TC. Therefore, it is utilised as an efficacious probe for quantitative detection of TC in real samples of river water and tablet. The outcome of the present study possesses special aspects and offers many advantages compared to earlier literature study: (i) The synthesis of LP-CQDs utilizes a readily available and eco-friendly biowaste with reduced time requirement, (ii) The synthesis was done without the incorporation of any harsh chemicals and complex technique, (iii) High quantum yield was observed with nanomolar level detection of TC, and (iv) The sensor is free from metallic components, enabling its safe application across various fields without any adverse effects.

5.2 Experimental Section

5.2.1 Materials and Methods

Lemon peels were taken from local juice shop in Patiala, India. Tetracycline hydrochloride was procured from Sigma Aldrich and used as such. Dialysis membrane-110 was acquired from HiMedia Laboratories Private Limited. The chemicals essential to make solutions of metal ions and other analytes were bought from Loba Chemie. Deionized water (D.I.) was used for experiments.

5.2.2 Synthesis of Lemon Peel-Carbon Quantum Dots (LP-CQDs)

Firstly, lemon peels were thoroughly cleaned with deionized (D.I.) water and oven dried at 90 °C, followed by grinded in a mixer. The powder was carbonised at 200 °C for 2 hrs in muffle furnace. The collected black powder was dispersed in D.I. water, sonicated for 1 hr and transferred to vial which was retained for heating for 5 mins at 150 °C (300 W) under microwave irradiation. Collected solution was filtered with 0.22 μm syringe filter and then kept in dialysis bag (1 day) to obtain light brown coloured LP-CQDs (Scheme 5.1).

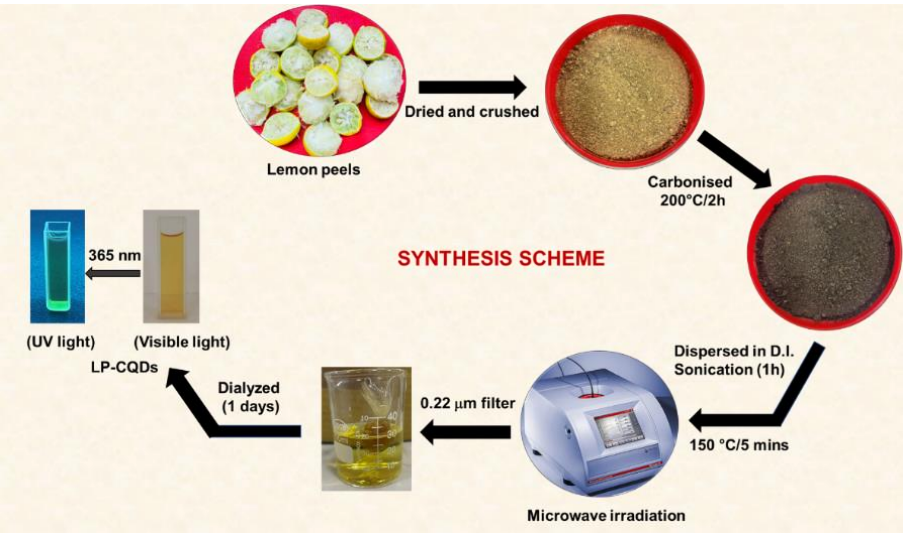

Scheme 5.1. Fabrication of LP-CQDs from *Citrus limon* peels.

5.2.3 Characterizations

The UV-Visible absorption spectrum was recorded by UV-Vis spectrophotometer instrument (Shimadzu UV 2600). Photoluminescence spectra were studied using a spectrofluorometer (Shimadzu, RF-6000) with light source i.e., xenon lamp. Time-resolved fluorescence measurements were carried by Deltaflex modular fluorescence lifetime spectrofluorometer (HORIBA Scientific) with a nano-LED pulse diode as excitation source at 340 nm. The morphology and size were observed through transmission electron microscopy (JEOL, JEM 2100 plus). Elemental composition was scrutinized using X-ray photoelectron spectroscopy (XPS) (PHI 5000 Versa Probe III). A Raman spectrometer (HORIBA LabRAM HR Evolution) with a 532 nm laser was used to assess the purity and structural defects of sample. FT-IR spectrometer (Shimadzu IRTracer-100) were used to detect functional groups within a range of 400-4000 cm^{-1} with 110 numbers of scans. Monowave-300 microwave synthesis reactor (Anton Paar, USA) was used for the synthesis process.

5.2.4 Sample Solutions Formulation

The standard solution (1mM) of different metal cations (Co^{2+}, Fe^{3+}, Zn^{2+}, Al^{3+}, Cr^{3+}, Cu^{2+}, Ni^{2+}, Hg^{2+}, Fe^{2+}) and analytes (Amoxicillin (AC), Ofloxacin (OFX), Ascorbic acid (AA), Ciprofloxacin (CPX), Tetracycline (TC), Nitrobenzene (NB), Levofloxacin (LF), Streptomycin (SPM), Chlortetracycline (CTC), Thiamethoxam (TM)) were prepared in D.I. water for the selectivity experiments of prepared LP-CQDs. 20 μL of LP-CQDs in 2 ml of D.I. water along with 0.1 mM of the analyte solution was pipetted in cuvette, and emission spectra were measured. The sensitivity was studied using stock solution of 1μM of tetracycline (TC).

5.2.5 Real Sample Analysis

To inspect the utility of developed sensing system, the study was carried out with real samples (River water). The water sample was collected from Bhakra River in Patiala. Collected sample were subjected to filtration using nylon filters before the analysis using nylon filters having pore size of 0.45 µm. Following the addition of specific concentrations of TC (spiking) to the samples, LP-CQDs were added. The fluorescence studies were carried out at 330 nm.

5.3 Results and Discussions

5.3.1 Characterizations

TEM was used to examine the morphology and size of the fabricated LP-CQDs. Figure 5.1a and 5.1b displays the nearly spherical shaped particles with monodispersity. Inset of Figure 5.1a illustrates the particle size histogram ranging from 2-7 nm, having particle size of 4.46 nm. Lattice fringes of 0.36 nm resembles the (002) graphitic plane (inset-Figure 5.1(b)).[15] Figure 5.1c depicts the XRD of LP-CQDS with a diffraction peak at 2θ=24.5°indexing to C(002) plane.[15] The d-spacing was determined by using Bragg's equation (nλ=2dsinθ) which is consistent with the HRTEM results.

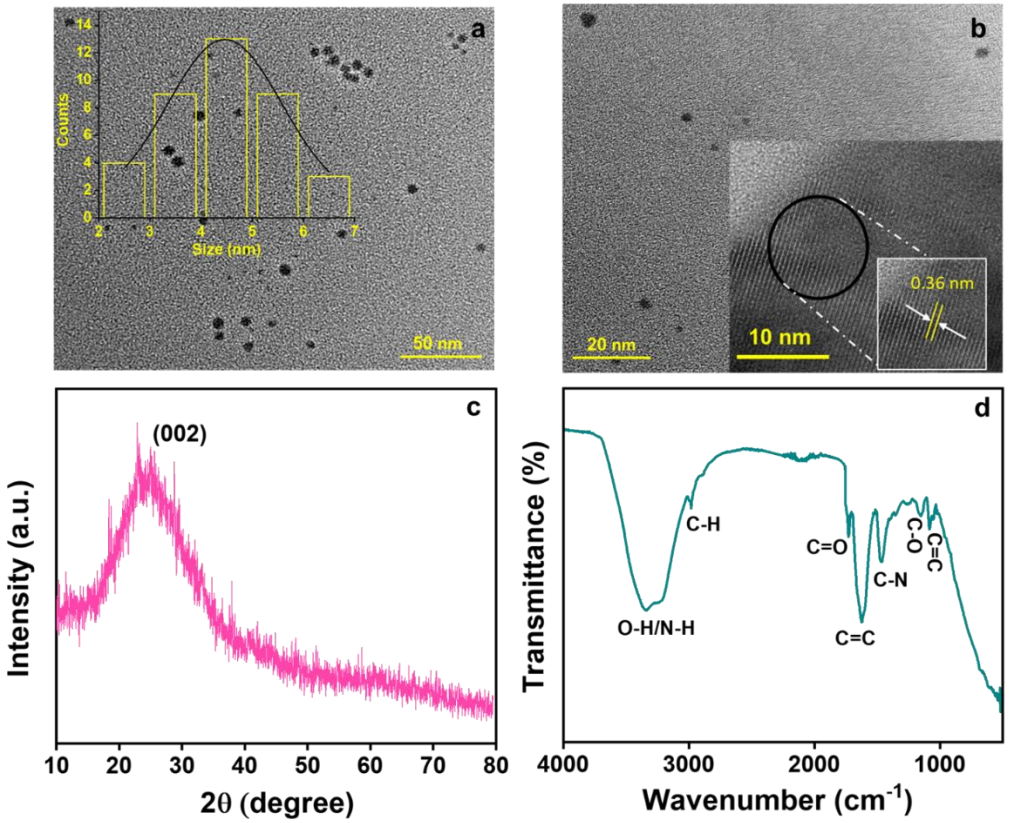

Figure 5.1. (a) TEM image of LP-CQDs with inset representing size distribution histogram, (b) TEM image with inset showing lattice spacing, (c) XRD spectrum, and (d) FT-IR spectra of LP-CQDs.

The FT-IR spectra shown in Figure 5.1d showed the broad peak at 3200-3400 cm^{-1}, which corresponds to O-H/N-H stretching vibrations. Minor band appears at 2976 cm^{-1} signifying C-H stretching vibration, signals at 1732 cm^{-1} and 1626 cm^{-1} attributed to C=O and C=C stretching vibrations, respectively. Signals at 1467 cm^{-1} resembles to C-N stretching. Peaks at 1266 and 1159 cm^{-1} confirms the C-O stretching. Peak at 1088 cm^{-1} attributed to C=C bending vibrations.[16] The occurrence of the hydrophilic functionalities on LP-CQDs as obtained from FT-IR analysis, signifying the reason of excellent water solubility.[14]

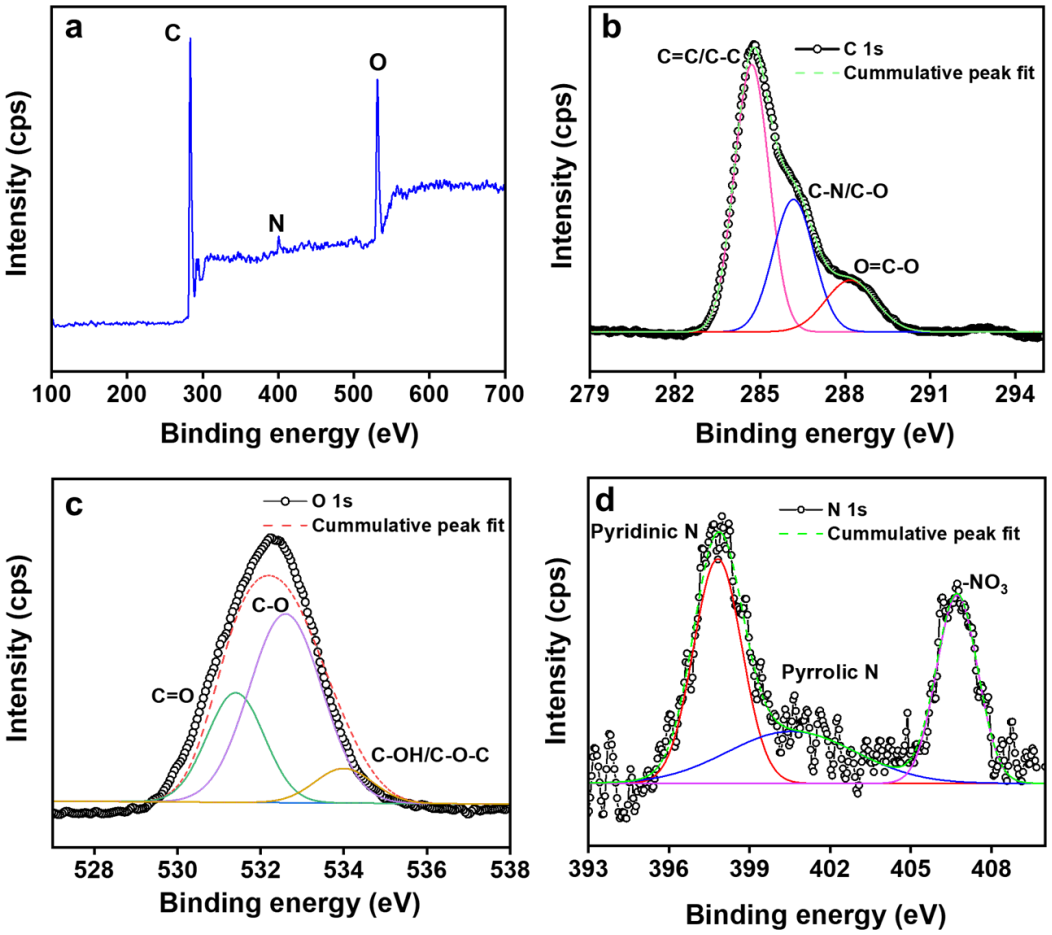

Figure 5.2. (a) Survey graph of LP-CQDs, High resolution spectrum of (b) C 1s, (c) O 1s, and (d) N1s of LP-CQDs.

An XPS analysis was conducted to determine the surface composition and oxidation states of LP-CQDs. Survey spectrum (Figure 5.2a) showed the peaks at 284.5 eV, 400.1 eV, and 532.2 eV allocated to C (78.96%), N (5.67%), and O (15.37%), respectively.[17] C1s (Figure 5.2b) high resolution spectra showed three peaks at 284.7, 286.2, and 288.2 eV ascribed to C-C/C=C, C-O/C-N, and C=O/C=N groups, respectively. O1s spectra exhibited peaks at 531.3, 532.6, and 534.0 eV conforming to C=O, C-O, and C-OH/C-O-C, respectively (Figure 5.2(c)).[14] N 1s spectra (Figure 5.2d) showed peaks at 397.8 eV and 400.3 eV corresponds to

Pyridinic and Pyrrolic N.[18] While, strong peak was seen at 406.8 which is due to existence of -NO_3.[19] The occurrence of these functional group indicates the hydrophilicity on LP-CQDs surface which aligns with FTIR results.

Raman Spectra (Figure 5.3a) of LP-CQDs displayed two broad peaks at 1368 cm^{-1} and 1574 cm^{-1} representing D (sp^3 hybridised disordered D) and G (sp^2 hybridised graphitic G) bands, respectively with I_D/I_G band intensity of 0.86.[14] The observed I_D/I_G ratio is less than one, signifying the well graphitized carbon components.[14] Raman results confirmed the existence of both sp^2 carbon (G) with defective sp^3 carbons (D) within LP-CQDs.[2]

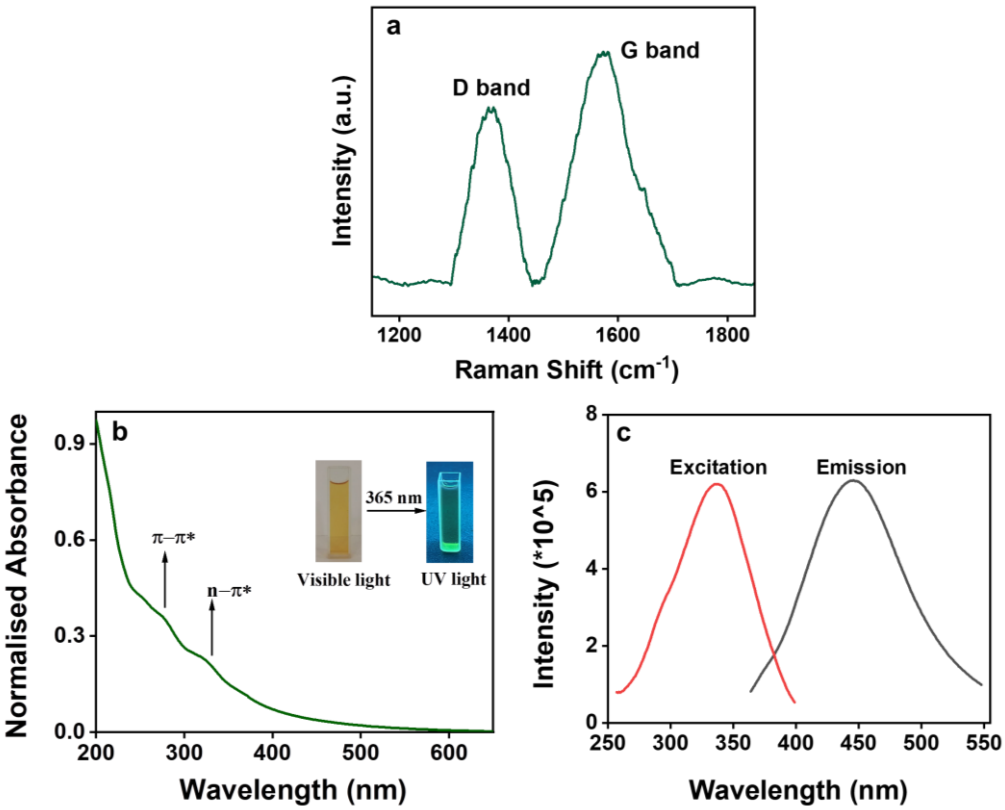

Figure 5.3. (a) Raman spectrum of LP-CQDs, (b) UV-Vis absorption spectra with inset showing LP-CQDs in UV and Visible light, and (c) excitation and emission spectra of LP-CQDs.

5.3.2 Optical Studies of LP-CQDs

UV-Vis absorption spectra were employed, in conjunction with fluorescence emission spectra, to investigate the optical properties. Figure 5.3b shows a shoulder band at around 272 nm and 320 nm, which are assigned to π-π* transitions of sp^2 C=C bonds and n- π* transitions of C=O of LP-CQDs.[20] The LP-CQDs emits a strong emissive green fluorescence upon UV light irradiation (365 nm) while, light brown under visible light as depicted in inset of Figure 3b. This fluorescence emission of LP-CQDs is believed to be a result of radiative

recombination between holes and electrons, which occurs due to photoinduced charge separation and surface sites trapping.[21] By employing equation 1.1, the fluorescence quantum yield of LP-CQDs was 49.5%. For studying fluorescence behaviour, the excitation and emission spectra were recorded as illustrated in Figure 5.3c. Upon excitation of 330 nm, LP-CQDs showed the maximum PL emission intensity at 445 nm.

The fluorescence emission spectra at different excitations wavelengths were studied as shown in Figure 5.4a. Bathochromic shift was observed in the emission wavelengths from 400-498 nm upon changing the λ_{ex}. The excitation-dependent emission observed in LP-CQDs can be attributed to factors, like the quantum confinement effect, presence of sp^2 aromatic domains, surface edge defects, and variations in size. These factors influence the fluorescence excitation energy.[22]

5.3.3 Stability Studies

Assessing the stability of LP-CQDs is a crucial factor to consider before proceeding with further sensing applications.

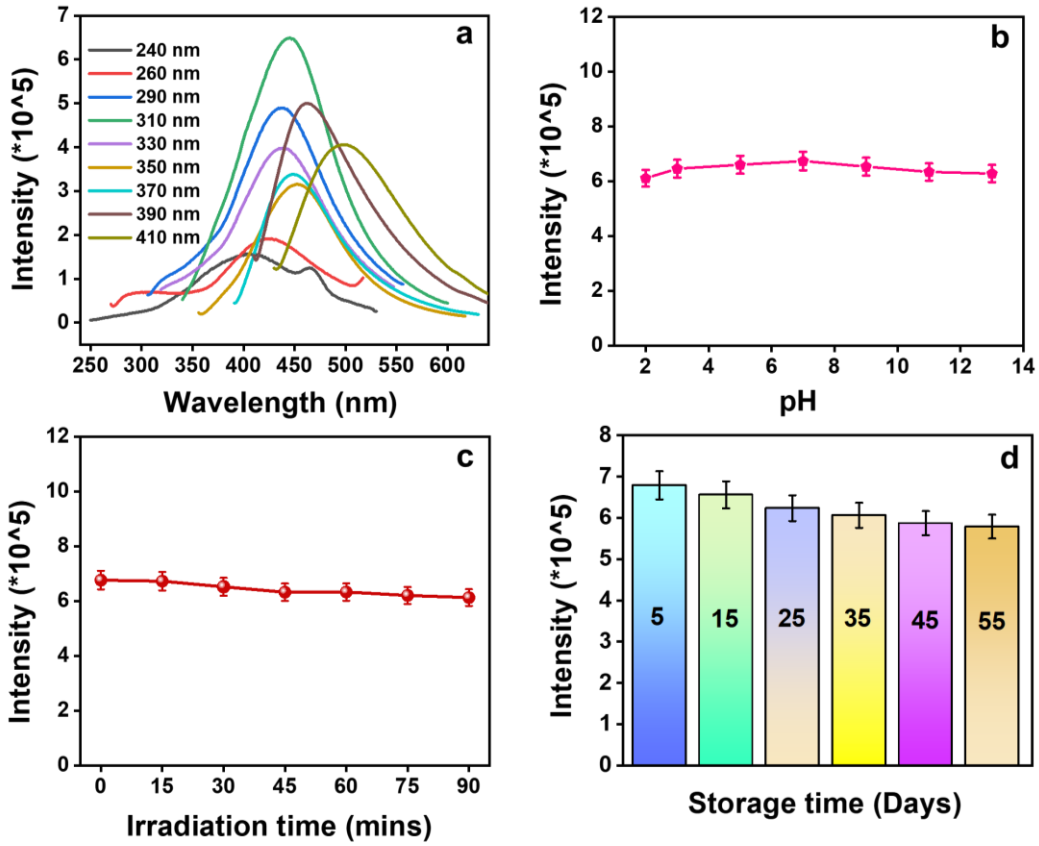

Figure 5.4. (a) PL emission spectra of LP-CQDs under various excitation wavelengths, (b) influence of pH (2-13) on PL emission behavior of LP-CQDs, (c) impact of irradiation time (in mins), and (d) effect of storage time (in days) on the fluorescence emission of LP-CQDs.

Influence of pH, storage days, irradiation time were studied on the PL intensity of LP-CQDs. Figure 5.4b shows that the slight increase in PL intensity as pH varied from 2-7. While, small decrease in PL intensity was seen as pH value shifts towards 13. Variation in PL intensity of LP-CQDs occurred as a result of protonation and deprotonation of emissive sites on the carbon quantum dot surface.[23,24] The maximum fluorescence intensity was seen at neutral pH and further studies were performed at pH 7 of LP-CQDs. To evaluate the photostability, LP-CQDs were irradiated with Xe-arc lamp up to 90 mins and no noticeable change in intensity was observed (Figure 5.4(c)). Additionally, LP-CQDs were subjected to storage period of 55 days and PL spectra were periodically measured. These PL emission spectra showed minimal change in intensity throughout the duration (Figure 5.4(d)). These studies confirm the remarkable stability of LP-CQDs.

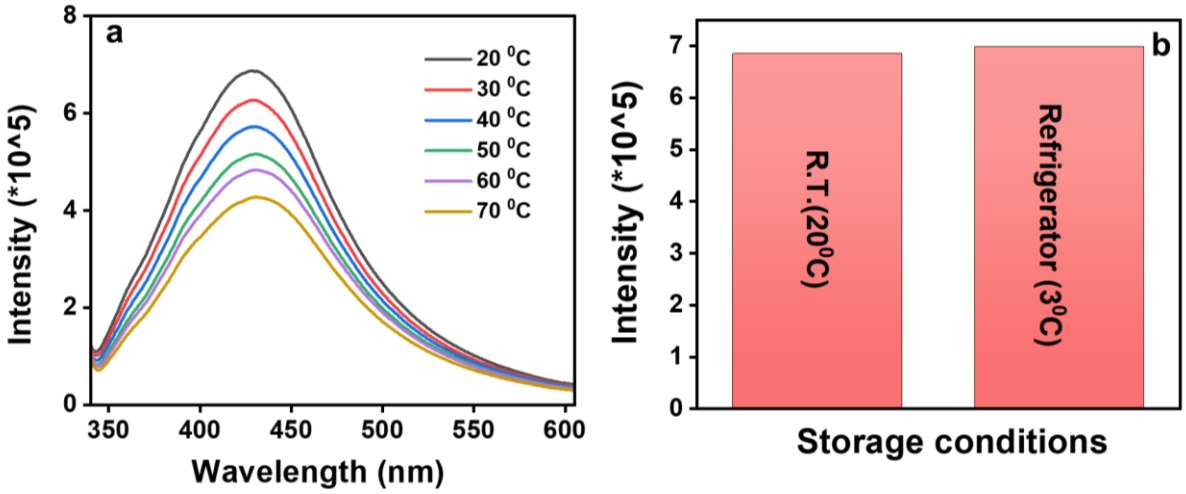

Figure 5.5. (a) Effect of temperature and (b) storage conditions on stability of LP-CQDs.

The temperature dependence (20-70°C) of the fluorescence spectrum of LP-CQDs at 330 nm excitation is shown in Figure 5.5(a). The PL intensity of the synthesized LP-CQDs decreases with increase in temperature as the stability of complex decreased.[25] This may be attributed to the reason that the non-radiative decay rate increases as the temperature increase which led to a decrease in quantum efficiency along with the PL intensity.[26] Also, synthesized LP-CQDs were stored at room temperature (20°C) and in refrigerator (3°C) to check the fluorescence stability and no significant difference in intensity was seen confirming the stability of LP-CQDs (Figure 5.5 (b)).

5.3.4 Method Validation

The method developed was validated following the guidelines specified in ICHQ2(R1) to ensure its reliability and accuracy.[27]

5.3.4.1 Linearity and Range

In order to assess the sensitivity of the prepared sensor, effect of different concentrations of TC (nM) on the PL intensity of LP-CQDs was examined. Figure 5.6a illustrates the gradual quenching of fluorescence intensity of LP-CQDs when exposed to different concentrations of TC. The quenching efficiency was evaluated by plotting the graph of F_0/F vs. quencher [Q] concentration, following the principles of the Stern-Volmer equation 1.7. Figure 5.6b illustrates a linear correlation among values of F_0/F and the concentrations of TC ranging from 0 to 345 nM through a linear regression equation:

$$F_0/F = 0.0066\,[TC] + 0.835 \qquad (R^2 = 0.992) \qquad (5.1)$$

The values of the correlation coefficient (R^2) approaching unity in Table 5.1 indicate the satisfactory linearity of the system.

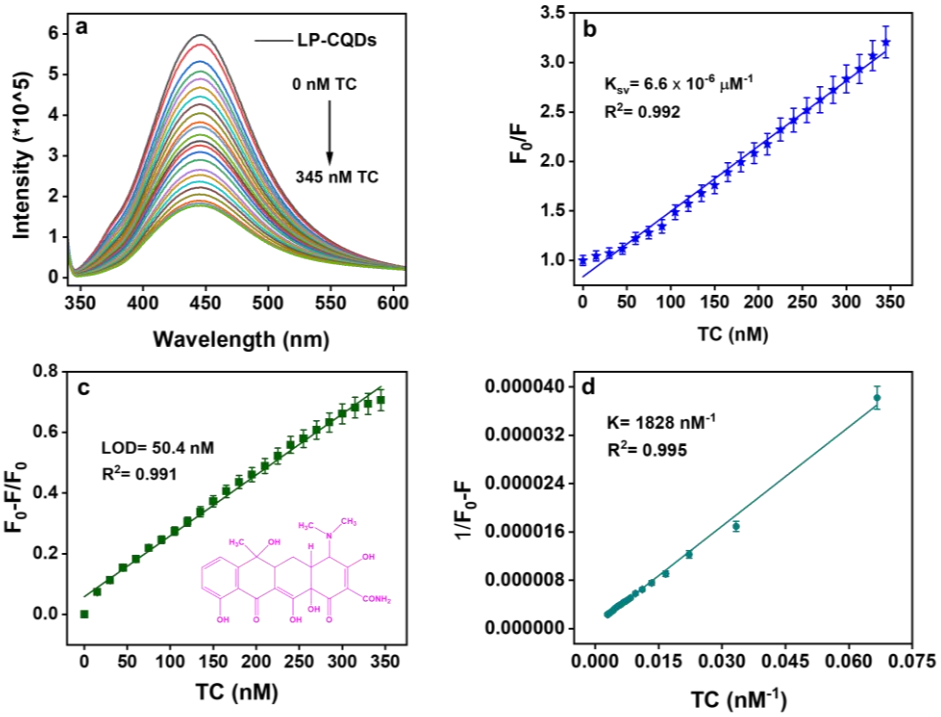

Figure 5.6. (a) Change in fluorescence intensity of LP-CQDs with the change in concentrations of TC, (b) Stern-Volmer plot of LP-CQDs, (c) linear relation between fluorescence response (F_0-F/F_0) and different concentrations of TC with inset image showing TC structure, and (d) B-H plot of TC with LP-CQDs.

5.3.4.2 Limit of Detection (LOD) and Limit of Quantification (LOQ)

The detection limit for TC can be computed using 3σ/K while, limit of quantification using 10σ/K (Table 5.1), where σ denote standard deviation (intercept) and K signifies the slope of linear line. The detection limit calculated from Figure 5.6c was 50.4 nM (Table 5.1).

The LOQ value comes out to be 168.1 nM. Table 5.2 demonstrates that the fabricated sensor demonstrates high sensitivity towards TC and boasts a lower detection limit when compared to other sensor systems documented in literature.

Table 5.1. Methodical sensing performance of developed sensor for TC.

Parameters	**TC**
Linearity range (nM)	0-345
Limit of Detection[a] (nM)	50.4
Limit of Quantification[b] (nM)	168.1
Regression equation	$F_0/F = 0.0066$ [TC] + 0.835
Correlation coefficient	0.992
Binding Efficacy (nM^{-1})	1828

[a]LOD =3σ/K, [b]LOQ =10σ/K, σ denotes intercept's standard deviation, K tells slope

Table 5.2. Comparison of CQDs as nanosensors for TC detection.

Sr. No.	**Sensory systems**	**Linear range**	**Detection limit**	**Ref.**
1	N-CQDs	0–100 μM	0.344 μM	6
2	CDs	10–400 μM	6.0 μM	28
3	Self-N-doped CQDs	0.158-40 μM	158 nM	29
4	CQDs	1.0-60 $\mu molL^{-1}$	0.17$\mu molL^{-1}$	30
5	N-GQDs	0-60 μM	0.21$\mu molL^{-1}$	31
6	S, N-CDs	0-60 μM	0.25 μM	32
7	S, N-CQDs	1.88–60 $\mu molL^{-1}$	0.56 $\mu molL^{-1}$	11
8	N-CQDs	0-600 nM	60 nM	14
9	LP-CQDs	0-345 nM	50.4 nM	Present work

5.3.4.3 Binding Efficiency

A 1:1 linear Benesi-Hildebrand (B-H) equation 1.8 was used to predict the excited-state binding constant in order to assess the binding interaction amid LP-CQDs and TC. Graph among ($1/F_0$-F) versus 1/[Q] shows linear line with binding constant, K = 1828 nM^{-1} and R^2 = 0.995 (Figure 5.6d, Table 5.1).

5.3.4.4 Precision Analysis

Three different concentrations and three replicas of each concentration were used in an experiment to determine the intra-day and inter-day precisions. The %RSD value, which was below 2%, indicates that the method exhibits acceptable precision (Table 5.3).

Table 5.3. Intraday and Inter day precision data for estimating TC by the developed sensor.

Analyte	Conc. taken (nM)	Intra Day[a]			Inter Day[b]		
		Conc. found ± S.D. (nM)	%RSD	%Error[c]	Conc. found ± S.D. (nM)	%RSD	%Error[c]
TC	100	99.73 ± 0.37	0.75	0.43	99.21 ±0.52	1.05	0.61
	200	201.43 ±0.61	0.60	0.35	200.76 ±0.64	0.63	0.36
	300	302.13 ±0.51	0.33	0.19	302.76 ±0.68	0.45	0.26

Each result is the average of three separate determinations.
[a]Within a day [b]Three consecutive days [c]%Error=%RSD/√n

5.3.5 Sensing of Tetracycline by LP-CQDs

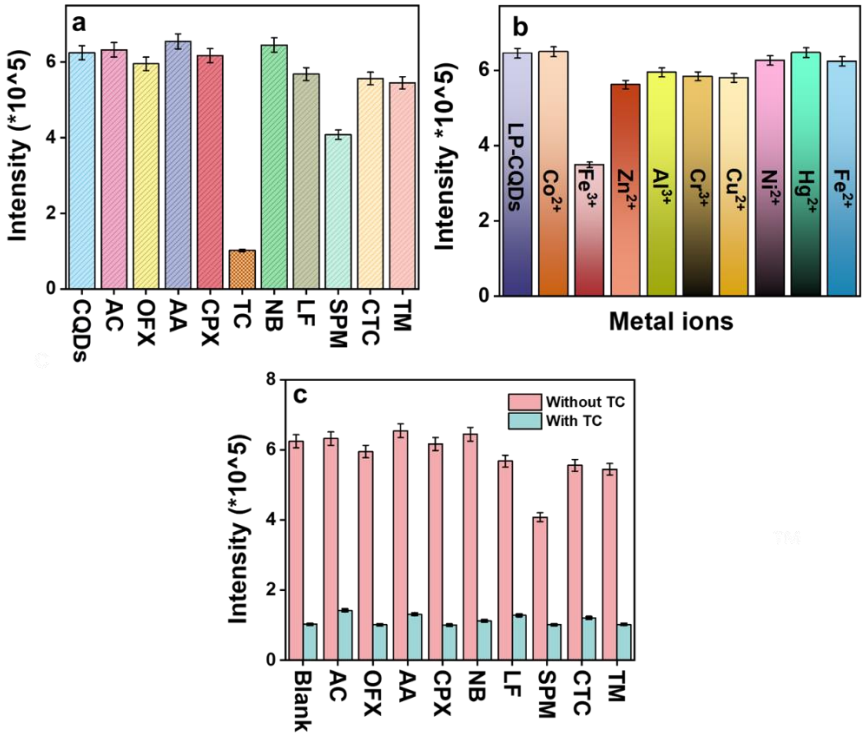

Figure 5.7. (a) Selectivity studies of LP-CQDs towards different analytes, (b) selectivity studies of LP-CQDs with different metal ions, and (c) Interreference study with and without TC with diverse analytes.

While developing a potent sensor, it is crucial to thoroughly investigate the parameter of selectivity. The variation in PL intensity of the LP-CQDs with 200 µL of the stock solution (1 mM) with different analytes was examined. It is clearly observed from Figure 5.7a that the maximum fluorescence intensity of LP-CQDs got reduced in presence of TC. However, streptomycin (SPM) showed some quenching in intensity of LP-CQDs possibly due to hydrogen bond formation with surface groups of LP-CQDs but very less as compared to tetracycline.[33] Fe^{3+} showed little quenching with LP-CQDs which may be due to coordination complex formation (Figure 5.7(b)).[34] Nevertheless, as shown by the interference investigations, none of these compounds significantly interfere with the detection of tetracycline (Figure 5.7c).

The selectivity was also studied under UV light illumination and it was seen that LP-CQDs has high selectivity for TC (Figure 5.8). The reason of high selectivity towards TC can be attributed that TC reacts with carboxyl and hydroxyl groups present on LP-CQDs surface, leading to quenching.[20]

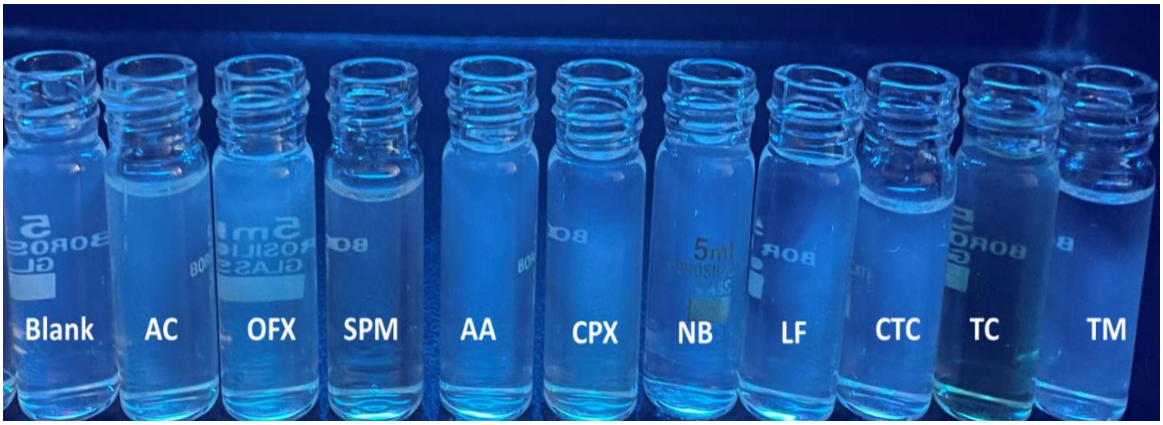

Figure 5.8. Selectivity photographs of LP-CQDs containing different analytes in UV light irradiation.

Under optimal conditions, a range of tetracycline concentrations (0-345 nM) were added to determine the linear dynamic range and sensitivity of LP-CQDs towards TC. As shown in Figure 5.6a, the intensity of LP-CQDs gradually decreased with an incremental rise in TC concentrations. Figure 5.6b showed the linear response of F_0/F with TC concentrations by regression equation (F_0/F = 0.0066 [TC] + 0.835) having 0.992 correlation coefficient. Detection limit was calculated to be 50.4 nM (Figure 5.6(c)) within the linear range of 0-345 nM, which is significantly lower than the sensitivity parameters reported in earlier studies (Table 5.2). The LOQ was calculated to be 168.1 nM. Binding efficiency plot between ($1/F_0$-F) vs. 1/[Q] shows linear line with K = 1828 nM^{-1}, R^2 = 0.995 (Figure 5.6(d)). Based on the results, the developed sensor offers rapid and facile detection of TC.

5.3.6 Quenching Mechanism

The fluorescence intensity of LP-CQDs got quenched (76.1%) in presence of TC. The underlying process of the plausible quenching mechanism was investigated through a number of experiments. Commonly, fluorescence quenching can be attributed to five main mechanisms, namely the inner filter effect (IFE), dynamic quenching, static quenching, photo-induced electron transfer (PET), and Forster energy resonance transfer (FRET).[35] Firstly, optical properties of LP-CQDs and TC was studied to investigate the possibility of IFE.

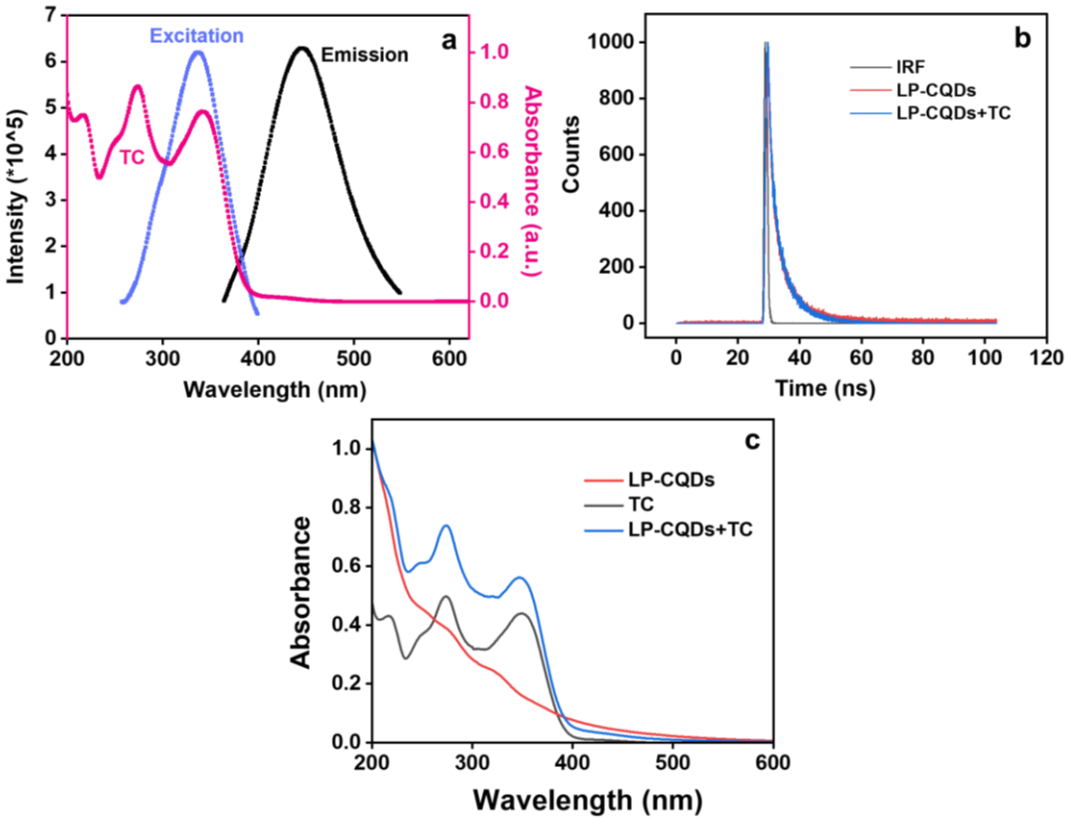

Figure 5.9. (a) Overlapping of absorption spectra of TC with excitation spectra of LP-CQDs, (b) Lifetime decay curves of LP-CQDs and LP-CQDs+ TC, and (c) UV-Vis absorption spectra of LP-CQDs, TC, and LP-CQDs+ TC.

Figure 5.9a exhibits the excitation and emission spectra of LP-CQDs along with the absorption spectra of TC. Here, the TC had a strong absorption peak at 274 nm and 341 nm which overlaps with the excitation spectra of LP-CQDs. The phenomenon referred to as the Inner Filter Effect occurs when there is an overlap between the absorption band of the absorber with the excitation/emission band of the fluorophore.[36] Hence, the fluorescence quenching is attributed to IFE. As a result, TCs would absorb the probe's excitation light, lowering its fluorescence intensity without affecting its lifetime.[37] Moreover, the fluorescence studies of

LP-CQDs with and without TC were performed to validate the quenching mechanism. Average lifetime value of LP-CQDs was 2.09 ns and 2.03 ns with the addition of TC, showing minimal change in the values of average lifetime (Figure 5.9b, Table 5.4) signifies negligible electron transfer between LP-CQDs and TC, thus the mechanism was attributed to the inner filter effect (Scheme 5.2).[38,39] Further, the mechanism was confirmed by UV-Vis spectrum of LP-CQDs, TC, and LP-CQDs +TC. Figure 5.9c shows the strengthening of absorption peak in presence of TC with no change in peak positions signifying that no new substance was formed from LP-CQDs and TC.[5]

Table 5.4. Fluorescence lifetime parameters of LP-CQDs in presence of TC.

System	τ_1 (ns)	a_1	τ_2 (ns)	a_2	τ_3 (ns)	a_3	#<τ_{av}>(ns)	χ^2
LP-CQDs	2.92	0.32	5.61	0.15	0.62	0.53	2.09	0.94
LP-CQDs + TC	1.97	0.28	5.89	0.22	0.38	0.50	2.03	0.93

<τ_{av}>(ns)= $\tau_1a_1+\tau_2a_2+\tau_3a_3$

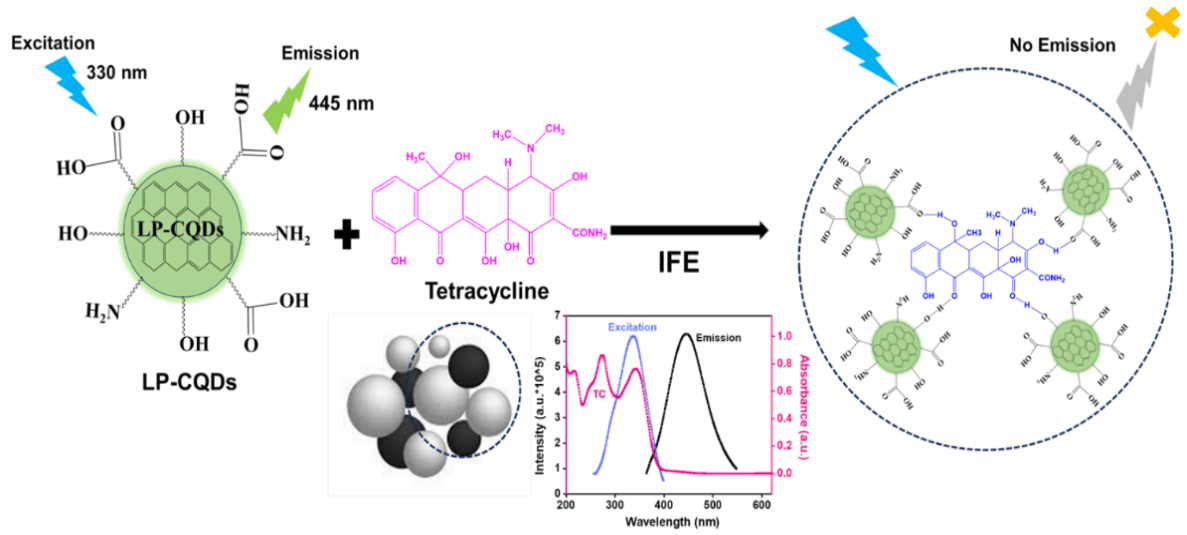

Scheme 5.2. Plausible mechanism of TC sensing.

5.3.7 Real Sample Analysis

To study the feasibility of the developed method, detection of TC in real samples was done. River water was collected from Bhakra River (Patiala) and tetracycline tablet (Abbott) was purchased from local market. Standard addition method was followed for the analysis. Table 5.5 represents the workability of LP-CQDs towards sensing of TC in river water and tablet dosage. The data indicated a favourable percentage of recovery and a relative standard deviation (%RSD). The measured values demonstrated satisfactory precision, affirming the suitability of the prepared LP-CQDs for effective detection of TC in real samples.

Table 5.5. Application of the fabricated sensor for TC detection in real samples.

Samples	Spiked (μM)	Found (μM)	Recovery (%)	RSD (%)
River water	0.5	0.48	96.60	1.26
	1	1.02	98.03	1.29
	1.5	1.48	98.66	1.78
TC supplement	0.5	0.47	94.80	1.46
	1	1.03	103	1.47
	1.5	1.49	99.53	1.39

5.3.8 Application of the Synthesized LP-CQDs as Fluorescent Ink

The green synthesis of LP-CQDs from *Citrus limon* peels exhibits intrinsic fluorescence and excellent aqueous stability, indicating potential for utilization in paper-based devices and fluorescent ink. The solution of LP-CQDs was used to write the fluorescent characters (handwritten words and images) as shown in Figure 5.10(a-b) without the requirement of any sample pre-treatment. Also, paper-based fluorescence strip was made using Whatman filter paper. It shows highly green luminescence under UV light irradiation (Figure 5.10(c)). The disappearance of green fluorescence was seen in presence of TC (Figure 5.10d) making it more reliable.

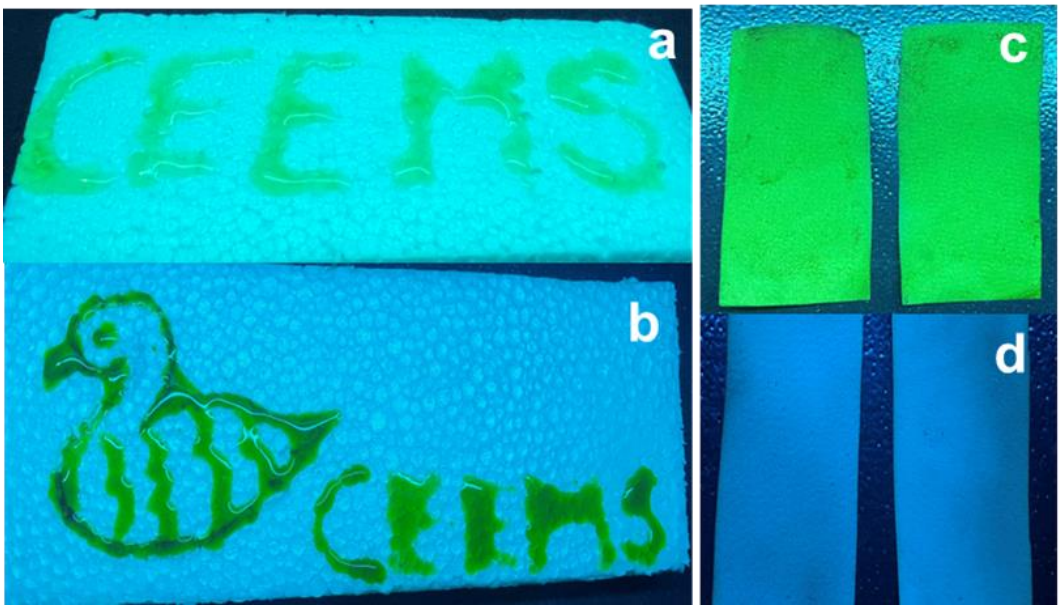

Figure 5.10. Photographs of LP-CQDs in fluorescent characters of handwritten (a) words and (b) images, (c) paper-based fluorescent strip of LP-CQDs, and (d) LP-CQDs in presence of TC.

Conclusions

The present study employed a cost-efficacious and environmentally friendly method to produce highly water-soluble fluorescent carbon quantum dots from lemon peel. Microwave irradiation was utilized without the addition of chemical substituents in the synthesis process. Intrinsic nitrogen-functionalized CQDs have been obtained without use of any dopants. Average particle size of fabricated LP-CQDs was 4.46 nm. LP-CQDs yielded a remarkable quantum yield of 49.5%, which displayed excellent photostability, storage time, storage condition, temperature, and pH stability. The prepared LP-CQDs emits green luminescence exhibiting excitation dependent emission ranging from 240-410 nm. LP-CQDs acts as nanosensor for the highly sensitive and selective detection of TC with 76.1% quenching with 50.4 nM detection limit in the concentration range of 0-345 nM. The fluorescence quenching was accredited to IFE. Validation of the prepared sensor was conducted following the recommendations outlined by ICH. Furthermore, the developed method was successfully employed to detect TC in real samples, demonstrating acceptable precision and %RSD values. Also, LP-CQDs were utilized as a fluorescent ink for drawing and writing without any chemical alteration. It was further successfully used to make paper-based fluorescence strip. The present method and detection strategy offers affordable, convenient, and sustainable approach for the detection of TC in diverse applications.

References

(1) Sudha, P. N.; Sangeetha, K.; Vijayalakshmi, K.; Barhoum, A. Nanomaterials History, Classification, Unique Properties, Production and Market. In *Emerging applications of nanoparticles and architecture nanostructures*; Elsevier, **2018**, *32*, 341–384. https://doi.org/10.1016/B978-0-323-51254-1.00012-9.

(2) Kundu, A.; Maity, B.; Basu, S. Rice Husk-Derived Carbon Quantum Dots-Based Dual-Mode Nanoprobe for Selective and Sensitive Detection of Fe^{3+} and Fluoroquinolones. *ACS Biomater. Sci. Eng.* **2022**, *8,* 4764-4776. https://doi.org/10.1021/acsbiomaterials.2c00798.

(3) Chatzimitakos, T.; Kasouni, A.; Sygellou, L.; Avgeropoulos, A.; Troganis, A.; Stalikas, C. Two of a Kind but Different: Luminescent Carbon Quantum Dots from Citrus Peels for Iron and Tartrazine Sensing and Cell Imaging. *Talanta* **2017**, *175*, 305–312. https://doi.org/10.1016/j.talanta.2017.07.053.

(4) Tyagi, A.; Tripathi, K. M.; Singh, N.; Choudhary, S.; Gupta, R. K. Green Synthesis of Carbon Quantum Dots from Lemon Peel Waste: Applications in Sensing and Photocatalysis. *RSC Adv.* **2016**, *6*, 72423–72432. https://doi.org/10.1039/c6ra10488f.

(5) Qi, H.; Huang, D.; Jing, J.; Ran, M.; Jing, T.; Zhao, M.; Zhang, C.; Sun, X.; Sami, R.; Benajiba, N. Transforming Waste into Value: Pomelo-Peel-Based Nitrogen-Doped Carbon Dots for the Highly Selective Detection of Tetracycline. *RSC Adv.* **2022**, *12*, 7574–7583. https://doi.org/10.1039/D2RA00134A.

(6) Wang, C.; Sun, Q.; Yang, M.; Liu, E.; Xue, W.; Fan, J. Preparation of Highly Luminescent Nitrogen-Doped Carbon Quantum Dots and Their Detection of Tetracycline Antibiotics. *Colloids Surfaces A Physicochem. Eng. Asp.* **2022**, *653*, 129982. https://doi.org/10.1016/j.colsurfa.2022.129982.

(7) Zhao, W.; Zuo, H.; Guo, Y.; Liu, K.; Wang, S.; He, L.; Jiang, X.; Xiang, G.; Zhang, S. Porous Covalent Triazine-Terphenyl Polymer as Hydrophilic–Lipophilic Balanced Sorbent for Solid Phase Extraction of Tetracyclines in Animal Derived Foods. *Talanta* **2019**, *201*, 426–432. https://doi.org/10.1016/j.talanta.2019.04.010.

(8) Kundu, A.; Maity, B.; Basu, S. Coal-Derived Graphene Quantum Dots with a Mn^{2+}/Mn^{7+} Nanosensor for Selective Detection of Glutathione by a Fluorescence Switch-off-on Assay. *New J. Chem.* **2022**, *46*, 7545–7556. https://doi.org/10.1039/d2nj00220e.

(9) Sohal, N.; Maity, B.; Basu, S. Morphology-Dependent Performance of MnO_2 Nanostructure-Carbon Dot-Based Biosensors for the Detection of Glutathione. *ACS Appl. Bio Mater.* **2021**, *4*, 5158–5168. https://doi.org/10.1021/acsabm.1c00353.

(10) Liu, M. L.; Chen, B. Bin; Yang, T.; Wang, J.; Liu, X. D.; Huang, C. Z. One-Pot Carbonization Synthesis of Europium-Doped Carbon Quantum Dots for Highly Selective Detection of Tetracycline. *Methods Appl. Fluoresc.* **2017**, *5*, 15003. https://doi.org/10.1088/2050-6120/aa5e2b.

(11) Fan, Y.; Qiao, W.; Long, W.; Chen, H.; Fu, H.; Zhou, C.; She, Y. Detection of Tetracycline Antibiotics Using Fluorescent "Turn-off" Sensor Based on S, N-Doped Carbon Quantum Dots. *Spectrochim. Acta Part A Mol. Biomol. Spectrosc.* **2022**, *274*, 121033. https://doi.org/10.1016/j.saa.2022.121033.

(12) Qi, H.; Teng, M.; Liu, M.; Liu, S.; Li, J.; Yu, H.; Teng, C.; Huang, Z.; Liu, H.; Shao, Q.; Umar, A.; Ding, T.; Gao, Q.; Guo, Z. Biomass-Derived Nitrogen-Doped Carbon Quantum Dots: Highly Selective Fluorescent Probe for Detecting Fe^{3+} Ions and Tetracyclines. *J. Colloid Interface Sci.* **2019**, *539*, 332–341. https://doi.org/10.1016/j.jcis.2018.12.047.

(13) Zhang, Z.; Fan, Z. Application of Cerium–Nitrogen Co-Doped Carbon Quantum Dots to the Detection of Tetracyclines Residues and Bioimaging. *Microchem. J.* **2021**, *165*, 106139. https://doi.org/10.1016/j.microc.2021.106139.

(14) John, B. K.; John, N.; Korah, B. K.; Thara, C.; Abraham, T.; Mathew, B. Nitrogen-

Doped Carbon Quantum Dots as a Highly Selective Fluorescent and Electrochemical Sensor for Tetracycline. *J. Photochem. Photobiol. A Chem.* **2022**, *432*, 114060. https://doi.org/10.1016/j.jphotochem.2022.114060.

(15) Atchudan, R.; Edison, T. N. J. I.; Perumal, S.; Lee, Y. R. Green Synthesis of Nitrogen-Doped Graphitic Carbon Sheets with Use of Prunus Persica for Supercapacitor Applications. *Appl. Surf. Sci.* **2017**, *393*, 276–286. https://doi.org/10.1016/j.apsusc.2016.10.030.

(16) Wang, J.; An, J.; Zhang, Z.; Zhu, H.; Liang, X.; Yang, S.; Sheng, K.; Chen, L.; Lu, H.; Wang, Y. High Fluorescent Nitrogen− Doped Carbon Dots Derived from Sanghuangporus Lonicericola for Detecting Tetracyclines in Aquaculture Water and Rat Serum Samples. *Microchem. J.* **2023**, *189*, 108517. https://doi.org/10.1016/j.jphotochem.2022.114060.

(17) Kundu, A.; Maity, B.; Basu, S. Orange Pomace-Derived Fluorescent Carbon Quantum Dots: Detection of Dual Analytes in the Nanomolar Range. *ACS Omega* **2023**, *8*, 22178–22189. https://doi.org/10.1021/acsomega.3c02474.

(18) Yang, F.; Bao, W.; Liu, T.; Zhang, B.; Huang, S.; Yang, W.; Li, Y.; Li, N.; Wang, C.; Pan, C.; Li, Y. Nitrogen-Doped Graphene Quantum Dots Prepared by Electrolysis of Nitrogen-Doped Nanomesh Graphene for the Fluorometric Determination of Ferric Ions. *Microchim. Acta* **2020**, *187*, 1–10. https://doi.org/10.1007/s00604-020-04294-8.

(19) Wang, C.; Pan, C.; Wei, Z.; Liu, J.; Song, Z.; Ma, W.; Wang, M.; Mao, L. One-Step Synthesis of Nitrogen-Doped Multi-Emission Carbon Dots and Their Fluorescent Sensing in HClO and Cellular Imaging. *Microchim. Acta* **2021**, *188*, 1–11. https://doi.org/10.1007/s00604-021-04973-0.

(20) Liang, Y.-M.; Yang, H.; Zhou, B.; Chen, Y.; Yang, M.; Wei, K.-S.; Yan, X.-F.; Kang, C. Waste Tobacco Leaves Derived Carbon Dots for Tetracycline Detection: Improving Quantitative Accuracy with the Aid of Chemometric Model. *Anal. Chim. Acta* **2022**, *1191*, 339269. https://doi.org/10.1016/j.aca.2021.339269.

(21) Ding, H.; Yu, S. B.; Wei, J. S.; Xiong, H. M. Full-Color Light-Emitting Carbon Dots with a Surface-State-Controlled Luminescence Mechanism. *ACS Nano* **2016**, *10*, 484–491. https://doi.org/10.1021/acsnano.5b05406.

(22) Gan, Z.; Xu, H.; Hao, Y. Mechanism for Excitation-Dependent Photoluminescence from Graphene Quantum Dots and Other Graphene Oxide Derivates: Consensus, Debates and Challenges. *Nanoscale* **2016**, *8*, 7794–7807. https://doi.org/10.1039/c6nr00605a.

(23) Kurniawan, D.; Chiang, W.-H. Microplasma-Enabled Colloidal Nitrogen-Doped Graphene Quantum Dots for Broad-Range Fluorescent PH Sensors. *Carbon N. Y.* **2020**, *167*, 675–684. https://doi.org/10.1016/j.carbon.2020.05.085.

(24) Sohal, N.; Bhatia, S. K.; Basu, S.; Maity, B. Nanomolar Level Detection of Metal Ions by Improving the Monodispersity and Stability of Nitrogen-Doped Graphene Quantum Dots. *New J. Chem.* **2021**, *45*, 19941–19949. https://doi.org/10.1039/D1NJ04551B.

(25) Zhang, J.; Na, L.; Jiang, Y.; Lou, D.; Jin, L. Graphene Quantum Dots as a Fluorescence-Quenching Probe for Quantitative Analysis of Ponceau 4R Solution. *Anal. Methods* **2016**, *8*, 7242–7246. https://doi.org/10.1039/C6AY02203K.

(26) Li, C.; Yue, Y. Fluorescence Spectroscopy of Graphene Quantum Dots: Temperature Effect at Different Excitation Wavelengths. *Nanotechnology* **2014**, *25*, 435703. https://doi.org/10.1088/0957-4484/25/43/435703.

(27) Guideline, I. C. H. H. T. Validation of Analytical Procedures: Text and Methodology. *Q2* **2005**, *1*, 5.

(28) Yan, Y.; Liu, J. H.; Li, R. S.; Li, Y. F.; Huang, C. Z.; Zhen, S. J. Carbon Dots Synthesized at Room Temperature for Detection of Tetracycline Hydrochloride. *Anal. Chim. Acta* **2019**, *1063*, 144–151. https://doi.org/10.1016/j.aca.2019.02.047.

(29) Zhou, R.; Chen, C.; Hu, J.; Liao, X.; Hu, H.; Tong, Z.; Liang, J.; Huang, F. The Self-Nitrogen-Doped Carbon Quantum Dots Derived from Morus Alba L. Leaves for the Rapid Determination of Tetracycline. *Ind. Crops Prod.* **2022**, *188*, 115705. https://doi.org/10.1016/j.indcrop.2022.115705.

(30) Wei, X.; Lv, L.; Zhang, Z.; Guan, W. Preparation of Molecularly Imprinted Fluorescence Sensor Based on Carbon Quantum Dots via Precipitation Polymerization for Fluorescence Detection of Tetracycline. *J. Appl. Polym. Sci.* **2020**, *137*, 49126. https://doi.org/10.1002/app.49126.

(31) Yang, Y.; Liu, Z.; Chen, D.; Gu, B.; Gao, B.; Wang, Z.; Guo, Q.; Wang, G. Multifunctional N-Doped Graphene Quantum Dots towards Tetracycline Detection, Temperature Sensing and High-Performance WLEDs. *J. Photochem. Photobiol. A Chem.* **2021**, *405*, 112977. https://doi.org/10.1016/j.jphotochem.2020.112977.

(32) Xing, X.; Huang, L.; Zhao, S.; Xiao, J.; Lan, M. S, N-Doped Carbon Dots for Tetracyclines Sensing with a Fluorometric Spectral Response. *Microchem. J.* **2020**, *157*, 105065. https://doi.org/10.1016/j.microc.2020.105065.

(33) Shi, W.; Guo, F.; Han, M.; Yuan, S.; Guan, W.; Li, H.; Huang, H.; Liu, Y.; Kang, Z. N, S Co-Doped Carbon Dots as a Stable Bio-Imaging Probe for Detection of Intracellular Temperature and Tetracycline. *J. Mater. Chem. B* **2017**, *5*, 3293–3299. https://doi.org/10.1039/C7TB00810D.

(34) Deng, X.; Feng, Y.; Li, H.; Du, Z.; Teng, Q.; Wang, H. N-Doped Carbon Quantum

Dots as Fluorescent Probes for Highly Selective and Sensitive Detection of Fe^{3+} Ions. *Particuology* **2018**, *41*, 94–100. https://doi.org/10.1016/j.partic.2017.12.009.

(35) Zu, F.; Yan, F.; Bai, Z.; Xu, J.; Wang, Y.; Huang, Y.; Zhou, X. The Quenching of the Fluorescence of Carbon Dots: A Review on Mechanisms and Applications. *Microchim. Acta* **2017**, *184*, 1899–1914. https://doi.org/10.1007/s00604-017-2318-9.

(36) Lin, M.; Zou, H. Y.; Yang, T.; Liu, Z. X.; Liu, H.; Huang, C. Z. An Inner Filter Effect Based Sensor of Tetracycline Hydrochloride as Developed by Loading Photoluminescent Carbon Nanodots in the Electrospun Nanofibers. *Nanoscale* **2016**, *8*, 2999–3007. https://doi.org/10.1039/C5NR08177G.

(37) Zhao, C.; Jiao, Y.; Gao, Z.; Yang, Y.; Li, H. N, S Co-Doped Carbon Dots for Temperature Probe and the Detection of Tetracycline Based on the Inner Filter Effect. *J. Photochem. Photobiol. A Chem.* **2018**, *367*, 137–144. https://doi.org/10.1016/j.jphotochem.2018.08.023.

(38) Han, L.; Fan, Y. Z.; Qing, M.; Liu, S. G.; Yang, Y. Z.; Li, N. B.; Luo, H. Q. Smartphones and Test Paper-Assisted Ratiometric Fluorescent Sensors for Semi-Quantitative and Visual Assay of Tetracycline Based on the Target-Induced Synergistic Effect of Antenna Effect and Inner Filter Effect. *ACS Appl. Mater. Interfaces* **2020**, *12*, 47099–47107. https://doi.org/10.1021/acsami.0c15482.

(39) Zhang, L.; Wang, Y.; Jia, L.; Bi, N.; Bie, H.; Chen, X.; Zhang, C.; Xu, J. Ultrasensitive and Visual Detection of Tetracycline Based on Dual-Recognition Units Constructed Multicolor Fluorescent Nano-Probe. *J. Hazard. Mater.* **2021**, *409*, 124935. https://doi.org/10.1016/j.jhazmat.2020.124935.

Conclusions and Future Perspectives

In conclusion, the thesis highlights that GQDs and CQDs serve as dynamic fluorescent nanomaterials with significant potential for deployment in sensing applications. This is attributed to their alluring properties including excellent water solubility, biocompatibility photo-stability, tunable photoluminescence and low toxicity. GQDs/CQDs nanosensors play a pivotal role in implementing turn-off, turn-on, and turn off-on strategies for detecting specific analytes. The main target of this thesis is to synthesize GQDs from different Indian coals and CQDs from different biowaste resources for the detection of metal ions/biomolecules/organic compounds by using fluorescence spectroscopy.

In Chapter 2, the sensors were fabricated based on fluorescent nanomaterials that is GQDs using different Indian coals i.e., anthracite and bituminous coals labelled as A-GQDs and B-GQDs, respectively. The developed GQDs was high selective and sensitivity for Mn^{n+} (2+, 7+) ions. In the presence of Mn^{2+} and Mn^{7+} systems, the fluorescence of A-GQDs and B-GQDs was quenched through a static quenching mechanism. GQDs-Mn^{n+} nanoprobe is effective for the sensitive and selective analysis of GSH by fluorescence "turn-off-on" mechanism. The fluorescence turn-on of A and B-GQDs in the case of Mn^{2+} quencher is majorly accredited to the stable complex formation formed by reduced GSH with Mn^{2+}. Where, Mn^{2+} is bi-coordinated with O atoms from the carboxyl group of glycine residue and N atom from the amine group of glutamyl. While, the fluorescence recovery of A and B-GQDs in the presence of Mn^{7+} quencher is because of the redox reaction amid $KMnO_4$ (7+) and GSH.

In Chapter 3, highly water soluble, strong fluorescent (56.2%), and stable RH-CQDs were prepared through hydrothermal treatment of rice-husk (biowaste). RH-CQDs act as nanosensor for highly sensitive and selective detection of Fe^{3+} with 66.4% quenching and detection limit of 149 nM. The fluorescence turn-off is due to high chelating speed of Fe^{3+} for the formation of coordination complexes results in fluorescence quenching. Different photophysical parameters such as quantum yield (ϕ), average lifetime [τ_{av} (ns)], radiative (k_r) rate constant, non-radiative (k_{nr}) rate constant, rate of electron transfer (k_{ET}), and efficiency of electron transfer (ϕ_{EET}) were studied for RH-CQDs in presence and absence of Fe^{3+}. Also, RH-CQDs were used for the detection of OFX and CPX by fluorescence enhancement technique. The reason for high selectivity and sensitivity among various analytes towards fluoroquinolones is because of hydrogen bond formation between the carboxyl of RH-CQDs and amine of piperazine ring. The interference free detection is because of hydrogen bonding and charge transfer between RH-CQDs and OFX/CPX. Here, integration of two different

mechanisms (fluorescence quenching and fluorescence enhancement) was followed to construct a single sensing platform for accurate quantification of dual-mode nanosensors for the detection of metal ions and fluoroquinolones by excited state electron transfer and hydrogen bonding mechanism respectively. Therefore, this study also stimulates the detection of more than one analyte.

In Chapter 4, eco-friendly, green methodology and cheaper approach was used for synthesis of highly water soluble fluorescent CQDs from biomass waste (orange pomace) by the microwave irradiation without incorporation of chemical substituents. CQDs acts as nanosensor for the sensitive detection of Cr^{6+} with 82% quenching and a detection limit of 59.6 nM within the concentration range of 0-480 nM. The PL quenching was attributed to IFE. Also, the prepared CQDs were applied for the detection of the extremely important mono-nitrophenols with respect to environmental concern. CQDs reacted well towards 4-NP with 14 nM limit of detection. This is possibly because of formation of zwitterionic spirocyclic Meisenheimer complex and IFE. Validation of the as-prepared sensor was performed in accordance with ICH recommendations. Moreover, the developed method was used to effectively detect chromium (Cr^{6+}) and 4-nitrophenol (4-NP) in real water samples with acceptable %RSD and precision.

At last, in Chapter 5 fabrication of highly fluorescent lemon-peel derived CQDs (LP-CQDs) having inherent nitrogen functionality was done using microwave pyrolysis technique. LP-CQDs displayed encouraging results for tetracycline (TC) detection using a PL turn-off approach. LP-CQDs acts as nanosensor for the highly sensitive and selective detection of TC with 76.1% quenching with 50.4 nM detection limit. Fabricated LP-CQDs showed fluorescence quenching towards TC, elucidated by inner filter effect (IFE) mechanism. Practicality of the detection method was assessed through the analysis of real samples, resulting in satisfactory recovery percentage and relative standard deviation with respect to the developed probes. Furthermore, LP-CQDs were used as a fluorescent ink and to fabricate the paper-based fluorescent strips.

Future Perspectives

- Modification in the surface functionalisation of coal-derived GQDs to enhance the limit of detection for analytes like biomolecules.
- Application of biowaste derived CQDs for intracellular imaging.
- Implementation of prepared sensor in real-time portable sensor.
- Study the effect of different heteroatom doping on CQDs for the detection of analytes.

List Of Publications

A. Related to Ph.D. work (Objectives)

1. **A. Kundu,** B. Maity, S. Basu, Coal-derived graphene quantum dots with a Mn^{2+}/Mn^{7+} nanosensor for selective detection of glutathione by a fluorescence switch-off–on assay. *New Journal of Chemistry* **2022**, *46(16),* 7545-6556. https://doi.org/10.1039/D2NJ00220E (I.F. = 3.3)
2. **A. Kundu,** B. Maity, S. Basu, Rice-Husk Derived Carbon Quantum Dots-Based Dual-Mode Nanoprobe for Selective and Sensitive Detection of Fe^{3+} and Fluoroquinolones. *ACS Biomaterials Science & Engineering* **2022**, *8(11)*, 4764-4776. https://doi.org/10.1021/acsbiomaterials.2c00798 (I.F. = 5.8)
3. **A. Kundu,** B. Maity, S. Basu, Orange Pomace-Derived Fluorescent Carbon Quantum Dots: Detection of Dual Analytes in the Nanomolar Range. *ACS Omega* **2023**, *8(24)*, 22178–22189. https://doi.org/10.1021/acsomega.3c02474 (I.F. = 4.1)
4. **A. Kundu,** S. Basu, B. Maity, Upcycling Waste: *Citrus limon* peels derived Carbon Quantum Dots for Sensitive Detection of Tetracycline in Nanomolar Range. *ACS Omega* **2023**, *8(39)*, 36449-36459. https://doi.org/10.1021/acsomega.3c05424 (I.F. = 4.1)

B. Review articles

1. S. Sharma, **A. Kundu,** S. Basu, N. P. Shetti, T. M. Aminabhavi, Sustainable environmental management and related biofuel technologies. *Journal of Environmental Management* **2020**, *273*, 111096. https://doi.org/10.1016/j.jenvman.2020.111096 (I.F. = 8.7)

2. **A. Kundu,** N. P. Shetti, S. Basu, K. R. Reddy, M. N. Nadagouda, T. M. Aminabhavi, Identification and removal of micro-and nano-plastics: Efficient and cost-effective methods. *Chemical Engineering Journal* **2021**, *421*, 129816. https://doi.org/10.1016/j.cej.2021.129816 (I.F. = 15.1)

3. **A. Kundu,** N. P. Shetti, S. Basu, K. Mondal, A. Sharma, T. M. Aminabhavi, Versatile Carbon Nanofiber-Based Sensors. *ACS Applied Bio Materials* **2022**, *5(9)*, 4086-4102. https://doi.org/10.1021/acsabm.2c00599 (I.F. = 4.7)

4. **A. Kundu,** N. P. Shetti, S. Basu, M. N. Nadagouda, T. M. Aminabhavi, Exposure pathways to hazardous per- and polyfluoroalkyl substances. *Chemosphere* (**Revision submitted**) (I.F. = 8.8)

C. Other Publications

1. **A. Kundu,** S. Sharma, S. Basu, Modulated BiOCl Nanoplates with Porous g-C_3N_4 Nanosheets for photocatalytic degradation of Color/Colorless Pollutants in Natural Sunlight. *Journal of Physics and Chemistry of Solids* **2021**, *154*, 110064. https://doi.org/10.1016/j.jpcs.2021.110064 (I.F. = 4.0)
2. **A. Kundu, S.** Basu, N. P. Shetti, A. K. Malik, T. M. Aminabhavi, The COVID-19 Paradox: Impact on India and Developed Nations of the World. *Sensors International* **2020**, *1*, 100026. (IF=Yet to come)
3. S. Sharma, **A. Kundu,** S. Basu, N. P. Shetti, T. M. Aminabhavi, Indians vs. COVID-19: The scenario of mental health. *Sensors International*, **2020**, *1*, 100038. (IF=Yet to come)

D. Book Chapter

1. **A. Kundu,** S. Basu, Microplastics and Nanoplastics in Aquatic Environment: Challenges and Threats to Aquatic Organisms. *Assessing the Effects of Emerging Plastics on the Environment and Public Health* **2022**, 71-89. IGI Global. 10.4018/978-1-7998-9723-1.ch004

Conferences and Workshops

1. Poster presentation on the topic "**Synthesis of graphene quantum dots from anthracite and bituminous coals with Mn nano-sensor for GSH sensing"** at 7th International Conference on Bio-sensing Technology organized by Elsevier in Sitges, Spain from 22nd-25th May, 2022.
2. Oral presentation on the topic "**Rice husk derived Carbon Quantum Dots as dual mode nanosensor for the detection of metal ions and fluoroquinolones"** at International Conference on Emerging Material for Sustainable Development (EMSD-2022) under the theme "Material for sensors" organized by CSIR-CSIO, Chandigarh and IEEE AcSIR-CSIO student chapter in CSIR-CSIO, Chandigarh from 9th-11th October, 2022. **(Best oral presentation award)**
3. Attended seven days *FCS XIV*: 14TH National Workshop and Conference on Fluorescence and Raman Spectroscopy from 9-15th December, 2023 and poster presentation on the topic entitled **"Orange Pomace Derived Fluorescent Carbon Quantum Dots: Detection of Dual Analytes in Nanomolar Range"** organized by Fluorescence Society, IISER Mohali, INST, and TIFR.
4. Attended seven days workshop on "**Emerging Materials: Synthesis and Characterization Techniques**" from 14th-20th December, 2022 under the auspices of DST, Government of India under STUTI Program.
5. Attended three days training workshop on "**Mendeley Reference Manager**" from 4th to 6th July, 2020 organized by Nuhianwali Education Society.
6. DST& ACS virtual workshop "**Mastering the publishing process**" on 28th July 2020.